THE UNIVERSITY OF CHICAGO

COLLECTIVE ELECTRODYNAMIC EXCITATIONS AND NON-CONSERVATIVE DYNAMICS IN OPTICAL MATTER AND META-ATOM SYSTEMS

A DISSERTATION SUBMITTED TO
THE FACULTY OF THE DIVISION OF THE PHYSICAL SCIENCES
IN CANDIDACY FOR THE DEGREE OF
DOCTOR OF PHILOSOPHY

DEPARTMENT OF PHYSICS

BY
JOHN ALAN PARKER

CHICAGO, ILLINOIS
AUGUST 2020

TABLE OF CONTENTS

LIST OF FIGURES

LIST OF TABLES

LIST OF ACRONYMS

BD	Brownian Dynamics.
CVB	Cylindrical Vector Beam.
FDTD	Finite-Difference Time-Domain.
GLMT	Generalized Lorenz-Mie Theory.
GMMT	Generalized Multiparticle Mie Theory.
GMT	Generalized Mie Theory.
HG	Hermite-Gaussian.
LD	Langevin Dynamics.
LG	Laguerre-Gaussian.
LHC	Left Handed Circular.
MST	Maxwell Stress Tensor.
NA	Numerical Aperture.
OAM	Orbital Angular Momentum.
OM	Optical Matter.
PDA	Point-Dipole Approximation.
RHC	Right Handed Circular.
RNG	Random Number Generator.
RT	Rotation-Translation.
SAM	Spin Angular Momentum.
SD	Stokesian Dynamics.
SDE	Stochastic Differential Equation.
SLM	Spatial Light Modulator.
SLR	Surface Lattice Resonance.
TT	Translation-Translation.
VSHW	Vector Spherical Harmonic Wavefunctions.

ACKNOWLEDGMENTS

First and foremost, I would like to thank my advisor Norbert Scherer for mentoring me over the years and introducing me to the fascinating field of plasmonics and optical matter. Norbert has provided me with many great insights that have helped me steer my research in the right direction. Norbert's passion and enthusiasm for my research has kept me motivated and has helped me see the bigger picture.

I would also like to thank Stephen Gray for co-advising me on the theory and simulation involved in my work. Stephen has a great and very encompassing knowledge of the scientific field and literature, and he always provided me with the right books and papers that helped me grow my knowledge and pursue new research. Any time I had a question, Stephen either had the answer or he had a reference to pursue the answer in the back of his mind.

Additionally, I would like to thank the members of the Physics Department at the University of Chicago. Special thanks to David Reed, Stuart Gazes, Putri Kusumo, Zosia Grusberg, and Amy Schulz for providing me with assistance and advice. I am grateful to my thesis committee for providing useful feedback and interesting questions about my research.

The Research Computing Center (RCC) at the University of Chicago has been a very useful resource to me. The RCC's computing resources have provided me with over a million compute hours that have made a large number of results and figures in this dissertation possible. Additionally, the RCC has held many seminars I have attended over the years that have taught me new computational and programming skills.

All current and former members of the Scherer Lab have had a large impact on my research. I would like to thank Curtis Peterson, Yuval Yifat, Delphine Coursault, Nishant Sule, Nolan Shepherd, Uttam Manna, Tiansong Deng, and Zijie Yan for all of the discussions and collaborations we have had over the years. Many of you worked tirelessly in the lab producing experimental results, and I have benefited from your hard labor.

Finally, I want to thank my friends, family, and my fiancé Katie. Without you, none of this would be possible.

ABSTRACT

Optical trapping and optical tweezers have been used to confine and control micron and nano-sized objects based on light–matter interactions. When multiple particles are in a single optical trap, they interact with one another and form organized arrays referred to as optical matter. Optical matter is a unique formation of matter in that the interactions between particles are controlled by an external light source and its properties can be tuned with the properties of light, such as intensity, polarization, and phase. The persistent flux of the optical field that is inherent to optical matter provides novel dynamical properties, making optical matter systems inherently non-equilibrium and creating non-conservative forces and non-reciprocal interactions. As will be shown in this thesis, these properties can be utilized to build functional materials that do work at the nano-scale.

The role of non-conservative forces acting on a single optically trapped particle has been studied, but less attention has been given to the role of non-conservative interactions present in optical matter. We demonstrate that non-conservative interactions give rise to a non-reciprocal net-force in an optically bound hetero-dimer. More generally, when there are many identical particles forming an array, a single non-identical intruder particle is expelled from the array due to non-reciprocal interactions. This principle is used to segregate mixtures of optically trapped nanoparticles by size and material. We also demonstrate that non-conservative interactions give rise to positive and negative orbital torques in optical matter arrays. These arrays convert the incident spin angular momentum of light into scattered outgoing orbital angular momentum. This conversion processes is used to design a stochastic optical matter machine that utilizes non-conservative driving forces and Brownian forces for its operation.

A common theme that emerges is the importance of collective electrodynamic excitations in structured nanoparticle arrays. The selective excitation of different collective scattering modes is achieved using scalar and cylindrical vector beams. These principles are used to design and analyze a core-satellite meta-atom that has strong near-field coupling and can support magnetic modes at optical frequencies. Such meta-atoms are potential building blocks for meta-fluids and meta-materials. Optical matter and meta-atom systems are efficiently simulated using a developed generalized Mie theory software that can be coupled to a Langevin equation of motion.

CHAPTER 1
INTRODUCTION

It has long been known that light exerts a force on matter. In 1619, Johnannes Kepler introduced the idea that comet tails point away from the sun due to radiation pressure from the sun on comet dust particles. [1] In 1865, James Clerk Maxwell developed the wave theory of light that demonstrated light carries momentum. [2] In 1900, Pyotr Lebedev confirmed in experiment that light exerts a force on matter, validating the theory of Maxwell. [3] Since then, optical forces have been the subject of intense study. At the nanoscale, optical forces on nanoparticles become significant relative to Brownian fluctuation forces, which has led to the development of optical tweezers.[4, 5]

Optical trapping and optical tweezers have been widely used to trap, manipulate, and control the position of mesoscopic objects at the micro and nano-scale.[4, 6–9] The incident complex-valued electric field used to trap particles is given by an intensity, phase, and polarization profile

$$\boldsymbol{E}(\boldsymbol{r}) = E_0(\boldsymbol{r}) \exp\left[i\varphi(\boldsymbol{r})\right] \boldsymbol{n}_{\boldsymbol{E}}(\boldsymbol{r}) \tag{1.1}$$

The functional form of this field must satisfy Maxwell's equations. A particle in this field will feel intensity, phase, and polarization gradient forces that can be used to confine its position, which can be done in all three spatial dimensions.

Historically, optically tweezers have been used to trap a single object. However, it is possible to trap multiple particles in a single optical trap, where the particles will then be interacting with one another electrodynamically. [9–18] We call this optically trapped collection of interacting particles *optical matter*. The concept of optical matter was first introduced by creating a two-dimensional landscape of optical tweezers[19, 20], which can now be achieved using a spatial light modulator (SLM) or diffractive optical element (DOE) in the lab. [20–22] This is a form of "top-down" assembled optical matter, since the positions of the particles are determined by the chosen positions of the incident beams. Instead, when a single, wider optical beam is used to trap multiple particles, the resulting structures that form are "bottom-up" assembled optical matter. In this case, the electrodynamic interactions dictate the structures that form and determine the driven motion of the system.

Yan et al. have in recent years performed experiments and simulations capable of assembling optical matter arrays in two-dimensional trapping conditions using the intensity gradient force of light. [23–26] Optical angular momentum and phase gradient forces can be used to drive optical matter arrays and non-equilibrium steady-state dynamics can be achieved. [27–32] By changing the polarization of the light, the geometric structure of optical matter arrays can be altered to prefer one-dimensional chains or two-dimensional hexagonal packing. [33–35] Thus, by using the intensity, phase, and polarization of light, the properties of optical matter can be tuned on-demand by changing the properties of the incident light source in Equation (1.1). This raises the question of how the properties of light and the resulting light–mater interactions in optical matter can be used to create functional materials that can perform useful tasks.

An interesting aspect of optical matter systems is that the forces and interactions can have non-conservative components. This has been demonstrated for a single trapped particle that is driven in a unidirectional toroidal motion in the presence of thermal fluctuations, which is the simplest realization of a *stochastic machine*. [36–38] Yan et al. and Figliozzi et al. have utilizied these non-conservative forces to create driven optical matter arrays. [39–42] With multiple particles of dissimilar size or material, the non-conservative interactions can give rise to non-reciprocal interactions that cause the optical matter to be driven. [43, 44]

Since optical matter is an open system, the mechanical linear momentum of the system need not be conserved as linear momentum can be freely exchanged with the electromagnetic field. Consequently, a net force acting on a hetero-dimer was recently predicted to result in a net optical force,[44] and this non-reciprocal interaction was confirmed in simulation and experiment by Yifat et al. [45] There, the net force was identified in a plane wave and a ring trap, each of which result in the directed transport of the hetero-dimer in one or two dimensions. In this published work, I developed a theory for the dynamics of a hetero-dimer when it is instead confined in two-dimensions by a Gaussian trap. This is then extended to the case of N identical particles in the presence of a single intruder particle, where the non-reciprocal interactions lead to the expulsion of the intruder. Additionally, I considered the case of optically trapped mixtures of nanoparticles, which are novel dynamical systems where non-reciprocal interactions dominate the dynamical behavior.

The mechanical angular momentum of optical matter also need not be conserved since angular

momentum can be freely exchanged with the electrodynamic field. Sule et al. recently identified the positive and negative torque on optically bound dimers in simulation and experiment[46], which has been extended by Yan et al. to the case of N particle arrays. [35] In this published work, I developed a theory for positive and negative torque from the perspective of collective electrodynamic modes and the multipolar analysis of the scattered angular momentum from optical matter arrays. Using this theory, the collective modes are utilized to trap a probe particle near the optical matter array that is then angularly transported by driven non-conservative forces. [47] The optical matter array achieves a counter-rotating non-equilibrium steady-state, which is a realization of a stochastic machine, i.e. it relies on thermal fluctuations for its operation. Single optically trapped particles have been demonstrated to form such stochastic machines [36, 38, 48, 49], and this work is an extension of that to the case of N electrodynamically interacting particles.

To rapidly and accurately simulate the electrodynamic interactions in optical matter, a generalized Mie theory (GMT) is developed in combination with a Langevin dynamics (LD) integrator. The finite-difference time-domain (FDTD) method [50] has been used in other work, but the runtime performance restricts the study of optical matter to short time intervals.[51, 52] The discrete-dipole approximation (DDA) [53] has also been used to measure optical forces and torque, but it is also computationally expensive. [54, 55] GMT has been used to simulate photonic clusters before, but the implementation was limited to plane-wave sources and isotropic particles in the absence of thermal fluctuations.[43] Anisotropic particles in optical traps have been simulated, but the implementation was limited to a single particle. [56, 57] In this thesis, I develop a simulation method, GMT-LD, to solve the interactions for generally anisotropic particles illuminated by an arbitrary beam with analytic force and torque evaluation. GMT-LD is very efficient and can compute $\sim 1,000$ time-steps per CPU second, enabling the study of dynamical behavior of optical matter systems on the order of seconds ($dt \sim 1\,\mu s$), which is not feasible using FDTD or DDA.

In chapter 2, the principles of optical trapping and creation of optical matter are introduced. Intensity and phase gradient optical forces and torques are reviewed, and trapping of a single particle is demonstrated using the GMT-LD simulations. The optical binding energy between two particles under different light polarizations (linear, circular, and unpolarized) is used to understand the formation of larger arrays of optical matter. For two particles, work landscapes are constructed

to demonstrate the emergence of non-conservative forces when using circularly polarized light. The emergence of surface lattice resonances in optical matter arrays due to long range periodic electrodynamic interactions is shown to increase the stability of optical matter arrays of increasing size.

In chapter 3, the emergence of a non-reciprocal net-force on a hetero-dimer is demonstrated in simulation and experiment.[45] These non-reciprical interactions are used to expel a larger "intruder" particle from an array of smaller particles. A Gaussian beam defocused at the Rayleigh range [58] is shown to be the optimal beam to trap these asymmetric arrays. In mixtures of nanoparticles, the non-reciprocal interactions are shown to segregate two or more species of nanoparticles by size and material. A theoretical model is developed to explain the segregation where the steady-state behavior of the system is determined by all electric dipoles having the same phase.

In chapter 4, the spin angular momentum (SAM) of light is used to create optical orbital torques in optical matter arrays. [35, 46] The net torque can be positive or negative in sign, and a theory for the (positive and negative) scattered orbital angular momentum (OAM) per multipolar mode of the collective electrodynamic system is developed. An optical matter array is shown to operate as an SAM–OAM optical converter based on angular momentum selection rules for rotationally symmetric arrays. This converter is used to construct an optical matter stochastic machine that uses non-conservative driving forces and Brownian fluctuations for its operation.

In chapter 5, the collective electrodynamic properties of nanoparticles and nanoparticle arrays are analyzed towards creating a core-satellite meta-atom. Cylindrical vector beams (CVB) are used to selectively excite families of multipolar modes in the system. A theory for the electrodynamic coupling strength in nanoparticle arrays is developed using the generalized multiparticle Mie theory. Core-satellite meta-atoms are realized in experiment and simulation and are shown to demonstrate a magnetic response at optical frequencies.[59, 60] Additionally, CVBs are used to selectively excite dark plasmons in gold dimers and electrodynamic anapoles in silicon nano-spheres. [61, 62]

In chapter 6, the efficient simulation of optical matter using generalized multiparticle Mie theory is discussed. The theory solves the electrodynamic interactions between N particles illuminated by an arbitrary beam of light, and analytic expressions for the forces and torques are provided. These forces and torques are used as input to a Brownian, Langevin, or Stokesian dynamics simulation.

Stokesian dynamics is used to incorporate the hydrodynamic coupling interactions due to fluid flow around the particles.

CHAPTER 2
OPTICAL TRAPPING AND OPTICAL MATTER

Optical trapping and optical tweezers have been widely used to trap, manipulate, and control the position of mesoscopic objects at the micro and nano-scale.[4, 6–8] Optical tweezers use the force exerted by tightly focused light to create stable trapping conditions in all 3 dimensions for the trapped object. In addition, the incident light has phase and polarization properties that can affect the interactions with the trapped particle. For example, using a circularly polarized optical tweezer, referred to as an "optical torque wrench", the trapped object can be made to continuously rotate. [63, 64]

When a second particle is introduced to the optical trap, the two particles scatter the incident field and interact with one another electrodynamically. The interaction force is oscillatory as the separation between the two particles is varied, resulting in attractive and repulsive interaction forces. For certain separations, the interaction is stabilizing and the two particle form an optically bound pair, referred to as *optical binding*. [10, 13, 65, 66] Optical binding interactions can be used to trap more than two particles and build stable arrays. The resulting arrays are referred to as *optical matter*. [11, 19]

This chapter introduces the concepts of optical trapping and optical matter starting with nanoscale optics and Mie theory. The generalized Mie theory is used to solve the interactions between particles and determine the optical forces and torques that can be used in a time-stepped Langevin dynamics simulation. The role of light polarization in optical matter is discussed and how circularly polarized light can generate non-conservative forces. Increasingly large optical matter arrays are shown to support collective electrodynamic excitations, known as surface lattice resonances, that lead to increasingly stable arrays due to long-range optical binding interactions.

2.1 Nanoscale optics and Mie theory

Nanoscale optics operates in a regime where the principles of geometric optics are no longer valid and the full wave nature of electromagnetic fields is required. We consider time-harmonic fields of

frequency ω, e.g. the time-dependent electric field is of the form

$$\boldsymbol{E}(\boldsymbol{r},t) = \mathrm{Re}\left[\boldsymbol{E}(\boldsymbol{r})\exp(-i\omega t)\right] \tag{2.1}$$

where $\boldsymbol{E}(\boldsymbol{r})$ is the complex-valued electric field. In this representation, the macroscopic Maxwell's equation are [67]

$$\begin{aligned}
\boldsymbol{\nabla}\times\boldsymbol{E}(\boldsymbol{r}) &= i\omega\boldsymbol{B}(\boldsymbol{r}) \\
\boldsymbol{\nabla}\times\boldsymbol{H}(\boldsymbol{r}) &= -i\omega\boldsymbol{D}(\boldsymbol{r}) + \boldsymbol{j}(\boldsymbol{r}) \\
\boldsymbol{\nabla}\cdot\boldsymbol{D}(\boldsymbol{r}) &= \rho(\boldsymbol{r}) \\
\boldsymbol{\nabla}\cdot\boldsymbol{B}(\boldsymbol{r}) &= 0
\end{aligned} \tag{2.2}$$

where $\boldsymbol{D}(\boldsymbol{r},\omega) = \varepsilon_0\varepsilon(\boldsymbol{r},\omega)\boldsymbol{E}(\boldsymbol{r},\omega)$ is the electric field displacement and $\boldsymbol{B}(\boldsymbol{r},\omega) = \mu_0\mu(\boldsymbol{r},\omega)\boldsymbol{H}(\boldsymbol{r},\omega)$ is the magnetic field displacement. With these expressions, we assume any material response is linear and spatially local, i.e. ε and μ does not depend on the wavevector $\boldsymbol{k}$. The material response can generally be temporally dispersive, i.e. ε and μ depend on ω. At visible frequencies, all natural materials are not magnetic, i.e. $\mu = 1$, so μ will be dropped throughout. The imaginary part of ε is associated with energy dissipation in the medium.

Optical matter systems consist of a collection of nanoparticles in an arbitrary optical field in an open, mechanically dissipative medium. The medium (generally water) has a real-valued uniform permittivity ε_m. Each nanoparticle has a complex permittivity $\varepsilon_i(\omega)$, and we assume that each particle has no free charge ($\rho_i = 0$) and hence no free currents ($\boldsymbol{j}_i = 0$). Maxwell's equations for the optical matter system then reduce to a piecewise homogeneous vector Helmholtz equation [67]

$$\begin{aligned}
(\boldsymbol{\nabla}^2 + k_i^2)\boldsymbol{E}_i(\boldsymbol{r}) &= 0 \\
(\boldsymbol{\nabla}^2 + k_i^2)\boldsymbol{H}_i(\boldsymbol{r}) &= 0
\end{aligned} \tag{2.3}$$

where $k_i = \sqrt{\varepsilon_i}\omega/c$ is the wavenumber in medium i. Additionally, the boundary conditions for Maxwell's equations must be satisfied on every boundary between the surfaces of medium i and

medium j

$$\begin{aligned} \hat{\boldsymbol{n}} \times (\boldsymbol{E}_i - \boldsymbol{E}_j) = 0 \\ \hat{\boldsymbol{n}} \times (\boldsymbol{H}_i - \boldsymbol{H}_j) = 0 \end{aligned} \tag{2.4}$$

Note that the boundary conditions for the normal field components are automatically satisfied if Equation (2.3) and Equation (2.4) are satisfied everywhere.

The simplest system to consider is a single spherical particle illuminated by an x-polarized plane-wave. The solution to Equation (2.3) and Equation (2.4) for this system can be obtained analytically through the well known Mie theory. [68–70] Mie theory uses the vector spherical harmonic wavefunctions (VSHW) $N_{pnm}^{(J)}(\boldsymbol{r}, \omega)$, which are the eigenfunctions of the Helmholtz operator $(\boldsymbol{\nabla}^2 + k^2)$. J can be 1 or 2 for propagating and counter-propagating solutions or 3 or 4 for spherically outgoing and ingoing solutions; the p index is 0 for electric modes or 1 for magnetic modes; the n index is a positive integer for the order of the mode (1 is dipole, 2 is quadrupole, 3 is octupole, etc.); the m index ranges from $-n$ to n and quantifies the angular momentum of the mode. Mie theory then provides the analytically exact solution for the scattered field ($\boldsymbol{E}_{\text{scat}}$) and internal field ($\boldsymbol{E}_{\text{int}}$)

$$\boldsymbol{E}_{\text{scat}}(r) = \sum_{n=1}^{\infty} E_n (i a_n \boldsymbol{N}_{0n1}^{(3)} - b_n \boldsymbol{N}_{1n1}^{(3)}) \tag{2.5}$$

$$\boldsymbol{E}_{\text{int}}(r) = \sum_{n=1}^{\infty} E_n (c_n \boldsymbol{N}_{0n1}^{(1)} - i d_n \boldsymbol{N}_{1n1}^{(1)}) \tag{2.6}$$

where a_n, b_n, c_n, and d_n are the Mie coefficients that have analytically exact expressions and E_n is a normalization factor. [69] Similar expressions exist for the magnetic field $\boldsymbol{H}$.

Mie theory has been generalized to more complex scenarios in several ways since its discovery. The generalized Lorenz-Mie theory (GLMT) extends the solution to an arbitrary incident source by decomposing the incident wave into VSHW functions. [71–73] The generalized multiparticle Mie theory (GMMT) extends the solution to multiple particles using the translation addition theorm for the VSHW functions. [74, 75] The T-matrix method extends the solution to non-spherical particles by numerically solving the boundary condition for more complex geometries. [76, 77] Additionally, a planar surface can be incorporated by matching the boundary condition on its surface using a plane

wave decomposition. [78] Taken together, we refer to the combination of these generalizations as generalized Mie theory (GMT). The full theory of GMT, including its software implementation, is covered in Chapter 6.

In optical matter, we will often make use of metal nanoparticles, such as silver or gold. Light's interaction with these metals is dominated by the motion of free conduction band electrons in the nanoparticle. The free electrons oscillate about 180° out-of-phase with the incident field, causing the permittivity to be negative and the surface to be highly reflective. For finite-sized particles, the electron gas can have surface and volume charge density oscillations that lead to what is known as plasmon resonances. [67, 79] In the Drude-Sommerfield model for the electron gas, the complex permittivity of the metal is [67]

$$\varepsilon(\omega) = 1 - \frac{\omega_p}{\omega^2 + i\omega\gamma} \tag{2.7}$$

where ω_p is the plasma frequency and γ is the electron damping term. More generally, we can account for the possible interband transitions using a Drude-Lorentz model [67]

$$\varepsilon(\omega) = \varepsilon_\infty + \sum_n \frac{\sigma_n \omega_n^2}{\omega_n^2 - \omega^2 - i\omega\gamma_n} \tag{2.8}$$

where σ_n is the strength of each pole.

Equation (2.8) can be used as a model where the coefficients are fit with experimental measurements of $\varepsilon(\omega)$. Figure 2.1 shows the experimentally measured permittivity of silver and gold from Johnson and Christy. [80] For comparison, a dielectric material (Si) is shown that has an index of refraction $n \approx 3.7$. Gold has a larger imaginary part to its permittivity than silver or silicon and consequently suffers more absorption and subsequent thermal losses.

For each of these 3 materials, Figure 2.1 shows the scattering and absorption cross-sections for a 150 nm diameter nanoparticle in water. The cross-sections are obtained analytically from the Mie

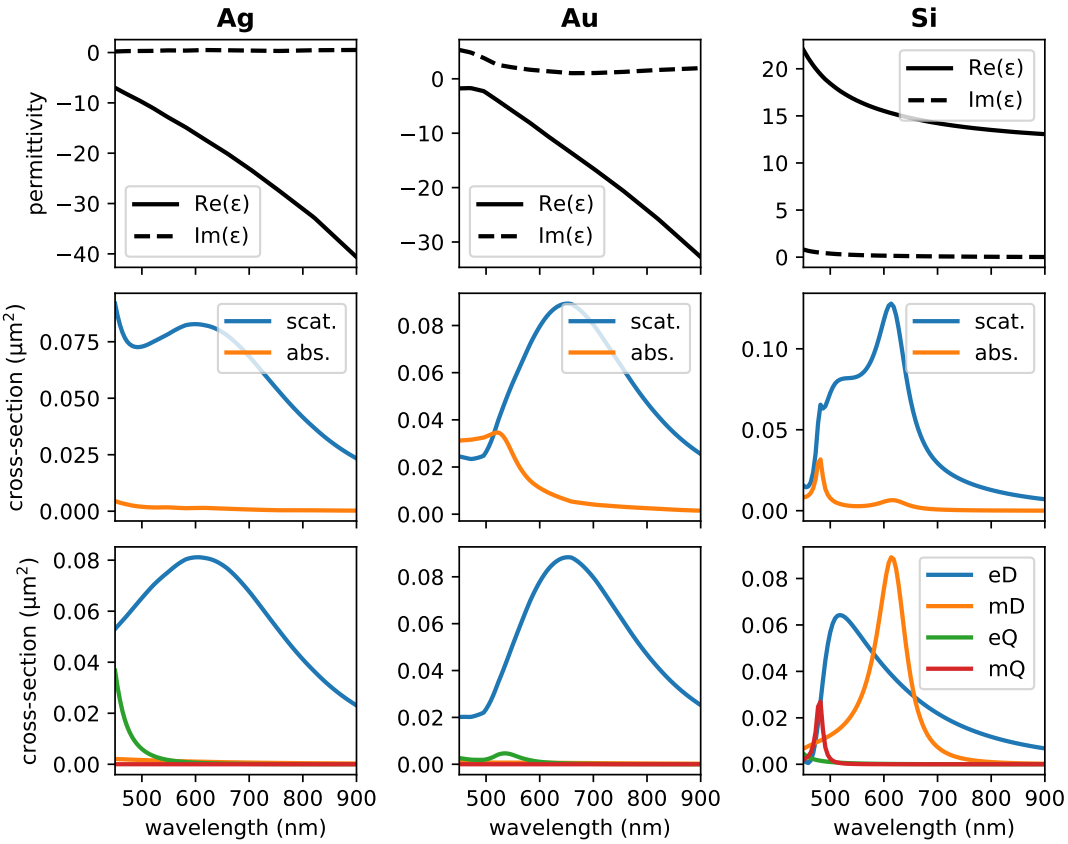

Figure 2.1: Electromagnetic excitation of different nanoparticles. (top) Permittivity (real and imaginary) as a function of wavelength for silver, gold, and silicon. (middle) Cross-sections (scattering and absorption) of a nanoparticle of diamter 150 nm as a function of wavelength for the same materials. (bottom) Cross-sections per multipolar mode for the same particles calculated using Mie theory.

coefficients of the particle

$$C_{\text{scat}} = \frac{2\pi}{k^2}\sum_{n=1}^{\infty}(2n+1)(|a_n|^2 + |b_n|^2) \tag{2.9}$$

$$C_{\text{ext}} = \frac{2\pi}{k^2}\sum_{n=1}^{\infty}(2n+1)\text{Re}(a_n + b_n) \tag{2.10}$$

$$C_{\text{abs}} = C_{\text{ext}} - C_{\text{scat}} \tag{2.11}$$

All three particles have resonances at visible frequencies (silver and gold have plasmon resonances while silicon has a Mie resonance). Figure 2.1 reveals the multipolar character of these resonances for each particle. The Ag and Au nanoparticles are dominated by electric dipole radiation; at

shorter wavelengths, the Ag particle has an emerging electric quadrupole mode while for the Au particle the electric dipole is diminished by increasing absorption due to interband transitions. The silicon nanoparticle has both electric and magnetic dipole radiation at visible wavelengths; at shorter wavelengths a magnetic quadrupole resonance emerges. These silicon nanoparticles have sharper resonances than their plasmonic counterparts and can generally support magnetic modes.

2.2 Optical forces and optical tweezers in 2D

An optical matter system must conserve the total linear momentum of the system, which includes both particle momentum and electromagnetic field momentum. The Maxwell stress tensor (MST), $\overleftrightarrow{\boldsymbol{T}}$, measures the rate of electromagnetic field momentum density transfer at a point

$$\overleftrightarrow{\boldsymbol{T}} = \varepsilon_0 \varepsilon_m \boldsymbol{E} \otimes \boldsymbol{E} + \mu_0 \boldsymbol{H} \otimes \boldsymbol{H} - \frac{1}{2}(\varepsilon_0 \varepsilon_m E^2 + \mu_0 H^2) \overleftrightarrow{\boldsymbol{I}} \tag{2.12}$$

By conservation of linear momentum, the amount of (time-averaged) field momentum exiting a closed surface S surrounding a particle must be equal to the mechanical (time-averaged) force on the particle

$$\langle \boldsymbol{F} \rangle = \int_S \langle \overleftrightarrow{\boldsymbol{T}} \rangle \cdot d\boldsymbol{S} \tag{2.13}$$

In GMT, the MST can be integrated analytically over the VSHW incident and scattering wavefunctions. The complete force expressions are given in Section 6.1.10.

A simplified force equation can be obtained in the Rayleigh approximation where a particle is approximated as a point dipole source. Consider a general optical field with position-dependent amplitude, $E_0(\boldsymbol{r})$, position-dependent phase, $\varphi(\boldsymbol{r})$, and a globally constant polarization vector, $\boldsymbol{n}_E$. The field is then

$$\boldsymbol{E} = E_0(\boldsymbol{r}) e^{i\varphi(\boldsymbol{r})} \boldsymbol{n}_E \tag{2.14}$$

The induced dipole moment in the particle is given from the particle's polarizability and the local field

$$\boldsymbol{p} = \alpha(\omega) \boldsymbol{E}(\boldsymbol{r}) \tag{2.15}$$

where α is the complex polarizability $\alpha = \alpha' + i\alpha''$. The cycle-averaged force acting on the point dipole particle can be obtained by analytically integrating the MST over the incident and scattered fields produced by the dipole [67]

$$\langle \boldsymbol{F} \rangle = \frac{\alpha'}{4} \boldsymbol{\nabla} E_0^2 + \frac{\alpha''}{2} E_0^2 \boldsymbol{\nabla} \varphi \tag{2.16}$$

The first term in Equation (2.16) is referred to as the *intensity gradient force*, and the second term is referred to as the *phase gradient force*. For a particle in a plane-wave, the intensity gradient vanishes and the phase gradient is along the direction of propagation, $\boldsymbol{k}$, and is therefor responsible for the radiation pressure acting on the particle. For a particle in a Gaussian beam, the intensity gradient force is non-vanishing and can be used to trap the particle, with forces directed towards the focus of the beam. If the numerical aperture (NA) of the beam is sufficiently high, the intensity gradient in the $-\boldsymbol{k}$ direction can be stronger than the radiation pressure, resulting in stable trapping in all three dimensions. We call this *optical trapping*, and the tightly focused (high NA) beam used to trap a single particle an *optical tweezer*. Optical tweezers have been used to precisely control the position of micro and nano-scale sized objects. [7]

For a Gaussian beam of any polarization, the incident field intensity and phase are

$$I = E_0^2 \frac{w_0^2}{w(z)^2} \exp(-2\rho^2 / w(z)^2) \tag{2.17}$$

$$\varphi = kz + \frac{k\rho^2}{2R(z)} - \psi(z) \tag{2.18}$$

where $R(z)$ is the beam's radius of curvature, w_0 is the beam waist, $w(z)$ is the evolving beam width, and $\psi(z)$ is the Gouy phase. The lateral optical forces are due to intensity and phase gradients, $\boldsymbol{\nabla}_\rho I$ and $\boldsymbol{\nabla}_\rho \varphi$, which results in the following expression for the total lateral force on a single particle trapped in a Gaussian beam using Equation (2.16)

$$\boldsymbol{F} = -\hat{\boldsymbol{\rho}} \rho E_0^2 \frac{w_0^2}{w(z)^2} \exp(-2\rho^2 / w(z)^2) \left[\frac{\alpha'}{w(z)^2} - \frac{k\alpha''}{2R(z)} \right] \tag{2.19}$$

The first term in brackets is due to the intensity gradient and is always radially inward. The second

term in brackets is due to the phase gradient and can be attractive or repulsive depending on the sign of the radius of curvature. For $z > 0$, $R(z) > 0$ and the phase gradient term is repulsive, i.e. a diverging beam is less stable than a focused beam. For $z < 0$, $R(z) < 0$ and the phase gradient is attractive. Whether this increases the trap stability depends on the phase of the particle's polarizability α. The intensity gradient force (proportional to the real part of α) is weakened due to the evolving beam width, while the phase gradient force (proportional to the imaginary part of α) increases.

For small displacements from the center of the beam ($\rho \ll 1$), the optical force becomes harmonic, $\boldsymbol{F} = -k\boldsymbol{\rho}$, where the trap stiffness, k, is

$$k = \frac{E_0^2 w_0^2}{w(z)^2}\left[\frac{\alpha'}{w(z)^2} - \frac{k\alpha''}{2R(z)}\right] \tag{2.20}$$

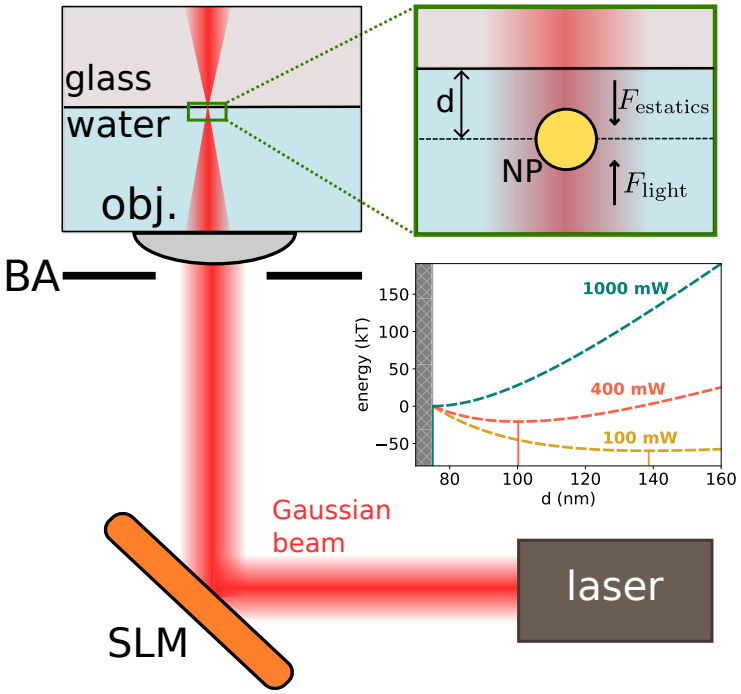

Figure 2.2: Optical setup for 2D optical trapping in an inverted microscope. A Gaussian laser source is modulated by an SLM and focused by a water objective onto a sample plane near the glass–water interface. A nanoparticle can become trapped at the center of this beam a distance d away from the interface. The value of d is determined by a balance between the light's radiation pressure and the electrostatic repulsion from the charged interface.

For many applications, having such a tightly focused (high NA) beam may not be desirable

and thus trapping in the z-direction cannot be obtained. An alternative approach is to trap in the z-direction using a balance of forces between radiation pressure and screened double-layer electrostatics at a glass-water interface. [41] The total force in the z-direction is

$$F_z = \frac{\alpha''}{2} E_0^2 k - C \exp\left[(z-a)/\lambda_D\right] \tag{2.21}$$

where a is the radius of the particle, λ_D is the Debye (screening) length of the medium, and C is constant that depends on the dielectric properties of the medium and the surface charge potentials of the particle and glass-water interface. The full expression for C is provided in Section 6.2.4. The particle reaches a zero force condition when

$$z = a - \lambda_D \log\left(\frac{\alpha'' E_0^2 k}{2C}\right) \tag{2.22}$$

When $\alpha'' E_0^2 k > 2C$, the particle is pushed against the surface.

Figure 2.2 shows a simplified picture of the optics to create such a two-dimensional trapping condition. A Gaussian laser source, optionally phase-modulated by a spatial light modulator (SLM), is focused by a water objective towards the glass-water interface, where the water contains a prepared sample of (electrically charged) nanoparticles. A nanoparticle in the water is pushed in by the radiation pressure of the beam to the top water–glass interface, but stops short of colliding due to the electrostatic repulsion between the charged ligands on the NP's surface and the charged glass interface. [81] The potential energy of the trapped NP along the z-direction depends on the power of the incident beam; as the power increases, the stable plane at $z = d$ moves towards the interface according to Equation (2.22). For a Gaussian beam with power $P = 1\,\mathrm{W}$ and width $w_0 = 1500\,\mathrm{nm}$, the radiation pressure overcomes the electrostatics and causes the NP to stick to the surface of the glass.

In such an optical setup, the z positions of the particles are effectively constrained to $z = d$. Forces in the x and y directions will only come from optical fields and Brownian motion. Thus, we have an optical trapping environment that works for lower NA beams in two dimensions. Figure 2.3(a) shows the electric field of a y-polarized Gaussian beam used for trapping; the forces due to this optical trap acting on a silver nanoparticle in the xy plane is shown in Figure 2.3(b). These optical

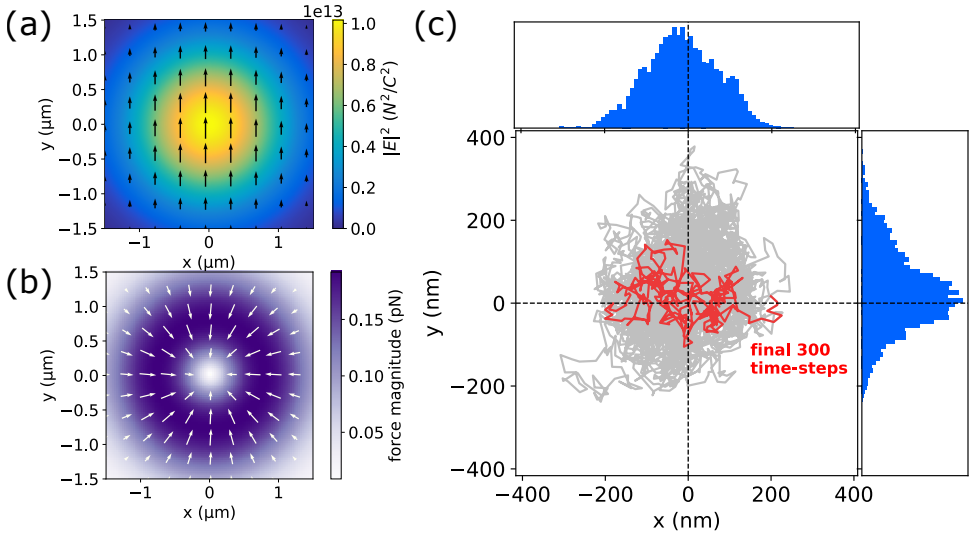

Figure 2.3: Trapping using a single particle optical tweezer setup. (a) Electric field intensity for a y-polarized Gaussian optical trap. (b) The forces acting on a 150 nm diamter Ag nanoparticle in a Gaussian beam trap ($w_0 = 1500\,\text{nm}$, $P = 50\,\text{mW}$). (c) A single particle trajectory in the trap obtained from a Langevin dynamics simulation ($T = 300\,\text{K}$, $dt = 5\,\mu\text{s}$, $t_f = 250\,\text{ms}$).

forces can then be used in a Langevin equation of motion for the particle that takes into account the drag on the particle due to fluid flow and thermal fluctuation forces. Figure 2.3(c) shows the trajectory and stable optical trapping of the silver nanoparticle.

There are three global polarization states $\boldsymbol{n}_E$ for the incident beam of interest. For linear polarization, $\boldsymbol{n}_E$ is a real valued two-dimensional vector along the direction of polarization. For circular polarization, $\boldsymbol{n}_E = \frac{1}{\sqrt{2}}(\hat{\boldsymbol{x}} \pm \hat{\boldsymbol{y}})$, where $+$ is taken for right-handed polarized light and $-$ is taken for left-handed polarized light. Elliptical polarization is any combination of linear and circular polarized light. Unpolaralized light is a special case where we assume the fields have spatial coherence while having no temporal coherence. The forces on particles in unpolarized light are obtained by adding the forces for x and y-polarized light (as opposed to adding the fields, which would result in light polarized at 45°)

$$\boldsymbol{F}^{\text{unpol}} = \frac{1}{2}(\boldsymbol{F}^{x\text{-pol}} + \boldsymbol{F}^{y\text{-pol}}) \tag{2.23}$$

2.3 Dynamics of a dimer pair: optical binding

The example in Figure 2.3 has a single trapped nanoparticle. If instead there are N particles trapped in the beam, all mutually interacting with one another, we call the resulting cluster of interacting particles *optical matter*. In addition to the intensity and phase gradient of the incident light in Equation (2.16), there will now be additional field gradient forces due to the light scattered by each particle. Interactions in optical matter are generally N-body forces – the light continues to scatter and re-scatter in a way that cannot be represented as pair-wise forces.

To understand optical matter, we first consider the case of two interacting particles. If two particles are placed in a linearly polarized plane wave, there will be no direct intensity or phase gradient forces in the lateral plane of the form Equation (2.16). However, the light scattered by one particle will produce a field that has intensity and phase gradients at the second particle. This leads to optical forces in the lateral plane even though the incident light is uniform. Consider a particle at the origin and a second particle at polar coordinates (r, ϕ). The total field at the second particle, to first-order scattering, is a superposition of incident and scattered fields

$$\boldsymbol{E}_{\text{total}} = \boldsymbol{E}_{\text{inc}} + \boldsymbol{E}_{\text{scat}} = E_0 \hat{\boldsymbol{x}} - \frac{k^2 \alpha E_0}{4\pi\varepsilon_0 \varepsilon_m r} \sin(\phi) \exp(ikr) \hat{\boldsymbol{\phi}} \tag{2.24}$$

The resulting phase and intensity of the total field are

$$\varphi = kr \tag{2.25}$$

$$I = |\boldsymbol{E}|^2 = E_0^2 + \left(\frac{k^2 \alpha E_0}{4\pi\varepsilon_0 \varepsilon_m r} \right)^2 \sin^2 \phi + \frac{k^2 \alpha E_0^2}{2\pi\varepsilon_0 \varepsilon_m r} \sin(\phi) \cos(kr) \tag{2.26}$$

There are both intensity and phase gradients of the combined field that result in lateral forces on a second particle. The magnitude of these gradient forces increases with the polarizability of the particle because more polarizable particles generate more interference with the incident wave. For this reason, highly polarizable particles with large scattering cross-sections – such as plasmonic particles (Ag and Au) that have plasmon resonances or high-index dielectric particles (Si) that have Mie resonances – are ideal for constructing optical matter.

Figure 2.4 shows the optical binding energy of two silver nanoparticles in a plane-wave and

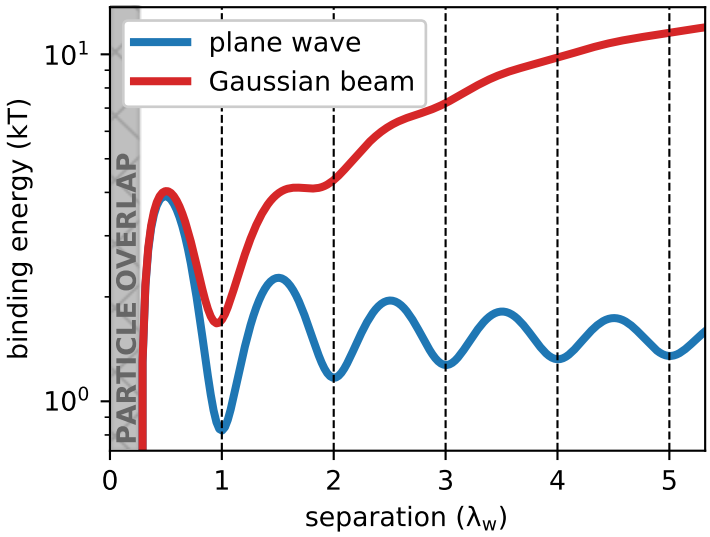

Figure 2.4: Optical binding energy between a pair of 150 nm diameter Ag nanoparticles in a plane wave and a Gaussian beam ($w_0 = 1500\,\text{nm}$) in units of k_BT ($T = 300\,\text{K}$). In the plane wave, the energy is a minimum at integer multiples of the wavelength (in water). In the Gaussian beam, additional energy is required to pull the particles out of the trap.

a Gaussian beam. For a plane wave, the binding energy is a minima at integer multiples of the wavelength in water, and the binding energy weakens as $1/r$. Additionally, the particles can form an electrodynamically bound dimer pair as the surface-to-surface distance goes to zero and the electrodynamic interaction becomes attractive. If instead the particles are in a Gaussian beam, there is additional work required to pull the particles apart as work has to be done against the intensity gradient forces present in the beam. The Gaussian beam makes the first optical binding separation ($r = \lambda_w$) significantly more favorable than the subsequent optical binding separations.

The point dipole approximation can be used to explicitly construct the force on a dimer pair. [65] In the far-field limit ($kr \gg 1$), the binding force (F_r) and azimuthal force (F_ϕ) for two particles in linearly polarized light is given by

$$F_r = \frac{|\alpha|^2|E_0|^2k^2}{8\pi\varepsilon_m\varepsilon_0 r^2}\left[kr(\cos^2\phi - 1)\sin(kr) + 2(2\cos^2\phi - 1)\cos(kr)\right] \tag{2.27}$$

$$F_\phi = \frac{|\alpha|^2|E_0|^2k^2}{8\pi\varepsilon_m\varepsilon_0 r^2}\sin(2\phi)\cos(kr) \tag{2.28}$$

where r is the center-to-center distance and ϕ is the angle of the dimer relative to the incident

polarization. The azimuthal force exerts a torque on the dimer that tends to align the dimer along a direction perpendicular to the incident polarization ($\phi = \pi/2$), where the azimuthal force vanishes. For this stable orientation, the optical binding force becomes

$$F_r = \frac{|\alpha|^2 |E_0|^2 k^3}{8\pi\varepsilon_m\varepsilon_0 r}\sin(kr) + \mathcal{O}\left(\frac{1}{r^2}\right) \tag{2.29}$$

The optical binding energy is then

$$U_r = -\int_{\infty}^{r'} F_{r'} dr' \approx -\frac{|\alpha|^2 |E_0|^2 k^2}{8\pi\varepsilon_m\varepsilon_0 r^2}\cos(kr) + \mathcal{O}\left(\frac{1}{r^3}\right) \tag{2.30}$$

The binding energy is a minimum when $kr = 2\pi n$, where $n = 1, 2, 3\ldots$, resulting in stable binding at distances $r_n = n\lambda_m$. We refer to these stable binding separations as *first optical binding site*, *second optical binding site*, etc. The energy of each optical binding site decreases as n increases. The wavelength of the light in the medium defines the length scale of the optical binding interaction.

In unpolarized light, the azimuthal force vanishes and the binding energy remains the same. A dimer in unpolarized light will be bound, but have no preferred orientation and its angular dynamics are diffusive. In circularly polarized light, the azimuthal force instead results in a net torque acting on the dimer while the binding energy remains the same. A dimer in circularly polarized light will be bound and azimuthally driven by this net torque.

2.4 Conservative and non-conservative force fields

In Figure 2.2, we calculated the energy of the particle along the z-coordinate, and in Figure 2.4 we calculated the energy of an optically bound pair and approximated the energy in Equation (2.30). However, the energy is only well-defined if the force-fields are conservative, i.e. if $\boldsymbol{\nabla} \times \boldsymbol{F} = 0$. This is generally not true in optics and optical matter, as can be seen by taking the curl of Equation (2.16)

$$\boldsymbol{\nabla} \times \boldsymbol{F} = \frac{\alpha''}{2}\boldsymbol{\nabla} \times (E_0^2 \nabla\varphi) \neq 0 \tag{2.31}$$

The curl of the intensity gradient term vanishes, but the curl of the phase gradient term is generally non-zero. Consequently, the work required to move a particle around a closed loop is generally

non-zero and path-dependent.

As the simplest example, consider one particle fixed at the origin, and a second particle that is moved in the resulting optical force field. For any point $\boldsymbol{r}$ of the second particle, we can construct some pathway from a reference point $\boldsymbol{r_0}$ to calculate the work required to get there

$$W(\boldsymbol{r}) = -\int_{\boldsymbol{r_0}}^{\boldsymbol{r}} \boldsymbol{F} \cdot d\boldsymbol{S} \tag{2.32}$$

where S is some pathway connecting $\boldsymbol{r_0}$ and $\boldsymbol{r}$.

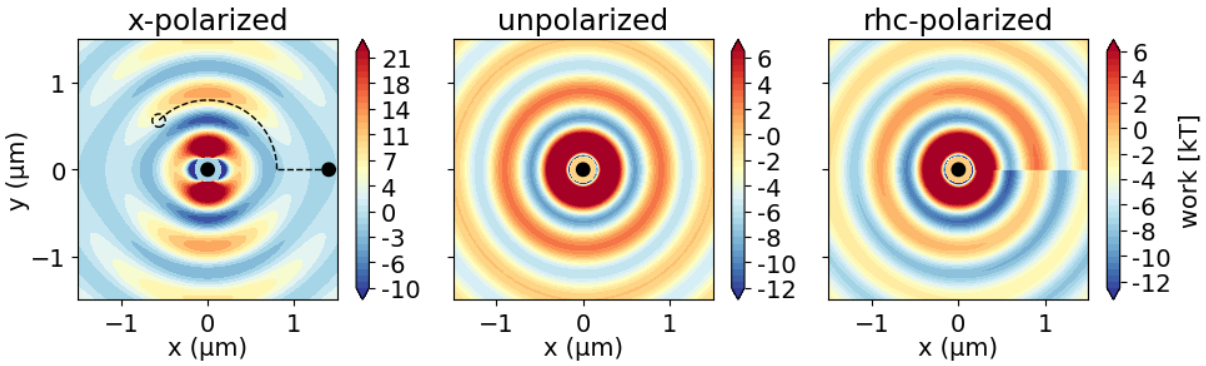

Figure 2.5: Two-dimensional work landscapes for a second particle ($R = 75\,\text{nm}$) illuminated by a plane wave in the presence of a particle fixed at the origin for 3 different light polarizations: x-polarized (left), unpolarized (center), and right handed circularly (RHC) polarized (right). The work curve is discontinuous and path-dependent for RHC polarized light (path taken shown by dashed lined). The wavelength of light in the water medium ($n = 1.33$) is $\lambda_w = 600\,\text{nm}$.

Figure 2.5 shows the two-dimensional work function, $W(\boldsymbol{r})$, along a specified path for 3 different incident light polarizations (x-polarized, unpolarized and RHC polarized). The reference point is chosen to be $\boldsymbol{r_0} = (x_0, 0)$, and the path S is chosen to be a counter-clockwise semi-circle followed by a radial path to the final point $\boldsymbol{r}$, resulting in the following work

$$W(\phi, \rho) = -\int_0^{\phi} F_\phi(\phi', \rho = x_0) d\phi' - \int_{x_0}^{\rho} F_\rho(\phi = \phi, \rho') d\rho' \tag{2.33}$$

For x-polarized light, the work profile can effectively be thought of as a potential energy surface, as has been done earlier by Yan et al. [25] There are energy minima at the optical binding site along the y-direction, and a near-field minimum for contact along the x-direction. For unpolarized light, the work profile can again be thought of as a potential energy surface, now with radial symmetry.

Optical binding separations and near-field coupling are present without any preferred orientation.

For circularly polarized light, the work profile is clearly non-conservative due to the discontinuity along $y = 0$ and thus an energy surface cannot be constructed. The work profile has the same radial symmetry as unpolarized light, but with a constant work gradient in the azimuthal direction. Consequently, a second particle placed at any of the optical binding sites will be azimuthally driven with the same handedness as the incident light.

Non-conservative optical forces for a single particle in optical tweezers have been observed. [36, 48, 82] When the optically trapped particle fluctuates away from the center of the trap, it experiences so-called spin-curl forces that bias its motion with a particular handedness in a toroidal motion. This is the simplest realization of a *stochastic optical matter machine*: a system capable of doing work in a closed loop due to thermal fluctuations and driven by non-conservative optical forces.

2.5 Building and simulating optical matter arrays

The optical binding interaction of two particles can be used to build larger optical matter arrays. The total electric field is a sum of the incident field and the scattered fields from every particle. The resulting field intensity is

$$I(x,y) = |\boldsymbol{E}(x,y)|^2 = \left| \boldsymbol{E}^{\text{inc}}(x,y) + \sum_i \boldsymbol{E}_i^{\text{scat}}(x,y) \right|^2 \tag{2.34}$$

Figure 2.6 shows the field intensity outside an optical matter array as it's built particle by particle in a circularly polarized plane-wave.

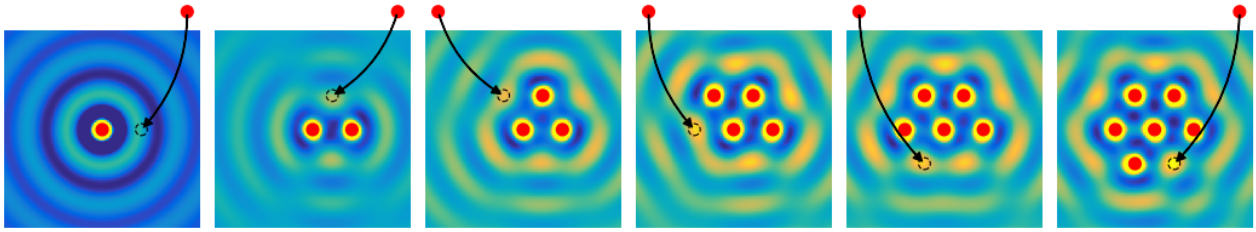

Figure 2.6: The electric field intensity around optical matter arrays consisting of 1 to 6 Ag nanoparticles. The arrays are illuminated by a RHC polarized plane-wave. An additional particle is attracted to regions of high field intensity; each panel shows an example of where an additional particle might go as the array is built.

When a particle is added to an existing array, it feels strong intensity gradient forces due to the interference of the incident and scattered fields. For a given optical intensity landscape $I(x, y)$, the force field is proportional to the gradient of the intensity, $\boldsymbol{F}(x, y) \propto \boldsymbol{\nabla} I(x, y)$. Consequently, new particles are attracted to regions of maximum field intensity. In Figure 2.6, particles are added to such maximum intensity regions. For circularly polarized light, the interference patters are such that optical matter typically form hexagonal arrays. In principle, optical matter arrays of any size (any number of particles) can be constructed provided the incident light has sufficient power density over the extent of the array.

To simulate the dynamics of optical matter arrays, consider N particles in an optical field near a glass–water interface. Figure 2.7 shows 2D and 3D schematics of the optical matter arrays. Using GMT, the interactions of the particles with each other and the interface can be solved for. For each nanoparticle, the force acting on it is calculated by integrating the Maxwell stress tensor. The forces

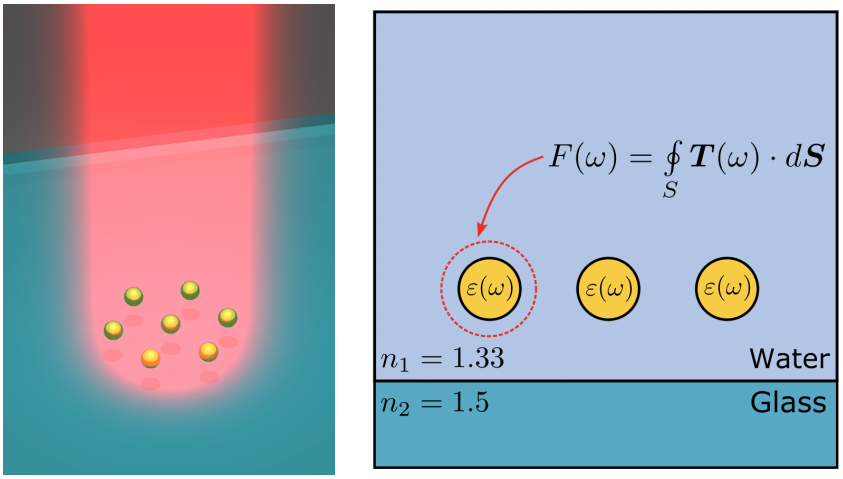

Figure 2.7: Schematics of optical matter assembly. (left) 3D schematic of a 7 nanoparticle optical matter array trapped and assembled in a Gaussian beam near a glass–water interface. (right) 2D projection of the optical matter array from a side view. For each nanoparticle, the optical force is calculated by integrating the Maxwell stress tensor around it.

can be inserted into a Langevin equation of motion to obtain a simulated trajectory of the optical matter array

$$\overbrace{m_i \frac{d\boldsymbol{v}_i(t)}{dt}}^{\text{inertia}} = \overbrace{-\Gamma_i \boldsymbol{v}_i(t)}^{\text{friction}} + \overbrace{\alpha_i \boldsymbol{\eta}_i(t)}^{\text{noise}} + \overbrace{\boldsymbol{F}_i(t)}^{\text{electrodynamic}} \tag{2.35}$$

The Langevin equation of motion accounts for the inertia of the particles, the frictional force due

to the fluid medium, Brownian noise fluctuation forces from the thermal bath, and the driving electrodynamic forces. A full description of the theory and computation of the dynamics, including rotational motion and hydrodynamic coupling interactions, is in Section 6.2.

2.6 Polarization of light controls structure formation

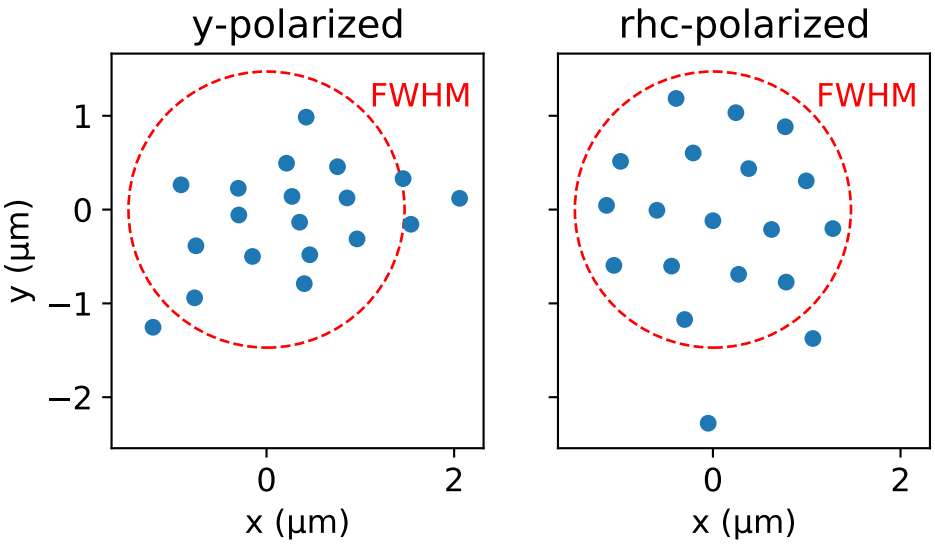

Figure 2.8: Array formation of optical matter in different field polarizations. (left) 19 nanoparticles (150 nm diameter Ag) in a y-polarized Gaussian trap. The particles prefer to form chains elongated along the x-axis (perpendicular to the polarization). (right) 19 nanoparticles in a rhc-polarized Gaussian trap. The particles prefer to form hexagonal arrays.

When there are many nanoparticles in the beam, they will form lattices of some geometry with a lattice spacing governed by the wavelength of light. If the incident light is linearly polarized, the particles prefer to form chains perpendicular to the direction of polarization, as shown in Figure 2.8(a). If the incident light is circularly polarized, the particles prefer to form a hexagonal lattice, as shown in Figure 2.8(b). The reason for this is the rotational symmetry of the incident light field: linear polarization breaks the xy symmetry, while circular polarization preserves it. The intensity of the

scattered field from a particle for each incident polarization is

$$|\boldsymbol{E}^{\mathrm{x}}|^2 = \left(\frac{\varepsilon_0\varepsilon_m\alpha E_0}{4\pi r}\right)^2 \sin^2(\phi) \tag{2.36}$$

$$|\boldsymbol{E}^{\mathrm{y}}|^2 = \left(\frac{\varepsilon_0\varepsilon_m\alpha E_0}{4\pi r}\right)^2 \cos^2(\phi) \tag{2.37}$$

$$|\boldsymbol{E}^{\mathrm{rhc}}|^2 = |\boldsymbol{E}^{\mathrm{lhc}}|^2 = |\boldsymbol{E}^{\mathrm{unpol}}| = \left(\frac{\varepsilon_0\varepsilon_m\alpha E_0}{4\pi r}\right)^2 \tag{2.38}$$

x-polarized and y-polarized light have a ϕ dependence in their in-plane scattering. RHC, LHC, and unpolarized light all have uniform scattering intensity independent of ϕ. The difference between them is that unpolarized light carries no angular momentum while RHC and LHC polarized light carries $\pm\hbar\omega$ units of spin angular momentum per photon.

The formation of chains in optical matter formed by linearly polarized behavior is consistent with experiments and simulations performed by Yan et al. [34]

2.7 Surface lattice resonances: collective modes

As more particles are added to an optical matter system, the resulting array becomes increasingly strongly coupled due to the long range interaction of optical binding (Equation (2.30)). These larger arrays can support surface lattice resonances (SLR): narrow spectral modes that propagate along the lattice with minimal loss. [83–86] For a hexagonal lattice, the resonance wavelength of the SLR satisfies the following (approximate) relation [84]

$$\lambda_{ij}^{\mathrm{SLR}} = \delta\left[\frac{4}{3}(i^2+ij+j^2)\right]^{-1/2}\left(\frac{\varepsilon(\lambda_{ij}^{\mathrm{SLR}})\varepsilon_m}{\varepsilon(\lambda_{ij}^{\mathrm{SLR}})+\varepsilon_m}\right)^{1/2} \tag{2.39}$$

where i and j are integers that determine different SLR resonances in the lattice.

Figure 2.9 shows the emergence of a collective scattering mode at the expense of the single particle resonance. As more particles are added, this collective mode becomes spectrally more narrow. This collective mode results in field enhancements ($|\boldsymbol{E}_{\mathrm{total}}|/|\boldsymbol{E}_{\mathrm{inc}}|$) outside the array up to a factor of 2. These intensity hot-spots are attractive regions for additional particles due to intensity gradient forces. As the array gets larger, the field enhancement continues to increase, and the binding energy

increases.

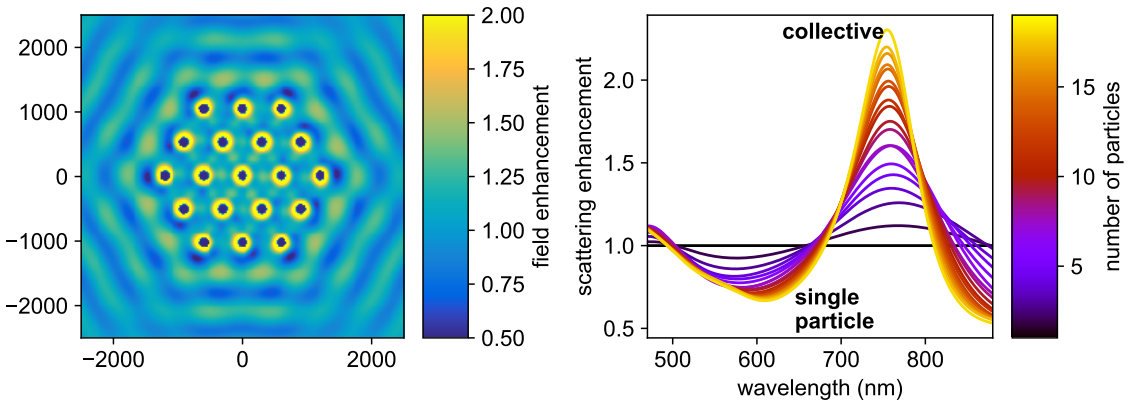

Figure 2.9: Emergence of a surface lattice resonance in optical matter arrays. (left) Field enhancement around 19 Ag nanoparticles ($R = 75\,\text{nm}$) in a hexagonal lattice ($\delta = 600\,\text{nm}$) illuminated by a rhc-polarized plane wave ($\lambda = 755\,\text{nm}$, $n_b = 1.33$). (right) Scattering spectra of arrays composed of 1–19 particles, normalized by the single particle spectra. The single particle Mie resonance diminishes in favor of a red-shifted collective surface lattice resonance at $\lambda = 755\,\text{nm}$.

To quantify the stability and order of larger optical matter arrays, we consider three approaches: (1) linear stability analysis, (2) the ψ_6 order parameter, and (3) calculating $-\log \text{PDF}$ as a type of energy.

In linear stability analysis, one first determines the equilibrated array by performing gradient descent until the forces vanish (possibly in a translating and rotating reference frame). Then a force matrix, K_{ij}, is constructed by measuring force gradients due to small displacements, $\boldsymbol{\epsilon}_j$, of every particle [43]

$$\boldsymbol{f}_i = K_{ij}\boldsymbol{\epsilon}_j \tag{2.40}$$

The force matrix can be diagonalized to construct eigenmodes with complex eigenvalues k_i. The real part of k_i measures the stability (negative is restoring, positive is unstable), while the imaginary part measures the non-conservative component of the eigenmode's motion. Figure 2.10(a) shows the real part of the eigenvalues for increasingly larger arrays up to 169 particles (7 layers in hexagonal packing) illuminated by a plane-wave. The average k_i continues to decrease linearly with the number of layers, demonstrating the increased stability of the array's eigenmodes as the array gets larger.

The ψ_6 order parameter measures the 6-fold hexagonal order of a two-dimensional collection of

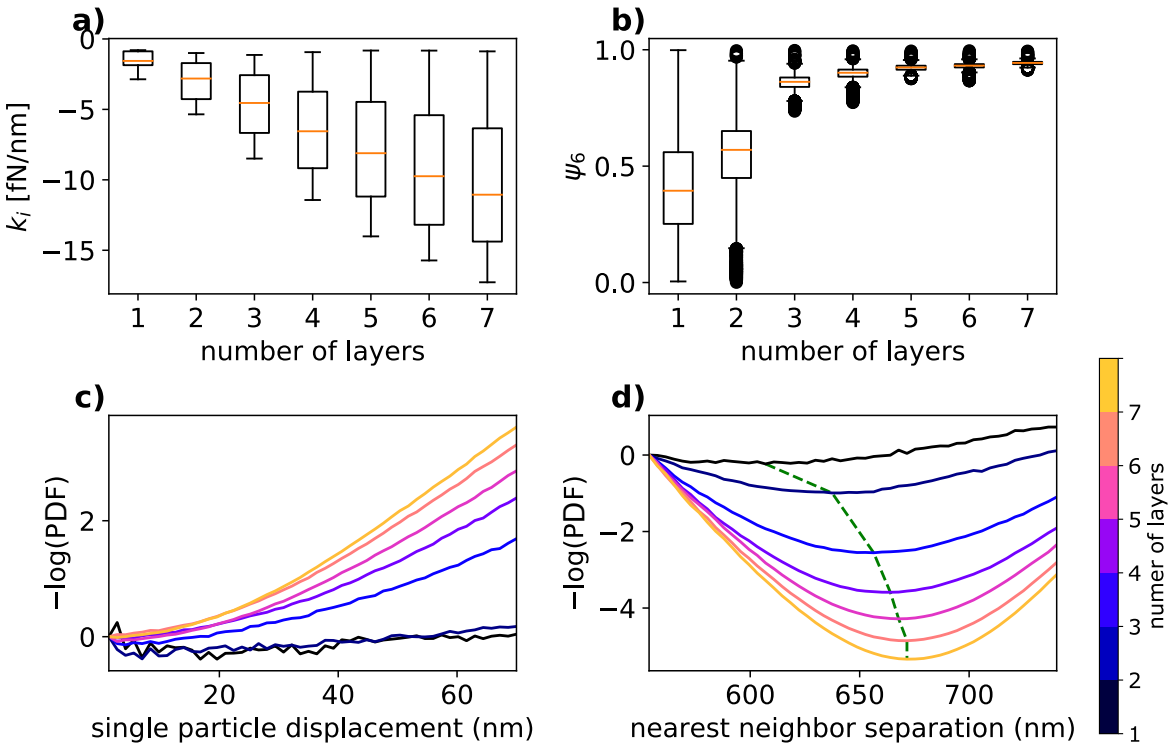

Figure 2.10: Stability of optical matter containing 1 to 7 layers of nanoparticles (7 to 169 particles). (a) Eigenvalues (real part) of the force constant matrix at equilibrium positions. (b) ψ_6 over a thermal trajectory ($T = 300\,\mathrm{K}$). (c) Average displacement of particles from equilibrium position in thermal trajectory (PDF = probability distribution function). (d) Nearest neighbor separations in thermal trajectory. The dashed-line shows the minimum of the $-\log(\mathrm{PDF})$.

particles

$$\psi_6(t) = \left| \frac{1}{N} \sum_i \sum_{j \in \text{neighbors}} \frac{1}{N_j} \exp[6i\theta_{ij}(t)] \right| \tag{2.41}$$

where N is the total number of particles, θ_{ij} is the relative angle between particles i and j, and N_j is the number of neighbor particles around particle j. ψ_6 ranges from 0 (no hexagonal order) to 1 (perfect hexagonal order). Figure 2.10(b) shows $\psi_6(t)$ over a thermal trajectory. As more layers are added to the array, ψ_6 approaches unity, demonstrating the increased order of the array.

Lastly, the stability of arrays can be assessed by calculating probability density functions (PDF). The equilibrium coordinates $\boldsymbol{r}_i^{\mathrm{eq}}$ of the particles can be obtained by gradient descent and switching to a translated and rotating reference frame such that the array does not move or rotate. Deviations from the equilibrium, $\epsilon_i(t) = |\boldsymbol{r}_i(t) - \boldsymbol{r}_i^{\mathrm{eq}}|$, can be binned over a long trajectory to obtain a PDF,

which can be converted to an effective energy $U = -kT\log(\text{PDF})$. Figure 2.10(c) shows U increases with more layers in the array.

A PDF can also be constructed for the first optical binding interaction. By binning nearest neighbor separations over a thermal trajectory, a similar effective energy can be constructed. Figure 2.10(d) shows U for binding becomes stronger with more layers. Additionaly, the optical binding distance is seen to become larger as more particles are added. While for two particle the optical binding distance is 600 nm ($\lambda_w = 600\,\text{nm}$), for 169 particles the optical binding distance shifts to 670 nm: the array stretches with more particles.

The increasing stability of optical matter arrays shown here is consistent with recent work performed by Yan et al. [87]

2.8 Optical torques: spin and orbital angular momentum

In addition to optical forces, light exerts a torque on matter when it is circularly polarized. [88] The total angular momentum of the optical matter system is conserved, and the mechanical torque acting on a particle is given by the MST

$$\langle \boldsymbol{T} \rangle = \int_S \langle \boldsymbol{r} \times \overleftrightarrow{\boldsymbol{T}} \rangle \cdot d\boldsymbol{S} \tag{2.42}$$

When integrated over a single particle, Equation (2.42) gives the spin torque acting on the particle. Exact expressions for the spin torque in GMT are in Chapter 6. Figure 2.11 shows the spin torque for 3 different particle types in a circularly polarized plane-wave.

Additionally, light can carry orbital angular momentum (OAM). From the perspective of the Maxwell stress tensor, this angular momentum is due to the optical force calculated in Equation (2.42) that results in an orbital torque $\boldsymbol{r} \times \boldsymbol{F}$. Incident light fields, such as Laguerre-Gaussian beams, can carry OAM that can be imparted on particles. Figure 2.11 shows the orbital force and phase profile of an LG beam with a topological charge $l = 5$. This shows that the orbital torque is due to the phase-gradient forces.

In Chapter 4, we will discuss how the spin angular momentum of light can exert an orbital torque on optical matter. Consequently, even when the incident light does not carry OAM, optical matter

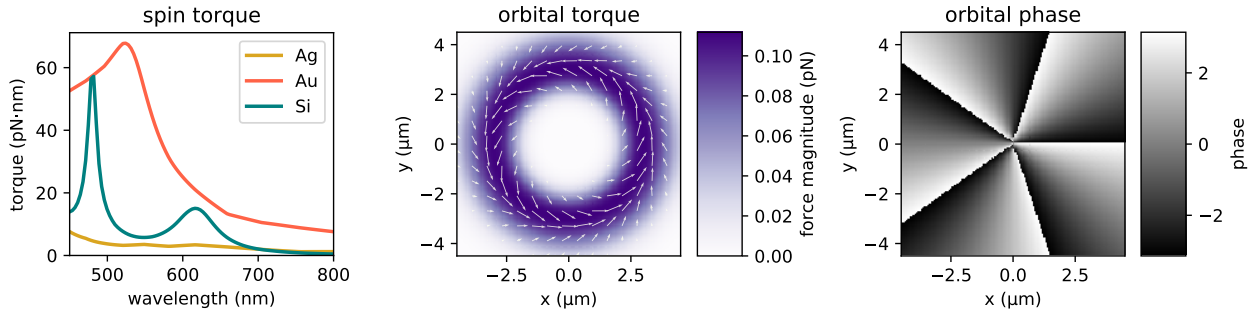

Figure 2.11: Spin and orbital torque in optical matter. (left) Spin torque on 3 different types of 150 nm diameter nanoparticles as a function of wavelength in a rhc-polarized plane wave ($n_b = 1.33$). (middle) Orbital forces acting on a Ag nanoparticle in an $l = 5$ Laguerre-Gaussian beam. (right) Phase profile of the Laguerre-Gaussian beam in the xy-plane indicating five 2π phase sifts around a closed circular path.

arrays can scatter light that *does* carry OAM. This principle leads to novel physical behavior and applications such as optical negative torque and the creation of optical matter stochastic machines.

CHAPTER 3
NON-CONSERVATIVE DYNAMICS AND LINEAR MOMENTUM: REARRANGING OPTICAL MATTER ARRAYS

Optical matter systems are *open systems*, therefore the mechanical energy and momentum of the nanoparticles need not be conserved. There is mechanical momentum in the nanoparticle motion and there is field momentum in the electromagnetic field. The total linear momentum of the optical matter system is [89]

$$\boldsymbol{P}_{\text{total}} = \boldsymbol{P}_{\text{mech}} + \boldsymbol{P}_{\text{field}} = \sum_i m_i \boldsymbol{v}_i + \varepsilon_0 \int_V \boldsymbol{E}(\boldsymbol{r},\omega) \times \boldsymbol{H}(\boldsymbol{r},\omega) d^3 r \tag{3.1}$$

where the integral occurs over all of space. If we are only looking at the motion of the nanoparticles, $\boldsymbol{P}_{\text{mech}}$ is not generally conserved as momentum can flow to and from the field. Consequently, there are cases where Newton's third law (action equals reaction) appears to be violated. From the perspective of Newton's laws of motion, the particle interactions are *non-reciprocal*. [90]

In this chapter, we explore the effects of such non-reciprocal forces in optical matter systems. The simplest system that exhibits a non-reciprocal force is a heterodimer (two particles of dissimilar size and/or material), which is demonstrated to be driven in a ring trap. A generalization is that the phase of the light scattered between electrodynamically interacting particles can result in non-reciprocal forces. [32] A more complex system is that of N identical particles plus a single dissimilar "intruder" particle, where the non-reciprocal forces expel the intruder to the outside. Lastly, we consider a mixture of nanoparticles composed of two or more different species of nanoparticles. This non-reciprocal system is shown to rearrange and phase separate under the appropriate selected trapping conditions.

In Appendix 3.A, a derivation for the net force acting on an optically bound heterodimer is derived. Appendix 3.B demonstrates how to simulate a bound near-field dimer using the generalized Mie theory. In Appendix 3.C, a novel many-body mechanism of creating non-reciprocal forces is demonstrated due to many-body electrodynamic interactions in a bent trimer. Consequently, N particles in a $l = 0$ ring trap are shown to be driven around the ring solely due to this many-body force. In Appendix 3.D, the effects of hydrodynamic translation-translation (TT) coupling in driven

optical matter is discussed.

This chapter is based, in part, on a publication on non-reciprocal forces in optical matter realized in simulation and experiment. [45]

3.1 Net force on an optically bound heterodimer

In order to have a net force on a dimer, the reflection symmetry of the optical matter system has to be broken. This can be done in one of three ways: (i) particles of different sizes, (ii) particles of different material, or (iii) different properties of the incident field at each nanoparticle. The third method can be obtained easily by taking a homodimer (identical particles) oriented along the $\boldsymbol{k}$-vector of a plane-wave. If the particles are separated by a distance d, the fields at each particle is different by a phase $\Delta\Phi = kd$ and results in a net force along the direction of propagation. This force is acting in addition to the radiation pressure on each particle.

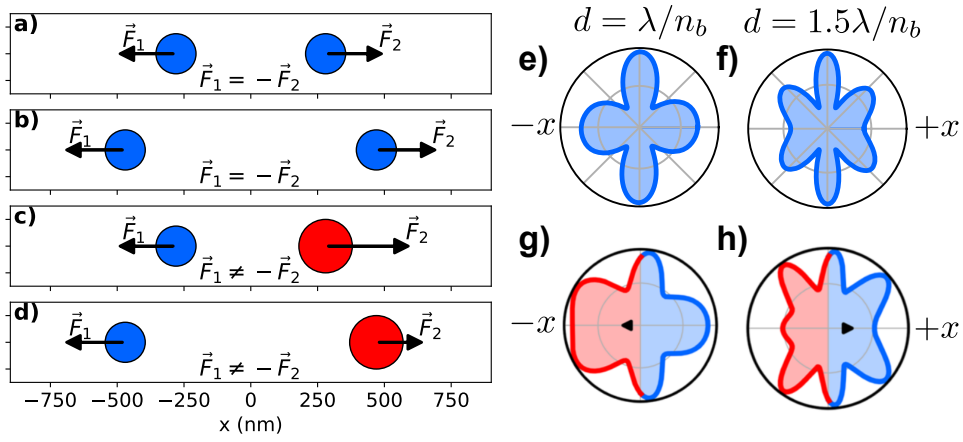

Figure 3.1: Asymmetric scattering and non-reciprocal interactions in heterodimers. (a-d) Force diagrams for a homodimer (a,b) and a heterodimer (c,d) at stable and unstable interparticle separations. The interactions are non-reciprocal in the heterodimer; a net force acts in the $+x$ direction at stable separations and the $-x$ direction at unstable separations. (e-h) Far-field angular scattering distributions of a homodimer and heterodimer at interparticle separations of λ (stable) and $3\lambda/2$ (unstable). The homodimer has symmetric scattering while the heterodimer has asymmetric scattering.

If we suppose that the field is uniform in the plane lateral to its propagation, a lateral net force is obtained by changing the size or material of one of the particles. This net force has been predicted for size disparity [91] and material disparity. [44] As an example, we take the case of a $R_{NP} = 75\,\text{nm}$

Ag particle and a $R_{NP} = 100\,\text{nm}$ Ag particle illuminated by a circularly polarized plane-wave. Figure 3.2(a-d) shows example force diagrams for this heterodimer compared to a homodimer (both particles with $R_{NP} = 75\,\text{nm}$) at stable ($d = \lambda_w$) and unstable ($d = 3\lambda_w/2$) separations. For the heterodimer, *action does not equal reaction*, and consquently there is a net force acting on the heterodimer.

For each of the four dimers shown in Figure 3.2(a-d), Figure 3.2(e-h) shows the far-field angular distribution of the x-momentum integrated over θ

$$S_x(\phi) = \int_0^\pi S_x(\theta,\phi) r^2 \sin(\theta) d\theta = \int_0^\pi \hat{\boldsymbol{r}} \cdot \hat{\boldsymbol{x}} |\boldsymbol{E}(\theta,\phi)|^2 r^2 \sin(\theta) d\theta \tag{3.2}$$

The homodimer has symmetric scattering at all interparticle separations and there is no net force acting on it. On the other hand, the heterodimer has asymmetric scattering that is dependent on interparticle separation that results in a net force on the heterodimer. When $d = \lambda_w$, the field has more momentum propagating in the $-x$ direction than the $+x$ direction, and by conservation of momentum there is a net force acting on the dimer. When $d = 3\lambda_w/2$ (an unstable separation), the direction of momentum flow switches towards the $+x$ direction and causes a net force in the $-x$ direction.

Figure 3.2(a) shows the net force ($F_{2x} + F_{1x}$) and force difference ($F_{2x} - F_{1x}$) as a function of d, the separation, for a heterodimer and homodimer. When the force difference is zero with negative slope, that separation is stable. We see that for a heterodimer, net force and force difference are oscillating roughly $\pi/2$ out of phase with each other, so that the net force is a maximum at stable separations and a minimum at unstable separations.

The net force on a heterodimer was observed in an experiment where two particles were trapped in a circularly polarized $l = 0$ ring trap (the incident light carries no OAM). The field creates a quasi-1D system where each particle's position is characterized by a fixed radius R of the ring and their angles $\theta_1(t)$ and $\theta_2(t)$. The center of geometry angle, $\theta_c(t) = \frac{1}{2}(\theta_1(t) + \theta_2(t))$, is then tracked over time. Figure 3.2(b) shows $\theta_c(t)$ from experiment for a homodimer and a heterodimer, where the heterodimer is observed to be driven in the clock-wise (CW) or counter-clock-wise (CCW) direction depending on its orientation. The results show that the heterodimer is driven around the ring (the

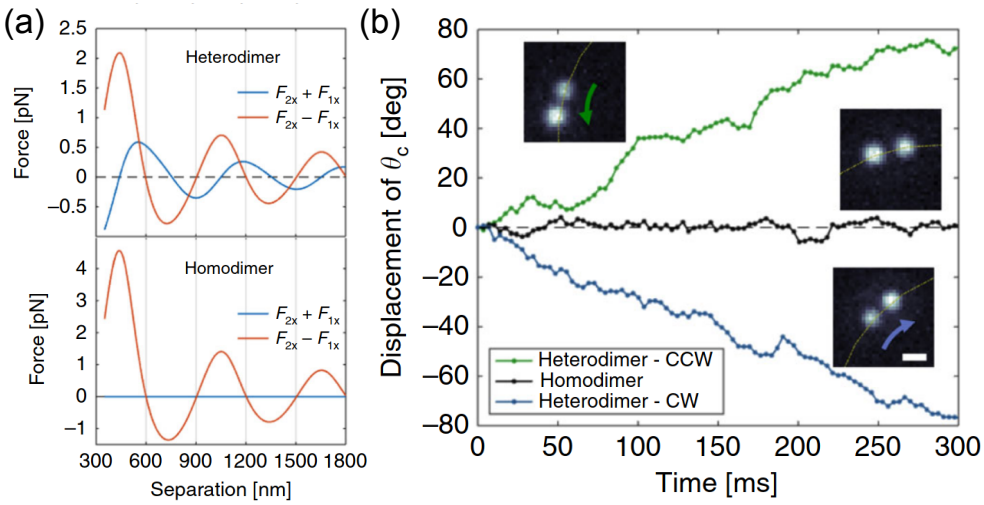

Figure 3.2: Net force acting on an optically bound heterodimer in simulation and experiment. (a) The net force and force difference as a function of separation for a heterodimer and a homodimer. The dimer is stable when the force difference vanishes and has a negative slope. (b) Experimental confirmation of the driven heterodimer motion in a ring trap. Reversing the handedness of the light changes the direction of motion. A homodimer is not driven. [45]

net force points from the smaller particle to the larger particle), while the homodimer only exhibits Brownian motion in the θ_c coordinate.

3.2 Confining asymmetric arrays using wavefront curvature

We now consider the case of a heterodimer trapped in a focused Gaussian beam. In addition to the net force and optical binding interaction, there are radially inward intensity gradient forces on each particle. In principle, these intensity gradient forces can counter the net force, resulting in a trapped dimer whose center of geometry is displaced relative to the center of the Gaussian. To measure the trapping "potential", we calculate the work required to moved the center of geometry through the Gaussian trap, $W(x) = \int_{\infty}^{x}(F_1(x) + F_2(x))dx$, for a fixed interparticle separation $d = 600\,\text{nm}$. The work curves for a homodimer and heterodimer are shown in Figure 3.3(b) for a focused Gaussian beam (blue curves). The takeaway is that the work curve for the heterodimer is asymmetric, requires much less work to escape in the $+x$-direction, and has a minimum near $r = 900\,\text{nm}$ instead of the beam center.

The trapping of the heterodimer can be significantly improved by defocusing the Gaussian beam

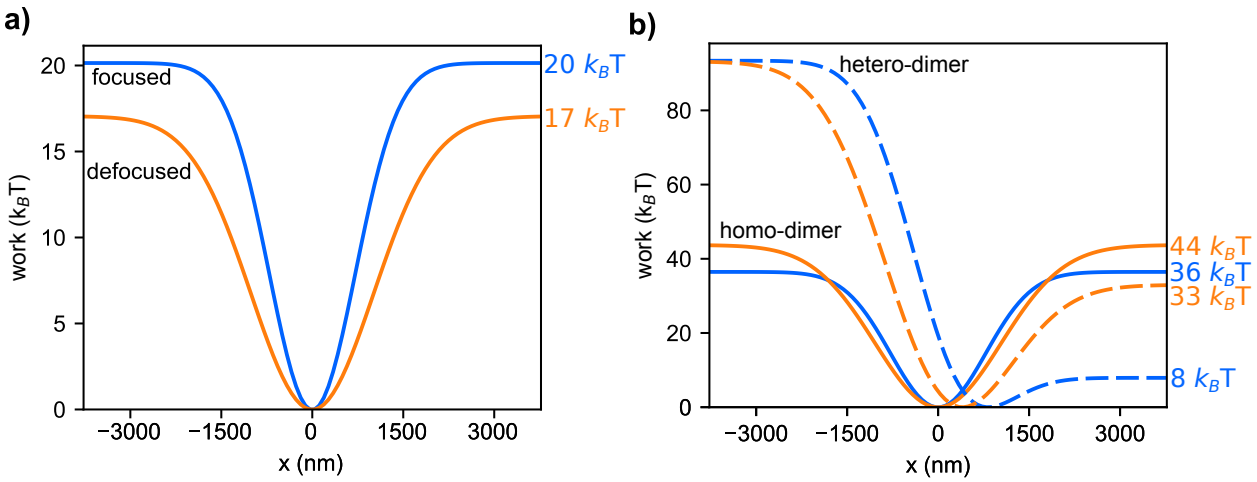

Figure 3.3: Comparison of the trapping potentials of monomers, homodimers, and heterodimers using a focused beam vs. an optimally defocused (converging towards $z = z_R$) beam with an inward phase gradient. (a) Trapping potential of a single nanoparticle for focused and optimally defocused beams. (b) Trapping potentials of a homodimer (solid) and heterodimer (dashed) for focused and optimally defocused beams. The work is expressed in units of thermal energy, k_BT, for $T = 298\,\mathrm{K}$.

so that it is converging towards the trapping plane, as shown in Figure 3.3(b) (orange curves). About $4\times$ more work is required to pull the heterodimer in the $+x$-direction, and the work minimum is shifted closer to the beam center. It should be emphasized that this is *not* due to inward phase gradient forces. Figure 3.3(a) shows the work curves for a single particle and a focused and defocused beam – the trade-off of intensity gradients for phase gradients actually decreases the trapping potential. Instead, the reason a heterodimer is better trapped in a defocused beam is due to a net *phase difference* force in the non-reciprocal interaction.

To obtain an equation for the net force on a heterodimer, the particles will be treated as non-interacting point dipoles, i.e. the incident field induces a dipole in each particle, and the total field is a sum of the incident and scattered fields without dipole-induced-dipole interactions. The static polarizability of a particle is given by [69]

$$\alpha_0(\omega) = 4\pi R^3 \varepsilon_b \varepsilon_0 m(\omega) \tag{3.3}$$

where $m(\omega) = (\varepsilon(\omega) - \varepsilon_b)/(\varepsilon(\omega) + 2\varepsilon_b)$. For silver at $\lambda = 800\,\mathrm{nm}$, $m \approx 1$. The static polarizability can then be corrected for higher frequencies, referred to as the dynamically corrected polarizability

[92]

$$\alpha(\omega) = \frac{\alpha_0(\omega)}{1 - ik^3\alpha_0(\omega)/6\pi\varepsilon_b\varepsilon_0} \tag{3.4}$$

We consider the case of the two particles, with polarizabilities α_i and α_j, in a Gaussian beam that has an incident electric field

$$E(\rho; z) = \hat{\boldsymbol{p}} E_0 \frac{w_0}{w(z)} \exp\left[\frac{-\rho^2}{w(z)^2}\right] \exp\left[-ik\frac{\rho^2}{2R(z)}\right] \tag{3.5}$$

where z is the beam defocus and is kept constant in the 2D trapping plane, $w(z)$ is the evolving beam width, and $R(z)$ is the beam's radius of curvature. Each particle then has an induced dipole whose amplitude and phase are position dependent. The net force acting on the heterodimer's center of mass, derived in Appendix 3.A, is

$$\boldsymbol{F}_{ij}^{\text{net}} = \hat{\boldsymbol{r}}_{ij} P|\alpha_i||\alpha_j| f(r_{ij}) \exp\left[-(r_i^2 + r_j^2)/w(z)^2\right] \sin\left(\Delta\Phi_{ij}\right) \tag{3.6}$$

where $\Delta\Phi_{ij}$ is the phase difference between the two particles, r_{ij} is the distance between the particles, and the scalar function $f(r_{ij})$ is approximately

$$f(r_{ij}) \approx A\frac{\cos(kr_{ij})}{r_{ij}} \tag{3.7}$$

To be precise, the net force also includes the sum of intensity and phase gradient forces acting on each particle

$$\begin{aligned}\boldsymbol{F}_{ij}^{\text{net}} = {} & \hat{\boldsymbol{r}}_{ij} P|\alpha_i||\alpha_j| f(r_{ij}) \exp\left[-(r_i^2 + r_j^2)/w_0^2\right] \sin\left(\Delta\Phi_{ij}\right) \\ & - \frac{I(r_i)\alpha_i'\boldsymbol{r}_i + I(r_j)\alpha_j'\boldsymbol{r}_j}{w(z)^2} + k\frac{I(r_i)\alpha_i''\boldsymbol{r}_i + I(r_j)\alpha_j''\boldsymbol{r}_j}{R(z)}\end{aligned} \tag{3.8}$$

where $I(r)$ is the intensity of the Gaussian field. In the limit of a plane-wave, these additional terms vanish.

The most important feature in Equation (3.7) is the $\sin\left(\Delta\Phi_{ij}\right)$ term. If the particles have the same phase, the net force will vanish. For small phase differences, the net force will point from the smaller phase particle towards the larger phase particle. The total phase difference between the two

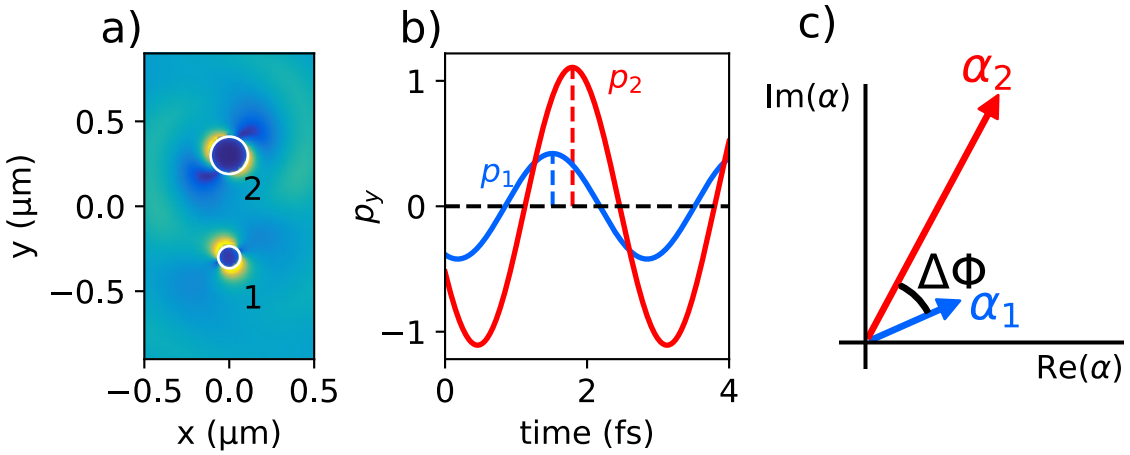

Figure 3.4: Phase difference of induced dipoles in an optically bound heterodimer. (a) Electric field around an optically bound heterodimer in an RHC polarized plane-wave. The larger nanoparticle (2; $R = 100\,\text{nm}$) has a dipole that is visibly phase advanced from the smaller nanoparticle (1; $R = 75\,\text{nm}$). (b) The y component of the induced dipole in each particle in the time-domain shows a phase difference. (c) The polarizabilities of the nanoparticles in the frequency domain also shows a phase difference.

particles is due to four separate contributions

$$\Delta\Phi = (\Delta\Phi)_{\text{size}} + (\Delta\Phi)_{\text{material}} + (\Delta\Phi)_{\text{beam}} + (\Delta\Phi)_{\text{scat}} \tag{3.9}$$

There is an intrinsic phase difference due to differences in size or material of the two particles. If the two particles are the same material and have radii R_i and R_j the phase difference is

$$(\Delta\Phi)_{\text{size}} = \angle(\alpha_j/\alpha_i) = \frac{\frac{2}{3}k^3 m(R_i^3 - R_j^3)}{1 + \frac{4}{9}k^6 R_i^3 R_j^3 m^2} \tag{3.10}$$

Figure 3.4 demonstrates the phase difference in an optically bound heterodimer. The phase difference of induced dipoles is visible in the near-fields and further confirmed by looking at the induced dipoles in the time-domain and the particles' polarizabilities in the frequency domain. The net force points towards the particle that is phase advanced – the larger particle in this case.

If the two particles are the same size and have different materials the phase difference is

$$(\Delta\Phi)_{\text{material}} = \angle(\alpha_j/\alpha_i) = \angle(m_j/m_i) \tag{3.11}$$

Additionally, the Gaussian beam provides an extrinsic, position dependent phase difference

$$(\Delta\Phi)_{\text{beam}} = \frac{k\Delta(\rho^2)}{2R(z)} = \frac{kz(\rho_i^2 - \rho_j^2)}{2(z^2 + z_R^2)} \tag{3.12}$$

where $z_R = kw_0^2/2$ is the Rayleigh range of the beam. If $z > 0$ (a diverging beam), this leads to an additional net force that points away the center of trap, effectively decreasing the trapping stability. If $z < 0$ (a converging beam), this leads to a net force pointing inward that increases the stability of the trap. Lastly, there is a phase difference due to multiple scattering events, $(\Delta\Phi)_{\text{scat}}$. The contribution from this term is likely small for a dimer, but becomes increasingly important for larger arrays where surface lattice resonances becomes important.

To see the effect of the net force on a trapped dimer, we perform Langevin dynamics of the heterodimer at different amounts of defocus. The steady-state motion of such a dimer must be such that the net force in the radial direction goes to zero; otherwise the dimer would continue to drift out of the trap. In Equation (3.8), the net force can go to zero if the inward phase and intensity gradient terms cancel out the outward net force due to phase differences. That is, there is some distance between the dimer's center of mass and trap center R such that the net force vanishes. Additionally, this distance generally depends on the defocus z because the beam's phase contribution, Equation (3.12), is z-dependent. To obtain optimal trapping, the defocus should be chosen to maximize the beam's radius of curvature, which happens when $z = z_R$, the Rayleigh range.

Figure 3.5(a) shows a snapshot of a trapped heterodimer at the optimal defocus; R measures the center of geometry distance from the center of the trap. The dimer is free to orbit around a circle of radius R. Figure 3.5(b) shows R and beam curvature as function of defocus: when the curvature is a maximum, R is close to the minimum value, despite that the size of the beam has increased by $2\times$. This is confirmed in Langevin dynamics simulations at variable defocus, shown in Figure 3.5(c). Note that the optimal defocus is actually a little less than z_R. This is due to the evolving beam width, $w(z)$, which causes the inward intensity and phase differences to become weaker. Rather than maximizing the beam's radius of curvature, the precise condition is to minimize the net force Equation (3.8) with respect to z, which will involve small corrections due to the gradient forces.

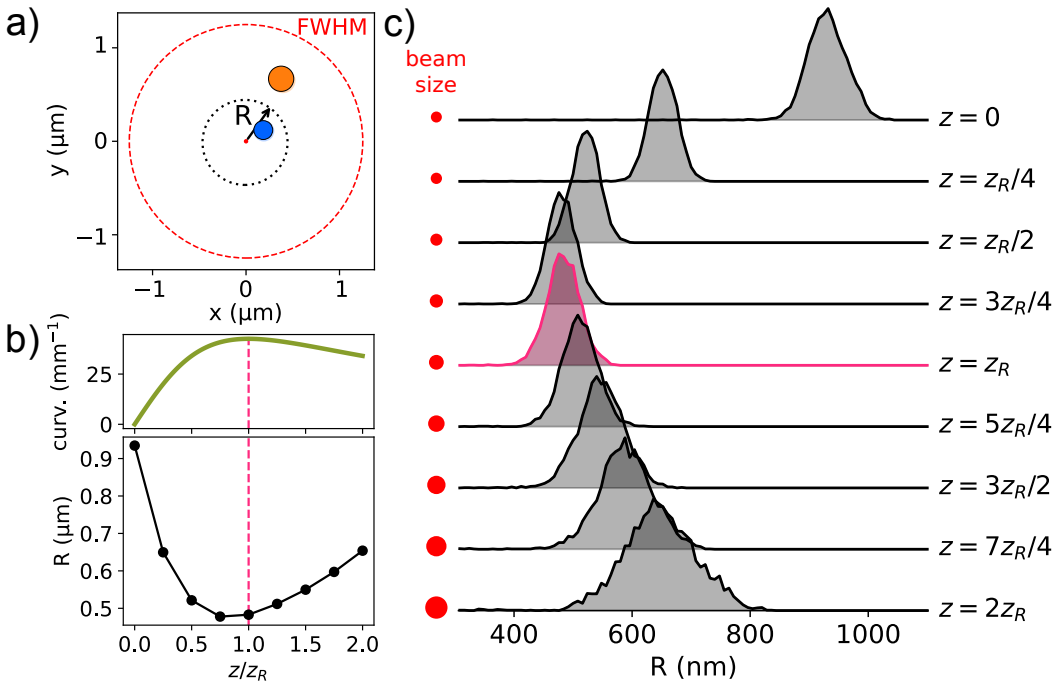

Figure 3.5: Optimally trapping a heterodimer using a Gaussian beam defocused at the Rayleigh range. (a) A heterodimer optically trapped in a defocused Gaussian beam at a center-of-geometry distance R. (b) R as function of beam defocus. Despite the increasing beam size, the heterodimer is brought inward with increasing defocus up to the Rayleigh range, z_R. (c) Distributions of R at variable defocus in a Langevin dynamics simulation.

3.3 Expulsion of an intruder particle

The previous section dealt with the net force on two particles due to their non-reciprocal interactions. This idea can be extended to the case of N particles. For simplicity, we start with the case of $N-1$ particles that are identical and a single particle that is different from the rest. We refer to this particle as the *intruder particle*.

Since it is not possible to create a random but ordered initial arrangement of nanoparticle mixtures in experiment, we will first consider the case of a special type of intruder that happens to occur in experiment. At short ranges, the electrodynamic interaction is extremely attractive (see work profiles in Section 2.4). Two particles can make contact and become bonded in the near-field to form a permanent dimer provided they overcome the repulsive electrostatic forces between the two particles. This dimer can act as an intruder particle; it's polarizability will have a larger magnitude and a different phase than the other monomers.

In experiment, dimers can form spontaneously. Figure 3.6 shows two particles coming together to form a dimer near the center of a larger array of monomers. The dimer is then seen to be expelled from the central region of the array and remains trapped at the outside. The various brighter particles drifting on the outer edge of the array are likely dimers that formed earlier and were expelled in a similar fashion. Because the dimer is still sub-wavelength, the optical microscope and camera only see a single object; objects will be brighter the more polarizable they are.

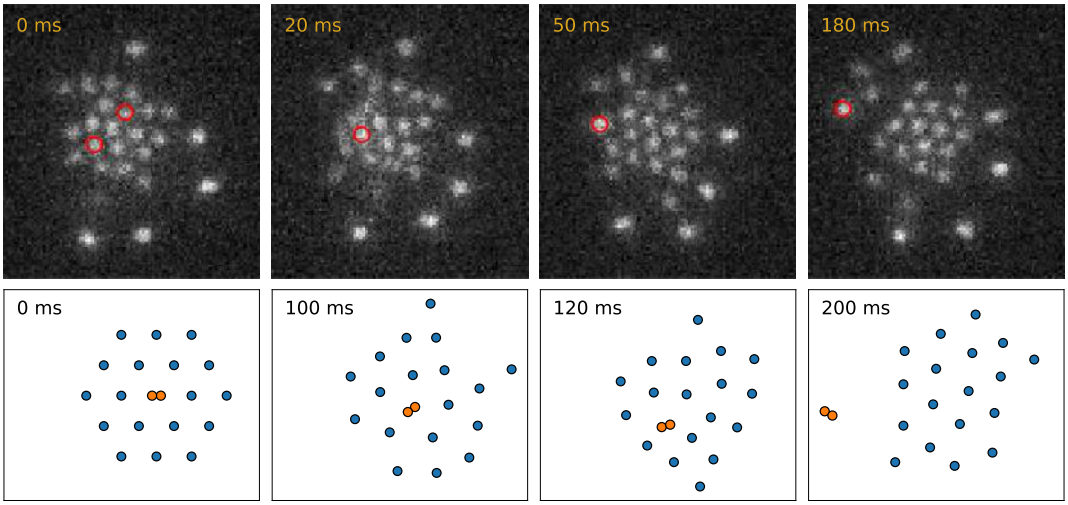

Figure 3.6: Expulsion of a bound dimer from an optical matter array in experiment and simulation. (top) In experiment, a pair of Ag particles (red circles) come together to form a dimer in an OM array. The dimer is expelled from the center of the array. (bottom) A GMT-LD simulation starting with a dimer at the center of a 19 particle array. After 200 ms, the dimer is pushed out of the array.

This behavior is confirmed in simulation using a unique initial condition. A 19 particle array is constructed where the central particle is a bound dimer; each particle has a radius of 75 nm (there are 20 total spherical particles). Appendix 3.B discusses how this simulation is achieved using the GMT since the dimer has to be treated with special care due to strong near-field interactions. The rotational dynamics of the dimer are achieved by calculating the torque on it and using a rotational Langevin equation. The dimer is ejected from the OM array in a similar time frame as the experiment (~ 200 ms) and remains trapped on the outskirts.

To simplify the above problem, we replace the dimer with a 100 nm radius nanoparticle, keeping all of the others at a radius of 75 nm. Additionally, the array is reduced to that of seven particles in a hexagonal shape, starting with the intruder in the center as shown in Figure 3.7(a). In this figure,

each arrow represents the non-reciprocal force acting on the particle calculated using Equation (3.7). As an assumption, we take the forces to be pairwise in nature for the N-body system, i.e. $\boldsymbol{f}_i \approx \sum_j \boldsymbol{f}_{ij}$ This assumption neglects the many-body nature of the forces due to multiple scattering events.

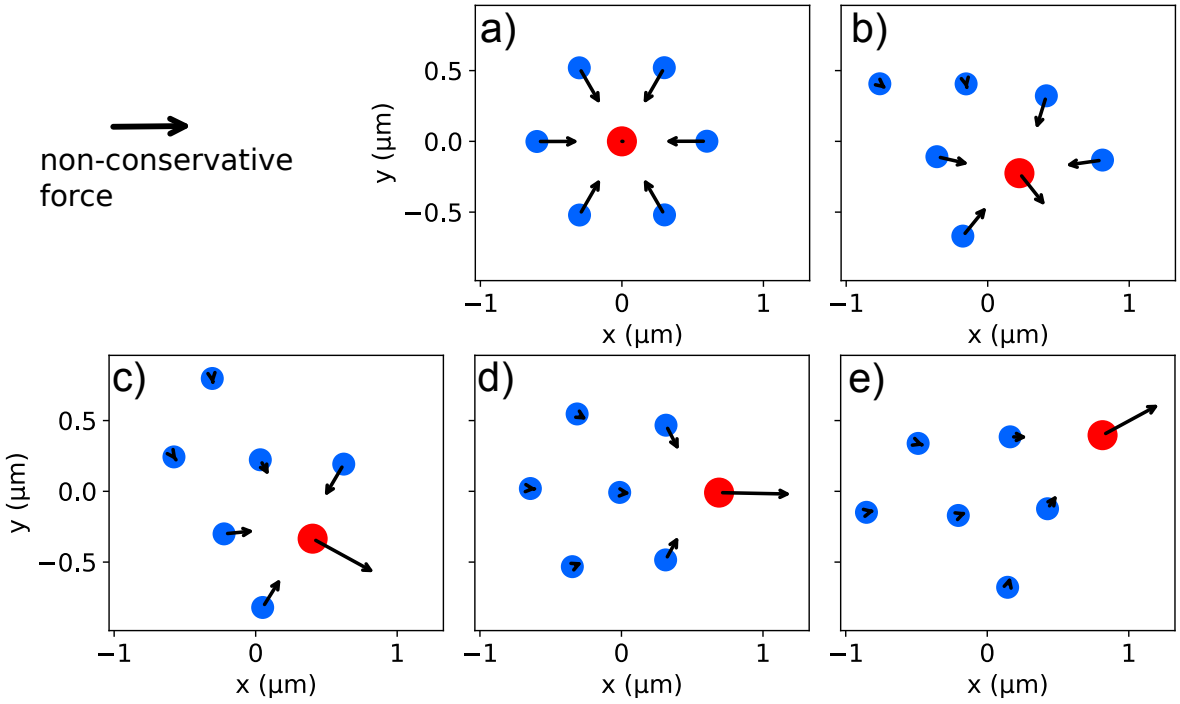

Figure 3.7: Snapshots of an intruder particle ($R_{NP} = 100\,\text{nm}$, Ag) starting in an initial condition (a) with 6 smaller particles ($R_{NP} = 75\,\text{nm}$, Ag) surrounding it. The intruder is expelled from the center; each panel shows a stable configuration of the array during the transition. Arrows over each particle depict the non-conservative part of the force acting on it.

Each panel in Figure 3.7 represents a stable configuration of the array during a dynamics simulation. It's important to note that the *total* force – which contains conservative and non-conservative components – can vanish while the arrows representing the non-reciprocal force are non-zero. When the particles thermally fluctuate away from their equilibrium positions, their motion will be biased in the direction of the arrows. Initially, the identical particles are all biased to move inward, and given enough time they eventually will push the intruder out of the center, as shown in Figure 3.7(b). At this point, the smaller particles continue to push towards the larger particle while the large particle feels a non-reciprocal force that pushes it outward. Figure 3.7(c-e) show the next sequence of states the system moves through. The intruder has been pushed to the outside and its motion remains biased to be radially outward rather than radially inward. Consequently, we expect

this transition to be irreversible – going backwards would require the particles to move against their non-reciprocal forces and would be energetically unfavorable compared to the forward (expulsion) process.

To quantify the transition process, we introduce two order parameters. The ζ order parameter measures the displacement of the intruder relative to the center of mass (com) of the array

$$\zeta(t) = |\boldsymbol{r}_I(t) - \boldsymbol{r}_{\text{com}}(t)| \tag{3.13}$$

The ψ_6 order parameter, defined in Equation (2.41), measures the hexagonal order of the array. These order parameters will change in time as the structure of the array changes over time.

Figure 3.8(a) shows $\zeta(t)$ during a single simulation. With the initial condition $\zeta(0) = 0$, the increase of ζ over time measures the progress of the intruder escape process. Figure 3.8(b) shows $\psi_6(t)$ during the same simulation. ψ_6 goes through several maxima and minima during the process due to structural changes in the array.

The relationship between ζ and ψ_6 can be determined by performing on ensemble of N_S simulations. Each simulation starts with the exact same initial condition and simulation parameters; the only difference is the seed in their random number generators in the Langevin equation which leads to different trajectories. With $N_S = 200$, the transition is observed enough times to construct a conditional probability relationship between the two order parameters, $\psi_6(R)$ The shaded region in Figure 3.8(c) shows the 25^{th} to 75^{th} percentile of $\psi_6(R)$ from the ensemble. $\psi_6(R)$ is seen to oscillate with R, confirming that the transition goes through multiple stable states that each have high hexagonal-like symmetry. In between stable (zero force) states, ψ_6 will be low due to a lack of hexagonal symmetry.

We observe 5 distinct peaks of ψ_6 in Figure 3.8(c). The corresponding 5 configurations of the array from a single simulation in the ensemble at $\max_i(\psi_6)$ are shown in Figure 3.8(d-h). Each configuration is shown centered around its center of mass with a global rotation such that the intruder escapes along the $+x$ axis. The circularly polarized light does cause the array to rotate with a net torque, but this rotation largely does not impact the non-reciprocal dynamics that causes the structural reconfigurations. From the ensemble, the positions of the identical particles can also

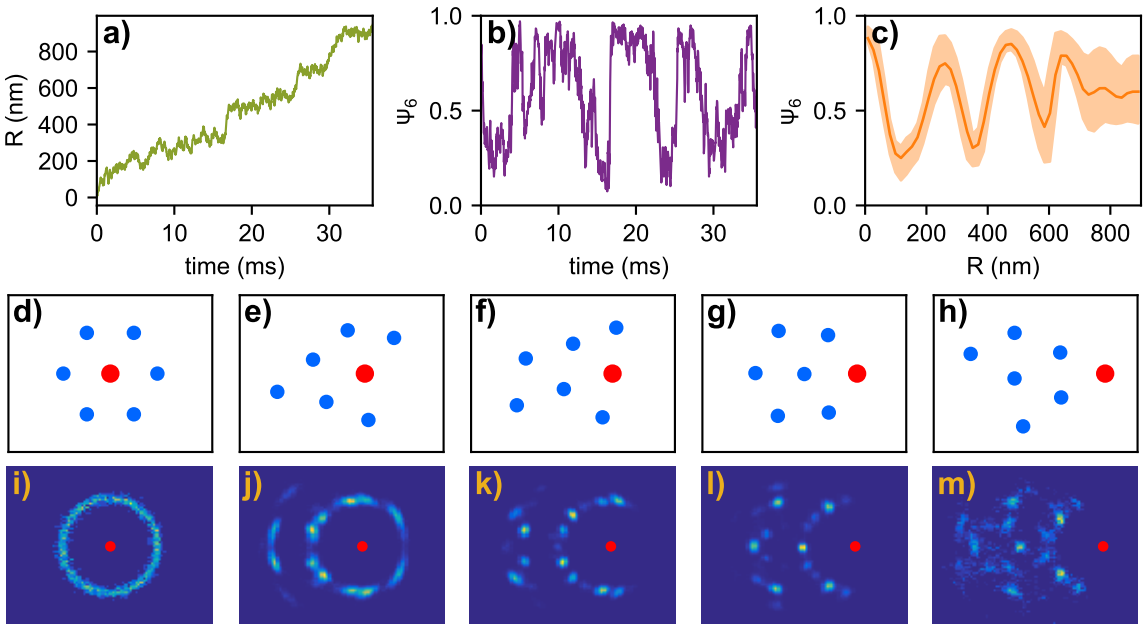

Figure 3.8: Trajectory and order parameter characterization of intruder particle ejection from a 7NP OM array. (a) R order parameter during the transition. (b) ψ_6 order parameter during the transition. (c) $\psi_6(R)$ obtained from an ensemble of transitions. (d-h) Sequence of $\max(\psi_6)$ stable configurations along the transition. (i-m) Ensemble statistics for the positions of the 5 blue particles at the stable (zero force) values of R.

be obtained by binning them and conditioning them on ζ at each $\max_i(\psi_6)$. 2D histograms of these positions are shown in Figure 3.8(i-m). The hexagonal order of the optical matter array during the intruder escape transition is manifest in the ensemble statistics.

Figure 3.8(d-h) shows a particular pathway the intruder chose to escape, but generally there are many pathways it can choose, which causes some of the spreading in the histograms in Figure 3.8(i-m). To construct a pathway tree –and hence the most favorable path of intruder escape – we require a way of classifying each configuration in the process in a way that it can be compared with other configurations in other simulations of the ensemble. Given a configuration A at $\max_i(\psi_6)$ with positions $\boldsymbol{p}_\alpha$ and another configuration B at the same $\max_i(\psi_6)$ with positions $\boldsymbol{p}_\beta$, we want to determine if A and B are the same configuration. If such a metric exists, a k-means clustering algorithm can be used to classify every configuration in the ensemble by grouping those that are close together. [93, 94] A simple choice of metric would be the Euclidean distance between the two configurations, $|\boldsymbol{p}_\alpha - \boldsymbol{p}_\beta|$. However, this choice is not permutation invariant and thus cannot be used

for a k-means clustering algorithm; two identical configurations can be far apart in this metric, i.e. if you simply swap any two identical particles they would be classified as different configurations.

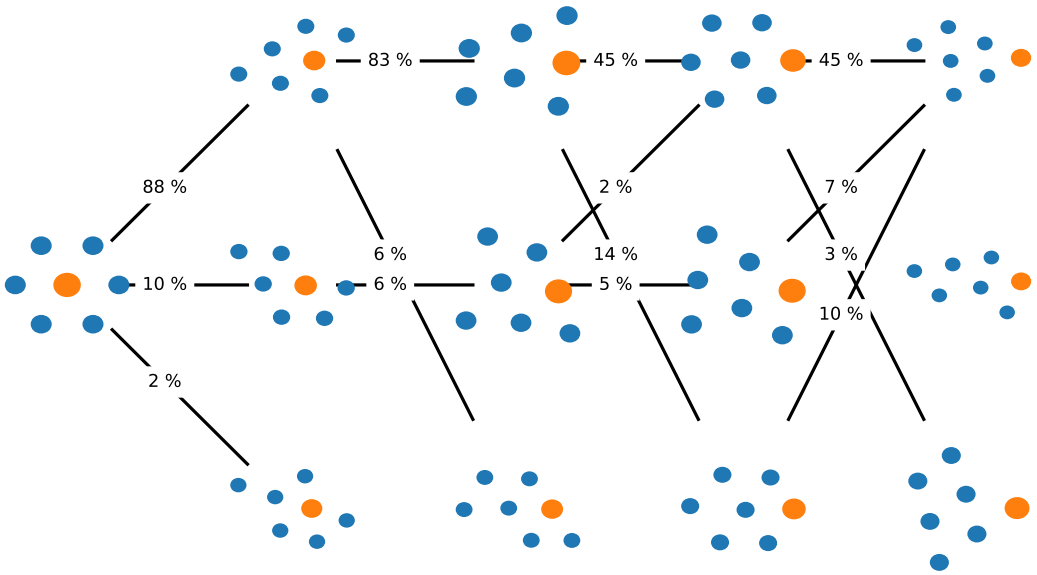

Figure 3.9: Transition path tree for intruder escape using a k-means clustering algorithm. The states are sorted by most likely to least likely from top to bottom (considering the 3 most likely states).

To obtain a permutation invariant metric for a given configuration, we calculate the various pairwise distances d_{ij} for all pairs and sort this set of numbers from small to large. For any two configurations, the metric is chosen to be the Euclidean distance between these two sorted sets. Such a metric is permutation invariant and can be used with the k-means clustering algorithm. For every simulation in the ensemble, a pathway can be constructed as a sequence of classified configurations. These pathways can then be binned to obtain a transition path tree, as shown in Figure 3.9. This tree is a truncated version of the full tree that shows just the 3 most most likely configurations at each $\max_i(\psi_6)$. The path along the top of the tree, which is labeled as $[0, 0, 0, 0, 0]$, is the most probable path of intruder escape.

The transition path tree is useful for calculating ensemble averaged quantities over specific pathways. Of particular interest is the work required to move along each pathway. It is not sufficient to calculate work from the original trajectory, since that would include work accumulated in thermal fluctuations that depends on the dwell times at each stable configuration. Instead, the trajectory

can be *coarse-grained* by averaging over thermal fluctuations. This is done by binning and averaging the particle positions from a single simulation, $\boldsymbol{p}_i$, conditioned on the ζ order parameter so that the pathway increases linearly with ζ rather than time. The work can then be obtained over this coarse-grained trajectory

$$W(\zeta) = -\int_0^{\zeta} \sum_i \boldsymbol{F}_i \cdot d\boldsymbol{r}_i(\zeta) \tag{3.14}$$

where $d\boldsymbol{r}_i(\zeta)$ is the displacement of particle i as a function of ζ. The integration starts at 0 where the intruder is at the center.

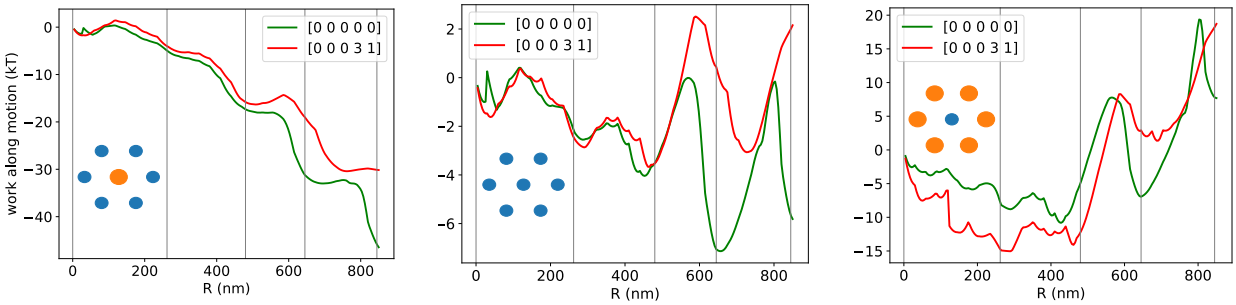

Figure 3.10: Work curves obtained by integrating the force over a coarse-grained trajectory. (a) Work for a larger intruder particle has a downhill slope. (b) Work for an equal-sized intruder particle has a constant slope. (c) Work for a smaller intruder particle has an uphill slope, meaning that work would need to be done to remove it from the array.

Figure 3.10(a) shows the work in units of k_BT for two different pathways: $[0, 0, 0, 0, 0]$ (the most probable) and $[0, 0, 0, 3, 1]$. For each pathway, the work is downhill with a series of minima along the way. The vertical lines show the values of R where $\psi_6(R)$ is a maximum in the ensemble, and therefore correspond to stable configurations. These work curves show that the intruder escape is a thermally activated process – it requires some thermal energy to escape the local minima. The downhill nature of the work indicates the irreversibility of the process, i.e. it requires $\sim 50k_bT$ of thermal energy for the reverse process.

For comparison, the work can also be calculated for an identical or smaller intruder. Since this process is not driven in such a way that increases ζ, we assume the coarse-grained trajectory is the same for these two cases as it is for the larger intruder. The work is calculated over the same path in Equation (3.14), except the forces $\boldsymbol{F}_i$ are changed for each configuration. The work required for an identical particle to escape is no longer downhill in Figure 3.10(b), and instead just

involves a sequence of work minima. For a smaller intruder, the work required for it to escape is uphill, requiring about $\sim 20k_BT$ thermal energy. When the intruder is smaller, the sign of the non-reciprocal switches directions and makes the intruder prefer to be towards the center than on the outside of the array.

These findings for the instability of large intruders and stability of small intruders in OM arrays are inconsistent with the notion that more polarizable particles seek the center of a focused optical beam. Intuition would suggest that larger (more polarizable) particles would have lower energy when at the center of the beam. Rather, the explanation for the intruder escape process resides with non-conservative and non-reciprocal interactions rather than conservative ones.

3.4 Optical segregation of a nanoparticle mixture by particle size

In the experiment shown in Figure 3.6, there are multiple brighter objects on the outskirts of the array. Combined with the results of the previous section, this provides a hint to the dynamics of N_1 particles of type 1 and N_2 particles of type 2. It appears that the brighter particles – whether they are dimers or larger particles – are pushed to the outside while the smaller particles remain in the center of the trap. We now consider the dynamics and steady-state behavior of such an optical matter system with non-reciprocal interactions.

In experiment, optical matter arrays are built particle by particle rather than starting from some chosen initial condition. Consequently, they are mostly already at their steady-state when observed and the dynamics of how such a steady-state is achieved are not revealed. Another experiment, shown in Figure 3.11(a), has brighter particles on the outside and dimmer particles on the inside for a particular frame from a video. The brightness distribution of particles over the video, Figure 3.11(b), reveals a bi-modal distribution that allows us to define a brightness cutoff and label the particles as 1 (dimmer) or 2 (brighter). Defining R to be the displacement of each particle relative to the center, Figure 3.11(c) shows how the brighter particles are spatially segregated from the dimmer particles.

This experiment reveals that in the steady-state, larger particles will end up on the outside of the array. In simulation, we can choose a more interesting initial condition that is far away from the steady-state behavior. The system is initialized with 37 particles in a hexagonally packed array where the identity of each particle is randomly assigned ($\mathbf{1} \rightarrow 75\,\text{nm}$ radius, $\mathbf{2} \rightarrow 100\,\text{nm}$ radius).

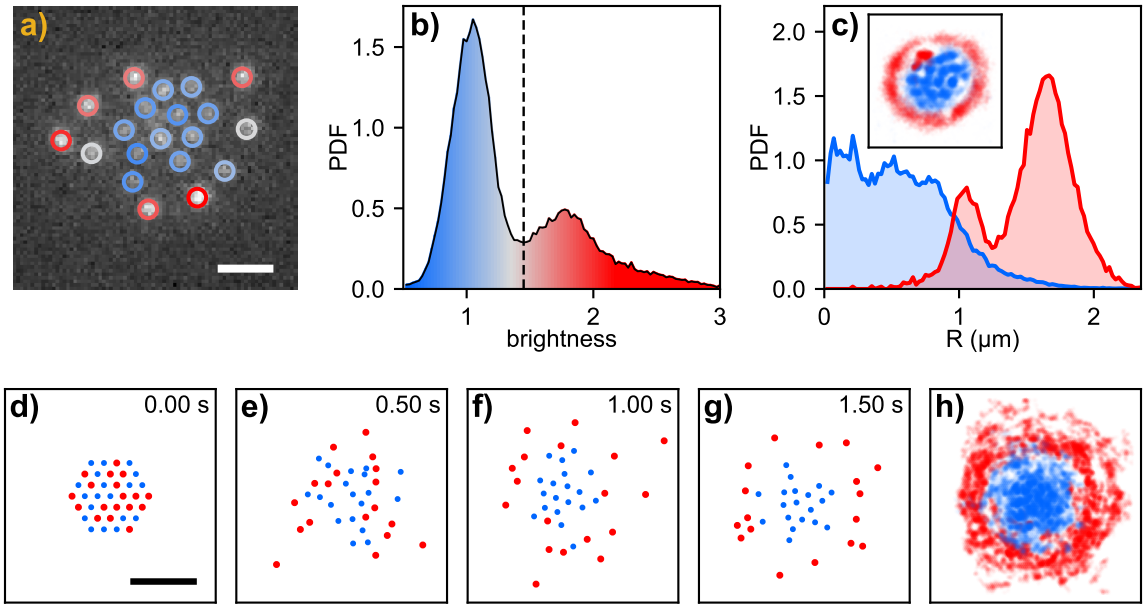

Figure 3.11: Trapped nanoparticle mixtures are segregated by size through their optical (electrodynamic) interactions. (a) Experimental snapshot of a 20 nanoparticle mixture (14 small, 6 large). Scale bar is 1 µm. (b) Probability density function for the brightness of each particle during the experiment. (c) Probability density functions for the radial position of small particles (blue) and large particles (red) taken from a video corresponding to (a). Inset shows the 2D probability density functions. (d-g) Time-series snapshots from a GMT-LD simulation of a 37 nanoparticle mixture (19 small, 18 large), with an initial condition of a perfect hexagonal lattice and random size assignment. Scale bar is 3 µm. (h) 2D probability density function from simulation after separation has occurred.

Time-series snapshots of the dynamics that follow are shown in Figure 3.11(d-g). On the timescale of 1 to 2 seconds, the steady-state is achieved where all the larger particles are on the outside. A 2D histogram of the steady-state positions, shown in Figure 3.11(e), agrees well with the steady-state 2D histogram from experiment, Figure 3.11(c).

To quantify the steady-state, consider two probability distributions, $P_1(r)$ and $P_2(r)$, that measure the probability of finding particles of type 1 or 2 at a radial position r away from the center of the beam. Given enough time in the steady-state, these distributions can be determined. The segregation parameter, S, calculates the area of overlap for the PDFs and measures the extent to which the two particle species separate

$$S = \int_0^\infty \min\left[P_1(r), P_2(r)\right] dr \tag{3.15}$$

The segregation parameter ranges from 0 (completely segregated) to 1 (completely mixed).

It's also important to provide sufficient confinement so that the larger species of particles at the periphery does not escape the optical trap. The confinement parameter measures the overlap of the PDF with the 2D Gaussian intensity distribution of the trapping beam

$$C_i = \int_0^\infty \exp\left(-r^2/w_0^2\right) P_i(r) dr \tag{3.16}$$

The confinement parameter ranges from 0 (poorly trapped) to 1 (well trapped) for each species of particles.

We now consider the effect of the difference in radius, $R_2 - R_1$, on the S and C_i parameters when the trapping beam is optimally defocused at $z = z_R$. In Figure 3.12(a), S is shown to decrease from 1 towards 0 with increasing radius difference. The confinement of the smaller particles is essentially unaffected while the confinement of the larger particles is diminished as they move to the outside of the array, Figure 3.12(b). The difference in radius is related to an intrinsic phase difference, given by Equation (3.10), that increases approximately linearly with increasing radius difference. When the phase difference is about 0.3 rad (when $R_2 = 90\,\text{nm}$), S reaches its minimum value where further increasing the phase difference does not provide additional segregation.

This behavior depends on the converging beam that provides the extrinsic phase difference in Equation (3.12). Looking at the dependence of C_i on the defocus z in Figure 3.12(c), the optical trap fails to confine the larger species of particles at weaker defocus. $C_1(z)$ continues to increase with increasing defocus until it saturates, while $C_2(z)$ is roughly independent of defocus. Thus, in order to both segregate and confine both species of nanoparticles, the Gaussian beam has to be defocused by at least the Rayleigh range.

To construct a simple model for the steady-state behavior of the optical matter array, consider the extrinsic and intrinsic contributions to the phase of each particle

$$\Phi_i(\rho) = \Phi_i^0 + \frac{kz\rho^2}{2(z^2 + z_R^2)} \tag{3.17}$$

where Φ_i^0 is the intrinsic (constant) phase of particle species i and the ρ-dependent term is the extrinsic phase due to the beam. In the steady-state, we want the net force Equation (3.7) to vanish,

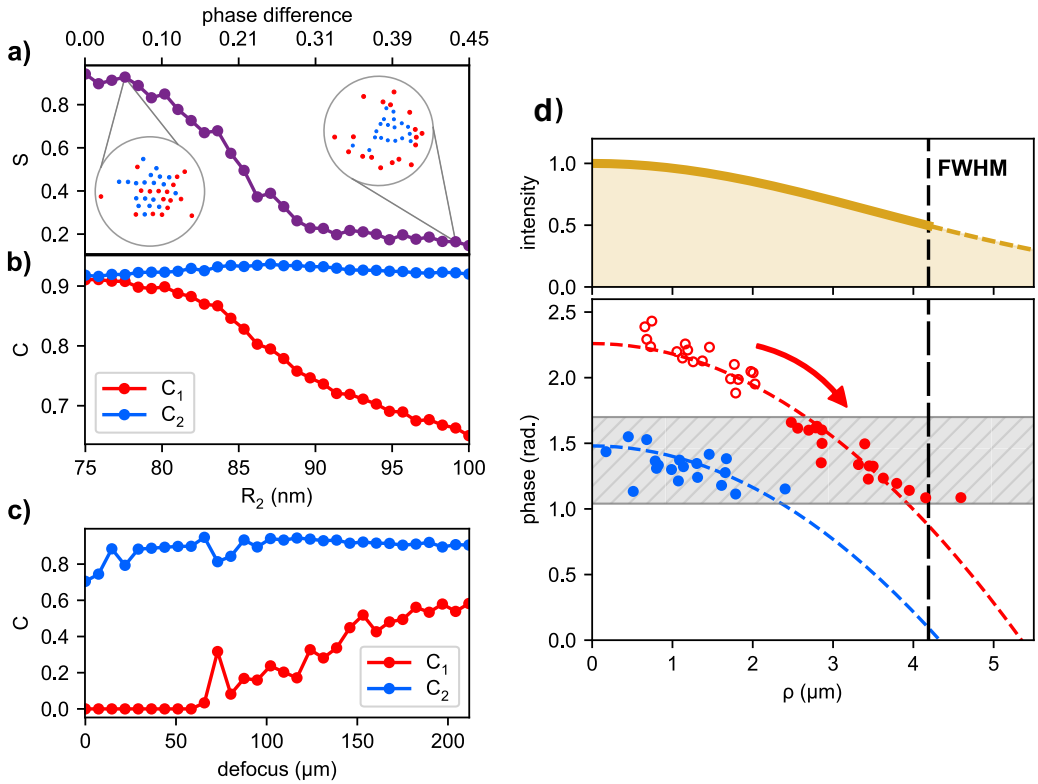

Figure 3.12: Segregation and confinement parameters at variable phase difference in nanoparticle mixtures. (a) Segregation parameter, (b) confinement parameters as function of the radius of the larger particles, R_2. (c) Confinement parameters as function of beam defocus. (d) Phase of each particle vs. radial position in beam at an instant in time after segregation has occurred. At steady-state, the blue and red particles have on average equal phase.

which can be done if $(\Delta\Phi)_{ij} \to 0$. Since the larger particles have a larger intrinsic phase ($\Phi_1^0 > \Phi_2^0$), their phase must be reduced in the steady state by the extrinsic part. If the beam defocus is chosen correctly, it is possible that the displacement ρ for the larger species of particles leads to an extrinsic phase that cancels out the difference in intrinsic phase, resulting in no net non-reciprocal force at the pairwise level (on average).

For optimal defocus at the Rayleigh range, $z = -z_R$, the phase of each particle is

$$\Phi_i(\rho) = \Phi_i^0 - \frac{k}{4z_R}\rho^2 \tag{3.18}$$

The sign of the defocus is negative so that the beam is converging and the phase gradient is inward. Thus, a particle has a lower phase at higher ρ and the curvature of this extrinsic phase is maximized

at the Rayleigh range.

Figure 3.12(d) shows how the phase of the particles evolve as the optical matter system approaches its steady state for optimal defocus. The larger particles initially begin with a larger phase Φ_1 (hollow red circles) than the smaller particles with phase Φ_2. After steady-state is achieved, the red particles move to larger ρ and consequently have a reduced phase that is, on average, equal to the phase of the smaller particles. Additionally, this equal phase condition is met within the full-width at half-maximum (FWHM) of the beam, which allows the particles to stay confined in the optical trap. If the larger particles were to increase their ρ any further, they would have a smaller phase than the smaller particles and the sign of the net non-reciprocal force would reverse and pull the particles back inward.

3.5 Optical matter alloys: segregation by nanoparticle material

Optical matter arrays can be composed of nanoparticles of different material, forming optical matter alloys. The same principle of optical segregation occurs for particles of different material composition since an intrinsic phase difference can be achieved, provided the phase difference due to material, Equation (3.11), is sufficiently large. Experimentally, it was demonstrated that a mixture of optically trapped silver and gold nanoparticles of the same size do not segregate and remain positionally mixed in the OM array. This is shown by measuring $P_1(r)$ and $P_2(r)$ by classifying particles by their color, see Figure 3.13(a-b). Because silver and gold have different scattering spectra, silver particles appear more yellow while gold particles appear more orange in a color-sensitive (RGB) detector. The reason these particles fail to segregate is that their intrinsic phase difference and hence their non-reciprocal interaction is too small relative to the thermal energy; for 75 nm radius particles, the phase difference is only 0.06 rad. Figure 3.13(c-d) shows the intrinsic phase for particles of different materials and of radius 75 nm and 100 nm.

From this diagram, it is evident that certain materials are too close in phase to segregate (such as Ag and Au, and other various metals) while other combinations (such as TiO_2 or Si combined with any of the metals) have a large enough phase difference to segregate. Figure 3.13(g-h) shows two examples of optical matter arrays segregating by material. It is also important to note that the intrinsic phase is wavelength dependent, i.e. while two materials may not segregate at one wavelength

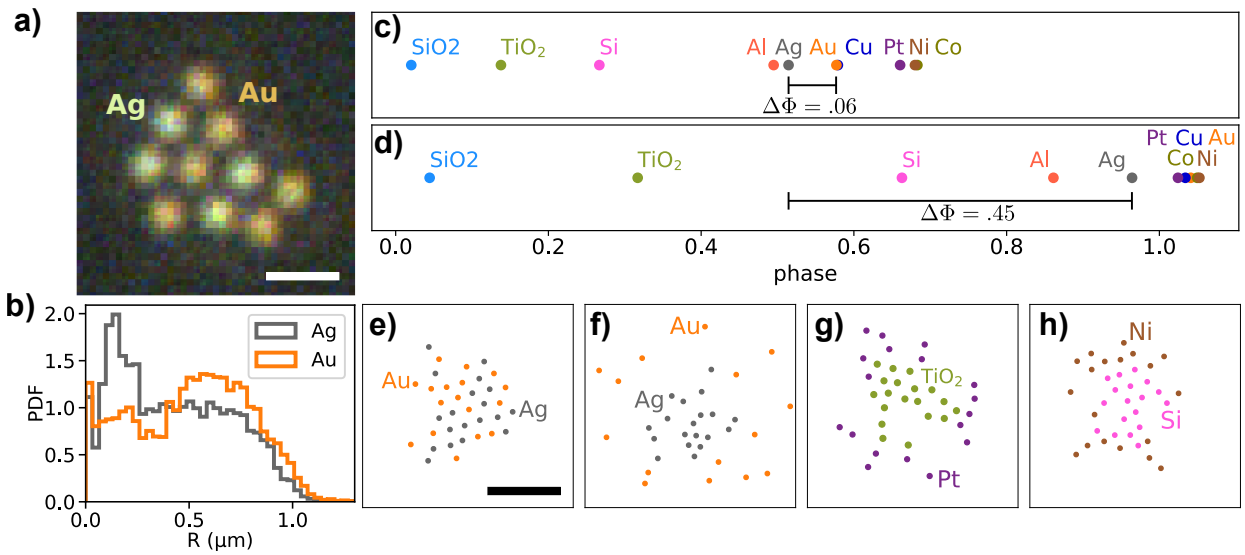

Figure 3.13: Segregation of optical matter alloys by material. (a) Experimental snapshot of a mixture of silver and gold nanoparticles taken with a color CCD camera. (b) PDF of the Au and Ag radial distances in the experiment. (c-d) Phase of different nanoparticles for particle radius 75 nm (c) and 100 nm (d). (e) Au-Ag mixture at $\lambda = 800$ nm; no segregation occurs. (f) Au-Ag mixture at $\lambda = 600$ nm; segregation occurs. (g-h) TiO_2-Pt mixture (g) and Ni-Si mixture (h) at $\lambda = 800$ nm; segregation occurs.

they may segregate at another wavelength. For example, gold and silver particles can be made to segregate at $\lambda = 600$ nm, where the phase difference is around 0.3 rad, see Figure 3.13(f).

This principle can also be applied to the case of four different species of particles: two different sizes (75 nm and 100 nm) and two different materials (Ag and Au). The wavelength dependence of the intrinsic phase for these four types of particles is shown in Figure 3.14(a). At $\lambda = 800$ nm, different materials have similar phase while different sized particles have a larger phase difference; consequently, the array segregates by size (Figure 3.14(b)). At $\lambda = 580$ nm, different sizes have similar phase while different materials have a larger phase difference; consequently, the array segregates by material (Figure 3.14(c)). Thus, by tuning the wavelength of the incident light, an optical matter alloy can be segregated by size or material. Figure 3.14(d-e) shows the various probability distributions for each particle type.

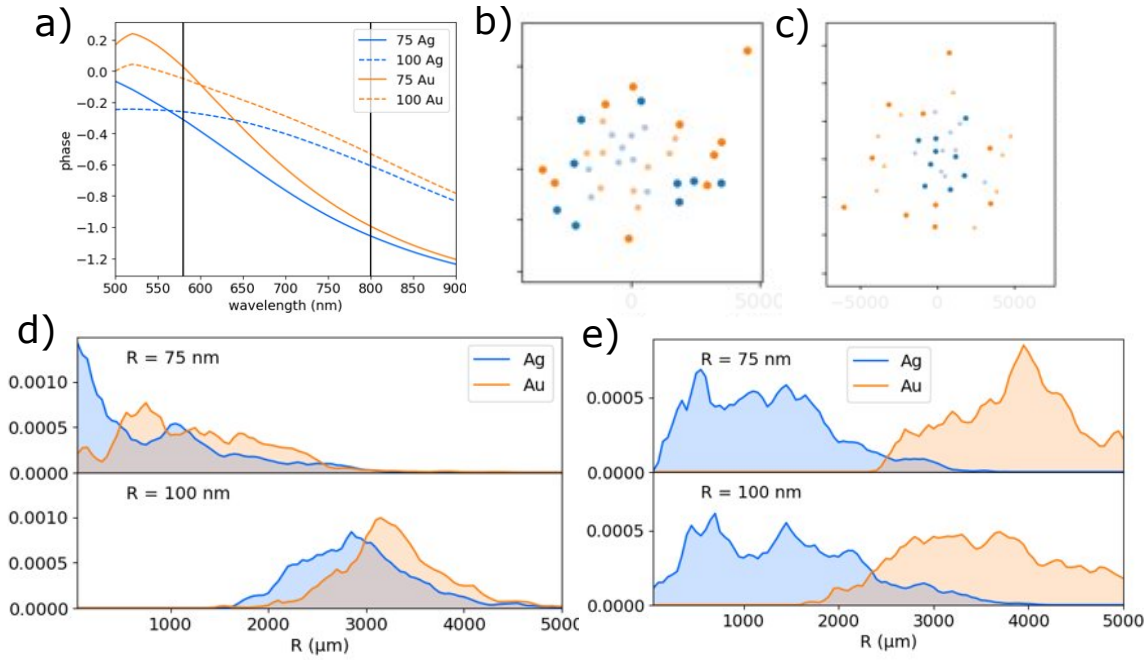

Figure 3.14: Segregation of optical matter alloys by size and material using the dispersive properties of metals. (a) Phase of 4 different nanoparticle species (combination of radius 75 nm and 100 nm, and Ag and Au materials) as function of wavelength. (b-c) Simulation snapshots at wavelengths of 800 nm and 580 nm, respectively. (d) At $\lambda = 800$ nm particles segregate by size and not material. (e) At $\lambda = 580$ nm particles segregate by material and not size.

3.6 Conclusion

In this chapter, non-reciprocal forces in optical matter were realized by breaking the symmetry between a pair of particles. This symmetry can be broken by either having different materials or different sizes of the nanoparticles (or having monomers vs. dimers). In either case, the reason for the net force is due to an intrinsic phase difference in the induced dipoles that results in an asymmetric scattering of light momentum. With many particles interacting together in the presence of a single intruder particle with a larger intrinsic phase, the non-reciprocal interactions cause the intruder to be ejected from the array.

For mixtures of two species of particles, the non-reciprocal interactions drive the larger phase particles to the outside of the trap, causing a phase separation of the two species. The optical matter array is kept stable and trapped by an extrinsic phase that is imposed by a defocused Gaussian beam. The stabilizing effect of this extrinsic phase is shown to be a maximum when the beam is defocused at the Rayleigh range, z_R. Thus, mixtures of nanoparticles can be segregated by particle

size or material using the phase properties of light, i.e. the phase difference of their non-reciprocal electrodynamic interactions.

3.A Derivation of the net force on a heterodimer

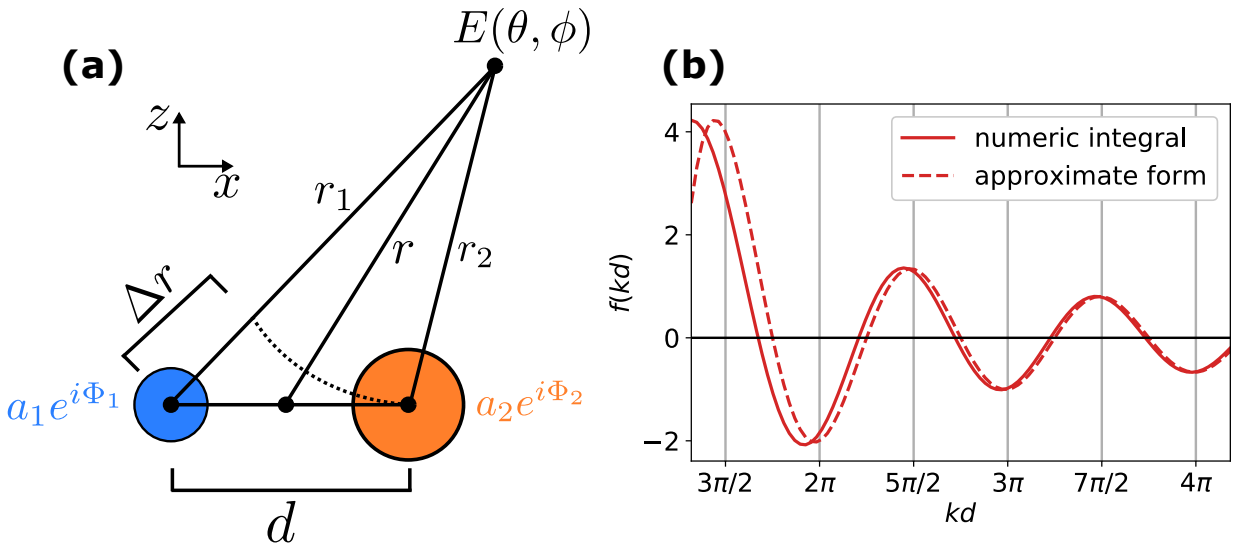

Figure 3.15: Analytic derivation of the net force on a heterodimer. (a) Schematic of a heterodimer where each particle has its own amplitude and phase. (b) The function $f(kd)$ calculated exactly by its integral form and compared to its approximate form in the limit $kd \gg 1$.

Consider two dipoles separated by a distance d, with induced dipoles $a_1 \exp(i\Phi_1)$ and $a_2 \exp(i\Phi_2)$, see Figure 3.15(a). To obtain an expression for the net force, the combined far-field due to the two dipoles needs to evaluated on the surface of a sphere of radius r as $r \to \infty$. In all equations that follow, only the leading terms of order d/r need to be kept. The distances $r_2 = r_-$ and $r_1 = r_+$ are

$$r_\pm = \sqrt{r^2 + \frac{d^2}{4} \pm rd\sin(\theta)\cos(\phi)} \approx r\sqrt{1 \pm \frac{d}{r}\sin(\theta)\cos(\phi)} \tag{3.19}$$

Taylor expanding Equation (3.19) to first order gives the difference between these distances as

$$\Delta r = r_2 - r_1 = -d\sin(\theta)\cos(\phi) \tag{3.20}$$

The far field electric field due to the coherent sum of these two dipole radiation fields is

$$\boldsymbol{E}(\theta,\phi) = \frac{\hat{\boldsymbol{\theta}}\sin(\theta)k^2}{4\pi\varepsilon_0\varepsilon_b}\left[\frac{a_1\exp[i(kr_1+\Phi_1)]}{r_1}+\frac{a_2\exp[i(kr_2+\Phi_2)]}{r_2}\right] \tag{3.21}$$

$$= \frac{\hat{\boldsymbol{\theta}}\sin(\theta)k^2}{4\pi\varepsilon_0\varepsilon_b r}\left[a_1\exp[i(kr_1+\Phi_1)]+a_2\exp[i(kr_2+\Phi_2)]\right] \tag{3.22}$$

since $r_1 = r_2 = r$ in the denominator in the limit $r \to \infty$ (note that r_1 and r_2 in the phase exponential remain since that expression does not converge to anything as $r \to \infty$). The resulting far-field intensity is

$$|\boldsymbol{E}(\theta,\phi)|^2 = \frac{k^4\sin^2(\theta)}{16\pi^2\varepsilon_0^2\varepsilon_b^2 r^2}\left[a_1^2+a_2^2+2a_1a_2\cos(k\Delta r+\Delta\Phi)\right] \tag{3.23}$$

where Δr is given be Equation (3.20) and $\Delta\Phi = \Phi_2 - \Phi_1$.

The rate of outgoing x-momentum is then given by a surface integral of the field momentum in the limit $r \to \infty$

$$S_x = \varepsilon_0\varepsilon_b\int_0^{\pi}\int_0^{2\pi}\hat{\boldsymbol{r}}\cdot\hat{\boldsymbol{x}}|\boldsymbol{E}|^2r^2\sin(\theta)d\phi d\theta \tag{3.24a}$$

$$= \frac{k^4}{16\pi^2\varepsilon_0\varepsilon_b}\int_0^{\pi}\int_0^{2\pi}\sin^4(\theta)\cos(\phi)\left[a_1^2+a_2^2+2a_1a_2\cos(k\Delta r+\Delta\Phi)\right]d\phi d\theta \tag{3.24b}$$

$$= \frac{2a_1a_2k^4}{16\pi^2\varepsilon_0\varepsilon_b}\int_0^{\pi}\int_0^{2\pi}\sin^4(\theta)\cos(\phi)\left[\cos(k\Delta r)\cos(\Delta\Phi)-\sin(k\Delta r)\sin(\Delta\Phi)\right]d\phi d\theta \tag{3.24c}$$

$$= -\frac{2a_1a_2k^4}{16\pi^2\varepsilon_0\varepsilon_b}\int_0^{\pi}\int_0^{2\pi}\sin^4(\theta)\cos(\phi)\sin(k\Delta r)\sin(\Delta\Phi)d\phi d\theta \tag{3.24d}$$

$$= \frac{2a_1a_2k^4\sin(\Delta\Phi)}{16\pi^2\varepsilon_0\varepsilon_b}\int_0^{\pi}\int_0^{2\pi}\sin^4(\theta)\cos(\phi)\sin[kd\sin(\theta)\cos(\phi)]d\phi d\theta \tag{3.24e}$$

In Equation (3.24a), $\hat{\boldsymbol{r}}\cdot\hat{\boldsymbol{x}} = \sin(\theta)\cos(\phi)$; in Equation (3.24b) the a_1^2 and a_2^2 terms can be dropped since the ϕ integral vanishes for these terms; Equation (3.24c) uses the trigometric identiy for $\cos(a+b)$; in Equation (3.24d) the ϕ integral vanishes again for the cos term; Equation (3.24e) uses Equation (3.20) for Δr. The final expression involves a non-vanishing integral that only depends on

the interparticle separation through kd. In the absence of an analytic solution to this integral, it is computed numerically at variable kd and the result is approximated by a fitted functional form

$$f(kd) = \int_0^{\pi} \int_0^{2\pi} \sin^4(\theta)\cos(\phi)\sin[kd\sin(\theta)\cos(\phi)]d\phi d\theta \approx -4\pi\frac{\cos(kd)}{kd} \tag{3.25}$$

The function $f(kd)$ and its approximate form are shown in Figure 3.15(b). The fit appears to be valid for $kd \gg 1$.

By conservation of linear momentum of the combined optical matter system, the net mechanical force acting on the pair of dipoles is

$$F_x = -S_x = -\frac{2a_1a_2k^4\sin(\Delta\Phi)f(kd)}{16\pi^2\varepsilon_0\varepsilon_b} \approx \frac{2a_1a_2k^3\sin(\Delta\Phi)\cos(kd)}{4\pi\varepsilon_0\varepsilon_b d} \tag{3.26}$$

3.B Simulating a near-field electrodynamically bounded dimer using GMT

In principle, a dimer can be simulated as two spheres that are electrodynamically interacting. Even though the particles individually only support dipole and quadrupole modes at these sub-wavelength sizes, the strong near-field coupling involves many higher order multipolar modes. To accurately simulate a dimer with a $\sim 5\,\text{nm}$ surface-to-surface gap, up to $n = 10$ in the multipolar expansion is required to accurately compute the near-field interactions. This is incredibly compute-time expensive and makes dynamics simulations come to a crawl.

To simulate the bound-dimer, the cluster T-matrix formalism is used. [77] Any collection of particles can be reduced to a single T-matrix that treats the composite object as a single electrodynamically scattering object. The aggregate T-matrix, $A_{ij\alpha\beta}$, describes the coupling between all pairs of electrodynamically interacting particles and can be calculated up to $n = 10$ multipoles. The cluster T-matrix is a reduction of this matrix to $A_{\alpha\beta}$ around a central coordinate, which can be reduced to $n = 2$ multipoles. This matrix is a standard T-matrix that can be used to treat the composite object as a single, anisotropic scattering object. The T-matrix can be rotated using the Wigner-d rotation matrices so that it does not need to be recomputed as the composite object rotates. See Section 6.1.3 for more details.

Note that in this T-matrix approach, there can be no vibration of the dimer. The composite

object cannot have any internal motion since that would require a recalculation of the aggregate T-matrix up to $n = 10$. With this assumption in mind, the dimer can be simulated to high accuracy and computational efficiency since only a maximum of 2 multipoles are needed.

3.C Linear momentum transfer via many-body forces in a ring trap

The non-reciprocal net-force realized in this chapter was achieved by breaking the mirror symmetry of the system by having dimers of different sizes or different materials. A related approach is to use the phase of the incident field to obtain phase differences between identical particles. [32] Another way of breaking this symmetry is using many-body electrodynamic interactions. This first occurs with three particles that are all identical forming a trimer. If the trimer is straight, there is no net force; however, if the trimer is bent, a net force acts on it. Figure 3.16 shows the net force acting on the trimer as a function of the bending angle in a circularly polarized plane-wave. When the trimer is bent into an equilateral triangle, the net force vanishes again.

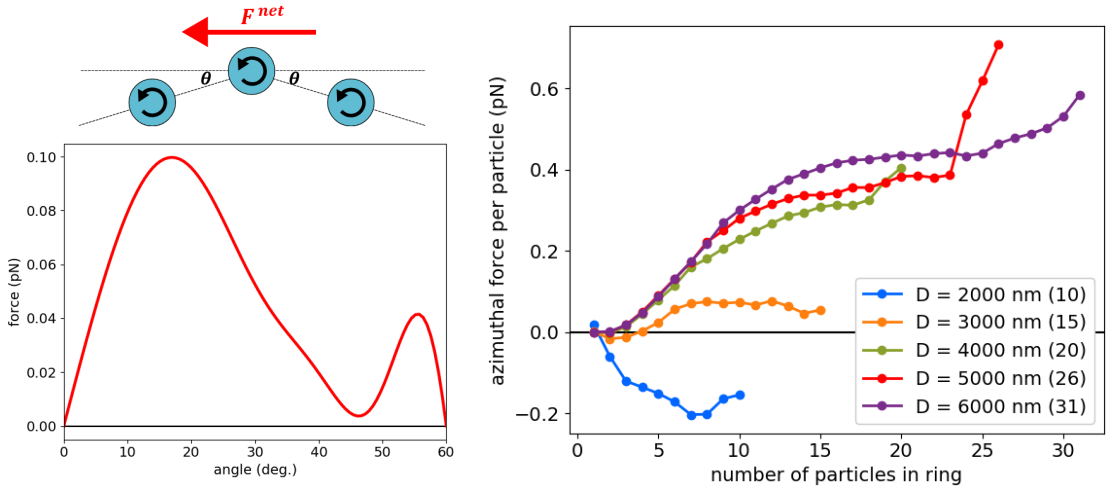

Figure 3.16: Net force on an optically bound bent trimer due to many-body interactions. (left) The net force on a trimer illuminated by circularly polarized light as a function of the bending angle. (right) Net azimuthal drive for N particles in $l = 0$ ring traps of different sizes. Despite a lack of incident orbital angular momentum, the particles are driven by the net force due to many-body interactions.

The net force is verified to be a many-body effect by looking at the dependence of F^{net} as a

function of the particle polarizability. The net force can be expressed as

$$F^{\text{net}} = c_1|\alpha| + c_2|\alpha|^2 + c_3|\alpha|^3 + \dots \tag{3.27}$$

Intensity and phase gradient forces due to an incident beam have $c_1 \neq 0$, i.e. these are first-order forces. Optical binding forces have $c_2 \neq 0$, i.e. these are pairwise forces. However, when the bent trimer is illuminated by a plane wave, simulation confirms that $c_1 = c_2 = 0$ and $c_3 \neq 0$. Thus, the force arises from a three-body effect where a third particle alters the dipole on a second particle, and that altered dipole interacting with the first particle results in a net force.

In a plane wave or Gaussian beam, the bent trimer is not a stable configuration and so the net force is not readily observed. To obtain a stable bent trimer, a ring trap can be used instead; the curvature of the intensity profile means that an optically bound trimer will have a bent angle depending on the curvature of the ring. This bound trimer will then experience a net force in the ring and move in an orbital motion. This is initially an unexpected behavior since in an $l = 0$ ring trap, particles are not driven one way or another due to zero OAM of the incident beam. Figure 3.16 shows the azimuthal driving force per particle for different ring sizes and number of particles in the ring. Having more than 3 particles in the ring continues to increase the magnitude of this many body non-reciprocal net force.

3.D Hydrodynamic coupling interactions (TT coupling)

Stokesian dynamics is an extension of Langevin dynamics that incorporates the hydrodynamic coupling interactions due to fluid flow in the medium. [95] Translation-translation (TT) coupling involves the translation of one particle generating a fluid flow that induces translation in another particle. In driven optical matter systems, this hydrodynamic coupling can be significant.

Figure 3.17 shows an example of many particles in a circularly polarized driven ring trap with a topological charge $l = 5$. Due to the phase gradient around the ring, particles are driven counter-clockwise around the ring while they interact electrodynamically and hydrodynamically. The average orbital angular velocity of the particles is shown with and without hydrodynamic coupling interactions for variable numbers of particles and three different materials. In all cases,

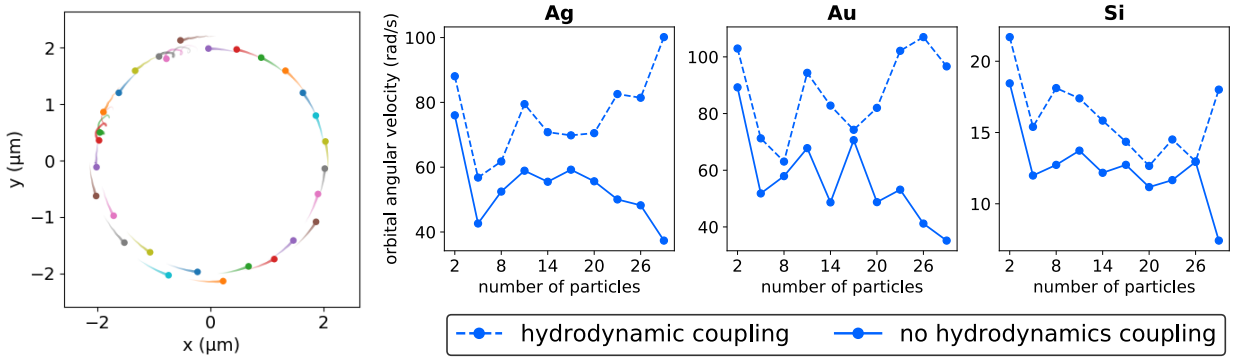

Figure 3.17: Effects of hydrodynamics on the driven dynamics of 2–30 nanoparticles (Ag, Au, and Si) in a circularly-polarized driven ring trap ($l = 5$). (left) Snapshot of 30 optically bound Ag particles being driven in the ring. Parameters: $w_0 = 2000\,\text{nm}$, $P = 15\,\text{mW}$, $R_{NP} = 75\,\text{nm}$, $\lambda = 800\,\text{nm}$, $n_b = 1.33$, $l = 5$. (right) Angular velocity of the nanoparticle arrays in the ring with and without hydrodynamic coupling interactions.

hydrodynamic interactions increase the angular velocity of the particles and the effect generally becomes stronger as more particles are added to the ring.

CHAPTER 4
NON-CONSERVATIVE DYNAMICS AND ANGULAR MOMENTUM: BUILDING OPTICAL MATTER MACHINES

The last chapter discussed the non-conservative forces that arose from linear momentum transfer between the electrodynamic field and the mechanical motion of the nanoparticles. A similar principle applies to angular momentum in optical matter arrays. An additional complication is that the field and nanoparticles have intrinsic (spin) and extrinsic (orbital) angular momentum. The total angular momentum of an optical matter system is then [89]

$$\begin{aligned}
\boldsymbol{L}_{\text{total}} &= \boldsymbol{L}_{\text{orbit}} + \boldsymbol{L}_{\text{spin}} \\
\boldsymbol{L}_{\text{orbit}} &= \boldsymbol{L}_{\text{mech,orbit}} + \boldsymbol{L}_{\text{field,orbit}} = \sum_i m_i \boldsymbol{r}_i \times \boldsymbol{v}_i + \varepsilon_0 \int_V \boldsymbol{E}(\boldsymbol{r},\omega) \cdot (\boldsymbol{r} \times \boldsymbol{\nabla}) \boldsymbol{A}(\boldsymbol{r},\omega) d^3 r \\
\boldsymbol{L}_{\text{spin}} &= \boldsymbol{L}_{\text{mech,spin}} + \boldsymbol{L}_{\text{field,spin}} = \sum_i I_i \boldsymbol{\omega}_i + \varepsilon_0 \int_V \boldsymbol{E}(\boldsymbol{r},\omega) \times \boldsymbol{A}(\boldsymbol{r},\omega) d^3 r
\end{aligned} \tag{4.1}$$

where $\boldsymbol{A}(\boldsymbol{r},\omega)$ is the vector potential and the integrals occur over all of space. There exist multiple types of spin–orbit interactions where the spin angular momentum (SAM) is converted into orbital angular momentum (OAM). For example, a tightly focused Gaussian beam (non-paraxial) converts the SAM of light into the OAM of light. [28] Light-matter interactions in optical matter arrays provide an additional mechanism of SAM–OAM conversion, as will be discussed in this chapter.

In this chapter, we explore spin and orbital angular momentum and their coupling in optical matter systems. The simplest system that exhibits a net-torque due to interactions is a dimer illuminated by circularly polarized light. This net torque can be realized in larger optical matter arrays, where an anomalous *negative torque* can occur where the net torque has the opposite handedness of the incident light.[35, 96, 97] Such a negative torque would violate angular momentum conservation in a conservative mechanical system, but can occur in optical matter arrays due to angular momentum exchange with the electromagnetic field. We show how these torques and the SAM–OAM conversion can be used to create an optical matter stochastic machine that utilizes non-conservative and Brownian forces for its operation.

Previous work has introduced the idea of controlling the spinning of individual nanoparticles

(NPs) using the spin angular momentum (SAM) of light in circularly polarized optical tweezers, referred to as "optical torque wrenches" [40, 64, 98–100]. This has been extended to arrays of NPs, where an optical torque wrench can generate orbital rotation through their interparticle interactions [35, 46, 96]. The possibility of using light-matter interactions to convert spin angular momentum into orbital angular momentum has been demonstrated and can be used as the driving mechanism of such machines. [101]

In Appendix 4.A, the effects of hydrodynamic rotation-translation (RT) coupling in driven optical matter systems are discussed. In Appendix 4.B, additional types of optical matter machines are proposed, including larger machines and patterned machines.

This chapter is based, in part, on a publication on the creation of optical matter stochastic machines that uses optical matter as a SAM to OAM converter. [47]

4.1 Net torque on an optically bound dimer

A single, spherical particle illuminated by circularly polarized light is known to spin with the same handedness as the light since it absorbs some of the incident photons. If the sphere is lossless, the torque vanishes. However, if the particle is non-spherical there is a net torque even if it is lossless due to the asymmetric scattering of light. [102]

An optically bound dimer is, essentially, a single composite anisotropic particle. [46] While the absorption of photons of the individual spheres leads to them spinning, the anisotropy of the bound dimer leads to an orbital motion of the dimer. This would not be the case if the particles were non-interacting; the binding of the particles is essential for it to be treated as a composite object.

Figure 4.1 shows the azimuthal force driving each particle in a bound dimer in right-handed circularly polarized light as a function of their separation (in a plane-wave or Gaussian beam). The net torque, $\tau = rF_\phi$, oscillates; for a plane-wave it oscillates around zero, while for the Gaussian beam it is shifted in the positive (right-handed) direction. The striking feature is the possibility of a *negative torque*: the dimer can be driven to orbit with a handedness that is the opposite of the incident light. [46] This behavior is due to the retardation of light in the interaction that yields a $2\pi r/\lambda_w$ phase factor. At stable separations, when $r = n\lambda_w$ is an integer multiple of the wavelength, the interactions are in phase and the torque is positive. Negative torque in a dimer generally occurs

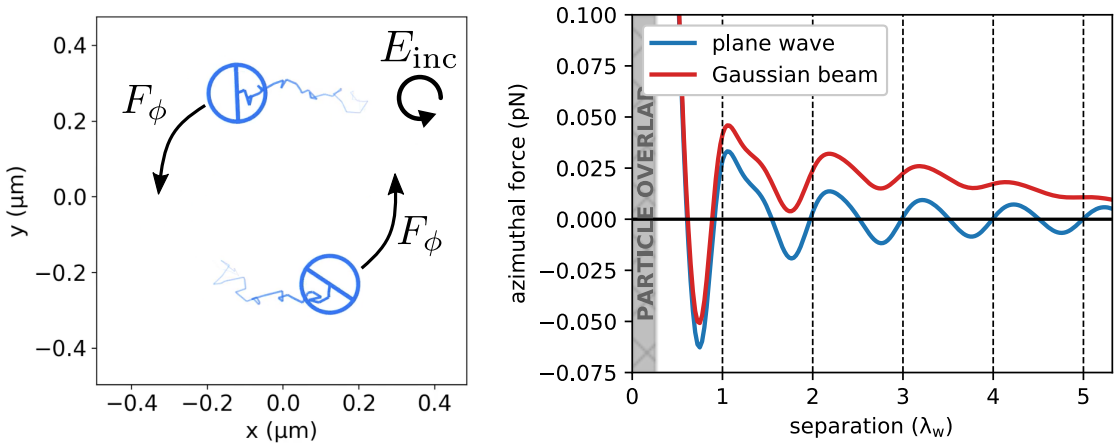

Figure 4.1: Net torque on an optically bound dimer. (left) An optically bound dimer (composed of two 150 nm diameter Ag nanoparticles) in a right-handed circularly polarized plane wave. The dimer experiences an azimuthal drive with the same handedness as the incident light. (right) Net azimuthal force (torque) on a dimer in a rhc-polarized plane wave and a Gaussian beam as function of particle separation.

at unstable separations.

The concept of negative torque does not violate angular momentum conservation because optical matter systems are open systems. A negative torque is allowed provided the dimer scatters an equal amount of positive angular momentum to the field, conserving total angular momentum in the combined opto-mechanical system.

In Figure 4.1, the torque is shown as a function of separation, but the separation is not a variable that is chosen since it is determined through the interactions. However, the wavelength of the incident light can be chosen, and this will set the length scale of the optical binding in the optical matter array. It is helpful to calculate two quantities as a function of both lattice spacing and wavelength: the total scattering cross-section, $C_{\text{scat}}(\delta, \lambda)$, and the net torque, $\tau_z(\delta, \lambda)$. These are shown as color maps in Figure 4.2. Also shown are the stable lattice spacings at each wavelength, $\delta_s(\lambda)$, calculated by performing gradient descent for the dimer. For $\lambda > 550\,\text{nm}$, the relationship between the two is very close to linear, $\delta_s = \lambda/n_b$. When $\lambda < 550\,\text{nm}$, the relationship can become non-linear since higher order multipolar modes (quadrupoles, etc.) begin to arise and modify the nature of the electrodynamic interactions.

For $\lambda > 670\,\text{nm}$, the torque is positive at stable binding, while for $\lambda < 670\,\text{nm}$ there is a region where the torque is negative at stable binding. Thus, it is possible to realize an optically bound

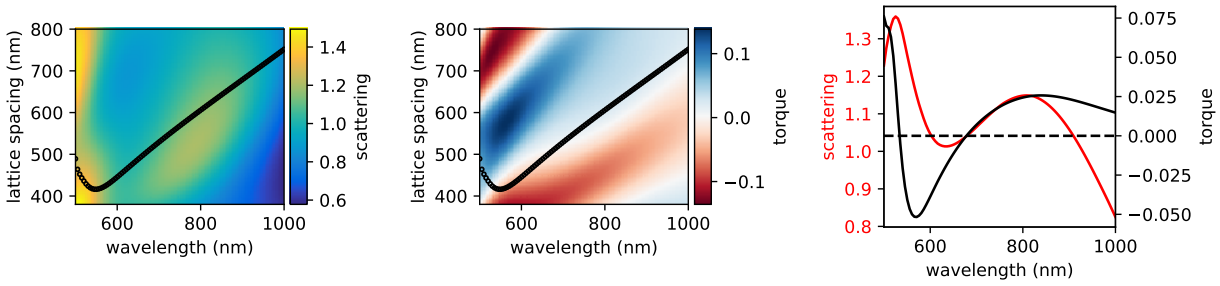

Figure 4.2: Net torque on a dimer at variable separation and incident wavelength. (left) Scattering intensity of the dimer at variable wavelength and separation. Black circles are stable optical binding positions. (center) Similar diagram for the net torque. (right) The scattering and net torque at variable wavelength when the particles are at their stable separations.

dimer spinning with the opposite handedness of the incident light by going to shorter wavelengths. Note that this coincides with a resonance in the scattering of the dimer. Resonances such as these can result in a π phase-shift of the induced dipoles, and the transition between positive and negative torque will often occur near these resonances.

4.2 Positive and negative optical torque in larger arrays

The orbital motion of the bound dimer extends to the case of N optically bound particles. Provided the incident power density is sufficiently large, particles in circularly polarized light will form a rigid array with hexagonal packing. A net torque acts on the rigid array, setting it into an orbital motion.

Figure 4.3(a) shows the net torque τ_z as a function of the number of particles N at a fixed wavelength $\lambda = 800\,\text{nm}$ and separation $\delta = 600\,\text{nm}$ ($n_b = 1.33$). For a dimer ($N = 2$), the torque is positive, while for $N > 2$ the torque is increasingly negative. Thus, negative torque can be observed at the given wavelength simply by adding more particles to the array, hinting that this phenomenon is a collective many-body effect. In Figure 4.3(b), the lattice spacing δ is varied for each value of N. For all of the arrays, the torque oscillates between positive and negative values as δ is varied. A phase space diagram for the sign of the torque can be constructed, $\tau_z(\delta, N)$, and is shown in Figure 4.3(c).

As in the case of the optically bound dimer, the lattice spacing δ is not a controllable variable other than through the wavelength of the incident light. Moreover, it can even become position-dependent

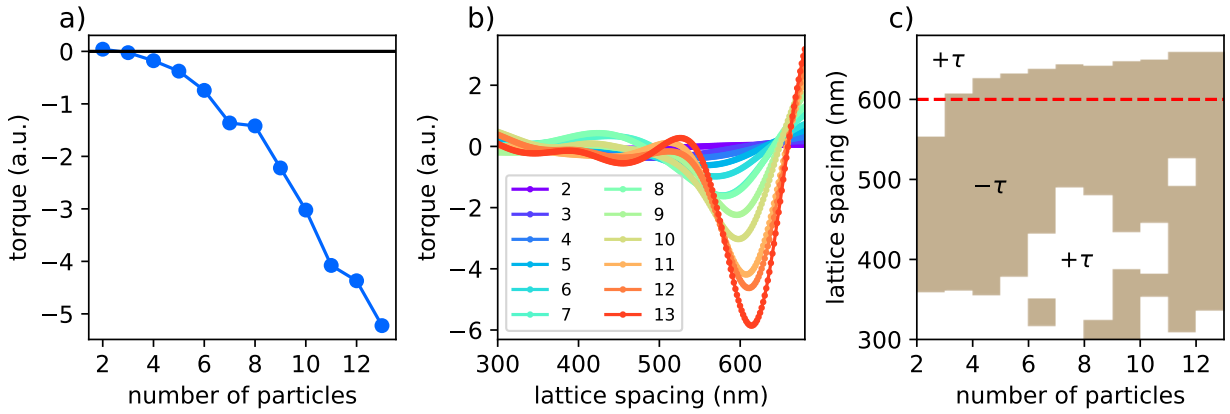

Figure 4.3: Positive and negative torque in larger optical matter arrays. (a) Net torque on an array of particles as a function of number of particles in the array. (b) Net torque as a function of lattice spacing at different numbers of particles. (c) Torque phase-space diagram that show regions of positive and negative torque. The dashed line is the stable first optical binding separation. [35]

since particles at the center of an array have a different environment from particles towards the edge of the array. Figure 4.4 shows the scattering cross-section and net torque for $N = 7$ particles, where it's assumed that δ is not position-dependent (position dependence becomes more relevant as more layers of particles are added). Again, the relationship between δ and λ is linear over longer wavelengths ($\lambda > 600\,\text{nm}$).

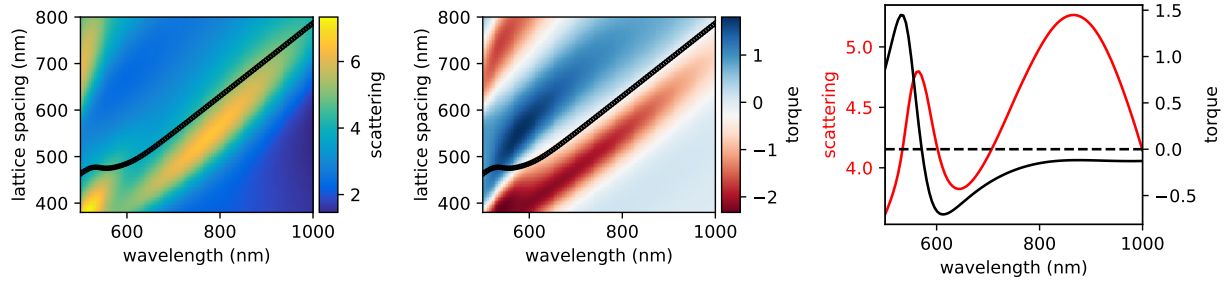

Figure 4.4: Net torque on a hexagonal optical matter array at variable separation and incident wavelength. (left) Scattering intensity of the hexagonal OM array at variable wavelength and separation. Black circles are stable optical binding positions. (center) Similar diagram for the net torque. (right) The scattering and net torque at variable wavelength when the particles are at their stable separations. [35]

The intense scattering feature between $\lambda = 600\,\text{nm}$ to $950\,\text{nm}$ is the emergence of a surface lattice resonance. The scattering at stable binding, when compared to that of the dimer in Figure 4.2, has its longer wavelength resonance (a collective mode) enhanced relative to its shorter wavelength

resonance (a single particle resonance). The stable binding distance is such that it is on the shorter wavelength side of this resonance. The net torque is negative for $\lambda > 580\,\text{nm}$ and positive for shorter wavelengths.

4.3 Collective electromagnetic modes and their angular momentum

The total rate of angular momentum scattered by an array of N particles can be obtained by analytically integrating the Maxwell stress tensor around a closed surface containing all of the particles. [103] A collection of electrodynamically interacting particles can be reduced to a cluster representation around a single origin (see Section 6.1.8 for details). The fields scattered by the cluster as a whole can then be written as an expansion over the vector spherical harmonic wavefunctions

$$\boldsymbol{E} = \sum_{n=1}^{\infty} \sum_{m=-n}^{n} a_{mn}\boldsymbol{N}_{mn} + b_{mn}\boldsymbol{M}_{mn} \tag{4.2}$$

Combined with a similar expansion for the magnetic field $\boldsymbol{H}$, the Maxwell stress tensor can be constructed and integrated analytically to obtain expressions for the outgoing angular momentum. The expression for the z-component of the rate of outgoing angular momentum, $\dot{L}_z$, is

$$\frac{dL_z}{dr} = \dot{L}_z = \frac{2\pi}{k^3} \sum_{n=1}^{N_{\max}} \sum_{m=-n}^{n} m\left\{ \varepsilon_b |a_{mn}|^2 + \mu_b |b_{mn}|^2 - \text{Re}\left[\varepsilon_b a_{mn} p_{mn}^* + \mu_b b_{mn} q_{mn}^* \right] \right\} \tag{4.3}$$

where ε_b and μ_b are the background permittivity and permeability, respectively.

$\dot{L}_z$ can be related to the scattering and absorption cross-sections on a term-by-term basis. For a RHC polarized plane wave, $p_{mn} = q_{mn} = 0$ if $m \neq 1$. So if $m \neq 1$:

$$\dot{L}_z^{mn1} = \frac{m\varepsilon_b}{2k} C_{\text{scat}}^{mn1} \tag{4.4}$$

$$\dot{L}_z^{mn2} = \frac{m\mu_b}{2k} C_{\text{scat}}^{mn2} \tag{4.5}$$

and if $m = 1$:

$$\dot{L}_z^{1n1} = -\frac{\varepsilon_b}{2k} C_{\text{abs}}^{1n1} \tag{4.6}$$

$$\dot{L}_z^{1n2} = -\frac{\mu_b}{2k} C_{\text{abs}}^{1n2} \tag{4.7}$$

For $m \neq 1$, the m index determines the sign of the outgoing angular momentum, and modes with larger values of m scatter more angular momentum.

The total rate of outgoing angular momentum is then a sum over all terms

$$\dot{L}_z = \sum_{r=1}^{2} \sum_{n=1}^{N_{\max}} \sum_{m=-n}^{n} \dot{L}_z^{mnr} \tag{4.8}$$

The net torque on the cluster in response to the outgoing angular momentum contains both spin (internal) and orbital (external) components

$$\tau_z^{\text{net}} = \hat{\boldsymbol{z}} \cdot \sum_i \boldsymbol{r}_i \times \boldsymbol{F}_i + \boldsymbol{\tau}_i = -\dot{L}_z \tag{4.9}$$

When treating the array of particles as a single composite object, it is not easy to disentangle the spin and orbital contributions to the total angular momentum. However, for isotropic Ag and Si particles, the absorption is minimal and the mechanical spinning of the particles is negligible. The equations reported here are similar to those reported by others. [96]

Selection rules that restrict the allowed values of m based on conservation of angular momentum have been reported for rotationally symmetric NP arrays [96, 104]. For an array with m_s–fold symmetry and incident light with m_{inc}, the allowed values of m are

$$m = m_{\text{inc}} + m_s q \tag{4.10}$$

where q is a positive or negative integer.

4.4 Optical matter gear

Because light exerts a net torque on an optical matter array, the array must scatter an equal and opposite amount of angular momentum. The outgoing vector spherical harmonic wavefunctions generally carry orbital angular momentum (OAM) and are excited by the incident spin angular momentum (SAM) of the light. Thus, an optical matter array operates as a SAM-to-OAM converter. This conversion raises the question of whether an optical matter heat engine can be designed, analogous to what has been done for single micrometer and nanometer-sized particles that convert heat into work. [105–107]. In principle, a particle placed outside of the optically bound array can couple to the scattered orbital angular momentum and be driven by non-conservative forces that do work on the particle in a closed loop.

A mechanical analog of an SAM–OAM converter is a planetary gear machine [108] – schematically shown in Figure 4.5(a). Work is performed in the gear system by rotating a crank connected to a large gear. Both the shaft and gear are shown exhibiting right-handed rotation (denoted by red arrows; the convention of pointing one's thumb towards the source is used). A second, smaller gear is coupled to the larger gear, causing it to rotate and orbit the large gear. The small gear rotates with an opposite left-handed rotation (denoted by green arrows). A fixed ring gear provides radial confinement and causes the small gear to perform a right-handed orbit around the large gear.

The corresponding optical matter (OM) machine is depicted in Figure 4.5(b). The crank is replaced with a right-hand circularly (RHC) polarized optical beam. The material constituents of the OM gear, Ag NPs of radius $R_p = 75\,\text{nm}$, are attracted to the high intensity region of the focused beam. Multiple particles trapped in the beam self-organize into a hexagonal lattice geometry due to rotationally symmetric optical binding interactions when the incident light is circularly polarized. An assembled 7NP OM array operates as an OM gear; the angular momentum of the scattered field provides the torque for the gear to rotate. For the NP properties and geometry considered here, the OM gear exhibits a negative torque.

When a "probe particle" (Ag NP with radius $R_p = 100\,\text{nm}$) is placed outside the OM gear, it orbits in the right-handed direction, analogous to the orbital motion of the small gear in the planetary gear mechanical machine (Figure 4.5). This observed counter-rotation can be understood as

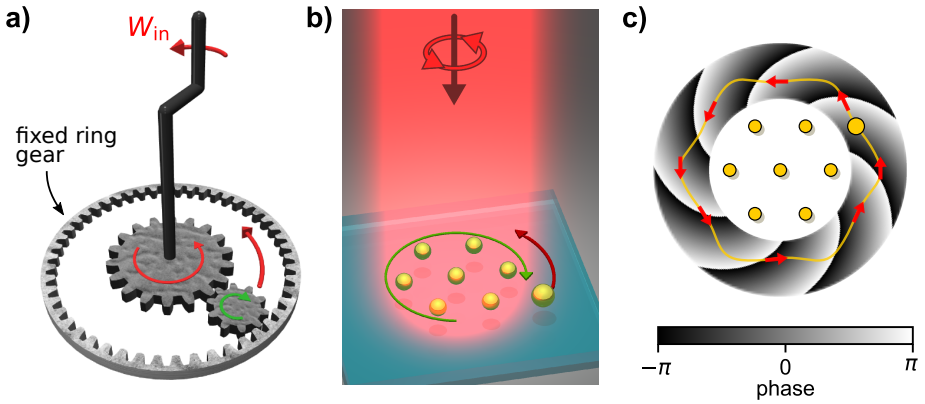

Figure 4.5: Designing an optical matter machine. (a) A planetary mechanical gear machine consisting of a large gear made to rotate by a crank and a small gear that is driven to rotate and orbit. A fixed ring gear provides radial confinement and causes the small gear to orbit the large gear. The gears couple such that the small gear rotates with the opposite handedness and orbits with the same handedness as the large gear's rotation. (b) An analogous optical matter machine. The 7NP array acts as a large OM gear that converts spin angular momentum into orbital angular momentum that is imparted on a smaller OM gear (the probe particle), driving its orbital motion. (c) The phase profile of the $e_{7,7}$ mode in the transverse plane outside the OM gear. The phase profile, $\psi \propto \exp(i7\phi)$, provides a circulation of momentum around the OM gear, with $m = 1 + 6$ phase wrappings. A path for the probe particle's orbital motion is shown in yellow. [47]

a demonstration of conservation of angular momentum: if the OM gear is rotating with the opposite handedness as the incident light, it must be that a net positive quantity of angular momentum is scattered by the OM gear. The probe particle feels this outgoing positive angular momentum and is driven to orbit around the OM gear (Figure 4.5(c)). Radial confinement of the probe is provided by an inward phase gradient of the converging beam optical trap, analogous to the use of a fixed ring gear that radially confines the small gear in the mechanical machine.

Since the total angular momentum of the system (electromagnetic field and NPs) is conserved, a negative torque on the gear necessitates increased angular momentum in the emanating field. Scattered light from the OM gear can be decomposed into collective multipolar modes, labeled $e_{n,m}$ and $m_{n,m}$ for electric and magnetic modes, respectively; n is the order and m is the azimuthal index of the mode. These modes are eigenfunctions of the angular momentum operator, with eigenvalue m; this description is analogous to that of quantum mechanical angular momentum states where the spherical harmonics are eigenfunctions of the angular momentum operator [109]. Each collective mode continuously carries angular momentum, L_z^{mn}, away from the OM gear at a rate given by

Equation (4.1). In response, the OM gear feels a net recoil torque (spin and orbit) due to conservation of angular momentum.

The angular momentum selection rules, Equation (4.10), form the basis of the optical matter SAM–OAM machine: photons with $m_{\text{inc}} = +1$ incident on the $m_s = 6$ -fold symmetric OM gear are converted into collective scattering modes with $m = -5, +1, +7$. Larger m values can be neglected due to the size of the OM gear as determined by Wiscombe's criterion [110].

The magnitude and directionality of light scattered by the $m = -5$ and $m = +7$ modes determines the field the probe particle experiences. The calculated phase profile of the $\mathrm{e}_{7,7}$ mode scattered in the transverse plane of the OM gear is depicted in Figure 4.5(c). The yellow curve is the preferred path of the probe particle around the OM gear. It will be demonstrated that the $\mathrm{e}_{7,7}$ mode is the dominant contribution to the transversely scattered OAM, and is therefore responsible for the right-handed driven orbital motion of the probe particle.

The relationship between angular momentum and scattering cross-sections in Equation (4.6) and Equation (4.7) motivates examination of the mode-dependent spectroscopic properties of the OM gear. The collective scattering modes in the OM gear emerge in the wavelength-dependent scattering cross-section of the OM gear as it is built particle-by-particle in an optical trap. The scattering cross-sections shown in Figure 4.6(a) demonstrate that the single particle Mie resonance ($\lambda = 600\,\text{nm}$) is converted into a surface lattice resonance ($\lambda = 740\,\text{nm}$) as particles are added to the array. We refer to this emergent peak as a *collective scattering resonance* (CSR) of the OM array. In the limit of a large lattice, the CSR becomes spectrally more narrow and approaches the well-known surface lattice resonance (SLR) of an infinitely extended array [111, 112]. Electric field intensity plots of the single particle Mie resonance and the CSR are shown as insets to Figure 4.6(a).

A multipole expansion of the scattered fields is performed to obtain the mode-dependent composition of the CSR and their contributions to the far-field angular scattering. A note on notation: if the azimuthal index m is omitted, a sum over m is applied while keeping n fixed, i.e. $\mathrm{e}_n = \sum_m \mathrm{e}_{nm}$ and $\mathrm{m}_n = \sum_m \mathrm{m}_{nm}$. Figure 4.6(b) shows the contribution of the e_n and m_n modes to the total scattering intensity up to $n = 7$ for the OM gear. Thus, the CSR is a superposition of many orthogonal modes; the e_1, e_5, e_7, and m_4 modes are most significant. The azimuthal index m obeys the rotational symmetry selection rule (Equation (4.10)) with $m_s = 6$ symmetry. Therefore,

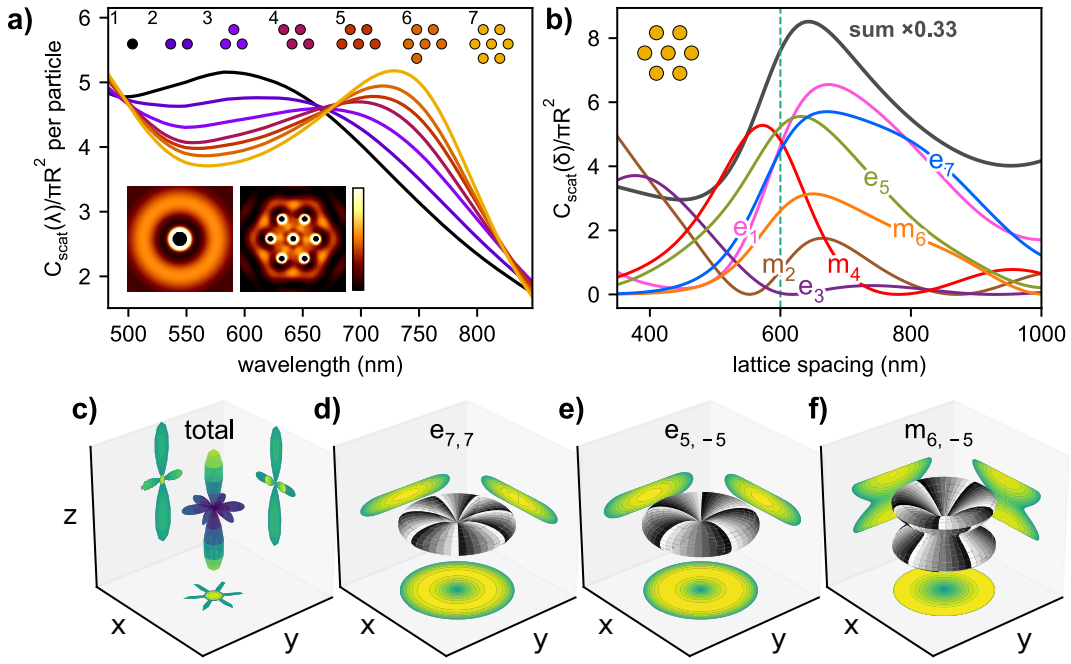

Figure 4.6: Building an OM gear using optical binding forces and collective modes. (a) Per particle scattering cross-section (normalized by πR_p^2, where $R_p = 75\,\text{nm}$ is the radius of a single NP) as the OM gear is built particle by particle with lattice spacing $\delta = 600\,\text{nm}$ in water ($n_b = 1.33$). A single particle Mie resonance ($\lambda = 600\,\text{nm}$) is converted into a collective scattering resonance ($\lambda = 740\,\text{nm}$). Insets show the field intensity of the single particle Mie resonance (left inset) and the CSR (right inset) at their respective resonant wavelengths. (b) Normalized scattering cross-sections of the non-vanishing multipole modes of the OM gear as a function of lattice spacing, δ, at $\lambda = 800\,\text{nm}$ (optical binding distance shown as vertical dashed line). (c) Total far-field angular scattering intensity from the OM gear and projections onto the Cartesian planes. (d-f) Far-field angular scattering and phase profiles of the $e_{7,7}$, $e_{5,-5}$, and $m_{6,-5}$ modes, respectively. [47]

the e_7 mode consists of three terms ($m = -5, 1, 7$), the e_5 mode consists of two terms ($m = 1, -5$), and the e_1 and m_4 modes consist of only one term ($m = 1$).

The far-field angular scattering of the OM gear shown in Figure 4.6(c) exhibits strong, narrow lobes along the forward and backward directions and 6 transverse lobes lying in the xy-plane. Far-field angular scattering of the $e_{7,7}$ and $e_{5,-5}$ modes shown in Figure 4.6(d,e) exhibit in-plane scattering with m phase wrappings. By contrast, the $m_{6,-5}$ mode in Figure 4.6(f) exhibits out-of-plane angular scattering. Consequently, the $e_{7,7}$ and $e_{7,-5}$ modes couple strongly with positive and negative signs, respectively, while the $m_{6,-5}$ mode couples weakly to a probe particle located in the transverse plane. The $e_{7,7}$ mode is of particular interest due to its large angular momentum content and extremely flat angular profile.

4.5 Counter-rotation of gear–probe machines

The azimuthal index m defines the rate of OAM scattered by the OM gear; modes with larger m have larger quantities of OAM. Figure 4.7(a) shows the mode-dependent contributions to the net angular momentum of the scattered light. The e_7 mode is strongest (and positive) due to the $m = 7$ term, while the e_5 and m_6 modes contribute negative angular momentum due to the $m = -5$ terms. The net angular momentum can be positive or negative depending on the lattice spacing, which results in a negative or positive recoil torque, respectively, on the OM gear. At the optical binding distance ($\delta = 600\,\mathrm{nm}$), the outgoing angular momentum is overall positive, resulting in a negative recoil torque on the OM gear.

We obtain a qualitative picture of the angular momentum around the OM gear by calculating the transverse Poynting vector, $\boldsymbol{S}_\parallel \propto (\boldsymbol{E} \times \boldsymbol{H})_\parallel$, in the xy-plane. Streamlines of $\boldsymbol{S}_\parallel$ are shown in Figure 4.7(b); the color-scale informs on the magnitude of $\boldsymbol{S}_\parallel$ relative to S_z of the incident field. Inside the OM gear $\boldsymbol{S}_\parallel$ spirals inward around each particle with the same handedness as the incident light. Outside the OM gear there is a counter-clockwise flow that the streamlines converge to. These streamlines suggest that if a probe particle is placed outside the OM gear it will feel a flow of electromagnetic energy and be driven to move along streamlines. The counter-clockwise flow primarily comes from the $e_{7,7}$ mode that has a positive OAM that is directed in the xy-plane.

The force on the probe particle can be separated into radial and azimuthal components, $\boldsymbol{F}(\boldsymbol{r}) = F_\rho(\boldsymbol{r})\hat{\boldsymbol{\rho}} + F_\phi(\boldsymbol{r})\hat{\boldsymbol{\phi}}$, that are shown in Figure 4.7(c,d), respectively. The probe particle will generally move in two dimensions in response to the electrodynamic forces, and the radial force provides confinement that restricts the motion of the probe to a smaller domain. We *define* the stable 1D path for orbital motion of the probe particle such that the radial force vanishes and begets stability, i.e. $F_\rho = 0$ and $\partial F_\rho/\partial\rho < 0$. This path is shown as the dashed line in Figure 4.7(c,d) and has a hexagonal-like shape. The probe is not restricted to the stable path, but on average moves along it.

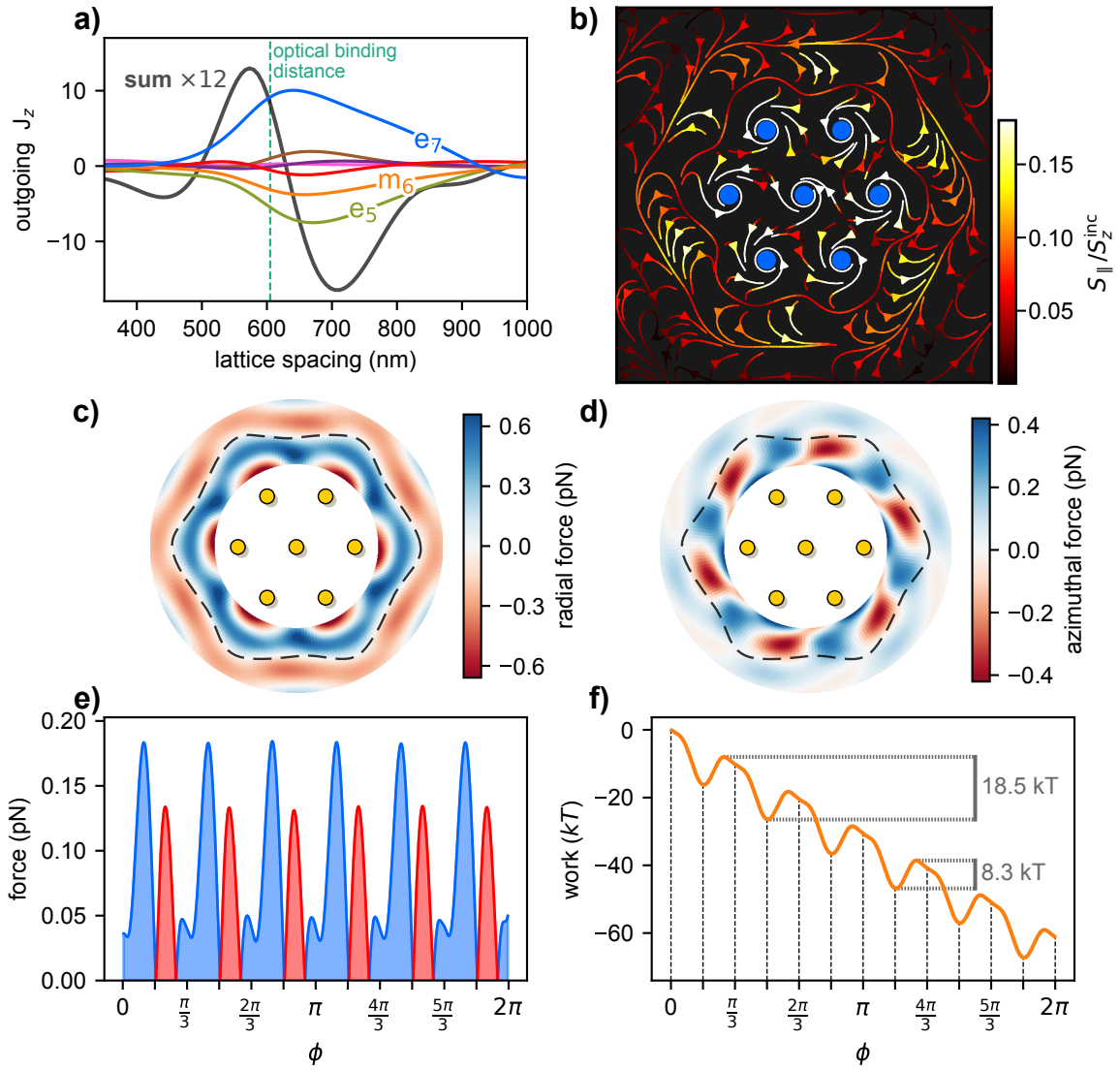

Figure 4.7: Orbital angular momentum scattered by the OM gear can be used to do work. (a) Angular momentum carried away by the collective modes of the OM gear at $\lambda = 800\,\text{nm}$. The net angular momentum is the sum of all such contributions, and can be positive or negative. The net outgoing angular momentum is positive at the optical binding distance ($\delta = 600\,\text{nm}$) (b) Streamlines of the transverse Poynting vector in and around the OM gear. (c) Radial force map of the probe particle in an annular region outside the OM gear. The dashed line is a stable path where $F_\rho = 0$ and $\partial F_\rho/\partial\rho < 0$, where ρ is the particle's radial coordinate. (d) Azimuthal force map of the probe particle. (e) Component of the force tangential to the stable path, F_t. Blue regions are positive (counter-clockwise) and red regions are negative (clockwise) force. (f) Work done on the probe particle as it moves along the stable path, $W = -\int F_t dl$ in units of $k_B T$, where k_B is Boltzmann's constant. [47]

The azimuthal force can be positive (counter-clockwise) or negative (clockwise) along the stable path. Stable positions along the path occur where the azimuthal force vanishes and begets stability along the path, i.e. $F_\phi = 0$ and $\partial F_\phi / \partial \phi < 0$. If the probe particle has enough thermal energy, it can hop from one stable position to another in either the clockwise or counter-clockwise direction. However, the probe particle prefers hopping in the counter-clockwise direction due to the positive OAM from the $e_{7,7}$ mode as demonstrated by the projection of the azimuthal force along the stable path shown in Figure 4.7(e). The positive forces generally outweigh the negative forces along the path. The work required to move the probe particle in the counter-clockwise direction along the path, $W(\phi)$, is then an integral of this force curve, as shown in Figure 4.7(f). $W(\phi)$ is periodic and titled, and the electrodynamic barrier for clockwise hops is about twice as large as that of counter-clockwise hops. This type of work curve is analogous to 1D transport caused by Brownian fluctuations in asymmetric periodic potentials seen in forced thermal ratchets [37, 113]. Although the work barriers are quite large for the probe to hop (8.3 $k_B T$), this calculation assumes the seven particles in the gear remain stationary. The actual work required could be much lower when all particles are allowed to fluctuate due to higher dimensional pathways for the intruder to hop.

While the gear has a perfect 6-fold symmetry, the presence of the probe particle breaks this symmetry and enables the combined machine to access azimuthal modes that violate the angular momentum selection rule, Equation (4.10). The effect of the probe on the gear causes it to scatter angular momentum into other azimuthal channels. However, the quantity of angular momentum is 50 times smaller than that carried by the $e_{7,7}$ mode and the probe can be considered a small perturbation to the scattered angular momentum selection rules.

Note that the OM gear does not need to be a six-fold symmetric hexagonal shape for the conversion of SAM to OAM to occur. Experimentally, the OM gear may contain additional particles or thermally fluctuate to different configurations. In such cases, the quantity of outgoing angular momentum in each of the modes (Figure 4.7(a)) will be different.

A schematic of the thermal hopping of the probe around the OM gear along the stable path is shown in Figure 4.8(a). The probe particle hops between 6 stable positions (denoted by solid orange squares) with a counter-clockwise bias. In addition to the thermal hopping of the probe particle, the OM gear experiences a net recoil torque due to angular momentum being carried by

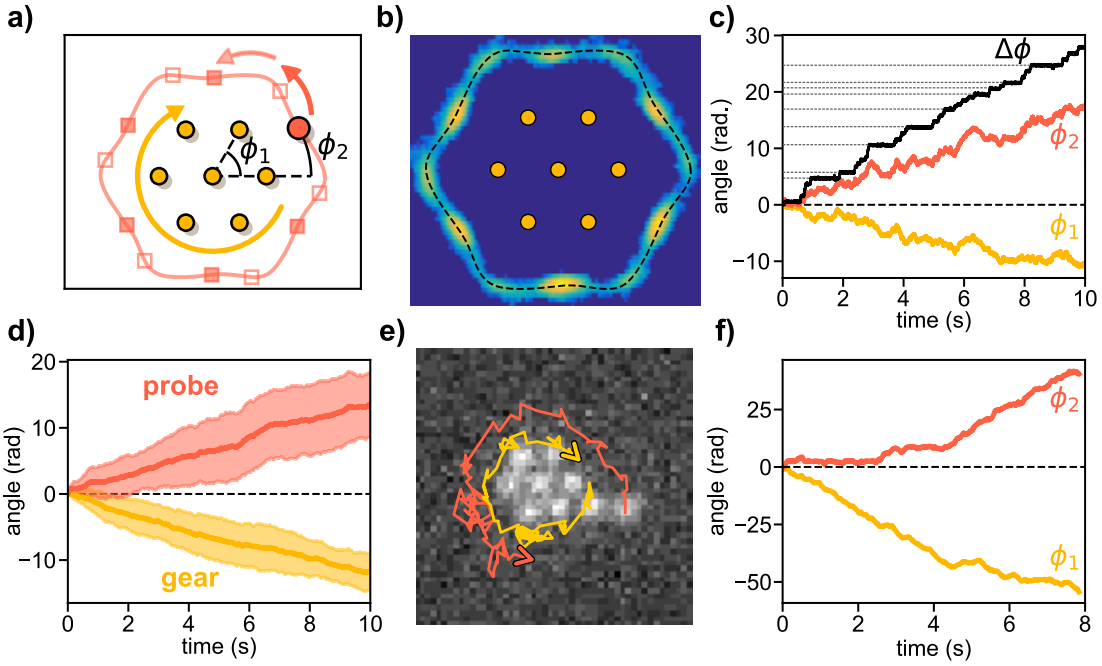

Figure 4.8: Realizing an optical matter machine. (a) Schematic of the OM machine. Arrows denote the direction of preferred angular rotation. Filled and unfilled squares denote stable and unstable probe positions, respectively. (b) Probability density function of the probe particle's position relative to the OM gear from a 10 s Brownian dynamics simulation. (c) Time trajectories of the angular positions of the OM gear and probe particle. The difference angle, $\Delta\phi(t) = \phi_2(t) - \phi_1(t)$, is a monotonically increasing stepped function. The steps represent angular jumps of the probe particle between stable positions. (d) Ensemble averaged angles of the probe and gear from 20 simulations. The shaded regions enclose the standard deviation of the angles at time t. (e) An image from a video of an experiment of an 8NP OM gear with a larger probe particle on its periphery. A 0.4 s trajectory of the OM gear and probe are superimposed. (f) Experimentally observed counter-rotation of the OM machine.

light scattered from the CSR modes. Figure 4.6(b) shows that the recoil torque is negative at the given lattice spacing of the OM gear ($\delta = 600$ nm) since the e_7 mode carries more positive angular momentum than the total negative angular momentum of the e_5 and m_6 modes. This leads to a clockwise rotation of the OM gear – in the opposite direction of the probe particle's orbital motion, resulting in the counter-rotation of the OM machine.

A defocused but converging Gaussian beam is used in the simulations to provide an inward phase gradient to enhance the stability of the OM machine. Without the inward radial phase gradient associated with the converging beam, the probe particle will escape the trap. The probe particle must also be dissimilar in size from those NPs constituting the OM gear to prevent particle exchanges

and rearrangement of the gear. Intuition suggests that a smaller probe particle may be preferred since it will scatter less light and cause less deformation in the OM gear. However, a smaller probe will force its way into the gear and break its structure. Therefore, as described in Chapter 3, the probe particle must be larger than the NPs constituting the OM gear due to "non-reciprocal forces" that arise in NP hetero-dimers [45].

Given that the probe particle can be trapped in a local minimum of the work in Figure 4.7(f), the driven transport of the probe particle will only occur in simulations with thermal energy and fluctuations. The counter-rotation of the OM machine was captured in a ($T = 298\,\mathrm{K}$) Brownian dynamics simulation that quantified the angular dynamics $\phi_1(t)$ of the OM gear and $\phi_2(t)$ of the probe particle as a function of time t. The path of the probe relative to the gear can be obtained by moving into a rotating reference frame such that the gear remains stationary and the probe orbits. A probability density function of the probe particle's position shown in Figure 4.8(b) reveals the hexagonal path of the probe and the 6 stable positions. The dashed line shows the stable path determined numerically in Figure 4.7 and demonstrates agreement with the probability density from the probe particle trajectories.

The angular trajectories $\phi_1(t)$ and $\phi_2(t)$ for a single 10 s simulation shown in Figure 4.8c confirm the counter-rotation of the gear and probe. With the starting condition $\phi_1(t = 0) = \phi_2(t = 0) = 0$ and defining the relative change in angle $\Delta\phi(t) = \phi_2(t) - \phi_1(t)$, we find that $\Delta\phi(t)$ strictly increases in time. The counter-rotation is shown to be statistically significant over an ensemble of 20 simulations for the same simulation conditions. Figure 4.8(d) shows the average and standard deviation of the ensemble of angular trajectories.

We experimentally confirmed the predicted counter-rotation of the OM machine where the OM gear consists of 8 equal sized NPs (150 nm diameter Ag) with a larger probe particle (180-200 nm diameter Ag). Figure 4.8(e) shows an image from an experiment with an 8NP OM gear (hexagonal array plus one) and of a probe particle on its periphery. Trajectories for the probe (orange) and the eighth particle in the gear (yellow) of length 0.4 s starting from the frame are superimposed on the image. Figure 4.8(f) shows the trajectories of the angular positions $\phi_1(t)$ and $\phi_2(t)$ and confirms the counter-rotation over a longer time. The experimentally observed counter-rotation for an 8NP OM machine suggests that these OM machines can be realized for a broader range of array geometries.

4.6 High-index dielectric optical matter machines

It is possible to build an OM machine out of dielectric nanoparticles – which have received attention in the photonics community for their tunable Mie resonances [114] – instead of plasmonic (Ag or Au) particles. High-index dielectric materials such as silicon (Si) are good candidates due to their enhanced scattering and sharp resonances. At $\lambda = 800\,\text{nm}$, silicon can be approximated with a constant index of refraction $n = 3.7$. Figure 4.9(a) shows the construction of the Si OM machine, where the gear particles are now larger than the probe particle. Unlike the plasmonic machine, this Si OM machine is stable and does not suffer the same intrusive dynamics. This unique behavior is likely due to the presence of a significant magnetic dipole mode for Si nanoparticles, see Figure 4.9(b).

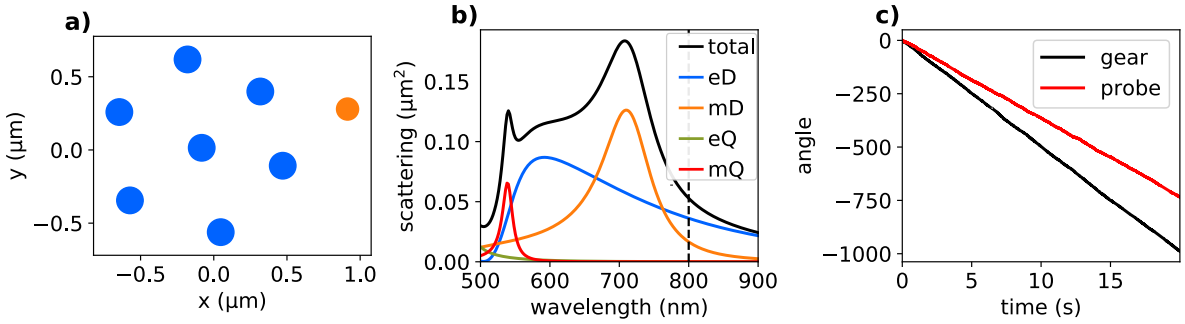

Figure 4.9: Realization of a silicon optical matter machine in simulation. (a) Snapshot of the machine with a gear made of 90 nm radius Si particles and an Si probe of radius 75 nm. (b) Multipolar scattering of the 90 nm radius Si particle. (c) Angles of the gear and probe over a simulation.

Angles of the gear and probe in the Si machine are shown in Figure 4.9(c). Similar to the plasmonic machine, the probe particle only hops in the counter-clockwise direction. Unlike the plasmonic machine, the gear spins much faster and with a negative torque such that counter-rotation of the gear–probe machine is not observed.

The presence of magnetic modes changes the binding interactions as well as the outgoing angular momentum. In the plasmonic machine, the $e_{7,7}$ mode emerged due to a collection of induced electric dipoles. The high-index dielectric machine has, in addition to the $e_{7,7}$ mode, the $m_{7,7}$ mode due to a collection of induced magnetic dipoles. Thus, the probe particle now has two channels with $m = 7$ that it can couple into, one that is electric in nature and the other that is magnetic in nature.

The performance of plasmonic and high-index dielectric machines can be compared by computing the efficiency of each machine under the same beam conditions. The efficiency of the OM machine can be defined as the rate of thermal hopping of the probe around the OM gear

$$\mathcal{E} = \lim_{t\to\infty}\left(\frac{\phi_2(t) - \phi_1(t)}{t}\right) \tag{4.11}$$

In general, $\mathcal{E}$ depends on the power of the incident beam. The power also effects the hexagonal order of the gear, which determines how well it operates as an SAM–OAM converter. Figure 4.10 shows $\mathcal{E}(P)$ of the machine and $\psi_6(P)$ of the gear for Ag, Au, and Si materials.

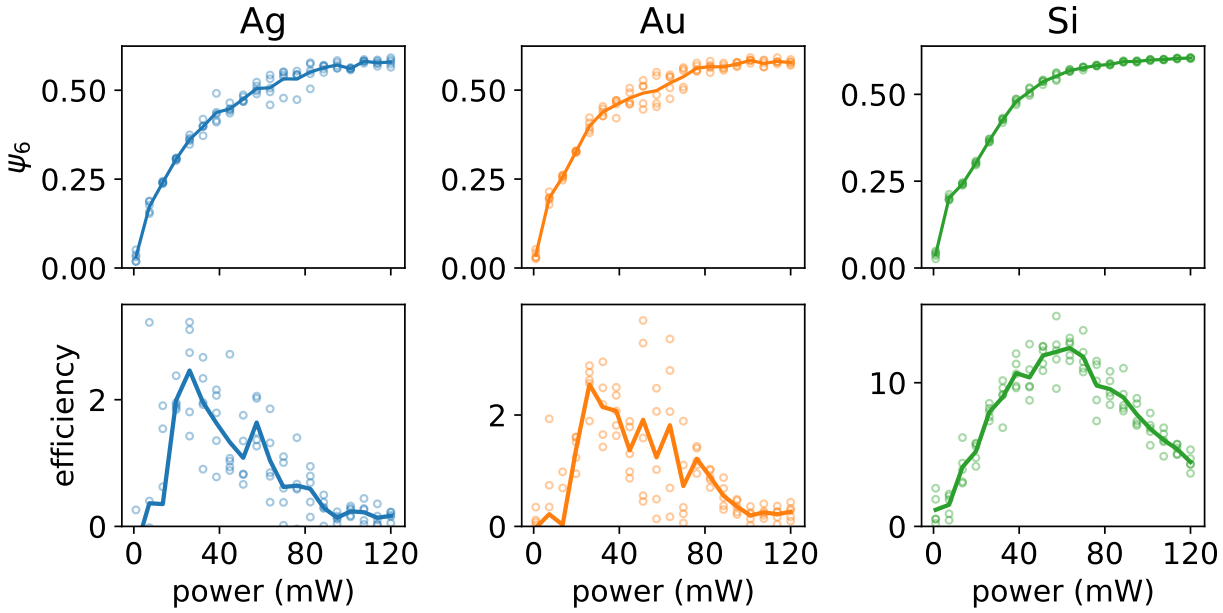

Figure 4.10: Demonstrating the stochastic nature of the optical matter machine. (top) ψ_6 of the gear as a function of the incident power for three different materials. (bottom) Efficiency of the machine as a function of the incident power. Each circle is a simulation result, with 5 simulations performed per power; solid lines are an average fit.

At low powers, ψ_6 trends to zero since the binding energy is not large enough to keep the gear together as a rigid unit. $\psi_6(P)$ increases with power and converges to a value less than unity; even at high powers, the probe particle outside the gear distorts the hexagonal symmetry of the gear. $\psi_6(P)$ is approximately the same for all 3 OM machines.

As the power goes to zero, $\mathcal{E}(P)$ goes to zero since the machine is not operable if the gear is not

a stable unit. On the other hand, as the power gets larger $\mathcal{E}(P)$ goes to zero since some thermal energy is required for the probe to hop and be driven. Consequently, the machine's efficiency is a maximum at some finite power and each of the 3 machines reach peak efficiency at different powers. This type of power dependence is expected of stochastic machines.

The Si machine is about 5× more efficient than the plasmonic machines and continues to operate at higher powers ($P > 100\,\mathrm{mW}$). This is likely due to the fact that the probe particle is smaller than the gear particles and is thus more susceptible to thermal fluctuations. Additionally, the $\mathrm{m}_{7,7}$ mode provides an additional channel of orbital angular momentum for the probe to couple into.

4.7 Conclusion

In this chapter, the orbital torque acting on an optically bound optical matter array in circularly polarized light was discussed. The net torque can be either positive or negative depending on the number of particles, their lattice spacing, and the incident wavelength of light. A multipolar analysis of the angular momentum scattered by the OM array is used as a theory to measure recoil torques and the directionality of outgoing field momentum.

An optical matter (OM) stochastic machine capable of doing work was realized using the non-conservative forces that emerge from a spin–orbit angular momentum conversion. The OM machine converts the incident spin angular momentum of the optical beam into outgoing orbital angular momentum through the collective scattering resonance of optically assembled NP arrays in an optical trap. Analysis of the scattered light reveals that the collective scattering resonance is composed of a multitude of modes, but only a few modes are significant in terms of outgoing angular momentum, specifically the $\mathrm{e}_{7,7}$, $\mathrm{e}_{5,-5}$, and $\mathrm{m}_{6,-5}$ modes. This OM gear is part of an OM machine that can transfer the angular momentum scattered in the transverse direction by its collective modes.

The OM machine operates on two principles. First, the 6-fold rotational symmetry of the OM gear allows it to convert the $m_{\mathrm{inc}} = 1$ spin angular momentum of incident light into $m = 7$ orbital angular momentum scattered into the transverse plane. This generates a counter-clockwise angular driving force on the probe particle, at the expense of a clockwise (negative torque) rotation of the OM gear, consistent with angular momentum conservation. Secondly, the optical binding interactions of the OM gear give rise to a path for the probe particle's orbital motion with 6 stable positions.

The probe is transported in the counter-clockwise direction: Brownian forces activate the particle out of a stable location while the asymmetric force field from the OM gear creates a bias, reminiscent of the concept of a Brownian ratchet [37, 113]. An all-dielectric optical matter machine was realized and shown to be more efficient than its plasmonic counterpart.

In principle, larger OM machines can be designed by increasing the size of the gear (more particles) or by combining multiple smaller gears. It was sufficient to consider $q \in [-1, 0, 1]$ in Equation (4.10) for the 7NP structure studied here, but larger gears can access larger outgoing m. With the 6-fold symmetry of hexagonal ordering, modes such as $e_{13,13}$ can be accessed which can create greater OAM and a flatter angular profile than the $e_{7,7}$ mode considered here. Such self-assembling OM machines provide a new and flexible way of controlling and driving matter at the nano-scale, including applications in nanofluidics and particle sorting [115].

4.A Hydrodynamic coupling interactions (RT coupling)

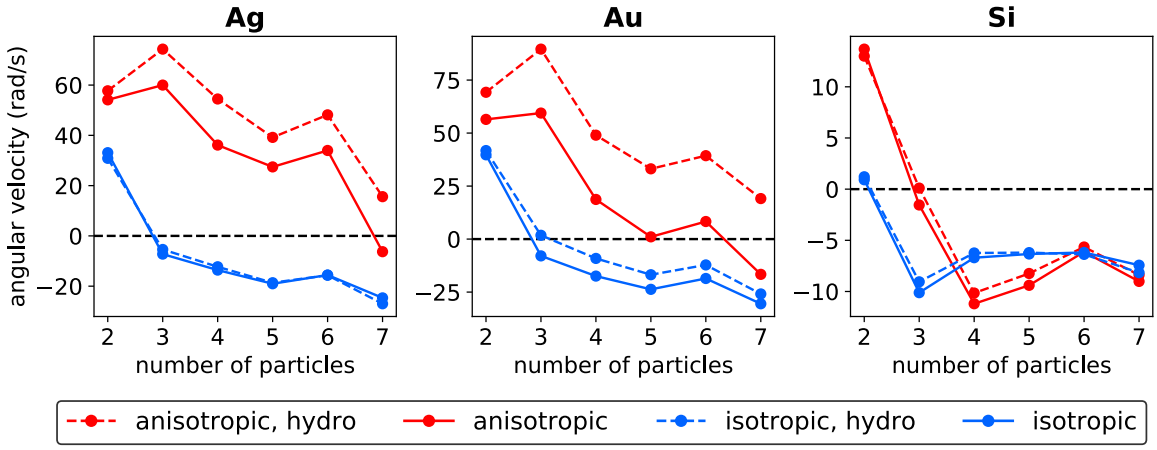

Figure 4.11: Effects of hydrodynamics and anisotropy on the net torque on arrays of 2–7 nanoparticles (Ag, Au, and Si). Generally, hydrodynamic RT coupling exerts a positive torque on the spinning array. Anisotropy increases the spinning of individual nanoparticles, causing stronger RT coupling. Parameters: $w_0 = 2000\,\text{nm}$, $P = 50\,\text{mW}$, $R_{NP} = 75\,\text{nm}$, $\lambda = 800\,\text{nm}$, $r_z/r_{xy} = 1.2$ for anisotropic particles.

Stokesian dynamics is an extension of Langevin dynamics that incorporates the hydrodynamic coupling interactions due to fluid flow in the medium. [95] In particular, rotation-translation (RT) coupling has been shown to be an important consideration. [116] Particles that are spinning in

circularly polarized light will generate vorticity flows in the fluid that can couple into the translational motion of other particles.

Electrodynamic interactions leads to a net torque on optical matter arrays that can be positive or negative. RT coupling will generally add a positive orbital motion because the spinning torque acting on each particle is always positive. There is also some translation-translation (TT) coupling that will have the same sign as the orbital motion. It is thus possible to have array that spins with negative torque without hydrodynamic coupling, but spins with a positive torque with hydrodynamic coupling interactions turned on.

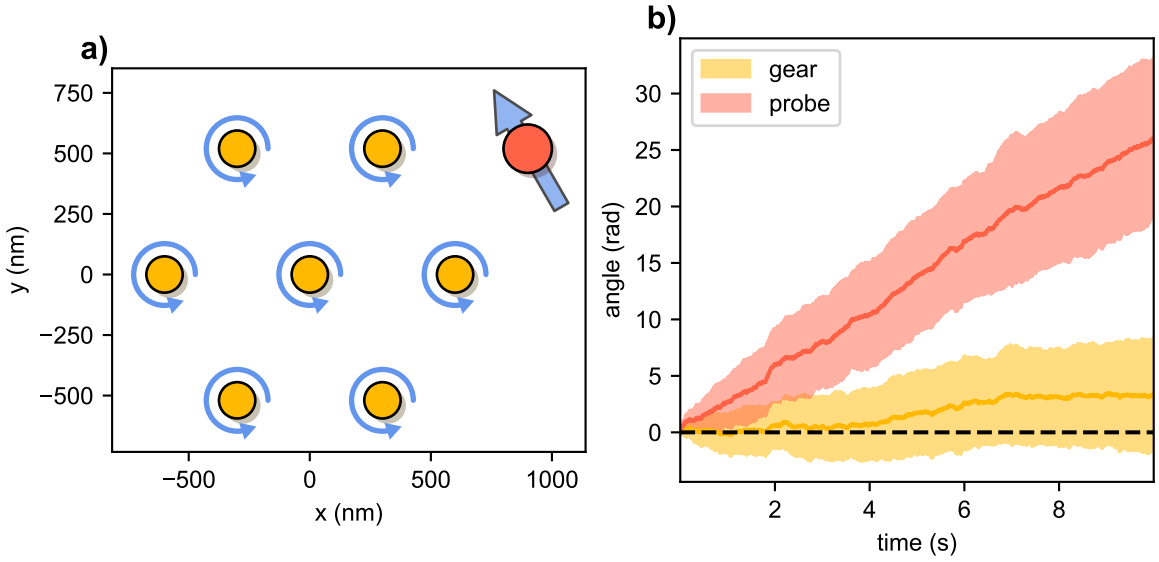

Figure 4.12: Hydrodynamic interactions in the OM gear – probe particle system. (a) The spinning of the particles inside the OM gear leads to translational fluid flow at the probe particle (hydrodynamic RT coupling). (b) Ensemble results (over 20 trajectories) for the angles of the OM gear and probe over time.

Figure 4.11 shows the net torque acting on arrays of 2–7 optically bound particles with hydrodynamic interactions turned on and off for 3 different materials. It is notable that Ag and Si have very little absorption compared to Au, and consequently Au particles spin faster which leads to stronger RT coupling. This assumes the particles are spherical; anisotropic particles (spheroids) will have a spin torque even if they do not absorb. Hydrodynamic RT coupling is seen to be much stronger for anisotropic particles than for isotropic ones. For silver and gold spheroids (aspect ratio 1.2), the cross-over from positive to negative torque happens at a higher number of particles than it does for

spherical particles.

In the OM machine, the Ag nanoparticles are spinning with a positive torque due to the incident spin of the RHC polarized light. This spinning leads to vorticity in the surrounding fluid that can generate additional translational motion of the probe particle, see Figure 4.12(a). Figure 4.12(b) shows the angles of the OM gear and probe, averaged over an ensemble of 20 trajectories. The hydrodynamic coupling causes the OM gear to rotate with a positive angular velocity, as opposed to the negative angular velocity without hydrodynamic coupling in Figure 4.8(d). However, we still obtain the clockwise biased hopping of the probe particle. Note that the hydrodynamic interactions implemented here do not take into account the water–glass interface, which might have a significant effect. [117]

4.B Constructing other types of optical matter machines

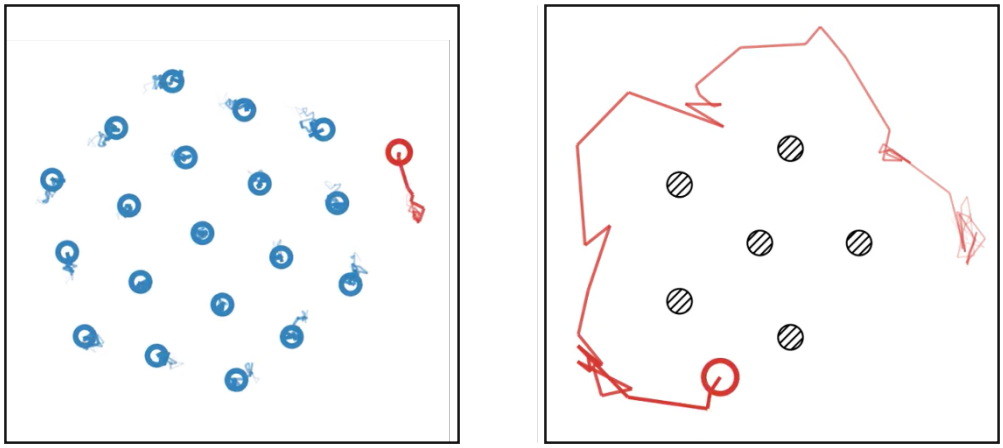

Figure 4.13: Constructing larger optical matter machines and patterned optical matter machines. (left) Simulation of a larger optical matter machine. The gear consists of 19 nanoparticles (150 nm diameter Ag particles), with a single probe particle on its periphery (200 nm diameter Ag particle). (right) Simulation of a patterned optical matter machine. The gear consists of 6 immobile particles arranged in a five-fold symmetric array, while the probe particle is free to move in the presence of the optical field.

The optical matter machine realized in this chapter can be realized in other configurations. Since optical matter arrays can, in principle, have any number of particles, the OM gear in the machine can be larger than the seven particle version considered before. A larger OM gear may offer several advantages over a smaller OM gear. Firstly, surface lattice resonances are known to emerge in larger

arrays that enhance the stability of optical matter arrays (demonstrated in Chapter 2). Secondly, the OM gear can access higher order multipolar modes, such as $e_{13,13}$, $e_{19,19}$, etc. These higher order modes carry larger quantities of angular momentum in an increasingly flat angular scattering profile. Consequently, the probe particle can be driven more aggressively with a larger OM gear. A simulation of an OM machine with an OM gear consisting of 19 particles is shown in Figure 4.13.

Another intriguing idea is to build OM gears by patterning the nanoparticles on the glass–water interface. In this way, the gear particles become immobile and only the probe particle moves in the presence of optical driving forces. The patterned OM gear effectively creates a non-conservative optical force field landscape for the probe particle to be driven in. A unique advantage of this approach to OM machines is that we are no longer restricted to the 6-fold symmetry that manifests in the non-patterned machines – the positions of the particles in the OM gear can be chosen freely. Figure 4.13 shows a simulation of a patterned OM machine where the OM gear consists of a 5-fold symmetric array. In such a machine, the $e_{6,6}$ mode becomes the dominant driving force acting on the probe particle.

CHAPTER 5
MATTER-RADIATION INTERACTIONS WITH OPTICAL SCALAR AND VECTOR BEAMS

In the previous chapters, optical matter arrays were constructed via their optical (electrodynamic) interactions. The resulting arrays often behaved in some collective way, such as the emergence of surface lattice resonances or converting spin into orbital angular momentum. This chapter introduces the theory of collective electrodynamic excitations. The theory begins with the case of a single sphere (Mie theory), followed by an anisotropic spheroid (T-matrix theory), and finally arrays of nanoparticles (generalized multiparticle Mie theory).

To study different kinds of electrodynamic excitations, it is useful to introduce vector beams. [67, 118] Vector beams provide a unique polarization state compared to linearly polarized Gaussian beams that can excite modes not otherwise accessible. The light-matter interactions between vector beams and nanoparticle arrays leads to selection rules for the allowed scattering modes of the array. For example, an azimuthally polarized vector beam can be used to selectively excite the magnetic modes of the array.

By moving away from far-field interactions towards near-field coupling, the collective electrodynamic modes become greatly enhanced. This principle is used to construct a core-satellite meta-atom that has a magnetic mode at optical frequencies. [60, 119–122] These meta-atoms are potential candidates for the building blocks of meta-fluids and meta-materials (specifically, negative index meta-materials that have a negative bulk permittivity and permeability [123–125]), which have potential novel applications, including designing superlenses that enable imaging below the diffraction limit [126, 127] and engineering optical cloaking devices. [128, 129]

In Appendix 5.A, the interaction of vector beams with gold dimers is used to excite dark plasmon modes. [61, 130] In Appendix 5.B, radially polarized beams are shown to selectively excite electrodynamic anapole modes – modes with electron current excitations that have no radiative losses – in a silicon sphere. [131, 132] In Appendix 5.C, the computational method of the multipole expansion is demonstrated using the Finite-Difference Time-Domain (FDTD) method.

5.1 Multipolar content of optical scalar and vector beams

In the general case of N particles illuminated by an arbitrary source, the fields around each particle can be expressed as a sum over the vector spherical harmonic wavefunctions (VSHW), which are a complete basis set for the piecewise homogeneous vector Helmholtz equation [67]

$$\boldsymbol{E}^j_{\text{src}} = -\sum_{n=1}^{N_{\max}} \sum_{m=-n}^{n} \sum_{r=1}^{2} iE_{mn} p^{j,\text{src}}_{mnr} \boldsymbol{N}^{(1)}_{mnr} \tag{5.1a}$$

$$\boldsymbol{E}^j_{\text{inc}} = -\sum_{n=1}^{N_{\max}} \sum_{m=-n}^{n} \sum_{r=1}^{2} iE_{mn} p^{j,\text{inc}}_{mnr} \boldsymbol{N}^{(1)}_{mnr} \tag{5.1b}$$

$$\boldsymbol{E}^j_{\text{scat}} = \sum_{n=1}^{N_{\max}} \sum_{m=-n}^{n} \sum_{r=1}^{2} iE_{mn} p^{j,\text{scat}}_{mnr} \boldsymbol{N}^{(3)}_{mnr} \tag{5.1c}$$

$\boldsymbol{E}^j_{\text{src}}$ is the field of the incident source at particle j, $\boldsymbol{E}^j_{\text{inc}}$ is the incident field at particle j that includes the source and all other particles, and $\boldsymbol{E}^j_{\text{scat}}$ is the field scattered by particle j. We call $\boldsymbol{N}^{(3)}_{mnr}$ the *electrodynamic scattering modes* of the particle and $\boldsymbol{N}^{(1)}_{mnr}$ the *electrodynamic incident modes*.

Given the electric fields of the incident source, $\boldsymbol{E}^{\text{src}}(\boldsymbol{r})$, the source can be decomposed into its expansion coefficients by integration around particle j

$$p^{j,\text{src}}_{mnr} = i \frac{\int_\Omega \boldsymbol{E}^{\text{src}} \cdot \boldsymbol{N}^{(1)*}_{mnr} \, d\Omega}{E_{mn} \langle \boldsymbol{N}^{(1)}_{mnr}, \boldsymbol{N}^{(1)}_{mnr} \rangle} \tag{5.2}$$

where Ω is a closed surface around particle j. To decompose arbitrary beams into the VSHW coefficients, it is easiest to use the angular spectrum of the beam to carry out the integral Equation (5.2). In the angular spectrum representation, beams are represented on a far-field hemisphere and the near-fields are computing using a Fourier transform. The angular spectrum of Gaussian, Hermite-Gaussian, and Laguerre-Gaussian beams are provided in Appendix C.

Beam polarization	**Electric field**	**Decomposition (origin)**
Linear ($\hat{\boldsymbol{x}}$)	$\mathrm{HG}_{00}(\boldsymbol{r})\hat{\boldsymbol{x}}$	$p^{\mathrm{src}}_{mnr} = 0$ if $m \neq \pm 1$
Azimuthal	$\mathrm{HG}_{01}(\boldsymbol{r})\hat{\boldsymbol{x}} - \mathrm{HG}_{10}(\boldsymbol{r})\hat{\boldsymbol{y}}$	$p^{\mathrm{src}}_{mnr} = 0$ if $m \neq 0$, $r \neq 1$
Radial	$\mathrm{HG}_{10}(\boldsymbol{r})\hat{\boldsymbol{x}} + \mathrm{HG}_{01}(\boldsymbol{r})\hat{\boldsymbol{y}}$	$p^{\mathrm{src}}_{mnr} = 0$ if $m \neq 0$, $r \neq 0$
Shear	$\mathrm{HG}_{01}(\boldsymbol{r})\hat{\boldsymbol{x}} + \mathrm{HG}_{10}(\boldsymbol{r})\hat{\boldsymbol{y}}$	$p^{\mathrm{src}}_{mnr} = 0$ if $m \neq \pm 2$

Table 5.1: Electric fields and VSHW decomposition of the scalar and vector beams. The decomposition rules are valid at the origin (center) of each beam.

Cylindrical vector beams (CVB) are of great interest due to their unique position-dependent polarization state.[67, 133]. The CVBs are created from linear combinations of the lowest-order Hermite-Gaussian modes. Together with the linearly polarized beam, they are given by the expressions in Table 5.1.

Each beam has a decomposition rule when Equation (5.2) is applied to beam at the center of the beam. Linearly polarized light has access to any electrodynamic scattering mode with $m = \pm 1$, where the contributions from each sign are equal since the light does not carry angular momentum. Azimuthally polarized light has the rule that $m = 0$ in addition to $r = 1$, i.e. azimuthal beams only support magnetic modes. Similarly, radially polarized light has the rule that $m = 0$ and $r = 0$, i.e. radial beams only support electric modes. Lastly, the shear polarized beam has access to any electrodynamic scattering mode with $m = \pm 2$. Shear beams can support electric or magnetic modes, with the interesting caveat that it does not support dipolar modes ($n = 1$) since it cannot have $m \in -1, 0, 1$.

The beams are named after their electric field polarization states, which are shown in Figure 5.1. The intensity of the CVBs at the focus are doughnut shaped since the polarization state at the center is not defined.

5.2 Selection rules for isotropic scatterers: generalized Lorenz-Mie theory

In the original Mie theory, a linearly polarized plane-wave illuminates a sphere and the boundary condition on the sphere is met using the VSHW functions. This allows only modes with $m = \pm 1$ to be scattered by the sphere. The generalized Lorenz-Mie theory (GLMT) is an extension of the Mie

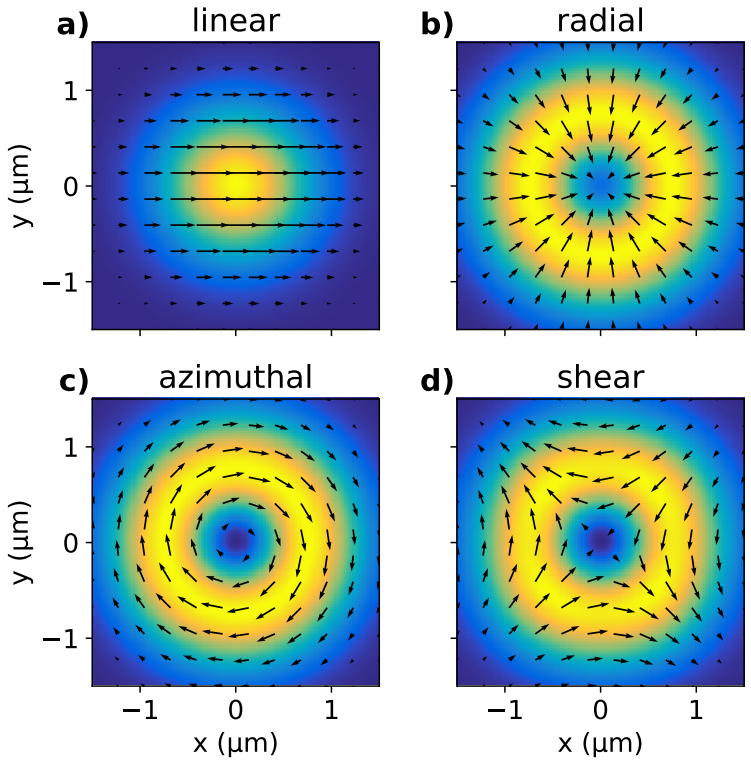

Figure 5.1: Scalar and vector beams at the focal plane with $w_0 = 1\,\mu\text{m}$. (a) x-polarized Gaussian beam. (b) Radially polarized vector beam. (c) Azimuthally polarized vector beam. (d) Shear polarized vector beam.

theory for arbitrary illumination of the spherical particle. [71] The relationship between the incident coefficients of the beam and the scattered coefficients of the particles is

$$p_{mnr}^{\text{scat}} = a_{nr} p_{mnr}^{\text{inc}} \tag{5.3}$$

where a_{nr} are the Mie coefficients of the particle and p_{mnr}^{inc} is computed using Equation (5.2) around the center of the particle. In GLMT, the particle can scatter electrodynamic modes with $m \neq \pm 1$ provided the incident source carries those electrodynamic modes.

A set of selection rules for the allowed scattering modes is determined by combining Equation (5.3) with the scalar beam and CVB decomposition rules in Table 5.1. With the azimuthal beam, the sphere has its electric modes suppressed and is only allowed to scatter magnetic modes. The radial beam does the inverse, suppressing the magnetic modes and only exciting electric modes in the sphere. The shear beam will excite electric and magnetic modes, but it will not excite any dipole

modes.

A 200 nm diameter silicon (Si) spherical particle is used to demonstrate these selection rules. Because Si is a high-index dielectric, it supports electric and magnetic dipole and quadrupole modes at optical frequencies and is therefore useful in combination with scalar and vector beams. Figure 5.2(a) shows the total scattering of the particle by each type of beam. The linearly polarized beam is seen to excite three resonances in the visible wavelengths. Each of the vector beams selectively excites a subset of these resonances.

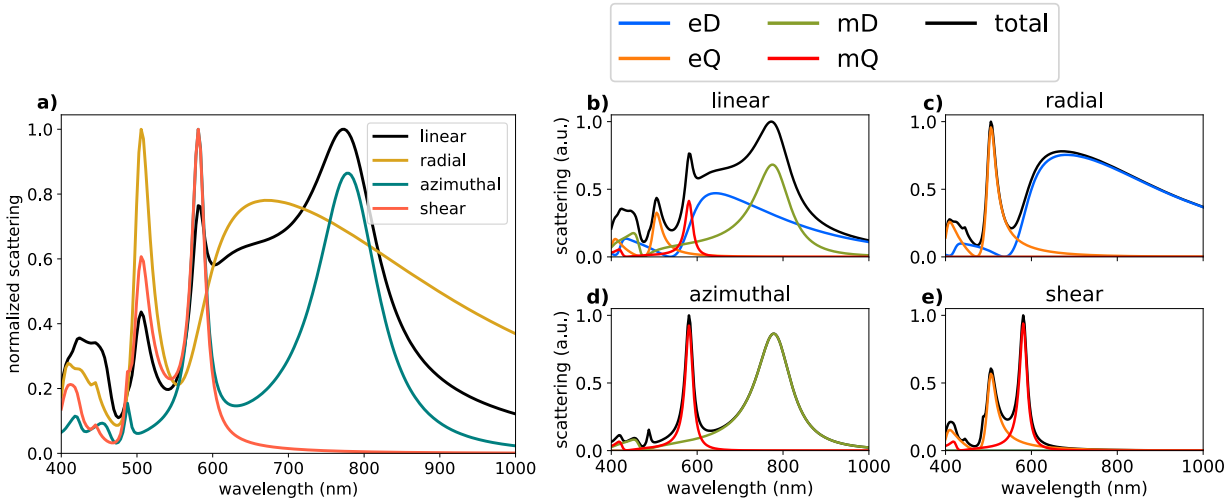

Figure 5.2: Scalar and vector beam illumination of a 200 nm diameter spherical silicon nanoparticle. (a) Total scattering cross-sections for each type of scalar and vector beam. (b-e) Multipolar scattering of the nanoparticle for each type of beam. eD = electric dipole, mD = magnetic dipole, eQ = electric quadrupole, mQ = magnetic quadrupole.

Figure 5.2(b-e) shows the scattering per multipolar mode for each of the beams. This verifies the selection rules determined earlier. The resonance frequencies of the modes for each beam illumination condition does not change, although the relative amplitudes of the multipolar modes are seen to change. Because the shear beam has no dipolar mode excitation of the nanoparticle, the particle experiences essentially no scattering at longer wavelengths since the quadrupole modes vanish.

5.3 Selection rules for anisotropic scatterers: T-matrix theory

The GLMT can be further generalized to that of non-spherical particles using transfer matrix (T-matrix) theory. In the T-matrix theory, the boundary condition of Maxwell's equations are met

on the surface of the scatterer by numerically intergrating projections of the VSHW functions over the surface of the object. [76] For an arbitrary non-spherical particle, the relationship between the incident and scattered field coefficients is

$$p_\alpha^{\text{scat}} = \mathcal{T}_{\alpha\beta} p_\beta^{\text{inc}} \tag{5.4}$$

where $\mathcal{T}_{\alpha\beta}$ is the particle's T-matrix and maps every possible incident field into every possible outgoing field.

Symmetries in the particle can reduce the number of non-vanishing T-matrix elements. In the case of axisymmetric particles (spheroids, cylinders), the azimuthal integral in the surface integrals can be carried out analytically. For these particles, the T-matrix becomes block-diagonal

$$\begin{bmatrix} p_{mn1}^{\text{scat}} \\ p_{mn2}^{\text{scat}} \end{bmatrix} = \begin{bmatrix} \mathcal{T}_{nm1n'm'1} & \mathcal{T}_{nm1n'm'2} \\ \mathcal{T}_{nm2n'm'1} & \mathcal{T}_{nm2n'm'2} \end{bmatrix} \begin{bmatrix} p_{mn1}^{\text{inc}} \\ p_{mn2}^{\text{inc}} \end{bmatrix} = \begin{bmatrix} \mathcal{T}_{nmn'm'}^{\text{ee}} & \mathbf{0} \\ \mathbf{0} & \mathcal{T}_{nmn'm'}^{\text{mm}} \end{bmatrix} \begin{bmatrix} p_{mn1}^{\text{inc}} \\ p_{mn2}^{\text{inc}} \end{bmatrix} \tag{5.5}$$

The selection rules that applied to the spherical particle are still partially applicable to spheroids. The radial beam can still only support electric modes, and the azimuthal beam can only support magnetic modes. The shear beam similarly cannot access dipole modes. However, even when the incident light only carries $m = \pm 1$, a non-spherical particle can now have $m \neq \pm 1$ modes excited.

Taking the Si sphere from the previous section, it can be stretched into a spheroid. Consider the case of minor and major radii $r_{xy} = 75\,\text{nm}$ and $r_z = 125\,\text{nm}$. Figure 5.3(a) shows the scattering response of this particle from each type of beam where the major axis of the particle is oriented along the x-direction. The multipolar scattering for each beam, Figure 5.3(b-e), reveals that the electric-magnetic selection rules are still valid.

However, unlike in Figure 5.2, the resonances generated by the CVBs do not align with those generated by the linearly polarized beam. This is due to the anisotropy of the particle and the type of electromagnetic modes that can be supported in its interior. For example, the azimuthal beam generates a magnetic dipole current in the xy-plane, which has an elliptical cross-section of 75 nm by 125 nm. The linearly polarized beam generates a magnetic dipole in the xz-plane, which has a circular cross-section of radius 75 nm. These two magnetic dipoles have a different orientation and a

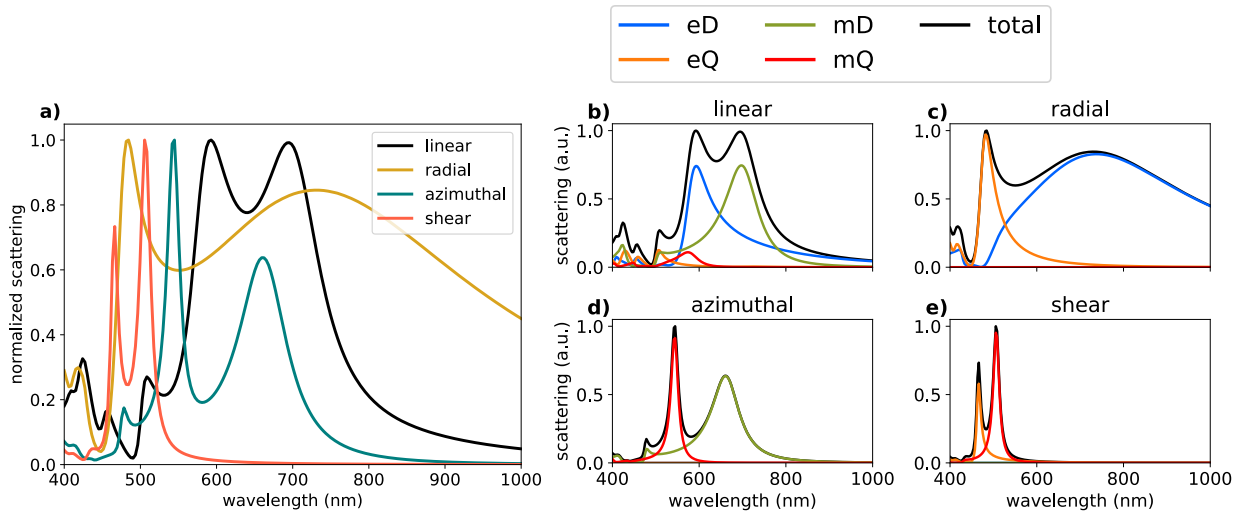

Figure 5.3: Scalar and vector beam illumination of a prolate spheroidal silicon nanoparticle with $r_{xy} = SI75nm$ and $r_z = 125\,\text{nm}$ with its major axis oriented along the x-direction. (a) Total scattering cross-sections for each type of scalar and vector beam. (b-e) Multipolar scattering of the nanoparticle for each type of beam. eD = electric dipole, mD = magnetic dipole, eQ = electric quadrupole, mQ = magnetic quadrupole.

different geometry in the particle, so their resonances do not align. This is similarly true for electric dipole modes and the radial beam, as well as quadrupole modes with the shear beam.

5.4 Collective electrodynamic scattering modes of nanoparticle arrays

The GLMT can be extended to a collection of N particles, known as the generalized multiparticle Mie theory (GMMT). [74] In GMMT, the goal is to find the expansion coefficients of every particle, p_α^{scat}, given a driving source field with expansion coefficients p_α^{src}. The particle interactions can be written in a matrix equation that uses the VSHW translation theorem that translates the scattering coefficients around one origin and converts them to a different set of incident coefficients around a different origin. [75] This leads to the following interaction equation

$$p_\alpha^{j,\text{inc}} = p_\alpha^{j,\text{src}} - \mathcal{T}_{\alpha\beta}^{jl} p_\beta^{l,\text{inc}} \tag{5.6}$$

where $\mathcal{T}_{\alpha\beta}^{jl}$ is the *particle aggregate T-matrix*. This T-matrix is different from the single-particle T-matrix defined earlier; its block diagonal entries are the T-matrices of individual particles while its block off-diagonal entries represent the coupling between particles. By setting $p_\alpha^{j,\text{inc}} = \delta_{\alpha\beta}\delta_{jl} p_\beta^{l,\text{inc}}$,

the interaction equation can be rewritten in the standard form for linear systems, $[A]x = b$, and has the solution

$$p_\beta^{j,\mathrm{inc}} = \left[\delta_{\alpha\beta}\delta_{jl} + \mathcal{T}_{\alpha\beta}^{jl}\right]^{-1} p_\alpha^{l,\mathrm{src}} = \mathcal{A}_{\alpha\beta}^{jl} p_\beta^{l,\mathrm{src}} \tag{5.7}$$

where $\mathcal{A}_{\alpha\beta}^{jl}$ (referred to as the A-matrix) provides the incident coefficients given the source coefficients at each particle. The scattering coefficients for each particle are then given by Equation (5.3) (for spheres) or Equation (5.5) (for non-spherical particles).

The A-matrix can be diagonalized to obtain its eigenvalues, a_α^j, and eigenmodes, $[p]_\alpha^{j,\mathrm{src}}$,

$$p_\alpha^{j,\mathrm{inc}} = a_\alpha^j \, [p]_\alpha^{j,\mathrm{src}} \tag{5.8}$$

In the eigenmode representation, the incident field coefficients at a particle are a constant multiplier (the eigenvalue) of the source field coefficients. The magnitude of the eigenvalue, $|a_\alpha^j|$, is a dimensionless measure of the strength of the electrodynamic coupling of that eigenmode.

The eigenmodes can be partially visualized by looking at the magnitude and polarization of the induced electric dipoles in every particle of an array. Figure 5.4 shows the twelve eigenmodes corresponding to the largest eigenvalues for seven silicon nanoparticles in a hexagonal array. The strongest mode, Figure 5.4(a), has all of the induced dipoles in the z-direction. The next strongest modes, Figure 5.4(b,c), are elliptically polarized dipoles in the xy-plane, all of the same handedness (red is right-handed, blue is left-handed). The next mode, Figure 5.4(d), has a dark central particle and radially polarized particles for the outer particles.

In principle, any of these modes be excited by an incident source, but many of the modes can be *dark modes*, i.e. modes not accessible through plane-wave illumination. For example, the radial mode in Figure 5.4(d) cannot be excited by any plane-wave, but a radially polarized beam *can* excite this mode.

For arrays of nanoparticles, the selection rules determined earlier for the single particle case do not generally apply except in certain situations. The total field scattered by the array can be represented around a single origin with a single set of scattering expansion coefficients, $p_\alpha^{\mathrm{cluster}}$. This is obtained by translating the scattering coefficients of each particle, solved for in Equation (5.7), to

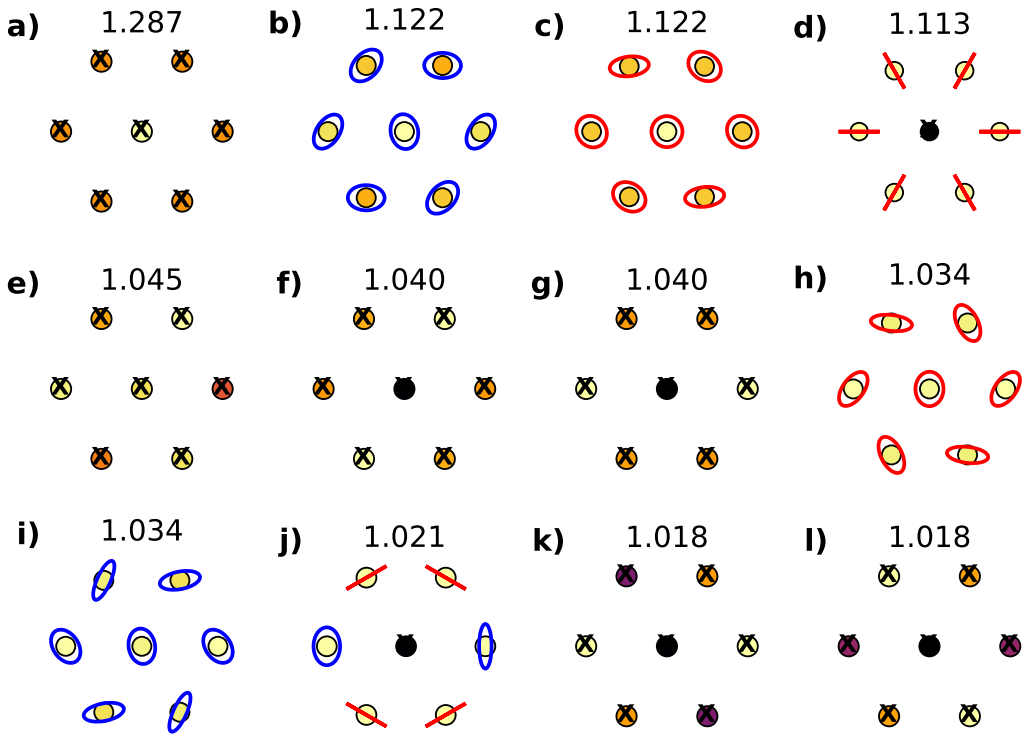

Figure 5.4: Eigenmodes of the interaction matrix $\mathcal{A}$ for seven 200 nm diamter silicon nanoparticles in hexagonal packing with $\delta = 600\,\text{nm}$. The polarization shown is either in-plane linear (lines), in-plane elliptical (ellipses where blue is RHC and red is LHC), or out-of-plane linear ($\times$ symbols). The particles are colored by the magnitude of their induced dipole (dark to yellow). Only the eigenmodes corresponding to the 12 highest eigenvalues of $\mathcal{A}$ are shown.

a single origin

$$p_\alpha^{\text{cluster}} = A_{\alpha\beta}^{(1)0j} p_\beta^{j,\text{scat}} \tag{5.9}$$

In this representation, the collection of nanoparticles is treated as a single scattering object. That collection has its own T-matrix, referred to as the *cluster T-matrix* and defined such that

$$p_\alpha^{\text{cluster}} = \mathcal{T}_{\alpha\beta}^{\text{cluster}} p_\beta^{0,\text{src}} = \begin{bmatrix} \mathcal{T}_{nm1n'm'1}^{\text{cluster}} & \mathcal{T}_{nm1n'm'2}^{\text{cluster}} \\ \mathcal{T}_{nm2n'm'1}^{\text{cluster}} & \mathcal{T}_{nm2n'm'2}^{\text{cluster}} \end{bmatrix} \begin{bmatrix} p_{mn1}^{\text{inc}} \\ p_{mn2}^{\text{inc}} \end{bmatrix} \tag{5.10}$$

That is, the cluster T-matrix treats the system of particles as if it were a single scattering object, hiding the internal details. In general, the off block-diagonal elements no longer vanish and it is no longer generally true that the azimuthally polarized beam only excites magnetic modes, the radially polarized beam only excites electric modes, etc.

Figure 5.5(a) shows the scattering of a hexagonal array composed of Si nanoparticles for each beam type. Unlike before, it does not appear that the CVBs are selectively exciting certain resonances excited by the linear beam. Figure 5.5(b-e) show the multipolar scattering for modes with $n \in 5, 6, 7$, and the radially polarized beam is seen to excite a weak m_6 mode and the azimuthally polarized beam excites a weak e_6 mode. However, it is significant to note that the resonance near 800 nm is primarily electric in nature for the radially polarized beam (e5 and e7 modes) and primarily magnetic in nature for the azimuthally polarized beam (m5 and m7 modes). This has a large effect on the spectral width of this resonance.

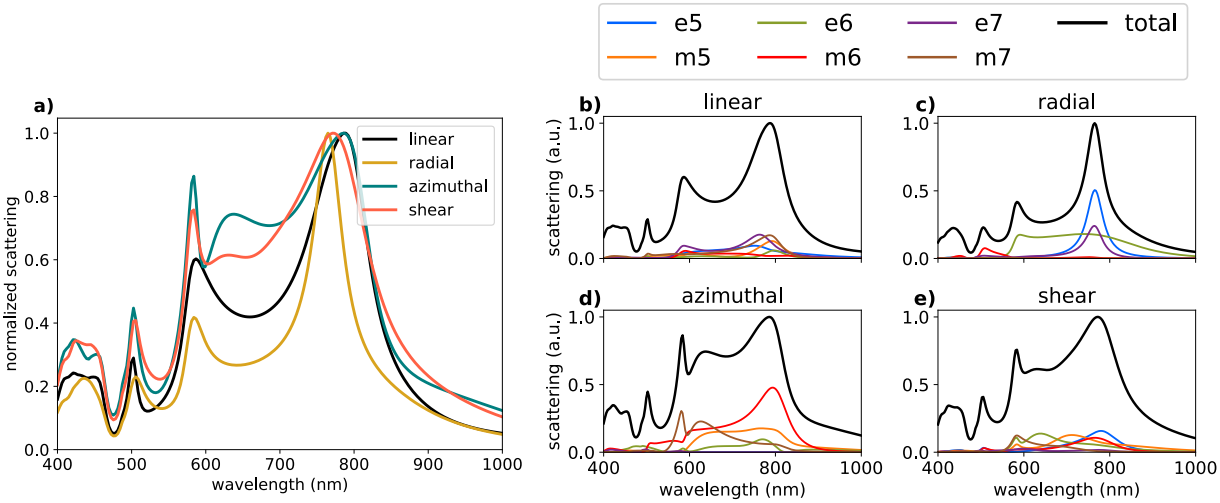

Figure 5.5: Scalar and vector beam illumination of seven 200 nm diamter silicon nanoparticles in hexagonal packing with $\delta = 600$ nm. (a) Total scattering cross-sections for each type of scalar and vector beam. (b-e) Multipolar scattering of the nanoparticle for each type of beam. eD = electric dipole, mD = magnetic dipole, eQ = electric quadrupole, mQ = magnetic quadrupole.

In these optical matter systems, we know that the electrodynamic coupling can be strong due to surface lattice resonances, which must be reflected in the A-matrix. As a measure of the strength of *potential* electrodynamic coupling, consider the maximum possible eigenvalue of the A-matrix (this assumes the eigenmode is excited by the source). Figure 5.6 shows this coupling strength as a function of lattice spacing δ for a larger array of 37 silver nanoparticles in hexagonal packing. A peak emerges near $\delta = 600$ nm, suggesting that such a lattice resonance is reflected in the A-matrix and is near the optical binding serparation.

Interestingly, as the surface-to-surface distance is reduced to zero in Figure 5.6, the maximum

magnitude of the eigenvalues approaches ~ 65 (modes with eigenvalues greater than 1 are considered "strongly" coupled modes). This near-field coupling is significantly stronger than the mid-field coupling at the surface lattice resonance. This result is not too surprising since plasmonic particles are known to have greatly enhanced near-field magnitudes due to their plasmon resonance, which results in greatly enhanced coupling between nearly-touching particles. [61, 134] These small separations cannot be easily realized in the world of optical matter where particles are free to move. However, this limit of near-field coupling is of interest in plasmonics where particle positions are fixed by chemical means. In the next section, these near-field interactions are realized and their illumination with CVBs is considered.

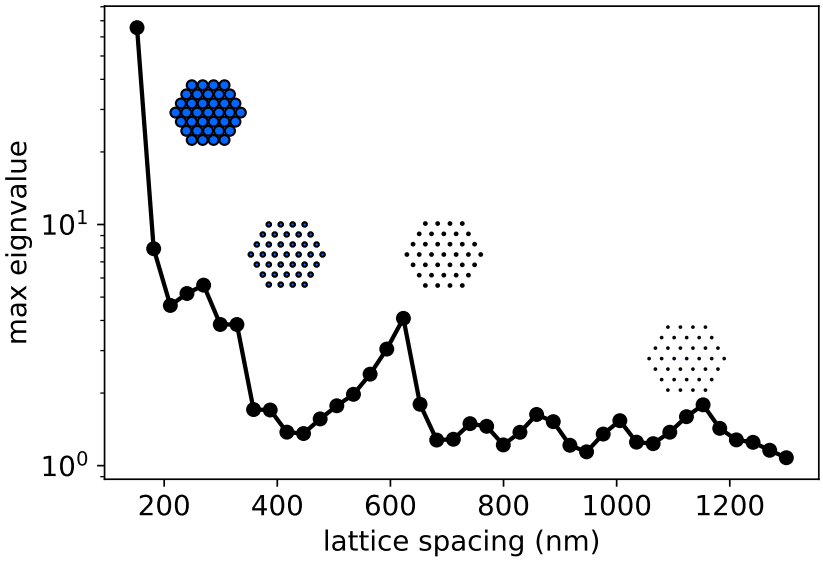

Figure 5.6: The maximum eigenvalue of the $\mathcal{A}$ matrix as the lattice spacing of an array is changed. The array is composed of 150 nm diameter Ag spherical particles and is illuminated by a circularly polarized plane-wave with $\lambda = 800$ nm.

5.5 Core-satellite meta-atom: optical magnetism at the nanoscale

A core-satellite nano-structure is specially designed such that small spherical metallic particles (the satellites) decorate the surface of a larger dielectric sphere (the core). The overall size of the core-satellite is sub-wavelength, and we therefore refer to it as a "meta-atom". The core-satellite meta-atom can potentially be used as a building block for meta-materials. The goal is to pack as

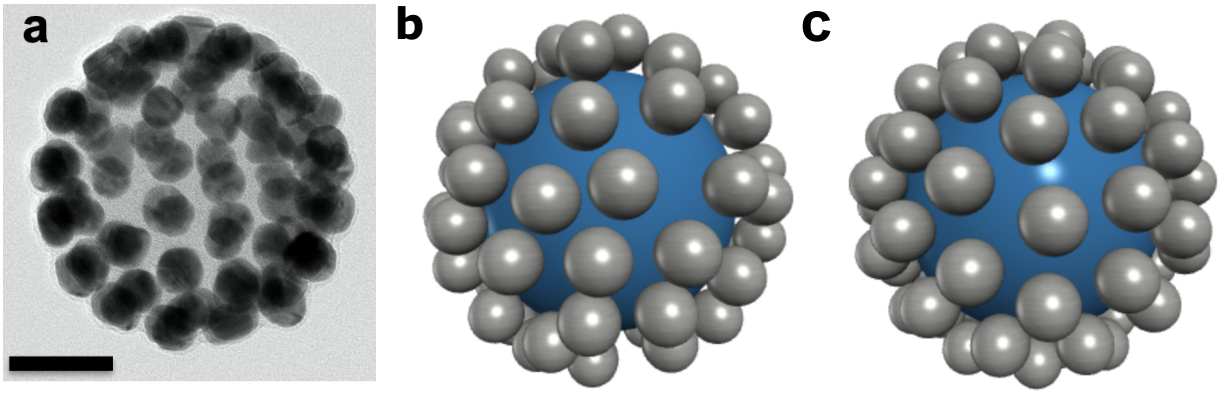

Figure 5.7: The core-satellite meta-atom in experiment and simulation. (a) Experimental TEM image of a core-satellite met-atom with Au nanoparticles on a silica core. Scale bar is 50 nm. (b) Construction of core-satellite meta-atom in simulation using the random placement algorithm. (c) Construction of the core-satellite meta-atom using the ordered placement algorithm.

many satellite particles on the core's surface that are not touching one another so that the coupling strength (eigenvalues of $\mathcal{A}$) is maximized. Figure 5.7(a) is a TEM image of an experimentally realized core-satellite with Au satellite particles and an SiO_2 core. [120]

In simulation, two types of core-satellite meta-atoms are considered: those with randomly positioned satellite particles and those with an ordered arrangement. To build a random arrangement, positions on the surface of the sphere (i.e. the SiO_2 dielectric core) are randomly and uniformly sampled by choosing two uniform random variables $\phi = U[0, 2\pi]$ and $\tau = U[-1, 1]$, and setting $\theta = \cos^{-1}(\tau)$. If the radius of the dielectric core is r_1 and the radius of a nanoparticle is r_2, then a metal nanoparticle is placed at spherical coordinates $(r_1 + r_2, \theta, \phi)$. The nanoparticle is placed only if it satisfies a minimum surface-to-surface separation distance of d_{sep} between all other nanoparticles. This process is repeated until N_p nanoparticles have been placed. A random core-satellite meta-atom is shown in Figure 5.7(b).

Ordered core-satellite meta-atoms are built via a minimum potential method, wherein each nanoparticle has a (fictitious) charge of +1. The potential energy of the system is

$$U(\theta_i, \phi_i) = \sum_{i<j} \sum_{j=1}^{N_p} \frac{1}{d_{ij}} \tag{5.11}$$

where d_{ij} is the distance between particle i and particle j. $U(\theta_i, \phi_i)$ is then minimized by gradient

descent in $2N_p$–dimensional configuration space. The computed spherical coordinates $(r_1 + r_2, \theta_i, \phi_i)$ are then used to create a core-satellite meta-atoms with an ordered nanoparticle arrangement. An ordered core-satellite meta-atom is shown in Figure 5.7(c).

Fig. 5.8(a) shows the total scattering spectra of a SiO_2-Ag core-satellite meta-atoms resulting from excitation by a linearly polarized beam and each of the three vector beams. Compared to the linearly polarized beam scattering, the azimuthally polarized beam exhibits enhanced scattering at 1.8 eV and the radially polarized beam has enhanced scattering at 2.8 eV. The beam has total scattering similar to that of the linearly polarized beam. A corresponding absorption spectrum for linearly polarized light and each vector beam is shown in Fig. 5.8(b). The absorption under vector beam illumination is found to also be enhanced relative to the absorption under linearly polarized beam excitation.

Fig. 5.8(c) shows the corresponding multipolar scattering for each of the four beams. The multipolar scattering of each vector beam excitation from the core-satellite meta-atoms is compared to the corresponding modes excited by the linearly polarized beam on the same y-scale. For linearly polarized beam excitation, the magnetic modes (bottom row) are stronger than the electric modes (top row) and occur at lower energies.

The magnetic modes of the radially polarized beam are weaker than the corresponding magnetic modes excited by the linearly polarized beam by a factor of 6. However, the electric modes of the radially polarized beam are enhanced by up to a factor of 8 relative to the electric modes from linearly polarized beam excitation. This multipolar analysis reveals that the radially polarized beam selectively excites and enhances the electric modes of the system.

By contrast, the azimuthally polarized beam selectively excites magnetic modes and enhances them up to a factor of 7 relative to the magnetic modes vs. linearly polarized beam excitation. The electric modes are weak under azimuthally polarized light relative to the electric modes excited by linearly polarized light, except in the energy range 1.6 eV to 2.2 eV, where the electric octupole mode is slightly enhanced. These enhancement factors for radially and azimuthally polarized beam excitations explain the corresponding enhancements in the total scattering in Fig. 5.8(a) at 1.8 eV and 2.8 eV.

For excitation with a shear polarized beam, both electric and magnetic modes are found to

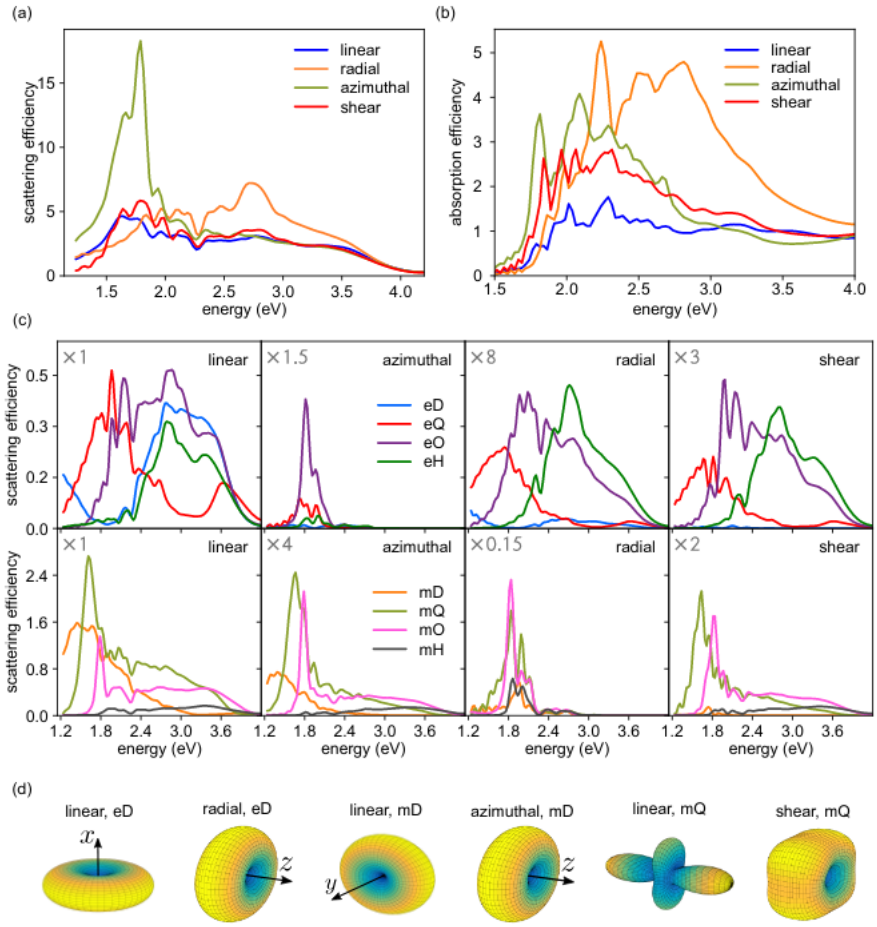

Figure 5.8: Scalar and vector beams have different selectivity in exciting, enhancing, and orienting the optical modes of the randomly arranged 165 nm radius core-satellite meta-atoms. (a) Total scattering efficiency for each type of beam. (b) Absorption efficiency for each type of beam. (c) Multipole scattering for each vector beam compared to scattering from a linearly polarized beam. The first row shows the electric modes and the second row shows the magnetic modes. Each axis has a multiplier to indicate its enhancement relative to the linearly polarized beam excitation, i.e. the azimuthally polarized beam enhances the magnetic dipole by a factor of 2 and the magnetic quadrupole by a factor of 4 over the corresponding linearly polarized beam modes. The labels indicate the multipolar mode: e = electric, m = magnetic, D = dipole, Q = quadrupole, O = octupole, H = hexadecapole. (d) Angular distribution of $|\boldsymbol{E}(\theta, \phi)|^2$ for different modes and beam excitations.

be enhanced vs. the modes from linearly polarized beam excitation, except the modes of dipolar order. Thus, the shear polarized beam selectively excites and enhances modes of quadrupole order or higher, both electric and magnetic modes. The enhancement factor of these modes is around 2 to 3, somewhat smaller than the enhancement factors from azimuthally and radially polarized beams.

The meta-atom approximately obeys the selection rules that were derived for a perfectly spherical (isotropic) particle. Although the meta-atom does not have perfect spherically symmetry it does have it in some approximate sense, i.e. the scattering of the meta-atom due to a plane-wave is approximately independent of the $\boldsymbol{k}$-vector direction. This means that the cluster T-matrix of the meta-atom, Equation (6.38), has non-zeros diagonal elements and relatively weak off-diagonal elements. The disorder of the satellite particles mean that the selection rules are not exactly valid. When the meta-atom is created using the ordered creation algorithm, it is much closer to being an isotropic scatterer.

Fig. 5.8(d) shows the angular distribution of the scattering intensity for different beams and multipolar modes. The linearly x-polarized beam excites an x-oriented electric dipole and y-oriented magnetic dipole. The electric dipole selectively excited by the radially polarized beam is oriented along the z-axis (the beam axis). Similarly, the magnetic dipole selectively excited by the azimuthally polarized beam is oriented along the beam axis. The associated distributions of scattered radiation can have important effects in experiments that only measure scattering intensity over a finite collection angle in a particular direction (e.g. forward, backward, perpendicular to the beam axis, etc.).

The magnetic quadrupole mode is also shown to be of a different nature in the case of shear polarized beam excitation. Any quadrupole mode can be expressed as a sum of 5 distinct quadrupole modes, denoted by $m = -2, -1, 0, 1, 2$. Different values of m correspond to different angular distributions of the quadrupole mode. The quadrupole mode excited by the linearly polarized beam contains equal parts of $m = -1$ and $m = 1$, while the mode excited by the shear polarized beam contains equal parts of $m = -2$ and $m = 2$. The magnetic quadrupole mode excited by the azimuthally polarized beam (not shown) only contains the mode with $m = 0$. Thus, each of the beams selectively excites a different kind of magnetic quadrupole. Similar results are obtained for the electric quadrupole mode excited by the linear, radial, and shear polarized beams.

To understand the spectroscopy of the core-satellite meta-atom and assign identities to spectroscopic features, meta-atoms of increasing nanoparticle density are constructed. The progression of some features also give insight into the collective magnetic modes being excited in the core-satellite meta-atom. Starting with 5 silver nanoparticles (40 nm diameter) placed randomly on the surface of

a dielectric core of radius 120 nm, additional nanoparticles are repeatedly added five at a time until 95 nanoparticles are placed, which corresponds to roughly maximum random packing density. A scattering spectrum for each of these meta-atoms is shown in Fig. 5.9(a).

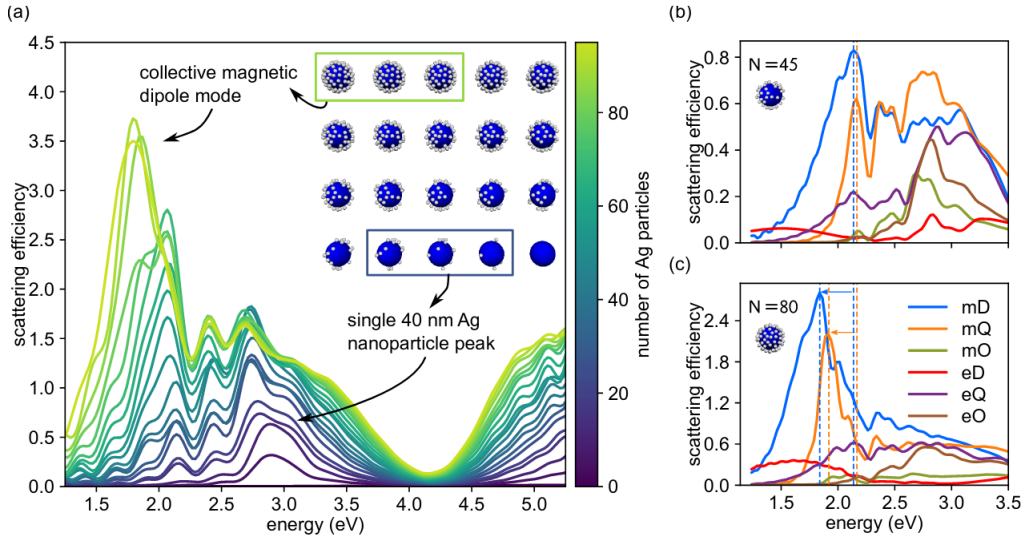

Figure 5.9: Emergence of optical magnetism in core-satellite meta-atoms with increasing nanoparticle density. (a) Scattering intensity by linearly polarized beam excitation of core-satellite meta-atoms with increasing nanoparticle coverage. The 2.9 eV peak corresponds to the single dipole resonance of a 40 nm Ag nanoparticle. The 1.8 eV magnetic dipole peak emerges at high nanoparticle coverage. (b) Multipole scattering for $N = 45$ nanoparticles. (c) Multipole scattering for $N = 80$ nanoparticles. This identifies the 1.8 eV peak in (a) as a magnetic mode. The magnetic dipole and magnetic quadrupole modes in (c) red-shift 0.3 eV relative to (b).

The major scattering feature for low particle densities (5 to 15 nanoparticles) occurs at 2.9 eV. This mode corresponds to the plasmon resonance of individual 40 nm Ag spheres since the nanoparticles are spatially separated enough to minimize near-field interaction. As the nanoparticle density increases (from 20 to 80 nanoparticles), features (modes) emerge at 2.2 eV and 2.5 eV due to near-field interactions. A new mode at 1.8 eV emerges at the highest densities (85-95 nanoparticles). This is the magnetic mode of the core-satellite that only occurs when the density is large enough that near-field interactions can generate a collective excitation around the core perimeter.

These assignments stem from a multipolar analysis performed for two clusters, one with $N_p = 45$ (Fig. 5.9(b)) and one with $N_p = 80$ (Fig. 5.9(c)). At the lower nanoparticle density, magnetic dipole and magnetic quadrupole modes are present and have a peak around 2.2 eV and additional features at higher energy. The intensity of these modes is slightly larger than electric quadrupole and electric

octupole modes present at higher energies. At the higher nanoparticle density, the two magnetic modes red-shift by about 0.3 eV relative to what was observed in the lower density meta-atom. The intensity of these magnetic modes are enhanced by about a factor of 4 relative to the lower density meta-atom, while the electric modes remain of similar magnitude. Thus, the emergence of the magnetic mode at 1.8 eV can be understood as a magnetic dipole–magnetic quadrupole pair that red-shifts and intensifies rapidly with increasing nanoparticle density.

The meta-atoms scatter light such that the forward scattering is much stronger than the backward scattering across all permutations for both linearly and azimuthally polarized light. The dominant scattering modes at low energies are magnetic dipole and magnetic quadrupole modes. The weak back-scattering can be understood by looking at the interference of these two modes. The scattering intensity of a field from an electric and magnetic mode is

$$\begin{aligned} |a_{lm}\boldsymbol{N}_{lm} + b_{l'm'}\boldsymbol{M}_{l'm'}|^2 = &\overbrace{|a_{lm}|^2|\boldsymbol{N}_{lm}|^2}^{\text{electric mode}} + \overbrace{|b_{l'm'}|^2|\boldsymbol{M}_{l'm'}|^2}^{\text{magnetic mode}} \\ &+ \underbrace{a_{lm}b^*{}_{l'm'}\boldsymbol{N}_{lm}\cdot\boldsymbol{M}^*{}_{l'm'} + a^*{}_{lm}b_{l'm'}\boldsymbol{N}^*{}_{lm}\cdot\boldsymbol{M}_{l'm'}}_{\text{electric – magnetic interference terms}} \end{aligned} \tag{5.12}$$

Fig. 5.10(a-d) shows the angular distribution of the magnetic dipole, magnetic quadrupole, interference term, and total scattering under linearly polarized beam excitation at 1.4 eV. Each distribution is obtained via the terms in Eq.(5.12) and visualized in spherical coordinates. In Fig. 5.10(c), regions of red correspond to destructive interference while blue regions correspond to constructive interference. The dashed horizontal line separates the forward scattering ($\theta < \pi/2$) from the backward scattering ($\theta > \pi/2$).

Fig. 5.10(e-h) show the same analysis for azimuthally polarized beam excitation. Although the dipolar and quadrupolar modes have a different angular distribution than the linearly polarized excitation (see Fig. 5.13(b)), these modes still destructively interfere in the backward direction. It is important to keep these interference effects in mind when interpreting the results of experiments that measure scattered light in a particular direction.

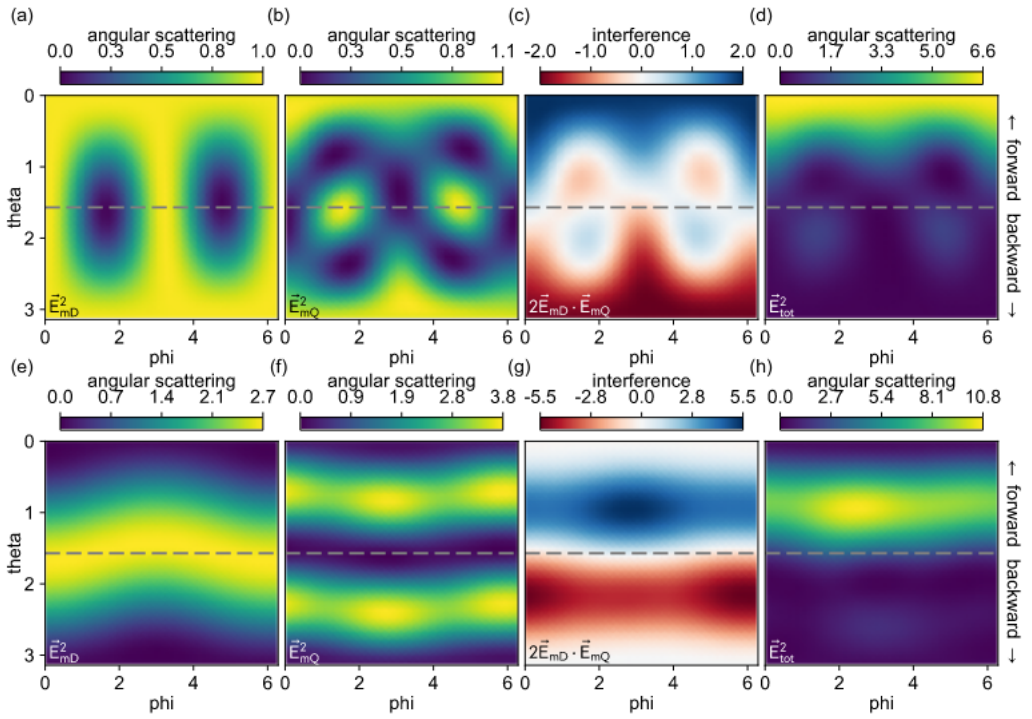

Figure 5.10: The magnetic dipole and magnetic quadrupole modes spatially interfere affecting the angular scattering distribution. (a-d) Angular scattering intensity by linearly polarized beam excitation for a magnetic dipole mode (a), magnetic quadrupole mode (b), magnetic dipole and magnetic quadrupole interference (c), and total scattering (d). (e-h) Corresponding angular scattering intensity by azimuthally polarized beam excitation. The dashed line separates the forward and backward scattering regions. All images are for a 1.4 eV source.

5.6 Conclusion

In this chapter, the selective excitation of multipolar modes and collective scattering modes using scalar and vector beams was discussed. In isotropic and axisymmetric anisotropic particles, the scalar and vector beams led to a set of selection rules for the allowed scattering modes. Linearly polarized light can excite the electric and magnetic modes, azimuthally polarized light can only excite magnetic modes, radially polarized light can only excite electric modes, and shear polarized light can only excite quadrupolar and higher order modes. These selection rules do not generally extend to collections of nanoparticles unless the collection has approximate isotropy, such as the core-satellite meta-atom considered here.

Collections of nanoparticles are coupled and have collective electrodynamic excitations. This was discussed analytically using T-matrix theory and generalized multiparticle Mie theory. The

A-matrix, $\mathcal{A}$, is a coupling matrix between all of the particles. Its eigenmodes correspond to all the possible electrodynamic excitations (including dark modes) of the nanoparticle collection and the corresponding eigenvalues measure the stength of electrodynamic coupling. The eigenvalues of the A-matrix are seen to be enhanced in an array near the optical binding separation, and greatly enhanced as the lattice spacing is reduced to zero and the particles become near-field coupled.

A near-field coupled collection of plasmonic particles is realized in the core-satellite meta-atom. By packing the surface with as many particles as possible, the coupling strength is enhanced and magnetic modes corresponding to circulation of displacement currents around the core emerge. The design of the core-satellite meta-atom is such that it is approximately isotropic and its light scattering properties are independent of the incident light direction, making it a good candidate for meta-fluids. Additionally, the selection rules for the vector beams apply to the core-satellite meta-atom, and the azimuthally polarized beam can be used to selectively excite its magnetic modes.

5.A Dark plasmons modes in gold dimers

A near-field plasmonic dimer is a useful example of the simplest possible system that exhibits strong electromagnetic coupling. As shown in the hexagonal arrays earlier, Figure 5.4, the dimer similarly has dark modes that are not accessible with plane-wave illumination. The vector beams can be used to selectively excite these dark modes.

A hybridization model can be used to describe the energetics of different modes in a near-field dimer. [135] While plane-waves can only excite dipoles in each particle that have the same orientation and phase, the vector beams can excite dipoles that have a π phase shift. This results in a different interparticle interaction and consequently a different amount of coupling and scattering resonance.

Figure 5.11(a) shows a TEM image of a gold near-field dimer in experiment. The scattering by linearly polarized light in simulation and experiment, Figure 5.11(b), shows three different resonances depending on the polarization direction. Resonances observed in Figure 5.11(c) caused by vector beams correspond to dark modes in the dimer.

Additional information on this experiment and simulation is available elsewhere. [61]

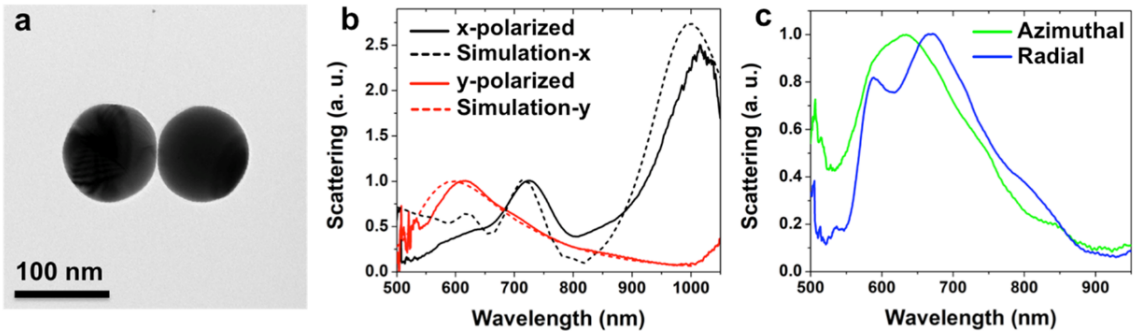

Figure 5.11: Measurements and FDTD simulations of the scattering spectra of an almost touching AuNP dimer excited by scalar (linear) beams andvector beams. (a) A TEM image of a 100 nm AuNP dimer with sub-nanometer gap. (b) Experimental (solid) and simulated (dashed) scattering spectraof the AuNP dimer in (a), excited by linear beams parallel (x-polarized, black) and perpendicular (y-polarized, red) to the dimer axis. The gap of theAuNP dimer is 0.6 nm in the simulations. (c) Experimental scattering spectra of the AuNP dimer excited by azimuthally (green) and radially (blue)polarized beams. [61]

5.B Selective excitation of electrodynamic anapoles

In anisotropic disk-shaped particles, electrodynamic anapole modes have been observed. [131] Anapoles are a unique current excitation that result in no radiative losses. It is possible to realize anapole modes in high-index dielectric spheres, and even selectively excite them using radially polarized beams. [132]

A toroidal moment in a spherical particle consists of currents that circulate around a toroid, and is given by the expression

$$\boldsymbol{T} = \frac{1}{10c}\int_V \left[(\boldsymbol{r}\cdot\boldsymbol{J}(\omega))\boldsymbol{r} - 2r^2\boldsymbol{J}(\omega)\right] d^3r \tag{5.13}$$

The toroidal moment ($\boldsymbol{T}$) generates the same far-field as the electric dipole current excitation ($\boldsymbol{P}$) . The total scattered electric far field is then

$$\boldsymbol{E}_{\text{scat}}(\boldsymbol{r},\omega) = \frac{k^2}{4\pi\varepsilon_0\varepsilon_b r}(\hat{\boldsymbol{r}}\times\boldsymbol{P}(\omega)\times\hat{\boldsymbol{r}} + ik\hat{\boldsymbol{r}}\times\boldsymbol{T}(\omega)\times\hat{\boldsymbol{r}}) \tag{5.14}$$

The condition for zero-scattering in the far-field (the anapole condition) is

$$\boldsymbol{P}(\omega) = -ik\boldsymbol{T}(\omega) \tag{5.15}$$

That is, an anapole consists of a combined cartesian dipole and toroidal dipole that produces no radiative losses (thermal losses, if any, are still present).

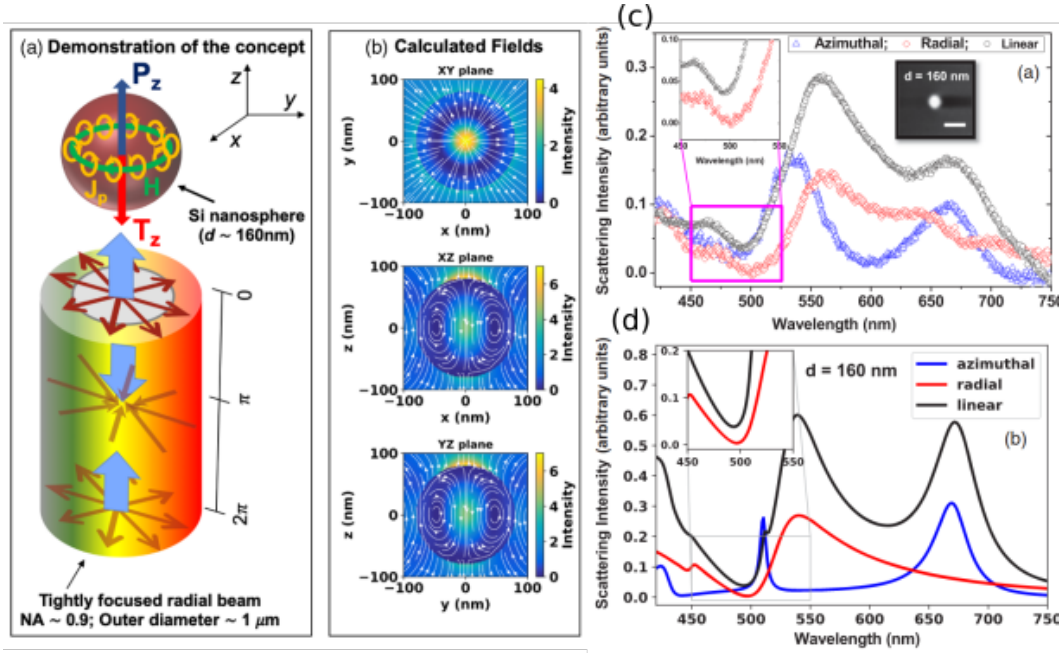

Figure 5.12: Selective excitation of electrodynamic anapole modes in silicon spheres using radially polarized beams. (a) Schematic diagram showing excitation of an Si nanosphere ($d \approx 160\,\text{nm}$) with a radially polarzied beam. The currents induced in the dipole have a toroidal character. (b) Streamlines of the total electric field. (c) Scattering spectra obtained from experiment. (d) Scattering spectra obtained from simulation. [132]

Figure 5.12(a) shows a schematic of the induced anapole mode in a Si nano-sphere illuminated by a radially polarized beam of light. The interior fields and scattered near-fields at the anapole condition are shown in Figure 5.12(b). The scattering in experiment, Figure 5.12(c), is compared with that from simulation, Figure 5.12(d). The anapole condition is met near $= 500\,\text{nm}$, resulting in near-zero scattering. The radial beam is seen to achieve a better anapole mode than the linear beam since it selectively excites the electric dipole modes while suppressing the magnetic modes, resulting in a near-perfect cancellation of the far-fields.

Additional information of the experiment, simulation method, and calculation of the toroidal moments can be found elsewhere. [132]

5.C Vector beams and multipolar analysis in FDTD

Scalar and vector beams can be used in the FDTD computational method as well. These sources are generated in FDTD simulations using an electric surface current density $\boldsymbol{J}_E(x, y)$ in a source plane away from the scattering object (see Fig. 5.13). The current sources for each beam are given the same spatial profile as the desired electric field based on the field equivalence principle [136],

$$\begin{aligned} \boldsymbol{J}_{\mathrm{E,lin}} &= \mathrm{HG}_{00}\hat{\boldsymbol{x}} \\ \boldsymbol{J}_{\mathrm{E,azi}} &= \mathrm{HG}_{01}\hat{\boldsymbol{x}} - \mathrm{HG}_{10}\hat{\boldsymbol{y}} \\ \boldsymbol{J}_{\mathrm{E,rad}} &= \mathrm{HG}_{10}\hat{\boldsymbol{x}} + \mathrm{HG}_{01}\hat{\boldsymbol{y}} \\ \boldsymbol{J}_{\mathrm{E,shear}} &= \mathrm{HG}_{01}\hat{\boldsymbol{x}} + \mathrm{HG}_{10}\hat{\boldsymbol{y}} \end{aligned} \tag{5.16}$$

These sources create vector beams that are focused at the source plane. The beam propagates to the sample and diverges slightly at and across the sample. For this reason, the source plane is chosen to be as close as possible to the scattering object (about 50 nm from the nanoparticle surface). This is an inherent disadvantage of this method compared to GMMT, although it can be circumvented using the total-field scattered-field (TFSF) formalism along with the field equivalence principle. [137]

The coordinate system is chosen such that the x and y-axes span the source plane and the $+z$-axis is along the direction of propagation. In the source plane, ϕ denotes the angle subtended by a vector $\vec{r}$ and the x-axis (see Fig. 5.13(a)). To perform the multipolar analysis, a spherical monitor is placed around the meta-atom that collects the scattered electric and magnetic fields. Equation (5.2) is then used to calculate the scattering expansion coefficients.

Additional information on this simulation method can be found elsewhere. [60, 138]

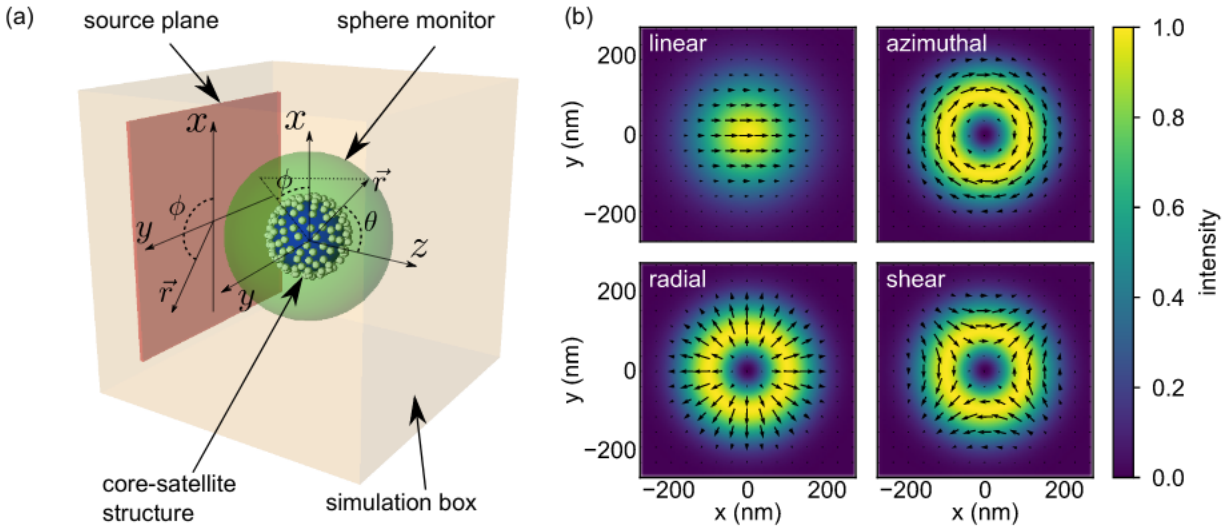

Figure 5.13: Details of the FDTD simulations of core-satellite meta-atoms. (a) Simulation box, including a core-satellite scattering object, a spherical monitor to collect the Fourier transformed scattered fields, and a plane for the incident source. Perfectly matching absorbing layers (not explicitly shown) are placed in the outermost regions of all sides of the simulation box (b) The four different sources used: linear, radial, azimuthal, and shear beams. The arrows indicate the instantaneous direction of electric field polarization in the source plane. [60]

CHAPTER 6
EFFICIENT SIMULATION OF ELECTRODYNAMICS AND DRIVEN OPTICAL MATTER SYSTEMS

Optical matter systems are simulated by solving a Langevin or Stokesian dynamics equation of motion for N particles. [95] At each time-step in the dynamics, the electrodynamics of the N particle configuration illuminated by some source field must be solved for. The computational approach used in solving the electrodynamics is crucial to the performance and runtime of such simulations. Methods such as the discrete dipole approximation (DDA)[53] or the finite-difference time-domain (FDTD)[50] are so slow that only a few thousand time steps can be done over a reasonable time ($\sim$ 100 CPU hours). [51] Moreover, there can be large numerical errors due to the finite grid-spacing in such algorithms.

A more efficient and accurate approach to simulating optical matter is the generalized multiparticle Mie theory (GMMT). [74, 77] GMMT is based on a generalization of the single particle Mie theory[68] to that of multiple particles illuminated by an arbitrary source using the translation theorems of the vector spherical harmonic wavefunctions. [74, 75] GMMT can be extended to non-spherical particles via the T-matrix method [76] and can include a planar interface.[78] GMMT excels for optical matter because sub-wavelength particles largely only emit dipolar and quadrupolar modes, and GMMT accounts for all possible interactions between these modes in each particle. Using GMMT, optical matter arrays consisting of 1–30 particles can be time-stepped a million times within about 1 CPU hour.

This chapter introduces the theory and computational implementation of GMMT for simulating optical matter systems. GMMT can be used to calculate the forces and torques on every particle, which are then fed into a Langevin or Stokesian dynamics equation to time-step the optical matter system. Stokesian dynamics accounts for the hydrodynamic correlations of the particles due to the fluid flow of the surrounding medium.

An open source software, `MiePy`, was developed to efficiently implement GMMT in an easy-to-use and flexible Python library. [139] Another software packaged, `Stoked`, was developed to perform Brownian, Langevin, and Stokesian dynamics with electrodynamic interactions and other particle

interactions present in optical matter. [140] Example Python scripts using `Stoked` and `MiePy` to simulate optical matter are available in Appendix 6.C.

6.1 Simulating the electrodynamics of optical matter using the Generalized Mie Theory

6.1.1 Vector spherical harmonic functions

The generalized multiparticle Mie theory (GMMT) is outlined, following Xu's work. [74] GMMT solves the piecewise homogeneous vector Helmholtz equation

$$\begin{aligned}(\boldsymbol{\nabla}^2 + k_i^2)\boldsymbol{E}_i(\boldsymbol{r}) = 0 \\ (\boldsymbol{\nabla}^2 + k_i^2)\boldsymbol{H}_i(\boldsymbol{r}) = 0\end{aligned} \tag{6.1}$$

inside all N particles, $i \in [1, 2, \ldots, N]$, and in the medium, $i = 0$, Additionally, the boundary condition on the surface of every particle has to be valid

$$\begin{aligned}\hat{\boldsymbol{n}} \times (\boldsymbol{E}_i - \boldsymbol{E}_j) = 0 \\ \hat{\boldsymbol{n}} \times (\boldsymbol{H}_i - \boldsymbol{H}_j) = 0\end{aligned} \tag{6.2}$$

The vector spherical harmonic wavefuncions (VSHW) are a complete basis set for incident and scattered fields. They are eigenmodes of the Helmholtz operator in Equation (6.1) and are given by

$$\begin{aligned}\boldsymbol{N}_{mn1}^{(J)} &= \hat{\boldsymbol{r}} n(n+1) P_n^m(\theta) \frac{z_n^{(J)}(kr)}{kr} e^{im\phi} \\ &\quad + \frac{1}{kr}\left[\hat{\boldsymbol{\theta}}\tau_{mn}(\theta) + \hat{\boldsymbol{\phi}} i\pi_{mn}(\theta)\right] \frac{d}{dr}\left[r z_n^{(J)}(kr) e^{im\phi}\right] \\ \boldsymbol{N}_{mn2}^{(J)} &= \left[\hat{\boldsymbol{\theta}} i\pi_{mn}(\theta) - \hat{\boldsymbol{\phi}}\tau_{mn}(\theta)\right] z_n^{(J)}(kr) e^{im\phi}\end{aligned} \tag{6.3}$$

where $J = 1, 2, 3, 4$. The radial functions $z_n^{(J)}$ are

$$\begin{aligned}z_n^{(1)}(x) &= j_n(x) & z_n^{(3)}(x) &= h_n^{(1)}(x) = j_n(x) + i y_n(x) \\ z_n^{(2)}(x) &= y_n(x) & z_n^{(4)}(x) &= h_n^{(2)}(x) = j_n(x) - i y_n(x)\end{aligned} \tag{6.4}$$

where j_n, y_n are the spherical Bessel functions of the first and second kind, and $h_n^{(1)}$, $h_n^{(2)}$ are the spherical Hankel functions of the first and second kind. The angular functions π_{mn} and τ_{mn} are

$$\pi_{mn}(\theta) = \frac{m}{\sin\theta} P_n^m(\cos\theta) \tag{6.5}$$

$$\tau_{mn}(\theta) = \frac{d}{d\theta} P_n^m(\cos\theta) \tag{6.6}$$

The associated Legendre polynomials P_n^m are defined without the Condon-Shortley phase, i.e.

$$P_n^m(x) = (1-x^2)^{m/2} \frac{d^m}{dx^m} P_n(x) \tag{6.7}$$

where $P_n(x)$ are the Legendre polynomials.

The VSHWs are an orthogonal (but not orthonormal) set when integrated over a closed surface Ω

$$\begin{aligned}
\langle \boldsymbol{N}_{mn1}^{(J)}, \boldsymbol{N}_{m'n'1}^{(J)} \rangle &= \int_\Omega \boldsymbol{N}_{mn1}^{(J)} \cdot \boldsymbol{N}_{m'n'1}^{(J)*} \, d\Omega \\
&= \delta_{mm'}\delta_{nn'} 4\pi \frac{n(n+1)(n+m)!}{(2n+1)(n-m)!} \left[\frac{\left| z_n^{(J)}(kr) + kr z_n^{(J)\prime}(kr) \right|^2 + n(n+1) \left| z_n^{(J)}(kr) \right|^2}{(kr)^2} \right] \\
\langle \boldsymbol{N}_{mn2}^{(J)}, \boldsymbol{N}_{m'n'2}^{(J)} \rangle &= \int_\Omega \boldsymbol{N}_{mn2}^{(J)} \cdot \boldsymbol{N}_{m'n'2}^{(J)*} \, d\Omega = \delta_{mm'}\delta_{nn'} 4\pi \frac{n(n+1)(n+m)!}{(2n+1)(n-m)!} |z_n^{(J)}(kr)|^2 \\
\langle \boldsymbol{N}_{mn1}^{(J)}, \boldsymbol{N}_{m'n'2}^{(J)} \rangle &= \int_\Omega \boldsymbol{N}_{mn1}^{(J)} \cdot \boldsymbol{N}_{m'n'2}^{(J)*} \, d\Omega = 0
\end{aligned} \tag{6.8}$$

Table 6.1 outlines the physical interpretation of the VSHWs.

6.1.2 Field expansions

The source, incident, scattered, and interior electric and magnetic fields of particle j can be expanded in terms of the VSHWs. The incident field includes the source field plus the incident field from all other particles in the system. Each of the four field expansions has their own set of (complex) expansion coefficients over the VSHWs.

Entity	Physical interpretation
$\boldsymbol{N}_{mn1}$	electric (TM) modes
$\boldsymbol{N}_{mn2}$	magnetic (TE) modes
n	multipolar order (1: dipole, 2: quadrupole, etc.)
m	azimuthal order (from $-n$ to n)
$J = 1$	propagating incident mode
$J = 2$	counter-propagating incident mode
$J = 3$	spherically outgoing mode
$J = 4$	spherically ingoing mode

Table 6.1: Physical description of different entities involved in the vector spherical harmonic wavefunctions.

The electric field expansions are

$$\boldsymbol{E}^j_{\text{src}} = -\sum_{n=1}^{N_{\max}} \sum_{m=-n}^{n} \sum_{r=1}^{2} iE_{mn} p^{j,\text{src}}_{mnr} \boldsymbol{N}^{(1)}_{mnr} \tag{6.9a}$$

$$\boldsymbol{E}^j_{\text{inc}} = -\sum_{n=1}^{N_{\max}} \sum_{m=-n}^{n} \sum_{r=1}^{2} iE_{mn} p^{j,\text{inc}}_{mnr} \boldsymbol{N}^{(1)}_{mnr} \tag{6.9b}$$

$$\boldsymbol{E}^j_{\text{scat}} = \sum_{n=1}^{N_{\max}} \sum_{m=-n}^{n} \sum_{r=1}^{2} iE_{mn} p^{j,\text{scat}}_{mnr} \boldsymbol{N}^{(3)}_{mnr} \tag{6.9c}$$

$$\boldsymbol{E}^j_{\text{int}} = -\sum_{n=1}^{N_{\max}} \sum_{m=-n}^{n} \sum_{r=1}^{2} iE_{mn} p^{j,\text{int}}_{mnr} \boldsymbol{N}^{(1)}_{mnr} \tag{6.9d}$$

and the magnetic field expansions are

$$\boldsymbol{H}^j_{\text{src}} = -\sqrt{\frac{\varepsilon_b}{\mu_b}} \sum_{n=1}^{N_{\max}} \sum_{m=-n}^{n} \sum_{r=1}^{2} E_{mn} p^{j,\text{src}}_{mn\bar{r}} \boldsymbol{N}^{(1)}_{mnr} \tag{6.10a}$$

$$\boldsymbol{H}^j_{\text{inc}} = -\sqrt{\frac{\varepsilon_b}{\mu_b}} \sum_{n=1}^{N_{\max}} \sum_{m=-n}^{n} \sum_{r=1}^{2} E_{mn} p^{j,\text{inc}}_{mn\bar{r}} \boldsymbol{N}^{(1)}_{mnr} \tag{6.10b}$$

$$\boldsymbol{H}^j_{\text{scat}} = \sqrt{\frac{\varepsilon_b}{\mu_b}} \sum_{n=1}^{N_{\max}} \sum_{m=-n}^{n} \sum_{r=1}^{2} E_{mn} p^{j,\text{scat}}_{mn\bar{r}} \boldsymbol{N}^{(3)}_{mnr} \tag{6.10c}$$

$$\boldsymbol{H}^j_{\text{int}} = -\sqrt{\frac{\varepsilon^j}{\mu^j}} \sum_{n=1}^{N_{\max}} \sum_{m=-n}^{n} \sum_{r=1}^{2} E_{mn} p^{j,\text{int}}_{mn\bar{r}} \boldsymbol{N}^{(1)}_{mnr} \tag{6.10d}$$

where $\bar{r} = 3 - r$ and E_{mn} is a normalization factor

$$E_{mn} = i^n \sqrt{\frac{(2n+1)(n-m)!}{n(n+1)(n+m)!}} \tag{6.11}$$

In GMMT, it is supposed that the source coefficients are known or can be computed. The incident coefficients are then determined by solving an interaction equation for all N particles. The scattered and interior coefficients are then determined by the boundary condition, Equation (6.2)

6.1.3 VSHW translation and rotation coefficients

In order to be able to write down interaction equations between N particles, the VSHW coefficients around one coordinate system need to transformed to a different coordinate system. The VSHWs functions evaluated at a point $\boldsymbol{r}_l$ can be translated to a point $\boldsymbol{r}_j$ by use of the VSHW translation coefficients $\widetilde{A}^{jl}_{mnruvs}$

$$\boldsymbol{N}^{(J)}_{mnr}(k\boldsymbol{r}_j) = \sum_{v=1}^{\infty} \sum_{u=-v}^{u=v} \sum_{s=1}^{2} \widetilde{A}^{(J)jl}_{mnruvs} \boldsymbol{N}^{(1)}_{uvs}(k\boldsymbol{r}_l) \tag{6.12}$$

Here, the fields being translated from are incident fields (hence $J = 1$), and the fields being translated to can correspond to any J value. If $J = 1$, $\widetilde{A}$ translates incident fields to scattered fields, and if $J = 3$, $\widetilde{A}$ translates incident fields to incident fields. Explicit formula for the translation coefficients can be found elsewhere. [141]

From the field expansions, Equation (6.9), the VSHW translation coefficients can be used to relate the incident expansion coefficients of particle l to the incident expansion coefficients around particle j,

$$p^{j,(J)}_{mnr} = f^{(J)} \sum_{v=1}^{\infty} \sum_{u=-v}^{u=v} \sum_{s=1}^{2} A^{(J)jl}_{mnruvs} p^{l,\mathrm{inc}}_{uvs} \tag{6.13}$$

where $A^{(J)jl}_{mnruvs}$ are the *normalized* translation coefficients

$$A^{(J)jl}_{mnruvs} = \frac{E_{uv}}{E_{mn}} \widetilde{A}^{(J)jl}_{mnruvs} \tag{6.14}$$

and $f^{(J)}$ is a ± 1 sign term

$$f^{(J)} = \begin{cases} +1 & \text{if } J = 3 \\ -1 & \text{otherwise} \end{cases} \tag{6.15}$$

The translation coefficients have the following useful symmetry relationships [142]

$$A^{ij}_{mnruvs} = (-1)^{n+v+r+s} A^{ji}_{mnruvs} \tag{6.16a}$$

$$= (-1)^{n+v+m+u} A^{ji}_{-uvs-mnr} \tag{6.16b}$$

$$= (-1)^{m+u} [A^{ji}_{uvsmnr}]^{*1} \tag{6.16c}$$

The expansion coefficients can also be transformed into a rotated coordinate system using the Wigner-D matrix

$$p'_{mnr} = D^n_{ms}(\hat{q}) p_{mns} \tag{6.17}$$

where $\hat{q}$ represents the rotation (typically a quaternion).

6.1.4 T-matrix formulation

The T-matrix of particle j, $\mathcal{T}^j_{mnruvs}$, relates the incident expansion coefficients to the scattered expansion coefficients for an arbitrary, non-spherical particle. To simplify the index notation, a multi-index is used to denote a given mode, i.e. $\alpha = (m, n, r)$. Greek letters are used to represent a multi-index. Furthermore, Einstein notation is used so that repeated multi-indices are summed over. Then the T-matrix is defined as

$$p^{j,\text{scat}}_\alpha = \mathcal{T}^j_{\alpha\beta} p^{j,\text{inc}}_\beta \tag{6.18}$$

The T-matrix does not depend on the source; it only depends on the particle's material, the particle's geometry, the wavelength of light, and the material of the surrounding medium. If the particle is a

1. The conjugate in Equation (6.16c) applies to everything but the radial function $z^{(J)}_n$ appearing in the sum found in the definition of A^{ij}. If $J = 1$ or $J = 2$ and the medium is non-absorbing, this exception can be ignored since z_n is real.

sphere, then the T-matrix is diagonal,

$$\mathcal{T}^j_{\alpha\beta} = t^j_{rn}\delta_{\alpha\beta} \tag{6.19}$$

where $t^j_{1n} = a^j_n$ and $t^j_{2n} = b^j_n$ are the classical Mie theory coefficients of the jth sphere.[69]

Once a particle's T-matrix is known, it does not have to be recomputed for a new orientation of the particle, provided the geometrical and material properties of the particle remain the same. Given a particle T-matrix in one coordinate system, the T-matrix in a rotated coordinate system is

$$\mathcal{T}'_{m'nru'vs} = D^n_{m'm}(\hat{q})[D^v_{u'u}(\hat{q})]^*\mathcal{T}_{mnruvs} \tag{6.20}$$

This is derived by rotating and inverse-rotating the incident coefficients using Equation (6.17).

A particle also has an *internal* T-matrix, $\mathcal{T}^{\text{int}}$, that relates the internal expansion coefficients to the incident coefficients

$$p^{j,\text{int}}_\alpha = \mathcal{T}^{j,\text{int}}_{\alpha\beta}p^{j,\text{inc}}_\beta \tag{6.21}$$

The numerical evaluation of these T-matrices is discussed in Appendix 6.A.

6.1.5 Interaction equations

Given the positions of all the particles, $\boldsymbol{r}_j$, the T-matrices of all of the particles, $\mathcal{T}^j$, and the source expansion coefficients at every particle, $p^{j,\text{src}}_\alpha$, the interaction equation among N particles can be written as

$$p^{j,\text{inc}}_\alpha = p^{j,\text{src}}_\alpha - A^{(3)jl}_{\alpha\beta}\mathcal{T}^l_{\beta\gamma}p^{l,\text{inc}}_\gamma \tag{6.22}$$

This is the full-interaction of N generally anisotropic particles. The only requirement is that for any two particles, their smallest circumscribing spheres do not overlap. This is due to the failure of the Rayleigh hypothesis. [143, 144] There is current research being done on how to circumvent this issue using a plane-wave expansion alongside the VSHW expansion. [145, 146]

To derive the simplified interaction equations for all spherical particles (where the Rayleigh hypothesis is always valid), consider first Equation (6.22) where the Einstein summation is now

explicit and the multi-indices are unraveled

$$p_{mnr}^{j,\mathrm{inc}} = p_{mnr}^{j,\mathrm{src}} - \sum_{l\neq j}^{(1,N)} \sum_{v=1}^{L_{\max}} \sum_{u=-v}^{v} \sum_{s=1}^{2} \sum_{v'=1}^{L_{\max}} \sum_{u'=-v'}^{v'} \sum_{s'=1}^{2} A_{mnruvs}^{(3)jl} \mathcal{T}_{uvsu'v's'}^{l} p_{u'v's'}^{l,\mathrm{inc}} \tag{6.23}$$

If the system consists entirely of spheres, then using Equation (6.19), the interaction equation reduces

$$p_{mnr}^{j,\mathrm{inc}} = p_{mn}^{j,\mathrm{src}} - \sum_{l\neq j}^{(1,N)} \sum_{v=1}^{L_{\max}} \sum_{u=-v}^{v} \sum_{s=1}^{2} A_{mnruvs}^{(3)jl} t_{sv}^{l} p_{uvs}^{l,\mathrm{inc}} \tag{6.24}$$

Whether the cluster is composed solely of spheres or more generally non-spherical particles, the interaction equation is always of the form

$$p_{\alpha}^{j,\mathrm{inc}} = p_{\alpha}^{j,\mathrm{src}} - \mathcal{T}_{\alpha\beta}^{jl} p_{\beta}^{l,\mathrm{inc}} \tag{6.25}$$

where $\mathcal{T}_{\alpha\beta}^{jl}$ is the *particle aggregate T-matrix*. By setting $p_{\alpha}^{j,\mathrm{inc}} = \delta_{\alpha\beta}\delta_{jl} p_{\beta}^{l,\mathrm{inc}}$, the interaction equation can be rewritten in the standard form for linear systems, $[A]x = b$,

$$\left[\delta_{\alpha\beta}\delta_{jl} + \mathcal{T}_{\alpha\beta}^{jl}\right] p_{\beta}^{l,\mathrm{inc}} = p_{\alpha}^{j,\mathrm{src}} \tag{6.26}$$

This equation can then be solved using any linear algebra software. Iterative solvers, such as BiCGSTAB [147], are particularly efficient for the linear systems often encountered in GMMT.

6.1.6 Interactions with a substrate

The interactions of the particles with the interface of a substrate can be included in the GMMT. This is done by simultaneously matching the boundary conditions on the surface of the particles (using VSHWs) and on the interface (using a plane wave expansion). [78] We introduce a reflection matrix $\widetilde{R}_{\alpha\beta}^{jl}$ from particle l to j, similar to that of direct translations in Equation (6.12)

$$\boldsymbol{N}_{\alpha}^{(3),\mathrm{ref}}(k\boldsymbol{r}_j) = \widetilde{R}_{\alpha\beta}^{jl} \boldsymbol{N}_{\beta}^{(1)}(k\boldsymbol{r}_l) \tag{6.27}$$

This equation relates the scattered, reflected VSHW functions in terms of incident VSHW functions around a different coordinate system. Expressions for the $\widetilde{R}^{jl}_{\alpha\beta}$ matrix in terms of substrate material and particle location is provided elsewhere. [78]

As before, these reflection coefficients are normalized to relate to the expansion coefficients

$$p^{j,\mathrm{ref,scat}}_{\alpha} = f^{(J)} \sum_{v=1}^{\infty} \sum_{u=-v}^{u=v} \sum_{s=1}^{2} R^{(J)jl}_{\alpha\beta} p^{l,\mathrm{inc}}_{\beta} \tag{6.28}$$

The interaction equations then become

$$p^{j,\mathrm{inc}}_{\alpha} = p^{j,\mathrm{src}}_{\alpha} + p^{j,\mathrm{src,ref}}_{\alpha} - \left(A^{(3)jl}_{\alpha\beta} + R^{jl}_{\alpha\beta} \right) \mathcal{T}^{l}_{\beta\gamma} p^{l,\mathrm{inc}}_{\gamma} \tag{6.29}$$

where $p^{j,\mathrm{src,ref}}_{\alpha}$ are the expansion coefficients of the source reflected off of the substrate. The reflected coefficients can be evaluated using the angular spectrum of light and the Fresnel equations for the reflection of plane-waves off the substrate. The interaction equation in Equation (6.29) is still a linear system, where the source field and interaction have been modified by the presence of the substrate.

This approach can be extended to multiple substrates (layered media) [148]. It can also be extended to non-spherical particles very close to the substrate where the Rayleigh hypothesis fails. [149]

6.1.7 Symmetries

Symmetries in the system can be used to reduce the total number of interaction equations. It is important to remember that not only do the particles have to satisfy a given symmetry (their position, size, orientation, and material), but that the incident source field must also satisfy it. In many cases, a phase factor must be included with a given symmetry depending on the incident field. For example, if the incident field is x-polarized and a mirror symmetry is in the yz plane, the mirrored fields will be $-x$-polarized. This can be corrected by including a π phase factor in the mirror symmetry (multiplying by -1). On the other hand, if the incident field is right-hand-circularly polarized and a mirror symmetry is imposed, the mirrored fields will be left-hand-circularly polarized.

This cannot be corrected by using a phase factor.

Translational symmetry (periodic boundary conditions) If the unit cell consists of a single particle, [150]

$$p_\alpha^{\text{inc}} = p_\alpha^{\text{src}} - \Phi^l A_{\alpha\beta}^{(3)0l} \mathcal{T}_{\beta\gamma} p_\gamma^{\text{inc}} \tag{6.30}$$

where l enumerates the unit cells and Φ^l is a phase factor. For a plane wave with a given $\boldsymbol{k}$ vector, $\Phi^l = \exp(-i\boldsymbol{k} \cdot \boldsymbol{r}^l)$. If the unit cell consists of N particles, let l enumerate the positions of the unit cell and j enumerate the positions of the particles relative to the unit cell position

$$p_\alpha^{j,\text{inc}} = p_\alpha^{j,\text{src}} - \Phi^l A_{\alpha\beta}^{(3)j0} A_{\beta\gamma}^{(3)0l} A_{\gamma\delta}^{(3)lj'} \mathcal{T}_{\delta\epsilon}^{j'} p_\epsilon^{j',\text{inc}} \tag{6.31}$$

Since three VSHW translations are performed (one to the center of the unit cell, one to the origin, and one back to a particle), this approach comes with a loss of information. This loss of information can be avoided by performing the translation directly, at the cost performance

$$p_\alpha^{j,\text{inc}} = p_\alpha^{j,\text{src}} - \Phi^{j'} A_{\alpha\beta}^{(3)jj'} \mathcal{T}_{\beta\gamma}^{j'} p_\gamma^{j',\text{inc}} \tag{6.32}$$

Mirror symmetry Suppose that there is a mirror plane that passes through the origin and has a normal vector of $\hat{\boldsymbol{x}}$, $\hat{\boldsymbol{y}}$, or $\hat{\boldsymbol{z}}$. Each particle at position $\boldsymbol{r}^j$ then has a corresponding mirror particle at position $\boldsymbol{r}'^j$. By symmetry, the expansion coefficients of the mirror particle are related to those of the original particle

$$p_{mnr}'^{j,\text{inc}} = \Phi(-1)^{r+1} p_{-mnr}^{j,\text{inc}} \tag{6.33}$$

i.e. the mirror negates the azimuthal index m and negates the TM modes ($r = 2$).

Rotational symmetry Suppose the system has a discrete rotational symmetry of order R. If a particle exists at position r^{j1}, then the symmetric particles are at position r^{jr}, where $r = 2..R$. By symmetry,

$$p_{mnr}^{jr,\text{inc}} = D_{mun}(\theta_r) p_{mur}^{j1,\text{inc}} \tag{6.34}$$

Note that this requires the polarization of the light to be circular.

6.1.8 Cluster coefficients and cluster T-matrix

The expansion coefficients of the entire cluster, $p_\alpha^{\text{cluster}}$, are computed by translating the individual particle coefficients $p_\alpha^{j,\text{scat}}$ to the origin $\boldsymbol{r_0}$

$$p_\alpha^{\text{cluster}} = A_{\alpha\beta}^{(1)0j} p_\beta^{j,\text{scat}} \tag{6.35}$$

Note that $J = 1$ in the translation coefficient since the translation is from the scattered fields around one origin to the scattered fields around a different origin.

The *particle aggregate T-matrix* is defined by

$$\mathcal{T}_{\alpha\beta}^{jl} = A_{\alpha\gamma}^{(3)jl} \mathcal{T}_{\gamma\beta}^{l} \tag{6.36}$$

and the interaction equation becomes

$$p_\alpha^{j,\text{inc}} = p_\alpha^{j,\text{src}} - \mathcal{T}_{\alpha\beta}^{jl} p_\beta^{l,\text{inc}} \tag{6.37}$$

The *cluster T-matrix* is defined such that

$$p_\alpha^{\text{cluster}} = \mathcal{T}_{\alpha\beta}^{\text{cluster}} p_\beta^{0,\text{src}} \tag{6.38}$$

That is, the cluster T-matrix treats the system of particles as if it were a single scattering object, hiding the internal details.

6.1.9 Cross-sections

The cross-sections can be computed via two methods: one that uses the cluster coefficients $p_\alpha^{\text{cluster}}$ and one that uses the individual particle coefficients p_α^j.

Cross-sections via individual particle coefficients

$$C_{\text{abs}} = \frac{4\pi}{k^2} \sum_{j=1}^{N} \sum_{\alpha} \text{Re}\left\{ (p_\alpha^{j,\text{inc}})^* p_\alpha^{j,\text{scat}} \right\} - |p_\alpha^{j,\text{scat}}|^2 \tag{6.39a}$$

$$C_{\text{ext}} = \frac{4\pi}{k^2} \sum_{j=1}^{N} \sum_{\alpha} \text{Re}\left\{ (p_\alpha^{j,\text{src}})^* p_\alpha^{j,\text{scat}} \right\} \tag{6.39b}$$

$$C_{\text{scat}} = C_{\text{ext}} - C_{\text{abs}} \tag{6.39c}$$

This approach is the most efficient way to compute the total cross-sections. Each term in the absorption/extinction cross-section sum can be interpreted as the absorption/extinction of that individual particle due to a given mode α.

Cross-sections via cluster coefficients [74]

$$C_{\text{scat}} = \frac{4\pi}{k^2} \sum_{\alpha} |p_\alpha^{\text{cluster}}|^2 \tag{6.40a}$$

$$C_{\text{ext}} = \frac{4\pi}{k^2} \sum_{\alpha} \text{Re}\left\{ (p_\alpha^{0,\text{src}})^* p_\alpha^{\text{cluster}} \right\} \tag{6.40b}$$

$$C_{\text{abs}} = C_{\text{ext}} - C_{\text{scat}} \tag{6.40c}$$

This approach has a benefit in its interpretation. Each term in the scattering sum corresponds to the multipolar scattering of the α mode, so that the scattering from the entire cluster can be identified as electric or magnetic in nature, dipole, quadrupole, etc. These equations should typically be avoided in calculating total cross-sections since there is a loss of information in using the cluster coefficients and they may not converge.

All of these cross-sections have units of (area)×(electric field)^2. If the source is a plane wave of amplitude E_0, then these cross-sections should be normalized by E_0^2. For non-plane wave sources, the cross-sections should be normalized depending on the convention being used, typically an averaged intensity over some area:

$$E_0^2 = \frac{1}{A} \int_A \boldsymbol{S}(\boldsymbol{r}) \cdot \hat{\boldsymbol{n}} \, dA \tag{6.41}$$

where $\boldsymbol{S} = \frac{1}{2}\boldsymbol{E} \times \boldsymbol{H}^*$ is the Poynting vector. For instance, the area A may be a circular aperture

(power striking a structure) or all of space (total power of the source, provided it is finite).

6.1.10 Force and torque

The time-average force $\langle \boldsymbol{F} \rangle$ and torque $\langle \boldsymbol{\tau} \rangle$ on a particle can be determined by integrating the Maxwell stress tensor $\langle \boldsymbol{T} \rangle$ over a closed surface Ω surrounding the particle:

$$\langle \boldsymbol{T} \rangle = \frac{1}{2}\mathrm{Re}\left[\varepsilon_b \boldsymbol{E} \otimes \boldsymbol{E}^* + \mu_b \boldsymbol{H} \otimes \boldsymbol{H}^* - \frac{1}{2}(\varepsilon_b E^2 + \mu_b H^2)\boldsymbol{I}\right] \tag{6.42a}$$

$$\langle \boldsymbol{F} \rangle = \oint_\Omega \langle \boldsymbol{T} \rangle \cdot d\boldsymbol{\Omega} \tag{6.42b}$$

$$\langle \boldsymbol{\tau} \rangle = \oint_\Omega \boldsymbol{r} \times \langle \boldsymbol{T} \rangle \cdot d\boldsymbol{\Omega} \tag{6.42c}$$

where $\boldsymbol{I}$ is a 3×3 identitiy matrix and $\otimes$ is the vector outer product.

The electric and magnetic fields around particle j can be calculated using the field expansions, Equations (6.9) and (6.10). The integration for the time-averaged force can then be carried out analytically in the far-field, resulting in a sum over the particle expansion coefficients. [151] For these equations, it is helpful to denote $a_{mn} = p^{j,\mathrm{inc}}_{mn1}$, $b_{mn} = p^{j,\mathrm{inc}}_{mn2}$, $p_{mn} = p^{j,\mathrm{scat}}_{mn1}$, and $q_{mn} = p^{j,\mathrm{scat}}_{mn2}$. Then, the force is given by

$$\begin{aligned}
F_x + iF_y =& \frac{\pi}{k^2}\sum_{n=1}^{N_{\max}}\sum_{m=-n}^{n}\frac{1}{n+1}\Bigg\{\frac{\sqrt{(n+m+1)(n-m)}}{n}\frac{\varepsilon_b}{\mu_b}\Big[2a_{mn}b^*_{m+1n} - a_{mn}q^*_{m+1n} \\
&- p_{mn}b^*_{m+1n} + 2b_{mn}a^*_{m+1n} - b_{mn}p^*_{m+1n} - q_{mn}a^*_{m+1n}\Big] \\
&- \sqrt{\frac{(n+m+2)(n+m+1)n(n+2)}{(2n+3)(2n+1)}}\Big[2\varepsilon_b a_{mn}a^*_{m+1n+1} - \varepsilon_b a_{mn}p^*_{m+1n+1} \\
&- \varepsilon_b p_{mn}a^*_{m+1n+1} + 2\frac{\varepsilon_b}{\mu_b}b_{mn}b^*_{m+1n+1} - \frac{\varepsilon_b}{\mu_b}b_{mn}q^*_{m+1n+1} - \frac{\varepsilon_b}{\mu_b}q_{mn}b^*_{m+1n+1}\Big] \\
&+ \sqrt{\frac{(n-m+1)(n-m+2)n(n+2)}{(2n+3)(2n+1)}}\Big[2\varepsilon_b a_{m-1n+1}a^*_{mn} - \varepsilon_b a_{m-1n+1}p^*_{mn} \\
&- \varepsilon_b p_{m-1n+1}a^*_{mn} + 2\frac{\varepsilon_b}{\mu_b}b_{m-1n+1}b^*_{mn} - \frac{\varepsilon_b}{\mu_b}b_{m-1n+1}q^*_{mn} - \frac{\varepsilon_b}{\mu_b}q_{m-1n+1}b^*_{mn}\Big]\Bigg\}
\end{aligned} \tag{6.43a}$$

$$
\begin{aligned}
F_z = &-\frac{2\pi}{k^2}\sum_{n=1}^{N_{\max}}\sum_{m=-n}^{n}\frac{1}{n+1}\mathrm{Re}\Bigg\{\frac{m}{n}\frac{\varepsilon_b}{\mu_b}\Big[2a_{mn}b_{mn}^{*}-a_{mn}q_{mn}^{*}-p_{mn}b_{mn}^{*}\Big] \\
&+\sqrt{\frac{(n-m+1)(n+m+1)n(n+2)}{(2n+3)(2n+1)}}\Big[2\varepsilon_b a_{mn+1}a_{mn}^{*}-\varepsilon_b a_{mn+1}p_{mn}^{*}-\varepsilon_b p_{mn+1}a_{mn}^{*} \\
&+2\frac{\varepsilon_b}{\mu_b}b_{mn+1}b_{mn}^{*}-\frac{\varepsilon_b}{\mu_b}b_{mn+1}q_{mn}^{*}-\frac{\varepsilon_b}{\mu_b}q_{mn+1}b_{mn}^{*}\Big]\Bigg\}
\end{aligned}
\tag{6.43b}
$$

Similarly, the torque can be integrated analytically,

$$
\begin{aligned}
\tau_x = &\frac{2\pi}{k^3}\sum_{n=1}^{N_{\max}}\sum_{m=-n}^{n}\sqrt{(n-m)(n+m+1)}\,\mathrm{Re}\Bigg\{\varepsilon_b a_{mn}a_{m+1n}^{*}+\mu_b b_{mn}b_{m+1n}^{*} \\
&-\frac{1}{2}\Big[\varepsilon_b a_{m+1n}p_{mn}^{*}+\varepsilon_b a_{mn}p_{m+1n}^{*}+\mu_b b_{m+1n}q_{mn}^{*}+\mu_b b_{mn}q_{m+1n}^{*}\Big]\Bigg\}
\end{aligned}
\tag{6.44a}
$$

$$
\begin{aligned}
\tau_y = &\frac{2\pi}{k^3}\sum_{n=1}^{N_{\max}}\sum_{m=-n}^{n}\sqrt{(n-m)(n+m+1)}\,\mathrm{Im}\Bigg\{\varepsilon_b a_{mn}a_{m+1n}^{*}+\mu_b b_{mn}b_{m+1n}^{*} \\
&+\frac{1}{2}\Big[\varepsilon_b a_{m+1n}p_{mn}^{*}-\varepsilon_b a_{mn}p_{m+1n}^{*}+\mu_b b_{m+1n}q_{mn}^{*}-\mu_b b_{mn}q_{m+1n}^{*}\Big]\Bigg\}
\end{aligned}
\tag{6.44b}
$$

$$
\tau_z = -\frac{2\pi}{k^3}\sum_{n=1}^{N_{\max}}\sum_{m=-n}^{n}m\Big\{\varepsilon_b|a_{mn}|^2+\mu_b|b_{mn}|^2-\mathrm{Re}\Big[\varepsilon_b a_{mn}p_{mn}^{*}+\mu_b b_{mn}q_{mn}^{*}\Big]\Big\} \tag{6.44c}
$$

While these equations are complicated to write down, they are very computationally efficient and much faster than integrating the fields numerically using the MST.

6.1.11 Far-field expansions

In the far-field, the VSHWs take on a simplified form from their exact expression in Equation (6.3). The radial component of $\boldsymbol{N}$ vanishes and the spherical Bessel functions approach an asymptotic form. For spherically outgoing modes, the spherical Hankel function of the first kind is $h_n^{(1)}(kr) \simeq i^{-n-1}e^{ikr}/(kr)$ as $kr \to \infty$.

Given a set of scattering expansion coefficients q_{mnr}, the far fields can be expanded over a single sum of the multipolar modes:

$$\begin{aligned} E_{\text{scat},\theta}(\theta,\phi) &= i\frac{e^{ikr}}{kr}\sum_{n=1}^{N_{\max}}\sum_{m=-n}^{n}(-i)^n E_{mn}\left[q_{mn1}\tau_{mn}(\cos\theta)+q_{mn2}\pi_{mn}(\cos\theta)\right]e^{im\phi} \\ E_{\text{scat},\phi}(\theta,\phi) &= -\frac{e^{ikr}}{kr}\sum_{n=1}^{N_{\max}}\sum_{m=-n}^{n}(-i)^n E_{mn}\left[q_{mn1}\pi_{mn}(\cos\theta)+q_{mn2}\tau_{mn}(\cos\theta)\right]e^{im\phi} \end{aligned} \tag{6.45}$$

One option is to set $q_{mnr} = p^{\text{cluster}}_{mnr}$, the cluster expansion coefficients. This approach comes with a loss of information, but has the physical interpretation that each term in the sum can be attributed to the far-fields of a given multipolar mode. To avoid the loss of information, a sum over particle pairs can be performed [152]

$$q_\alpha(\theta,\phi) = \sum_{l=1}^{N}\sum_{j=1}^{N}\sum_{\beta}\exp\left[i(\hat{\boldsymbol{k}}-\hat{\boldsymbol{r}})\cdot\boldsymbol{r}^l\right]\exp\left[i\hat{\boldsymbol{k}}\cdot(\boldsymbol{r}^l-\boldsymbol{r}^j)\right]\mathcal{T}^{lj}_{\alpha\beta}p^{\text{j,inc}}_{\beta} \tag{6.46}$$

where the expansion coefficients now depend on the angular position.

6.1.12 Source decomposition

To solve the particle interaction equation, Equation (6.22), the expansion coefficients of the source field must be known at each particle. Given the electric fields of the incident source, $\boldsymbol{E}^{\text{src}}(\boldsymbol{r})$, the source can be decomposed into expansion coefficients by integration around particle j

$$p^{j,\text{src}}_{mnr} = i\frac{\int_\Omega \boldsymbol{E}^{\text{src}}\cdot\boldsymbol{N}^{(1)*}_{mnr}\,d\Omega}{E_{mn}\langle\boldsymbol{N}^{(1)}_{mnr},\boldsymbol{N}^{(1)}_{mnr}\rangle} \tag{6.47}$$

where Ω is a closed surface around particle j.

For a plane wave, this decomposition can be carried out analytically. The direction of the incident $\boldsymbol{k}$ vector can be described by the two spherical angles θ and ϕ. A linear polarization of the plane wave is either TM ($\hat{\boldsymbol{\theta}}$) or TE ($\hat{\boldsymbol{\phi}}$). Elliptically polarized light is then a complex-valued linear combination

of TM and TE polarizations.

$$\begin{aligned} p^{j,\mathrm{src}}_{mn1} &= E_0 i^{-n} E_{mn} \tau_{mn}(\cos\alpha) \exp(-im\beta) \exp(i\boldsymbol{k}\cdot\boldsymbol{r}_j) \\ p^{j,\mathrm{src}}_{mn2} &= E_0 i^{-n} E_{mn} \pi_{mn}(\cos\alpha) \exp(-im\beta) \exp(i\boldsymbol{k}\cdot\boldsymbol{r}_j) \end{aligned} \tag{6.48}$$

For beams, the angular spectrum of light is the most convenient way to express $\boldsymbol{E}^{\mathrm{src}}$. This provides the fields in (θ, ϕ) coordinates and Equation (6.47) then corresponds to integrating over a far-field hemisphere to obtain the source coefficients

$$p^{j,\mathrm{src}}_{mnr} = i \frac{\int_0^{2\pi} \int_0^{\theta_{\max}} \boldsymbol{E}^{\infty}(\theta,\phi) \cdot \boldsymbol{N}^{(1)*}_{mnr} \exp(i\boldsymbol{k}\cdot\boldsymbol{r}_j) \sin(\theta)\, d\theta d\phi}{E_{mn} \langle \boldsymbol{N}^{(1)}_{mnr}, \boldsymbol{N}^{(1)}_{mnr} \rangle} \tag{6.49}$$

where $\boldsymbol{E}^{\infty}(\theta,\phi)$ is the angular spectrum of the beam, $\theta_{\max}$ is determined by the numerical aperature of the focusing objective ($\mathrm{NA} = n\sin(\theta_{\max})$), $\boldsymbol{k} = k(\sin(\theta)\cos(\phi), \sin(\theta)\sin(\phi), \cos(\theta))$ is the wavevector of the plane-wave with coordinates (θ, ϕ), and $\boldsymbol{r}_j$ is the position of particle j. The angular spectrum of Gaussian, Laguerre-Gaussian, and Hermite-Gaussian beams is provided in Appendix C.

6.1.13 Performance of GMMT compared to FDTD

The finite-difference time-domain (FDTD) method is an alternative well-known method of solving Maxwell's equations by time-marching the fields on a 3D grid. FDTD does offer some advantages over GMMT such as resolving the failure of the Rayleigh hypothesis and being able to simulate complex geometries or non-linear materials. However, FDTD is a much slower method: the fields have to be time-stepped until convergence is achieved, the grid spacing has to be small enough to achieved sufficient accuracy, and the Maxwell stress tensor has to be integrated numerically.

Figure 6.1 compares the runtime performance and accuracy of GMMT and FDTD on the same computer for an optical matter array consisting of N particles, where $N = 1, 2, 3, 4, 5, 6, 7$. GMMT is able to calculate one-million time-steps (a roughly 1 second trajectory) in 20 minutes of CPU time. FDTD takes about 700 days to do the same computation. Although FDTD can be parallelized or run on a GPU, it would require significant compute resources to be competitive with GMMT.

Even worse for FDTD, for these spherical sub-wavelength particles it proves to be less accurate

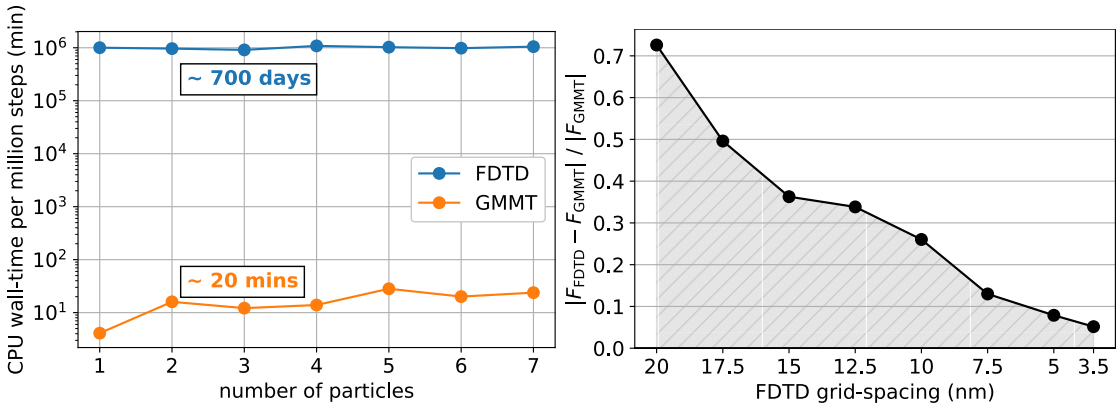

Figure 6.1: Computational performance and accuracy of the generalized multiparticle Mie theory (GMMT) compared to the finite-difference time-domain (FDTD) method. (left) Wall-times for GMMT and FDTD simulation methods for 1 – 7 particles (using a single CPU processor; AMD Ryzen 7 2700X). GMMT is 4 – 5 orders of magnitude faster. (right) Relative error between the forces in FDTD and GMMT for the 7 particle case. As the grid-spacing is lowered in FDTD, the forces converge to the values of F in GMMT, suggesting that GMMT is more accurate than FDTD.

than GMMT. The relative error in the forces on the particles is seen to approach zero as the FDTD grid spacing (Δx) is reduced. Unfortunately for FDTD, the runtime performance scales as $\mathcal{O}(\Delta x^4)$ and obtaining accurate results will take an extraordinarily long time.

For these reasons, GMMT is generally a superior method for simulating optical matter. It should be noted that GMMT is more niche than FDTD, and consequently there are few available codes for running GMMT while there are many available codes (open-source and commercial) for running FDTD. An open-sourced GMMT software, `MiePy`, was developed using the theory covered here and is demonstrated in Appendix 6.C.

6.2 Simulating the time-evolution of optical matter

6.2.1 Independent translational and rotational motion: Langevin dynamics

Langevin dynamics is used to simulate the motion of particles in a fluid at temperature T. There are both frictional forces due to motion in the fluid and Brownian forces due to random thermal kicks from the environment. Consider N particles with mass m_i, moment of inertia tensor $\overleftrightarrow{I}_i$, translational and rotational friction tensors $\overleftrightarrow{\Gamma}_i^t$ and $\overleftrightarrow{\Gamma}_i^r$, and translational and rotational noise tensors $\overleftrightarrow{\alpha}_i^t$ and $\overleftrightarrow{\alpha}_i^r$.

The Langevin equations of motion for translation and rotation is [153, 154]

$$m_i \frac{d\boldsymbol{v}_i(t)}{dt} = -\overset{\leftrightarrow}{\Gamma}^{\mathrm{t}}_i(t)\boldsymbol{v}_i(t) + \overset{\leftrightarrow}{\alpha}^{\mathrm{t}}_i(t)\boldsymbol{\eta}_i(t) + \boldsymbol{F}_i(t) \tag{6.50a}$$

$$\frac{d(\overset{\leftrightarrow}{I}_i(t)\boldsymbol{\omega}_i(t))}{dt} = -\overset{\leftrightarrow}{\Gamma}^{\mathrm{r}}_i(t)\boldsymbol{\omega}_i(t) + \overset{\leftrightarrow}{\alpha}^{\mathrm{r}}_i(t)\boldsymbol{\eta}_i(t) + \boldsymbol{\tau}_i(t) \tag{6.50b}$$

where $\boldsymbol{F}_i$ are other forces acting on particle i, $\boldsymbol{\tau}_i$ are other torques acting on particle i (either external or through particle interactions), and $\boldsymbol{\eta}_i$ is a random vector generated from a normal distribution with mean 0 and variance 1. All of the tensors are time-dependent as they depend on the orientation of the particle (except for spherical particles). The time dependence of any tensor can always be related to the tensor in a fixed reference frame related by the rotation matrix of the particle at time t: $\overset{\leftrightarrow}{\Gamma}(t) = \overset{\leftrightarrow}{R}(t)\overset{\leftrightarrow}{\Gamma}^{0}_i\overset{\leftrightarrow}{R}^{-1}(t)$, where $\overset{\leftrightarrow}{\Gamma}^{0}_i$ is a time-independent tensor. The orientation of particles is, for numerical purposes, best represented by quaternions, $\boldsymbol{q}_i$. [155, 156] The quaternion can be time-evolved by

$$\boldsymbol{q}_i(t+dt) = \left(1 + \frac{dt}{2}\boldsymbol{q}_\omega(t)\right)\boldsymbol{q}_i(t) \tag{6.51}$$

where $\boldsymbol{q}_\omega$ is a quaternion constructed from the angular velocity vector, $\boldsymbol{q}_\omega(t) = [0, \boldsymbol{\omega}_i(t)]$. The rotation matrix at time t can be constructed from the quaternion at time t.

The friction and noise tensors are related to each other by the fluctuation-dissipation theorem. [157] To satisfy the theorem, both rotation and translation tensors must satisfy

$$2k_BT\overset{\leftrightarrow}{\Gamma} = \overset{\leftrightarrow}{\alpha}\overset{\leftrightarrow}{\alpha}^{T} \tag{6.52}$$

This can be achieved by performing a Cholesky decomposition of the left-hand side of Equation (6.52). [158]

For ellipsoidal particles, there are analytic expressions for calculating the friction tensor. [159] For spherical particles, all of the tensor quantities become scalar variables and are no longer

time-dependent due to rotation of the particle

$$m_i \frac{d\boldsymbol{v}_i(t)}{dt} = -\Gamma_i^{\mathrm{t}} \boldsymbol{v}_i(t) + \alpha_i^{\mathrm{t}} \boldsymbol{\eta}_i(t) + \boldsymbol{F}_i(t) \tag{6.53a}$$

$$I_i \frac{d\boldsymbol{\omega}_i(t)}{dt} = -\Gamma_i^{\mathrm{r}} \boldsymbol{\omega}_i(t) + \alpha_i^{\mathrm{r}} \boldsymbol{\eta}_i(t) + \boldsymbol{\tau}_i(t) \tag{6.53b}$$

where $\Gamma_i^t = 6\pi\eta a_i$ and $\Gamma_i^r = 8\pi\eta a_i^3$ are the friction coefficients, η is the viscosity of the medium, and a_i is the radius of particle i. The noise scalars are then given by a trivial solution to Equation (6.52) for translation and rotation, $\alpha_i = \sqrt{2k_B T \Gamma_i}$.

Equation (6.50) and Equation (6.53) are stochastic differential equations (SDE) for the time-evolution of the particle positions. In a software implementation, the evolution depends on the random number generator (RNG) used as well as the seed used to generate random numbers. Solving the SDE a second time with identical parameters but a different seed will yield different results. For this reason, it is often needed to perform an ensemble of $\mathcal{N}$ simulations under identical parameters with different seeds and look at statistical properties of the ensemble (averages, variances, etc.).

Ideally, one would like to construct the probability distribution for the particle positions, $P(\boldsymbol{r}_1, \boldsymbol{r}_2, \ldots, \boldsymbol{r}_N)$. This can only be done approximately with a large enough ensemble $\mathcal{N}$. More-over, it will only sample regions of phase-space that the particles like to be in, while undersampling regions where rare-events or transitions are occurring. For a small number of particles (1 – 2), the Fokker-Plank equation can be solved numerically to obtain the time-evolution of the probability distributions [160, 161], but this approach suffers from the curse of dimensionality and does not scale to many particles. Rare-event sampling methods, such as umbrella sampling, can be used to measure the probability distributions during transitions. [162]

6.2.2 The over-damped limit: Brownian dynamics

The Reynolds number for particles in optical matter, $\mathrm{Re} = \rho v a/\nu$, measures the ratio of inertial to viscous forces, where ρ is the density of the fluid, v is the velocity of the particle, a is the radius of the particle, and ν is the viscosity of the fluid. Taking a maximum particle radius of 150 nm and the terminal velocity for a particle feeling a maximum force of 10 pN in water medium, an upper limit for the Reynolds number in optical matter is approximately 8×10^{-4}. At such low Reynolds numbers,

the inertial terms in the Langevin equation become unimportant and can be neglected, i.e. any acceleration is achieved essentially instantaneously in response to some force. In this *over-damped* limit, the equation of motion becomes

$$\boldsymbol{v}_i(t) = \overset{\leftrightarrow}{\mathcal{M}}{}^{\mathrm{t}}_i(t) \left[\overset{\leftrightarrow}{\alpha}{}^{\mathrm{t}}_i(t)\boldsymbol{\eta}_i(t) + \boldsymbol{F}_i(t)\right] \tag{6.54a}$$

$$\boldsymbol{\omega}_i(t) = \overset{\leftrightarrow}{\mathcal{M}}{}^{\mathrm{r}}_i(t) \left[\overset{\leftrightarrow}{\alpha}{}^{\mathrm{r}}_i(t)\boldsymbol{\eta}_i(t) + \boldsymbol{\tau}_i(t)\right] \tag{6.54b}$$

where $\mathcal{M} = \Gamma^{-1}$ is the mobility tensor, defined as the inverse of the friction tensor. For spherical particles, the mobility tensor becomes a scalar

$$\boldsymbol{v}_i(t) = \mathcal{M}^{\mathrm{t}}_i \left[\alpha^{\mathrm{t}}_i\boldsymbol{\eta}_i(t) + \boldsymbol{F}_i(t)\right] \tag{6.55a}$$

$$\boldsymbol{\omega}_i(t) = \mathcal{M}^{\mathrm{r}}_i \left[\alpha^{\mathrm{r}}_i\boldsymbol{\eta}_i(t) + \boldsymbol{\tau}_i(t)\right] \tag{6.55b}$$

Another fluid dynamics number of interest in driven thermal systems is the Péclet number. The Péclet number measures the ratio of deterministic drift to diffusion and is defined as $\mathrm{Pe} = Fa/k_BT$, where F is a characteristic magnitude of the forces on the particle. For a particle of radius 75 nm and a characteristic force of 1 pN in a fluid at 300 K, the Péclet number is approximately 18. Thus, for forces on the order of 1 pN, optical matter can be dominated by deterministic forces rather than diffusion.

6.2.3 Hydrodynamic translational and rotational coupling: Stokesian dynamics

The Langevin and Brownian dynamics equations assume that the fluid is still (its velocity field vanishes). Since particle motion causes the fluid to move in response, these equations are only truly valid for one particle in an open fluid. Stokesain dynamics is an extension of Langevin and Brownian dynamics that takes into account the hydrodynamic coupling interactions due to fluid flow. [95] The translational motion of the particle leads to a translation flow of the surrounding fluid and the rotation of the particle leads to vorticity in the surrounding fluid. The fluid flow can exert a hydrodynamic force and torque on a particle. There are then four types of coupling: TT, TR, RT,

and RR for each type of translational and rotational coupling. [163] The equation of motion is

$$\begin{pmatrix} \boldsymbol{\mathcal{V}} \\ \boldsymbol{\Omega} \end{pmatrix} = \begin{pmatrix} \mathcal{M}^{tt} & \mathcal{M}^{tr} \\ \mathcal{M}^{rt} & \mathcal{M}^{rr} \end{pmatrix} \left[\begin{pmatrix} \boldsymbol{\mathcal{F}} \\ \boldsymbol{\mathcal{T}} \end{pmatrix} + \begin{pmatrix} \mathcal{H}^{tt} & \mathcal{H}^{tr} \\ \mathcal{H}^{rt} & \mathcal{H}^{rr} \end{pmatrix} \begin{pmatrix} \boldsymbol{\mathcal{N}} \\ \boldsymbol{\mathcal{N}} \end{pmatrix} \right] \tag{6.56}$$

Here, $\boldsymbol{\mathcal{V}} = (\boldsymbol{v}_1, \ldots, \boldsymbol{v}_N)$ is the generalized velocity vector of the N particles and $\boldsymbol{\Omega} = (\boldsymbol{\omega}_1, \ldots, \boldsymbol{\omega}_N)$ is the generalized angular velocity vector. Similarly, $\boldsymbol{\mathcal{F}} = (\boldsymbol{F}_1, \ldots, \boldsymbol{F}_N)$ is the generalized force vector and $\boldsymbol{\mathcal{T}} = (\boldsymbol{\tau}_1, \ldots, \boldsymbol{\tau}_N)$ is the generalized torque vector. The $\mathcal{M}$ matrix is referred to as the *grand mobility matrix*. The grand mobility matrix couples every degree of freedom of the system into every other degree of freedom. The matrix elements are configuration dependent and are given in the Rotne-Prager approximation [164]

$$\mathcal{M}^{tt}_{ii} = \frac{1}{6\pi\eta a_i} \overleftrightarrow{I} + \mathcal{O}(r_{ij}^{-6}) \tag{6.57a}$$

$$\mathcal{M}^{rr}_{ii} = \frac{1}{8\pi\eta a_i^3} \overleftrightarrow{I} + \mathcal{O}(r_{ij}^{-6}) \tag{6.57b}$$

$$\mathcal{M}^{tt}_{ij} = \mathcal{M}^{tt}_{ji} = \frac{1}{8\pi\eta r_{ij}} \left(\overleftrightarrow{I} + \boldsymbol{r}_{ij} \otimes \boldsymbol{r}_{ij} \right) + \mathcal{O}(r_{ij}^{-3}) \tag{6.57c}$$

$$\mathcal{M}^{rr}_{ij} = \mathcal{M}^{rr}_{ji} = \frac{1}{16\pi\eta r_{ij}^3} \left(\boldsymbol{r}_{ij} \otimes \boldsymbol{r}_{ij} - \overleftrightarrow{I} \right) + \mathcal{O}(r_{ij}^{-9}) \tag{6.57d}$$

$$\mathcal{M}^{rt}_{ij} = \mathcal{M}^{rt}_{ji} = -\mathcal{M}^{tr}_{ij} = -\mathcal{M}^{tr}_{ji} = -\frac{1}{8\pi\eta r_{ij}^2} \overleftrightarrow{\varepsilon} \boldsymbol{r}_{ij} + \mathcal{O}(r_{ij}^{-8}) \tag{6.57e}$$

$$\mathcal{M}^{rt}_{ii} = \mathcal{M}^{tr}_{ii} = 0 + \mathcal{O}(r_{ij}^{-7}) \tag{6.57f}$$

where $\boldsymbol{r}_{ij}$ is the vector between particle i and particle j, $\overleftrightarrow{I}$ is the identity matrix, and $\overleftrightarrow{\varepsilon}$ is the Levi-Civita symbol and the sum occurs over its last index.

The second term in Equation (6.56) is the correlated random noise in the hydrodynamically coupled system. The $\mathcal{H}$ matrix is again given by a Cholesky decomposition of $\mathcal{M}$ such that $2k_BT\mathcal{M}^{-1} = \mathcal{H}\mathcal{H}^T$. The $\mathcal{N}$ generalized vector is simply uncorrelated normal variables with mean 0 and variance 1.

Stokesian dynamics can be extended to the case of particles near a no-slip interface. [117] The

"self-mobility" matrix for a particle interacting with itself through the interface is

$$M_{ii}^{tt} = -\frac{9h^{-1} - 2h^{-3} + h^{-5}}{16\pi\eta} \begin{pmatrix} 1 & 0 & 0 \\ 0 & 1 & 0 \\ 0 & 0 & 0 \end{pmatrix} - \frac{9h^{-1} - 4h^{-3} + h^{-5}}{8\pi\eta} \begin{pmatrix} 0 & 0 & 0 \\ 0 & 0 & 0 \\ 0 & 0 & 1 \end{pmatrix} \tag{6.58a}$$

$$M_{ii}^{rr} = -\frac{15}{64\pi\eta h^3} \begin{pmatrix} 1 & 0 & 0 \\ 0 & 1 & 0 \\ 0 & 0 & 0 \end{pmatrix} - \frac{3}{32\pi\eta h^3} \begin{pmatrix} 0 & 0 & 0 \\ 0 & 0 & 0 \\ 0 & 0 & 1 \end{pmatrix} \tag{6.58b}$$

$$M_{ii}^{tr} = -M_{ii}^{rt} = -\frac{3}{32\pi\eta h^4} \begin{pmatrix} 0 & -1 & 0 \\ 1 & 0 & 0 \\ 0 & 0 & 0 \end{pmatrix} \tag{6.58c}$$

where $h = z_i/a_i$ is the distance between the interface and the particle normalized by the particle's radius. The pair-wise hydrodynamic interactions through the interface are reported elsewhere. [117] Stokesian dynamics can also be extended to include near-field lubrication hydrodynamic interactions. [95, 165]

6.2.4 Additional interactions

Given the forces and torques acting on N particles, optical matter can be simulated using the BD, LD, or SD methods as described above. The electrodynamic forces and torques acting on every particle are calculated in GMMT using Equation (6.43) and Equation (6.44). In addition to the electrodynamic and hydrodynamic interactions there are three other interactions to consider: double-layer electrostatics, Van der Walls interactions, and hard-sphere collisions. For each of these interactions, there are also particle-wall type interactions.

The double-layer electrostatic interaction potential energy between two spheres is [166]

$$V(r_{ij}) = 32\pi\varepsilon_0\varepsilon_b \left(\frac{k_B T}{z_p e}\right)^2 \tanh\left(\frac{z_p \psi_i e}{4k_B T}\right) \tanh\left(\frac{z_p \psi_j e}{4k_B T}\right) \exp\left[-\kappa(r_{ij} - a_i - a_j)\right] \tag{6.59}$$

where e is the elementary charge, κ is the inverse Debye length, z_p is the ion valency, and ψ_i is the

Variable	Description	Value
μ	Fluid viscosity	8×10^{-4} Pa · s
T	Temperature of the bath	300 K
k_n	Hard-sphere collision parameter	5
ψ_i	Electrostatic potential (sphere)	−77 mV
ψ_s	Electrostatic potential (interface)	−35 mV
z_p	Electron ion valency	1
κ^{-1}	Debye length	27 nm
ε_m	Medium permittivity	80.4

Table 6.2: List of variables present in optical matter interactions and reasonable values for them.

surface potential of the spheres. For a sphere interacting with an interface, the potential energy is

$$V(d) = 16\pi\varepsilon_0\varepsilon_b \left(\frac{k_B T}{z_p e}\right)^2 \tanh\left(\frac{z_p \psi_i e}{4k_B T}\right) \tanh\left(\frac{z_p \psi_s e}{4k_B T}\right) \exp(-\kappa d) \tag{6.60}$$

where ψ_s is the surface potential of the interface.

For spherical particles that begin to overlap, a hard-sphere collision repulsive potential is used [167]

$$V(r_{ij}) = -\frac{2}{5} k_n (r_{ij} - a_i - a_j)^{5/2} \tag{6.61}$$

The same equation can be used for the overlap between a sphere and the interface.

The Van der Walls interactions is a short-range attraction force. The equations for this interaction are provided elsewhere. [41]

Table 6.2 lists the variables in these interactions and reasonable values to set them to in order to simulate optical matter.

6.A T-matrix evaluation

The T-matrix can be numerically evaluated using the so-called extended boundary condition method (EBCM). [76, 168, 169] In this method, the expansion coefficients are related to one another by the equivalence principle

$$\begin{aligned} p_\alpha^{\text{inc}} &= iQ_{\alpha\beta}^{31} p_\beta^{\text{int}} \\ p_\alpha^{\text{scat}} &= -iQ_{\alpha\beta}^{11} p_\beta^{\text{int}} \end{aligned} \tag{6.62}$$

where the Q matrices are given by integrals of the VSHW functions over the particle's surface

$$Q^{pq}_{\alpha\beta} = -f^{(p)}\frac{ik_m^2}{\pi}\left[\int_S (d\boldsymbol{S}\times\boldsymbol{N}^{(q)}_{\beta}(k\boldsymbol{r}))\cdot\boldsymbol{N}^{(p)}_{\hat{\alpha}}(k_m\boldsymbol{r}) + \sqrt{\frac{\varepsilon}{\varepsilon_m}}\int_S (d\boldsymbol{S}\times\boldsymbol{N}^{(q)}_{\hat{\beta}}(k\boldsymbol{r}))\cdot\boldsymbol{N}^{(p)}_{\alpha}(k_m\boldsymbol{r})\right] \tag{6.63}$$

where $f^{(p)}$ is defined in eq. (6.15) and the index notation $\hat{\alpha}$ means to swap electric and magnetic mode indices, i.e. if $\alpha = (m,n,r)$, then $\hat{\alpha} = (m,n,3-r)$. The T-matrices are then determined

$$\mathcal{T}_{\alpha\beta} = -Q^{11}_{\alpha\gamma}\left[Q^{31}_{\gamma\beta}\right]^{-1} \tag{6.64}$$

$$\mathcal{T}^{\text{int}}_{\alpha\beta} = -i\left[Q^{31}_{\alpha\beta}\right]^{-1} \tag{6.65}$$

A software implementation for calculating the T-matrix of particles using the null-field method with discrete sources (NFM-DS) is freely available. [170]

6.B Other conventions

A different convention for the field expansions used in other work [151] is presented here. These field expansions were used to evaluate analytic expressions for the force and torque.

Electric field

$$\begin{aligned}\boldsymbol{E}^j_{\text{inc}} = \sum_{n=1}^{N_{\max}}\sum_{m=-n}^{n}\Bigg\{&\hat{\boldsymbol{r}}\frac{1}{r^2}\left[n(n+1)p^j_{mn}\psi_n(kr)Y_{nm}(\theta,\phi)\right]\\ &+\hat{\boldsymbol{\theta}}\frac{k}{r}\left[p^j_{mn}\psi_n'(kr)\frac{\partial}{\partial\theta}Y_{nm}(\theta,\phi) - \frac{m}{\sqrt{\varepsilon_b}}q^j_{mn}\psi_n(kr)\frac{Y_{nm}(\theta,\phi)}{\sin\theta}\right]\\ &+\hat{\boldsymbol{\phi}}\frac{k}{r}\left[imp^j_{mn}\psi_n'(kr)\frac{Y_{nm}(\theta,\phi)}{\sin\theta} - \frac{i}{\sqrt{\varepsilon_b}}q^j_{mn}\psi_n(kr)\frac{\partial}{\partial\theta}Y_{nm}(\theta,\phi)\right]\Bigg\}\end{aligned} \tag{6.66a}$$

$$\begin{aligned}\boldsymbol{E}^j_{\text{scat}} = \sum_{n=1}^{N_{\max}}\sum_{m=-n}^{n}\Bigg\{&\hat{\boldsymbol{r}}\frac{1}{r^2}\left[n(n+1)a^j_{mn}\xi^{(1)}_n(kr)Y_{nm}(\theta,\phi)\right]\\ &+\hat{\boldsymbol{\theta}}\frac{k}{r}\left[a^j_{mn}\xi^{(1)\prime}_n(kr)\frac{\partial}{\partial\theta}Y_{nm}(\theta,\phi) - \frac{m}{\sqrt{\varepsilon_b}}b^j_{mn}\xi^{(1)}_n(kr)\frac{Y_{nm}(\theta,\phi)}{\sin\theta}\right]\\ &+\hat{\boldsymbol{\phi}}\frac{k}{r}\left[ima^j_{mn}\xi^{(1)\prime}_n(kr)\frac{Y_{nm}(\theta,\phi)}{\sin\theta} - \frac{i}{\sqrt{\varepsilon_b}}b^j_{mn}\xi^{(1)}_n(kr)\frac{\partial}{\partial\theta}Y_{nm}(\theta,\phi)\right]\Bigg\}\end{aligned} \tag{6.66b}$$

Magnetic field

$$\begin{aligned}\boldsymbol{H}^j_{\text{inc}} = \sum_{n=1}^{N_{\max}} \sum_{m=-n}^{n} \Bigg\{ & \hat{\boldsymbol{r}} \frac{1}{r^2} \left[n(n+1) q^j_{mn} \psi_n(kr) Y_{nm}(\theta,\phi) \right] \\ & + \hat{\boldsymbol{\theta}} \frac{k}{r} \left[q^j_{mn} \psi'_n(kr) \frac{\partial}{\partial\theta} Y_{nm}(\theta,\phi) + m\sqrt{\varepsilon_b} p^j_{mn} \psi_n(kr) \frac{Y_{nm}(\theta,\phi)}{\sin\theta} \right] \\ & + \hat{\boldsymbol{\phi}} \frac{k}{r} \left[im q^j_{mn} \psi'_n(kr) \frac{Y_{nm}(\theta,\phi)}{\sin\theta} + i\sqrt{\varepsilon_b} p^j_{mn} \psi_n(kr) \frac{\partial}{\partial\theta} Y_{nm}(\theta,\phi) \right] \Bigg\}\end{aligned} \tag{6.67a}$$

$$\begin{aligned}\boldsymbol{H}^j_{\text{scat}} = \sum_{n=1}^{N_{\max}} \sum_{m=-n}^{n} \Bigg\{ & \hat{\boldsymbol{r}} \frac{1}{r^2} \left[n(n+1) b^j_{mn} \xi^{(1)}_n(kr) Y_{nm}(\theta,\phi) \right] \\ & + \hat{\boldsymbol{\theta}} \frac{k}{r} \left[n^j_{mn} \xi^{(1)\prime}(kr) \frac{\partial}{\partial\theta} Y_{nm}(\theta,\phi) + m\sqrt{\varepsilon_b} a^j_{mn} \xi^{(1)}_n(kr) \frac{Y_{nm}(\theta,\phi)}{\sin\theta} \right] \\ & + \hat{\boldsymbol{\phi}} \frac{k}{r} \left[im b^j_{mn} \xi^{(1)\prime}_n(kr) \frac{Y_{nm}(\theta,\phi)}{\sin\theta} + i\sqrt{\varepsilon_b} a^j_{mn} \xi^{(1)}_n(kr) \frac{\partial}{\partial\theta} Y_{nm}(\theta,\phi) \right] \Bigg\}\end{aligned} \tag{6.67b}$$

where $\xi^{(1)}_n = \psi_n - i\chi_n$, ψ_n, χ_n are the Riccati-Bessel function of the first and second kind, and Y_{nm} are the spherical harmonics

$$\begin{aligned}\psi_n(x) &= x j_n(x) \\ \chi_n(x) &= -x y_n(x) \\ \xi^{(1)}_n(x) &= x[j_n(x) + i y_n(x)] = x h^{(1)}_n(x) \\ Y_{nm}(\theta,\phi) &= \sqrt{\frac{2n+1}{4\pi} \frac{(n-m)!}{(n+m)!}} P^m_n(\cos\theta) e^{im\phi}\end{aligned} \tag{6.68}$$

Denoting the coefficients of our convention $\bar{a}_n$, $\bar{b}_n$, $\bar{p}_{mn}$, $\bar{q}_{mn}$, $\bar{a}_{mn}$, $\bar{b}_{mn}$, the two conventions are

related by

$$\begin{aligned}
\bar{a}_n &= -a_n \\
\bar{b}_n &= -b_n \\
\bar{p}_{mn} &= \frac{k^2}{i^{n-1}}\sqrt{\frac{n(n+1)}{4\pi}}p_{mn} \\
\bar{q}_{mn} &= -\frac{k^2}{i^n}\sqrt{\frac{\mu_b}{\varepsilon_b}\frac{n(n+1)}{4\pi}}q_{mn} \\
\bar{a}_{mn} &= -\frac{k^2}{i^{n-1}}\sqrt{\frac{n(n+1)}{4\pi}}a_{mn} \\
\bar{b}_{mn} &= \frac{k^2}{i^n}\sqrt{\frac{\mu_b}{\varepsilon_b}\frac{n(n+1)}{4\pi}}b_{mn}
\end{aligned} \tag{6.69}$$

Another convention uses a different value for the E_{mn} normalization values [74]

$$E_{mn} = |E_0| i^n \frac{2n+1}{n(n+1)} \tag{6.70}$$

where $|E_0|$ is the amplitude of the source field. We have chosen to absorb this amplitude into the a, b, p, and q coefficients.

6.C `MiePy`: a GMMT Python library

`MiePy` is a software package that solves the GMMT for a cluster of particles illuminated by an arbitrary source. [139] `Stoked` is a software package that solves the BD, LD, and SD SDEs and allows arbitrary interactions between particles such as those computed by GMMT. [140] Below are example scripts for how to use these software packages and simulate optical matter systems.

`MiePy` script to calculate cross-sections, forces, and torques

```
import miepy
nm = 1e-9

# define materials and source
Ag = miepy.materials.Ag()
medium = miepy.materials.water()
source = miepy.sources.plane_wave(polarization=[1,0])

# build an Ag dimer with radii 75nm separated by 600nm in the x-direction
dimer = miepy.sphere_cluster(position=[[300*nm,0,0], [-300*nm,0,0]],
```

```
                                radius=75*nm,
                                material=Ag,
                                source=source,
                                wavelength=800*nm,
                                medium=water,
                                lmax=2)

    # obtain the cross-sections
    scat, absorb, extinct = dimer.cross_sections()

    # obtain the force and torque on the right particle
    F = dimer.force_on_particle(0)
    T = dimer.torque_on_particle(0)
```

MiePy and Stoked script to simulate the dynamics of an optically trapped dimer

```
    import miepy
    import stoked
    nm = 1e-9
    us = 1e-6

    # define materials and source
    Ag = miepy.materials.Ag()
    medium = miepy.materials.water()

    # a 50 mW, RHC-polarized Gaussian beam
    source = miepy.sources.gaussian_beam(width=1500*nm, polarization=[1,1j], power=.05)

    # build an Ag dimer with radii 75nm separated by 600nm in the x-direction
    dimer = miepy.sphere_cluster(position=[[300*nm,0,0], [-300*nm,0,0]],
                                radius=75*nm,
                                material=Ag,
                                source=source,
                                wavelength=800*nm,
                                medium=water,
                                lmax=2)

    class electrodynamics(stoked.interactions):
        """electrodynamic interactions using MiePy"""
        def __init__(self, cluster):
            self.cluster = cluster

        def update(self):
            pos = np.copy(self.position)
            self.cluster.update_position(pos)

        def force(self):
            return self.cluster.force()

        def torque(self):
            return self.cluster.torque()

    # include sphere collisions, double layer repulsive electostatics, and electrodynamics
    interactions=[stoked.collisions_sphere(radius=radius, kn=5),
                  stoked.double_layer_sphere(radius=75*nm, potential=-77e-3, temperature=300),
                  electrodynamics(dimer)]
```

```
41
42      # create a stokesian dynamics simulation
43      sd = stoked.stokesian_dynamics(position=dimer.position,
44                                     drag=stoked.drag_sphere(radius=75*nm, viscosity=8e-4),
45                                     interactions=interactions,
46                                     temperature=300,
47                                     dt=5*us)
48
49      # run for 10,000 steps and obtain the trajectory
50      trajectory = sd.run(Nsteps=10000)
```

APPENDIX A
OPTICAL TRAPPING OF ANISOTROPIC PARTICLES

In this Appendix, two experiments involving anisotropic particles are considered. In Appendix A.1 the spinning of anisotropic spheroids in a circularly polarized trap is measuried in experiment using a quadrant photodioide (QPD) and compared to simulation. In Appendix A.2 the scattering and multipolar modes of a large, thin gold nanoplate are analyzed in simulation. These nanoplates are capable of near-field optical binding interactions that have been realized in optical line traps in experiment. [171]

A.1 Spinning of spheroidal nanoparticles in circularly polarized beams

Consider a spheroidal NP of volume V and aspect ratio $\delta = a/b$, where a and b are the spheroid's major and minor radii. We define the 'equivalent radius' of the spheroid as $r_0 = (3V/4\pi)^{1/3}$, so that $a = \delta^{1/3} r_0$ and $b = r_0/\delta^{2/3}$. Two important overdamped rotational dynamical quantities are the spheroid's average angular velocity, $\overline{\omega_z(t)}$, and the rotational diffusion coefficient D_r, given by

$$\overline{\omega_z(t)} = \frac{\tau_z}{\gamma} \tag{A.1}$$

$$D_r = \frac{1}{2t}\overline{(\omega_z(t) - \overline{\omega_z(t)}t)^2} = \frac{kT}{\gamma} \tag{A.2}$$

where T is the temperature, τ_z is the external torque from the beam trap, and γ is the rotational drag coefficient.

For small particles, the torque acting on the spheroid due to a circularly polarized Gaussian beam is approximately [172, 173]

$$\tau_z = \frac{2P}{\pi w_0^2}\left[\alpha V + \beta V^{2/3}(\delta - 1)^2\right] \tag{A.3}$$

where P is the laser power, w_0 is the beam width, and α and β are constants intrinsic to the spheroid's material. The first term in Equation (A.3) is a torque due to the absorption of circularly polarized photons; the second term is a torque due to asymmetric scattering of photons due to the

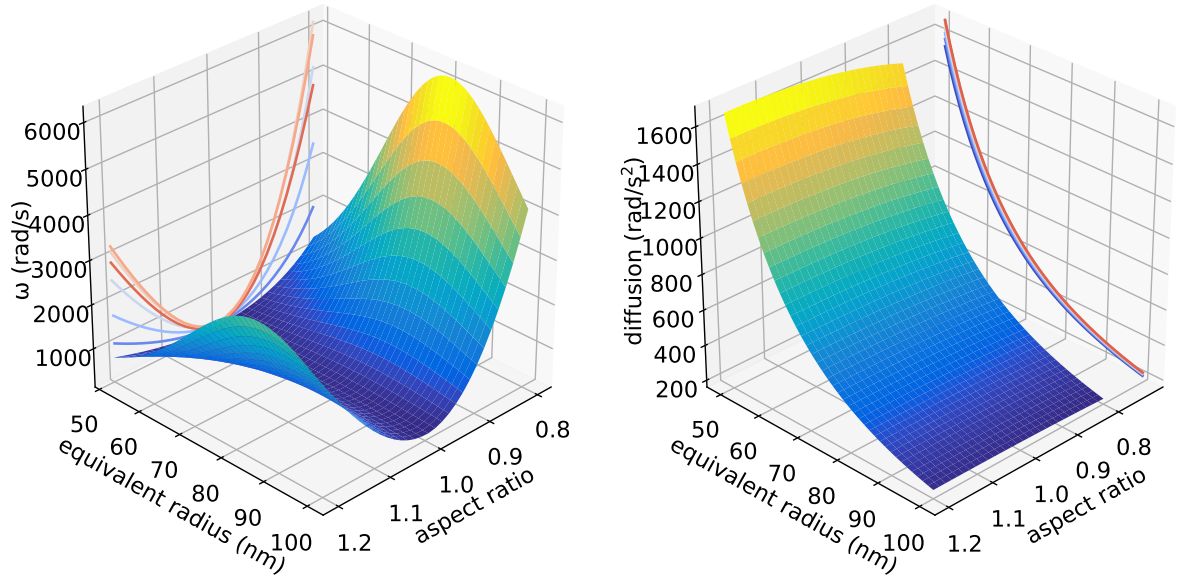

Figure A.1: Rotational spinning and diffusion of a spheroidal silver nanoparticle. (left) Calculated angular velocity of an Ag nanoparticle in circularly polarized Gaussian beam ($w_0 = 1200\,\text{nm}$, $P = 28mW$) at variable equivalent radius and aspect ratio. (right) Calculated rotational diffusion coefficient under the same parameters.

anisotropy of the particle. For silver at $\lambda = 800\,\text{nm}$,

$$\alpha = 1.61 \times 10^{-10}\,\text{N/m}^2 \tag{A.4}$$

$$\beta = 4.01 \times 10^{-14}\,\text{N/m} \tag{A.5}$$

In terms of the equivalent radius r_0, the torque is

$$\tau_z = \frac{8P}{3w_0^2}\left[\alpha r_0^3 + \beta r_0^2(\delta - 1)^2\right] \tag{A.6}$$

The rotational drag coefficient of the spheroid is approximately [159]

$$\gamma \approx \frac{16}{5}\pi r_0^3 \mu \left(\delta + \frac{3}{2}\delta^{-1}\right) \approx 8\pi r_0^3 \mu \tag{A.7}$$

The final expressions for the angular velocity and rotational diffusion are

$$\overline{\omega_z(t)} = \frac{P}{3\pi w_0^2 \mu}\left[\alpha + \frac{\beta}{r_0}(\delta - 1)^2\right] \tag{A.8}$$

$$D_r = \frac{kT}{8\pi r_0^3 \mu} \tag{A.9}$$

Note that the rotational diffusion in Equation (A.8) is mostly independent of the aspect ratio. These equations can be inverted to obtain r_0 and δ,

$$r_0 = \left(\frac{5kT}{16\pi\mu D_r}\right)^{1/3} \tag{A.10}$$

$$\delta = 1 + \sqrt{\frac{r_0}{\beta}\left(\frac{3\pi w_0^2 \mu}{5P}\overline{\omega_z} - \alpha\right)} \tag{A.11}$$

Thus, if the angular velocity and rotational diffusion of a particle can be measured in experiment, estimates can be made for the size and aspect ratio of the particles. The exact dependence of angular velocity and rotational diffusion on particle size and aspect ratio is calculated in Figure A.1. The numerical calculation is done using the T-matrix theory, where the T-matrix is evaluating using the null-field method with discrete sources. [174]

In experiment, the spinning of nanoparticles can be measured using a quadrant photodioide (QPD). [175, 176] Because these small particles emit dipoles and weak but significant quadrupoles, the QPD will collect light into 4 quadrants with differing intensity depending upon the orientation of the particle. By measuring the frequency of intensity oscillations in each quadrant of the QPD, the angular velocity of the particle can be measured. By looking at fluctuations in the spinning velocity, the rotational diffusion coefficient can also be constructed. Yuval Yifat performed experiments and simulations to measure the response of a QPD to a spinning spheroidal nanoparticle by measuring the power spectral density (PSD), see Figure A.2(a). [177] The simulated QPD measured a frequency of rotation that agreed well with the torque acting on the particle in the theory, see Figure A.2.

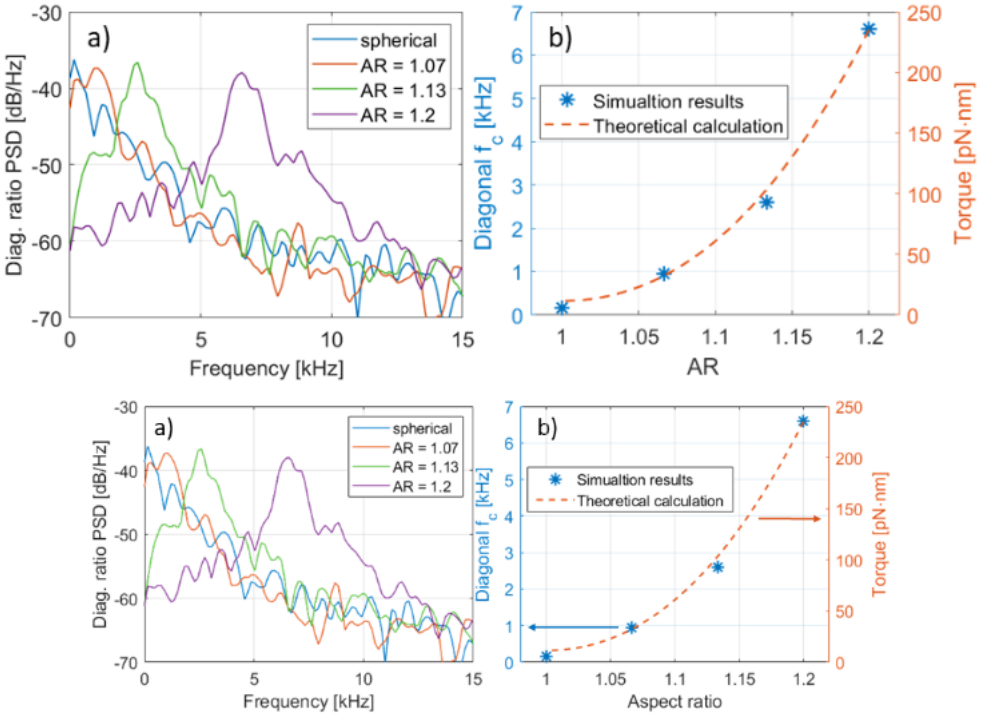

Figure A.2: Calculated and simulated dependence of the spinning frequency of a spheroidal NP on its AR. (a) Simulated PSDs of the diagonal QPD ratios of prolate Ag nanoparticles with a fixed volume and an effective radius of 75 nm. We simulated the dynamics of the NPs and used the resultant trajectories to simulate the effective QPD response. (b) Fitted peaks of the PSD of the diagonal ratio (blue stars) and torque acting on a prolate Ag nanoparticle with varying aspect ratios.

A.2 Dynamics of large nano-plate arrays in a line trap

The optical binding of large, thin gold nanoplates in an optical line trap was experimentally studied by Delphine Coursault. [171] The diameter of these nanoplates are approximately 700 nm while the thickness is only 20 nm. Despite their large diameter, the nanoplates are seen to form ordered arrays and bind optically, similar to the case of much smaller spherical particles. However, the coupling between these plates is very different from that of small spheres and involves near-field interactions. [178, 179]

A multipolar analysis of the nanoplates was performed to reveal the modes in these gold nanoplates. The results are shown in Figure A.3. At $\lambda = 800\,\text{nm}$, the most significant modes are an electric dipole, magnetic quadrupole, and electric octupole. The presence of these higher order modes will alter their optical binding interactions. [180]

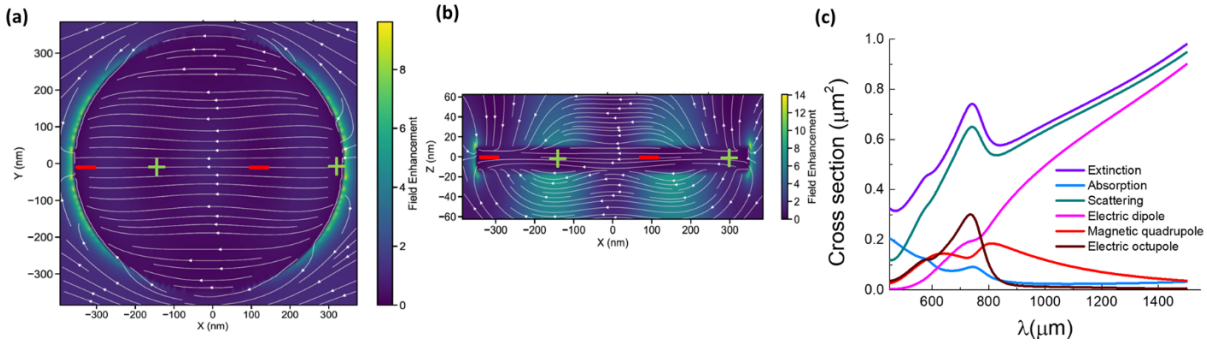

Figure A.3: FDTD simulations of a Au NPL (assumed to be a disk of 700 nm in diameter and 25 nm in height) in a medium with n= 1.33 for water.(a, b) Map of the electric field enhancement at = 800 nm (vacuum) for incident light propagating along the z direction and polarized along the x axis; field enhancement and field lines (a) in the XY plane, parallel to the plate, and (b) in the XZ plane perpendicular to the NPL. (c) Total extinction, absorption, and scattering cross-sections with modal decomposition of the scattering cross-section

APPENDIX B
POINT DIPOLE APPROXIMATION AND SIMULATING A MICROSCOPE

B.1 Point dipole approximation

The point dipole approximation (PDA) approximates a finite-volume scatterer as a singular point (Rayleigh approximation). These dipoles can then be coupled into each other in a matrix-interaction equation. [65] While the PDA is fast, it can often be quantitatively inaccurate. For example, particles of radius 75 nm illuminated by $\lambda = 800\,\text{nm}$ can have widely different forces in GMMT compared to PDA, suggesting that finite-volume effects are still relevant at this length-scale. The PDA is mostly useful to gain qualitative insights as it can often provide analytic expressions for the forces on particles.

In PDA, a particle of radius a is approximated by an electric polarizability [83]

$$\alpha(\omega) = \frac{\alpha_0(\omega)}{1 - \frac{ik^3\alpha_0(\omega)}{6\pi\varepsilon\varepsilon_0} - \frac{ik^2\alpha_0(\omega)}{6\pi\varepsilon\varepsilon_0 a}} \tag{B.1}$$

where $k = n_b\omega/c$ and the static polarizability of the particle is

$$\alpha_0(\omega) = 4\pi\varepsilon_0\varepsilon(\omega)a^3\frac{\varepsilon(\omega) - \varepsilon_0}{\varepsilon(\omega) + 2\varepsilon_0} \tag{B.2}$$

Equation (B.1) includes both a dynamic depolarization and radiation damping correction term to the static polarizability.

The field produced by a dipole at another particle is given by

$$\boldsymbol{E}(\boldsymbol{r}_2) = \boldsymbol{E}^{\text{inc}}(\boldsymbol{r}_2) + \alpha\overleftrightarrow{G}(\boldsymbol{r}_2, \boldsymbol{r}_1)\boldsymbol{E}^{\text{inc}}(\boldsymbol{r}_1) \tag{B.3}$$

where $\overleftrightarrow{G}$ is the dyadic Green's function

$$\overleftrightarrow{G}(\boldsymbol{r}_2, \boldsymbol{r}_1) = \frac{\exp(ikr_{12})}{4\pi\varepsilon_0\varepsilon_b r_{12}^3}\left[(3 - 3ikr_{12} - k^2r_{12}^2)\frac{\boldsymbol{r}_{12}\otimes\boldsymbol{r}_{12}}{r_{12}^2} + (k^2r_{12}^2 + 1kr_{12} - 1)\overleftrightarrow{I}\right] \tag{B.4}$$

where $\boldsymbol{r}_{12}$ is the vector pointing from particle 1 to particle 2. Given these propagators, the interaction

equations between N dipoles is

$$\boldsymbol{E}(\boldsymbol{r}_i) = \boldsymbol{E}^{\text{inc}}(\boldsymbol{r}_i) + \alpha_i \overleftrightarrow{G}(\boldsymbol{r}_i, \boldsymbol{r}_j)\boldsymbol{E}(\boldsymbol{r}_j) \tag{B.5}$$

The solution to the interaction equations yields the field at every particle

$$\boldsymbol{E} = \left[\overleftrightarrow{I} - \alpha\overleftrightarrow{G}\right]^{-1} \boldsymbol{E}^{\text{inc}} \tag{B.6}$$

where $\overleftrightarrow{G}$ is a grand Green's function where sub-blocks are filled with the dyadic Green's function for all particle pairs.

Once the fields are solved for at every particle, the forces and torques acting on the particles are determined by

$$\langle \boldsymbol{F} \rangle = \frac{1}{2}\text{Re}\left\{\alpha \boldsymbol{E} \cdot \boldsymbol{\nabla} \boldsymbol{E}\right\} \tag{B.7}$$

$$\langle \boldsymbol{\tau} \rangle = \frac{1}{2}\text{Re}\left\{(\alpha \boldsymbol{E})^* \times (\alpha_0^{-1}\alpha \boldsymbol{E})\right\} \tag{B.8}$$

The field gradients in the force equation can be determined numerically by using Equation (B.3) summed over all other particles.

The interaction equations in the PDA resemble those determined in the generalize multiparticle Mie theory. The VSHW translation coefficients are replaced by coefficients of the dyadic Green's function and the Mie coefficients are replaced by the electric polarizability of the particles. Again, in the PDA finite-volume effects are not accounted for. Magnetic modes and quadrupolar or higher order modes are also not accounted for, although the PDA theory can be extended to includes these multipoles. For anisotropic particles, the polarizability scalar can be upgraded to a polarizability tensor.

B.2 Imaging clusters using a simulated microscope

In experiment, optical matter is visualized using optical microscopy. This method of visualization can be simulated by taking the scattered (reflected) light from optical matter arrays, propagate them to a far-field hemisphere, and use a lens function to refocus and collect images of the array. Consider

an optical setup that consists of an objective lens (focal length f_1, medium n_1) and an imaging lens (focal length f_2, medium n_2). The objective lens is used to focus the incident light, and also used to turn the scattered light into a collimated beam. The collimated beam is then focused onto a camera with the second lens. Given the scattered far-fields $\boldsymbol{E}^{\infty}(\theta,\phi)$, the field at the image plane is [67]

$$\begin{aligned}\boldsymbol{E}^{\text{img}}(\rho,\varphi,z) = A\int_0^{\theta_{\max}}\int_0^{2\pi}\boldsymbol{E}^{\infty}(\theta,\phi)\exp\left[ik\frac{f_1}{f_2}\rho\sin(\theta)\cos(\phi-\varphi)\right] \\ \times\exp\left[\frac{1}{2}kz\left(\frac{f_1}{f_2}\right)^2\sin^2\theta\right]\sin(\theta)\sqrt{\cos(\theta)}d\phi d\theta\end{aligned} \tag{B.9}$$

where the factor A is

$$A = \frac{ikf_2\exp(-ik(f_2+z))}{2\pi}\sqrt{\frac{n_1}{n_2}}\left(\frac{f_1}{f_2}\right)^2 \tag{B.10}$$

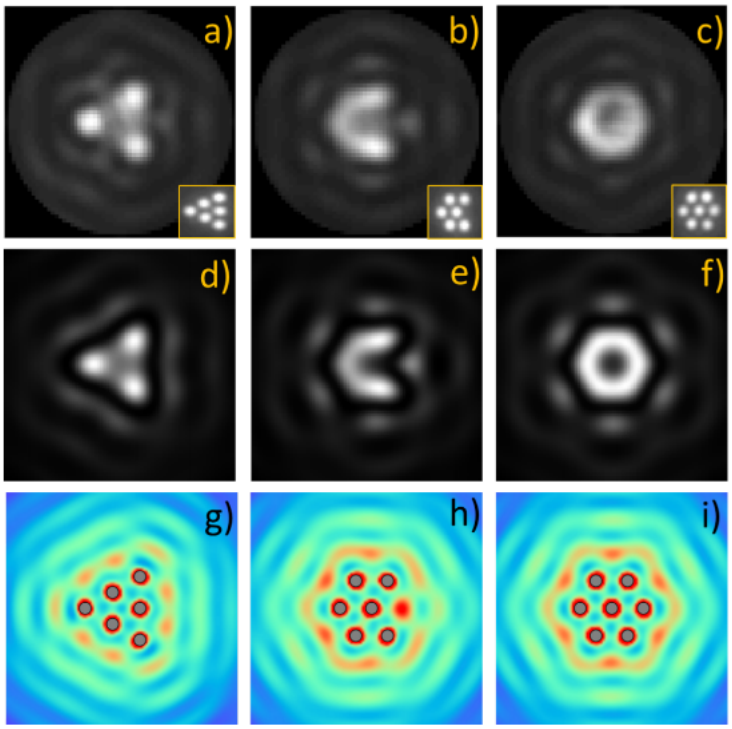

Figure B.1: Emergence of a collective scattering mode in nanoparticle arrays. (a-c) Experimental coherent (backscattered) images of OM arrays with 6 (a-b) and 7 (c) particles. The insets show the corresponding averaged incoherent (darkfield) images. (d-f) Simulated coherent (backscattered) images each of the three OM arrays as panels a, b, and c, respectively. (g-i) Simulated near-field electric field intensity for each of the OM arrays in a, b, and c, respectively.

Figure B.1(a-c) shows the experimentally measured images of three different optical matter

arrays. The corresponding images from simulation, Figure B.1(d-f), are in good agreement with the experiment. Additionally, Figure B.1(g-i) shows the near-fields around the optical matter array calculated in simulation. The interference fringes in the near field appear somewhat similar to those in the images.

To investigate the similarities between near-fields and far-field images, the two are compared analytically using the point dipole approximation. In the near-field of a single particle, the electric field is due to an incident field and a scattered field

$$E(\rho,\phi) = E_0 + \tilde{A}\frac{\exp(ik\rho)}{k\rho} \tag{B.11}$$

where $\tilde{A}$ is a complex constant related to the NP's polarizability. The intensity is then

$$I(\rho,\phi) = E_0^2 + 2E_0|\tilde{A}|\frac{\cos(k\rho+\varphi_s)}{k\rho} \tag{B.12}$$

where φ_s is a phase shift factor. This is the near-field image due to a single particle.

For a point dipole $\boldsymbol{\mu}_i$ located at the origin, the field in the image plane is

$$\boldsymbol{E}(\rho,\phi) = \frac{\omega^2}{\varepsilon_0 c^2}\overleftrightarrow{\boldsymbol{G}}_{\text{psf}}(\rho,\phi)\cdot\boldsymbol{\mu} \tag{B.13}$$

where $\overleftrightarrow{\boldsymbol{G}}_{\text{psf}}$ is the dyadic point-spread function. [67] In the paraxial limit, the field in the image plane is

$$\boldsymbol{E}(\rho,\phi) = \tilde{B}\frac{J_1[k\rho\sin(\theta_{\text{obj}})]}{k\rho}\boldsymbol{\mu} \tag{B.14}$$

where $\tilde{B}$ is a complex constant and J_1 is a Bessel function. The Bessel function can be replaced by its assymptotic form,

$$J_1[x] \approx -\sqrt{\frac{2}{\pi x}}\cos(x+\pi/4) \tag{B.15}$$

so that the electric field can be approximated as

$$\boldsymbol{E}(\rho,\phi) \propto \tilde{B}\frac{\cos(k\rho\sin(\theta_{\text{obj}})+\pi/4)}{(k\rho)^{3/2}}\boldsymbol{\mu} \tag{B.16}$$

If we include the field reflected off the water-glass interface, the far-field becomes

$$\boldsymbol{E}(\rho,\phi) \propto E_r + \tilde{B}\frac{\cos(k\rho\sin(\theta_{\text{obj}}) + \pi/4)}{(k\rho)^{3/2}}\boldsymbol{\mu} \tag{B.17}$$

and the intensity is

$$I(\rho,\phi) \propto E_r^2 + 2E_r|\tilde{B}||\boldsymbol{\mu}|\frac{\cos(k\rho\sin(\theta_{\text{obj}}) + \pi/4)}{(k\rho)^{3/2}} \tag{B.18}$$

Equation (B.18) is comparable to Equation (B.12). The image intensity modulation falls off faster as $\rho^{3/2}$ and has a permanent, fixed phase shift of $\pi/4$ that is independent of the particles polarizability. The length scale in image space is given by $1/k\sin(\theta_{\text{obj}})$, which is generally longer than the $1/k$ length scale of the near-field intensity. For a perfect objective ($\theta_{\text{obj}} = \pi/2$), the length scales are identical.

APPENDIX C
LIGHT FIELDS

The angular spectrum of light represents a beam of light in Fourier ($\boldsymbol{k}$) space, $\boldsymbol{E}_\infty(k_x, k_y)$. Given the angular spectrum, the fields focused by an objective can be evaluated using the theory developed by Richards and Wolfs [181, 182]

$$\boldsymbol{E}(\boldsymbol{r}) = \frac{ife^{-ikf}}{2\pi} \iint\limits_{(k_x^2+k_z^2)\leq k^2} \boldsymbol{E}_\infty(k_x, k_y) \exp(i\boldsymbol{k}\cdot\boldsymbol{r}) \frac{1}{k_z} dk_x dk_y \tag{C.1}$$

where $k_z = \sqrt{k^2 - k_x^2 - k_y^2}$, and f is the focal length of the objective. The integration occurs over all $\boldsymbol{k}$-vectors that satisfy the diffraction limit. If not for the $1/k_z$ factor in Equation (C.1), the focal fields and angular spectrum would be a Fourier transform pair. In the paraxial limit, $k_z \to k$ and they do become a Fourier transform pair.

Equation (C.1) can be represented in angular coordinates where it becomes an integration over a far-field hemisphere and the focal fields are in cylindrical coordinates

$$\boldsymbol{E}(\rho, \varphi, z) = \frac{ife^{-ikf}}{2\pi} \int_0^{\theta_{\max}} \int_0^{2\pi} \boldsymbol{E}_\infty(\theta, \phi) \exp(ikz\cos\theta) \exp(ik\rho\sin\theta\cos(\phi-\varphi)) \sin\theta d\phi d\theta \tag{C.2}$$

where $\theta_{\max}$ is determined by the numerical aperture of the objective ($\mathrm{NA} = n\sin(\theta_{\max})$).

The scalar angular spectrum for Gaussian, Hermite-Gaussian, and Laguerre-Gaussian type beams are known and listed below. [67, 183] The polarized angular spectrum is obtained by adding a global polarization state to the scalar angular spectrum. Paraxial expressions for each of the beams can be obtained by evaluating the above integrals in the appropriate limit. These paraxial expressions are also listed below for each beam. For tightly focused beams (high NA), the integrals above should always be used to calculate focal fields rather than the paraxial expressions.

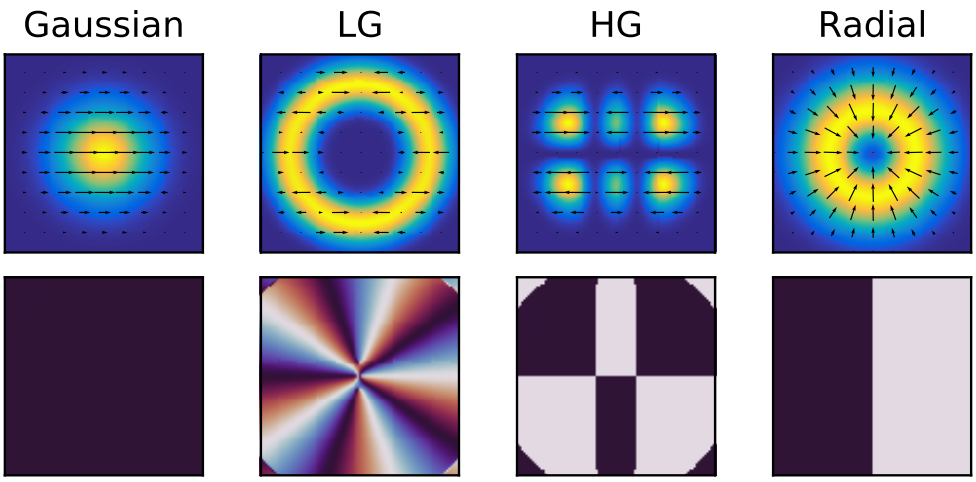

Figure C.1: Visualizing different beams of light. (top) Intensity and polarization of an x-polarized Gaussian, x-polarized LG beam ($p = 1$, $l = 5$), x-polarized HG beam ($l = 2$, $m = 3$), and radial polarized beam. (bottom) Corresponding phase profiles for E_x in the xy-plane for each beam.

C.1 Gaussian beams

Paraxial expression

$$\boldsymbol{E}(\rho, \phi, z) = \hat{\boldsymbol{p}} E_0 \frac{w_0}{w(z)} \exp \frac{-\rho^2}{w(z)^2} \exp \left[-i(kz + k\frac{\rho^2}{2R(z)} - \psi(z)) \right] \tag{C.3}$$

where $w(z) = w_0\sqrt{1 + (z/z_R)^2}$ is the evolving beam waist, $z_R = \frac{1}{2}kw_0^2$ is the Rayleigh range, $R(z) = z(1 + (z_R/z)^2)$ is the radius of curvature, and $\psi(z) = \arctan(z/z_R)$ is the Gouy phase shift.

Scalar angular spectrum

$$S(\theta, \phi) = \exp\left[(-kw_0 \tan(\theta)/2)^2\right] \tag{C.4}$$

C.2 Hermite-Gaussian beams

Paraxial expression

$$\boldsymbol{HG}_{l,m}(x, y, z) = H_l\left(\frac{\sqrt{2}x}{w(z)}\right) H_m\left(\frac{\sqrt{2}x}{w(z)}\right) \boldsymbol{HG}_{0,0}(x, y, z) \tag{C.5}$$

where (l, m) are integers defining the order of the HG beam, H_l, H_m are Hermite polynomials, and $\boldsymbol{HG}_{0,0}$ is a Gaussian beam. The Gouy phase is also changed from a Gaussian, $\psi(z) =$

$(l+m+1)\arctan(z/z_R)$.

Scalar angular spectrum

$$S(\theta,\phi) = (-i)^{l+m} H_l\left(\frac{kw_0}{\sqrt{2}}\tan(\theta)\cos(\phi)\right) H_m\left(\frac{kw_0}{\sqrt{2}}\tan(\theta)\sin(\phi)\right)\exp\left[(-kw_0\tan(\theta)/2)^2\right] \quad \text{(C.6)}$$

C.3 Laguerre-Gaussian beams

Paraxial expression

$$\boldsymbol{LG}_{l,p}(\rho,\phi,z) = \left(\frac{\sqrt{2}\rho}{w(z)}\right)^{|l|} L_p^{|l|}\left(\frac{2\rho^2}{w(z)^2}\right)\exp(-il\phi)\boldsymbol{LG}_{0,0}(\rho,\phi,z) \quad \text{(C.7)}$$

where p is an integer defining the order of the LG beam, l is the topological charge of the optical vortex, L_p^l are the generalized Laguerre polynomials, and $\boldsymbol{LG}_{0,0}$ is a Gaussian beam. The Gouy phase is also changed from a Gaussian, $\psi(z) = (|l|+2p+1)\arctan(z/z_R)$.

Scalar angular spectrum

$$S(\theta,\phi) = i(kw_0\tan(\theta)/\sqrt{2})^{|l|}\exp(il\phi)L_p^{|l|}\left[\left(\frac{kw_0}{2}\tan(\theta)\right)^2\right]\exp\left[(-kw_0\tan(\theta)/2)^2\right] \quad \text{(C.8)}$$

C.4 Vector beams

Vector beams are created by superimposing the lowest order Hermite-Gaussian beams.

Radially polarized vector beam

$$\boldsymbol{RP}(x,y,z) = \hat{\boldsymbol{x}}HG_{1,0}(x,y,z) + \hat{\boldsymbol{y}}HG_{0,1}(x,y,z) \quad \text{(C.9)}$$

Azimuthally polarized vector beam

$$\boldsymbol{AP}(x,y,z) = -\hat{\boldsymbol{y}}HG_{1,0}(x,y,z) + \hat{\boldsymbol{x}}HG_{0,1}(x,y,z) \quad \text{(C.10)}$$

Shear polarized vector beam

$$\boldsymbol{SP}(x,y,z) = \hat{\boldsymbol{y}}HG_{1,0}(x,y,z) + \hat{\boldsymbol{x}}HG_{0,1}(x,y,z) \quad \text{(C.11)}$$

C.5 Simulating a spatial light modulator using phase functions

A phase-only spatial light modulator modulates the phase of a propagating beam before it is focused by the objective. If a beam has an angular spectrum $S(\theta, \phi)$, then the angular spectrum modulated by an SLM is

$$S^{\text{SLM}}(\theta, \phi) = \exp(i\Phi(\theta, \phi))S(\theta, \phi) \tag{C.12}$$

where $\Phi(\theta, \phi)$ is the phase function on the SLM in spherical coordinates. In cartestian coordinates, the phase on the SLM is $\Phi(x, y)$, where $x = f\sin(\theta)\sin(\phi)$ and $y = f\sin(\theta)\cos(\phi)$ and f is the focal length of the objective. In this way, a 2D grid SLM with $N_x \times N_y$ pixels can be simulated in simulation.

REFERENCES

1. Kepler, J. De cometis libelli tres (1619).

2. Maxwell, J. C. VIII. A dynamical theory of the electromagnetic field. *Philosophical transactions of the Royal Society of London,* 459–512 (1865).

3. Lebedew, P. Untersuchungen über die Druckkräfte des Lichtes. *Annalen der Physik* **311,** 433–458 (1901).

4. Ashkin, A., Dziedzic, J. M., Bjorkholm, J. & Chu, S. Observation of a single-beam gradient force optical trap for dielectric particles. *Optics Letters* **11,** 288–290 (1986).

5. Pelton, M., Liu, M., Kim, H. Y., Smith, G., Guyot-Sionnest, P. & Scherer, N. F. Optical trapping and alignment of single gold nanorods by using plasmon resonances. *Optics Letters* **31,** 2075–2077 (2006).

6. Ashkin, A. History of optical trapping and manipulation of small-neutral particle, atoms, and molecules. *IEEE Journal of Selected Topics in Quantum Electronics* **6,** 841–856 (2000).

7. Grier, D. G. A revolution in optical manipulation. *Nature* **424,** 810–816 (2003).

8. Bowman, R. W. & Padgett, M. J. Optical Trapping and Binding. *Rep. Prog. Phys* **76,** 026401 (2013).

9. Simpson, S. H., Zemánek, P., Maragò, O. M., Jones, P. H. & Hanna, S. Optical binding of nanowires. *Nano Letters* **17,** 3485–3492 (2017).

10. Burns, M. M., Fournier, J. M. & Golovchenko, J. A. Optical Binding. *Phys. Rev. Lett.* **63,** 1233–1236. ISSN: 00319007 (1989).

11. Tatarkova, S. A., Carruthers, A. E. & Dholakia, K. One-Dimensional Optically Bound Arrays of Microscopic Particles. *Phys. Rev. Lett.* **89,** 283901 (2002).

12. Demergis, V. & Florin, E.-L. Ultrastrong Optical Binding of Metallic Nanoparticles. *Nano Lett.* **12,** 5756–5760 (2012).

13. Chvátal, L., Brzobohat, O. & Zemánek, P. Binding of a Pair of Au Nanoparticles in a Wide Gaussian Standing Wave. *Opt. Rev.* **22,** 157–161 (2015).

14. Albaladejo, S., Sáenz, J. J. & Marqués, M. I. Plasmonic Nanoparticle Chain in a Light Field: A Resonant Optical Sail. *Nano Lett.* **11,** 4597–4600 (2011).

15. Taylor, J. & Love, G. Spontaneous Symmetry Breaking and Circulation by Optically Bound Microparticle Chains in Gaussian Beam Traps. *Phys. Rev. A* **80,** 053808 (2009).

16. Damková, J., Chvátal, L., Ježek, J., Oulehla, J., Brzobohat, O. & Zemánek, P. Enhancement of the 'Tractor-Beam' Pulling Force on an Optically Bound Structure. *Light: Science & Applications* **7,** 17135 (2018).

17. Rodrigo, J. A. & Alieva, T. Light-driven transport of plasmonic nanoparticles on demand. *Scientific Reports* **6,** 33729 (2016).

18. Čižmár, T., Romero, L. D., Dholakia, K. & Andrews, D. Multiple optical trapping and binding: new routes to self-assembly. *Journal of Physics B: Atomic, Molecular and Optical Physics* **43,** 102001 (2010).

19. Burns, M. M., Fournier, J.-M. & Golovchenko, J. A. Optical matter: crystallization and binding in intense optical fields. *Science* **249,** 749–754 (1990).

20. Dufresne, E. R. & Grier, D. G. Optical tweezer arrays and optical substrates created with diffractive optics. *Review of Scientific Instruments* **69,** 1974–1977 (1998).

21. Korda, P. T., Taylor, M. B. & Grier, D. G. Kinetically locked-in colloidal transport in an array of optical tweezers. *Physical Review Letters* **89,** 128301 (2002).

22. Polin, M., Grier, D. G. & Quake, S. R. Anomalous vibrational dispersion in holographically trapped colloidal arrays. *Physical Review Letters* **96,** 088101 (2006).

23. Yan, Z., Shah, R. A., Chado, G., Gray, S. K., Pelton, M. & Scherer, N. F. Guiding spatial arrangements of silver nanoparticles by optical binding interactions in shaped light fields. *ACS Nano* **7,** 1790–1802 (2013).

24. Yan, Z., Manna, U., Qin, W., Camire, A., Guyot-Sionnest, P. & Scherer, N. F. Hierarchical photonic synthesis of hybrid nanoparticle assemblies. *The Journal of Physical Chemistry Letters* **4,** 2630–2636 (2013).

25. Yan, Z., Gray, S. K. & Scherer, N. F. Potential energy surfaces and reaction pathways for light-mediated self-organization of metal nanoparticle clusters. *Nature Communications* **5,** 1–7 (2014).

26. Bao, Y., Yan, Z. & Scherer, N. F. Optical printing of electrodynamically coupled metallic nanoparticle arrays. *The Journal of Physical Chemistry C* **118,** 19315–19321 (2014).

27. Svak, V., Brzobohat, O., Šiler, M., Jákl, P., Kaňka, J., Zemánek, P. & Simpson, S. Transverse spin forces and non-equilibrium particle dynamics in a circularly polarized vacuum optical trap. *Nature Communications* **9,** 1–8 (2018).

28. Nieminen, T. A., Stilgoe, A. B., Heckenberg, N. R. & Rubinsztein-Dunlop, H. Angular momentum of a strongly focused Gaussian beam. *Journal of Optics A: Pure and Applied Optics* **10,** 115005 (2008).

29. Roichman, Y., Sun, B., Roichman, Y., Amato-Grill, J. & Grier, D. G. Optical forces arising from phase gradients. *Physical Review Letters* **100,** 013602 (2008).

30. Roichman, Y. & Grier, D. G. *Three-Dimensional Holographic Ring Traps* in *Proc. SPIE* (eds Andrews, D. L., Galvez, E. J. & Nienhuis, G.) **6483** (Feb. 2007), 64830F. http://dx.doi.org/10.1117/12.701034%20http://proceedings.spiedigitallibrary.org/proceeding.aspx?doi=10.1117/12.701034.

31. Yan, Z., Sajjan, M. & Scherer, N. F. Fabrication of a material assembly of silver nanoparticles using the phase gradients of optical tweezers. *Physical Review Letters* **114,** 143901 (2015).

32. Peterson, C. W., Parker, J., Rice, S. A. & Scherer, N. F. Controlling the dynamics and optical binding of nanoparticle homodimers with transverse phase gradients. *Nano Letters* **19,** 897–903 (2019).

33. Yifat, Y., Sule, N., Figliozzi, P. & Scherer, N. F. *Polarization dependent particle dynamics in simple traps* in *Optical Trapping and Optical Micromanipulation XIII* **9922** (2016), 99220R.

34. Nan, F., Han, F., Scherer, N. F. & Yan, Z. Dissipative Self-Assembly of Anisotropic Nanoparticle Chains with Combined Electrodynamic and Electrostatic Interactions. *Advanced Materials* **30,** 1803238 (2018).

35. Han, F., Parker, J. A., Yifat, Y., Peterson, C., Gray, S. K., Scherer, N. F. & Yan, Z. Crossover from positive to negative optical torque in mesoscale optical matter. *Nature Communications* **9,** 1–8 (2018).

36. Roichman, Y., Sun, B., Stolarski, A. & Grier, D. G. Influence of nonconservative optical forces on the dynamics of optically trapped colloidal spheres: the fountain of probability. *Physical Review Letters* **101,** 128301 (2008).

37. Magnasco, M. O. Forced thermal ratchets. *Physical Review Letters* **71,** 1477 (1993).

38. Lee, S.-H. & Grier, D. G. One-dimensional optical thermal ratchets. *Journal of Physics: Condensed Matter* **17,** S3685 (2005).

39. Yan, Z., Jureller, J. E., Sweet, J., Guffey, M. J., Pelton, M. & Scherer, N. F. Three-dimensional optical trapping and manipulation of single silver nanowires. *Nano Letters* **12,** 5155–5161 (2012).

40. Yan, Z. & Scherer, N. F. Optical vortex induced rotation of silver nanowires. *The Journal of Physical Chemistry Letters* **4,** 2937–2942 (2013).

41. Figliozzi, P., Sule, N., Yan, Z., Bao, Y., Burov, S., Gray, S. K., Rice, S. A., Vaikuntanathan, S. & Scherer, N. F. Driven optical matter: Dynamics of electrodynamically coupled nanoparticles in an optical ring vortex. *Physical Review E* **95,** 022604 (2017).

42. Figliozzi, P., Peterson, C. W., Rice, S. A. & Scherer, N. F. Direct visualization of barrier crossing dynamics in a driven optical matter system. *ACS Nano* **12,** 5168–5175 (2018).

43. Ng, J., Lin, Z., Chan, C. & Sheng, P. Photonic clusters formed by dielectric microspheres: Numerical simulations. *Physical Review B* **72,** 085130 (2005).

44. Sukhov, S., Shalin, A., Haefner, D. & Dogariu, A. Actio et reactio in optical binding. *Optics Express* **23,** 247–252 (2015).

45. Yifat, Y., Coursault, D., Peterson, C. W., Parker, J., Bao, Y., Gray, S. K., Rice, S. A. & Scherer, N. F. Reactive optical matter: light-induced motility in electrodynamically asymmetric nanoscale scatterers. *Light: Science & Applications* **7,** 1–7 (2018).

46. Sule, N., Yifat, Y., Gray, S. K. & Scherer, N. F. Rotation and negative torque in electrodynamically bound nanoparticle dimers. *Nano Letters* **17,** 6548–6556 (2017).

47. Parker, J., Peterson, C. W., Yifat, Y., Yan, Z., Gray, S. K., Rice, S. A. & Scherer, N. F. An Optical Matter Machine: Angular Momentum Conversion by Collective Modes in Optically Bound Nanoparticle Arrays. *Optica (accepted)* (2020).

48. Yevick, A., Evans, D. J. & Grier, D. G. Photokinetic analysis of the forces and torques exerted by optical tweezers carrying angular momentum. *Philosophical Transactions of the Royal Society A: Mathematical, Physical and Engineering Sciences* **375,** 20150432 (2017).

49. Simpson, S. H. & Hanna, S. First-order nonconservative motion of optically trapped nonspherical particles. *Physical Review E* **82,** 031141 (2010).

50. Taflove, A. & Hagness, S. C. *Computational electrodynamics: the finite-difference time-domain method* (Artech house, 2005).

51. Sule, N., Rice, S., Gray, S. & Scherer, N. An electrodynamics-Langevin dynamics (ED-LD) approach to simulate metal nanoparticle interactions and motion. *Optics Express* **23,** 29978–29992 (2015).

52. McCormack, P., Han, F. & Yan, Z. Self-organization of metal nanoparticles in light: electrodynamics–molecular dynamics simulations and optical binding experiments. *The Journal of Physical Chemistry Letters* **9,** 545–549 (2018).

53. Draine, B. T. & Flatau, P. J. Discrete-dipole approximation for scattering calculations. *JOSA A* **11,** 1491–1499 (1994).

54. Xiao-Ming, Z., Jun-Jun, X. & Qiang, Z. Optical binding forces between plasmonic nanocubes: A numerical study based on discrete-dipole approximation. *Chinese Physics B* **23,** 017302 (2013).

55. Karásek, V. & Zemánek, P. *Optical binding—application of DDA* in *DDA-Workshop Institut für Werkstofftechnik Bremen, 23. March 2007* (), 7.

56. Bui, A. A., Stilgoe, A. B., Lenton, I. C., Gibson, L. J., Kashchuk, A. V., Zhang, S., Rubinsztein-Dunlop, H. & Nieminen, T. A. Theory and practice of simulation of optical tweezers. *Journal of Quantitative Spectroscopy and Radiative Transfer* **195,** 66–75 (2017).

57. Nieminen, T. A., Loke, V. L., Stilgoe, A. B., Knöner, G., Brańczyk, A. M., Heckenberg, N. R. & Rubinsztein-Dunlop, H. Optical tweezers computational toolbox. *Journal of Optics A: Pure and Applied Optics* **9,** S196 (2007).

58. Svelto, O. & Hanna, D. C. *Principles of lasers* (Springer, 2010).

59. Manna, U., Lee, J.-H., Deng, T.-S., Parker, J., Shepherd, N., Weizmann, Y. & Scherer, N. F. Selective induction of optical magnetism. *Nano Letters* **17,** 7196–7206 (2017).

60. Parker, J., Gray, S. & Scherer, N. F. *Optical magnetism in core-satellite nanostructures excited by vector beams* in *Photonic and Phononic Properties of Engineered Nanostructures VIII* **10541** (2018), 105411I.

61. Deng, T.-S., Parker, J., Yifat, Y., Shepherd, N. & Scherer, N. F. Dark plasmon modes in symmetric gold nanoparticle dimers illuminated by focused cylindrical vector beams. *The Journal of Physical Chemistry C* **122,** 27662–27672 (2018).

62. Manna, U., Parker, J., Sugimoto, H., Coe, B., Eggena, D., Fujii, M., Scherer, N. & Gray, S. Excitation of non-radiating anapoles in dielectric nanospheres. *Bulletin of the American Physical Society* **65** (2020).

63. Rubinsztein-Dunlop, H., Nieminen, T. A., Friese, M. E. & Heckenberg, N. R. in *Advances in quantum chemistry* 469–492 (Elsevier, 1998).

64. La Porta, A. & Wang, M. D. Optical torque wrench: angular trapping, rotation, and torque detection of quartz microparticles. *Physical Review Letters* **92,** 190801 (2004).

65. Dholakia, K. & Zemánek, P. Colloquium: Gripped by light: Optical binding. *Reviews of Modern Physics* **82,** 1767 (2010).

66. Andrews, D. L., Bradshaw, D. S. & Romero, L. C. D. Multiple light scattering and optomechanical forces. *Journal of Nanophotonics* **4,** 041565 (2010).

67. Novotny, L. & Hecht, B. *Principles of nano-optics* (Cambridge university press, 2012).

68. Mie, G. Beiträge zur Optik trüber Medien, speziell kolloidaler Metallösungen. *Annalen der Physik* **330,** 377–445 (1908).

69. Bohren, C. F. & Huffman, D. R. *Absorption and scattering of light by small particles* (John Wiley & Sons, 2008).

70. Hulst, H. C. & van de Hulst, H. C. *Light scattering by small particles* (Courier Corporation, 1981).

71. Lock, J. A. & Gouesbet, G. Generalized Lorenz–Mie theory and applications. *Journal of Quantitative Spectroscopy and Radiative Transfer* **110,** 800–807 (2009).

72. Maheu, B., Gouesbet, G. & Gréhan, G. A concise presentation of the generalized Lorenz-Mie theory for arbitrary location of the scatterer in an arbitrary incident profile. *Journal of Optics* **19,** 59 (1988).

73. Gouesbet, G., Grehan, G. & Maheu, B. Computations of the gn coefficients in the generalized Lorenz-Mie theory using three different methods. *Applied Optics* **27,** 4874–4883 (1988).

74. Xu, Y.-l. Electromagnetic scattering by an aggregate of spheres. *Applied Optics* **34,** 4573–4588 (1995).

75. Stein, S. Addition theorems for spherical wave functions. *Quarterly of Applied Mathematics* **19,** 15–24 (1961).

76. Waterman, P. Matrix formulation of electromagnetic scattering. *Proceedings of the IEEE* **53,** 805–812 (1965).

77. Mackowski, D. W. & Mishchenko, M. I. Calculation of the T matrix and the scattering matrix for ensembles of spheres. *JOSA A* **13,** 2266–2278 (1996).

78. Mackowski, D. W. Exact solution for the scattering and absorption properties of sphere clusters on a plane surface. *Journal of Quantitative Spectroscopy and Radiative Transfer* **109,** 770–788 (2008).

79. Hutter, E. & Fendler, J. H. Exploitation of localized surface plasmon resonance. *Advanced Materials* **16,** 1685–1706 (2004).

80. Johnson, P. B. & Christy, R.-W. Optical constants of the noble metals. *Physical Review B* **6,** 4370 (1972).

81. Doane, T. L., Chuang, C.-H., Hill, R. J. & Burda, C. Nanoparticle ζ-potentials. *Accounts of Chemical Research* **45,** 317–326 (2012).

82. Sukhov, S. & Dogariu, A. Non-Conservative Optical Forces. *Rep. Prog. Phys* **80,** 112001 (2017).

83. Humphrey, A. D. & Barnes, W. L. Plasmonic surface lattice resonances on arrays of different lattice symmetry. *Physical Review B* **90,** 075404 (2014).

84. Thio, T., Ghaemi, H., Lezec, H., Wolff, P. & Ebbesen, T. Surface-plasmon-enhanced transmission through hole arrays in Cr films. *JOSA B* **16,** 1743–1748 (1999).

85. Guo, R., Hakala, T. K. & Törmä, P. Geometry dependence of surface lattice resonances in plasmonic nanoparticle arrays. *Physical Review B* **95,** 155423 (2017).

86. Väkeväinen, A., Moerland, R., Rekola, H., Eskelinen, A.-P., Martikainen, J.-P., Kim, D.-H. & Törmä, P. Plasmonic surface lattice resonances at the strong coupling regime. *Nano Letters* **14,** 1721–1727 (2014).

87. Han, F. & Yan, Z. Phase Transition and Self-Stabilization of Light-Mediated Metal Nanoparticle Assemblies. *ACS Nano* (2020).

88. Nieminen, T. A., Heckenberg, N. R. & Rubinsztein-Dunlop, H. Optical measurement of microscopic torques. *Journal of Modern Optics* **48,** 405–413 (2001).

89. Jackson, J. D. *Classical electrodynamics* 1999.

90. Ivlev, A., Bartnick, J., Heinen, M., Du, C.-R., Nosenko, V. & Löwen, H. Statistical mechanics where Newton's third law is broken. *Physical Review X* **5,** 011035 (2015).

91. Karásek, V., Šiler, M., Brzobohat, O. & Zemánek, P. Dynamics of an optically bound structure made of particles of unequal sizes. *Optics Letters* **42,** 1436–1439 (2017).

92. Moroz, A. Depolarization field of spheroidal particles. *JOSA B* **26,** 517–527 (2009).

93. Forgy, E. W. Cluster analysis of multivariate data: efficiency versus interpretability of classifications. *Biometrics* **21,** 768–769 (1965).

94. Buitinck, L., Louppe, G., Blondel, M., Pedregosa, F., Mueller, A., Grisel, O., Niculae, V., Prettenhofer, P., Gramfort, A., Grobler, J., Layton, R., VanderPlas, J., Joly, A., Holt, B. & Varoquaux, G. *API design for machine learning software: experiences from the scikit-learn project* in *ECML PKDD Workshop: Languages for Data Mining and Machine Learning* (2013), 108–122.

95. Brady, J. F. & Bossis, G. Stokesian dynamics. *Annual Review of Fluid Mechanics* **20,** 111–157 (1988).

96. Chen, J., Ng, J., Ding, K., Fung, K. H., Lin, Z. & Chan, C. T. Negative optical torque. *Scientific Reports* **4,** 6386 (2014).

97. Chen, J., Wang, S., Li, X. & Ng, J. Mechanical effect of photonic spin-orbit interaction for a metallic nanohelix. *Optics Express* **26,** 27694–27704 (2018).

98. Pedaci, F., Huang, Z., Van Oene, M., Barland, S. & Dekker, N. H. Excitable particles in an optical torque wrench. *Nature Physics* **7,** 259 (2011).

99. Inman, J., Forth, S. & Wang, M. D. Passive torque wrench and angular position detection using a single-beam optical trap. *Optics Letters* **35,** 2949–2951 (2010).

100. Tong, L., Miljkovic, V. D. & Kall, M. Alignment, rotation, and spinning of single plasmonic nanoparticles and nanowires using polarization dependent optical forces. *Nano Letters* **10,** 268–273 (2009).

101. Canós Valero, A., Kislov, D., Gurvitz, E. A., Shamkhi, H. K., Pavlov, A. A., Redka, D., Yankin, S., Zemánek, P. & Shalin, A. S. Nanovortex-Driven All-Dielectric Optical Diffusion Boosting and Sorting Concept for Lab-on-a-Chip Platforms. *Advanced Science* **7,** 1903049 (2020).

102. Brzobohat, O., Šiler, M., Trojek, J., Chvátal, L., Karásek, V. & Zemánek, P. Non-spherical gold nanoparticles trapped in optical tweezers: shape matters. *Optics Express* **23,** 8179–8189 (2015).

103. Barton, J. P., Alexander, D. R. & Schaub, S. A. Theoretical Determination of Net Radiation Force and Torque for a Spherical Particle Illuminated by a Focused Laser Beam. en. *Journal of Applied Physics* **66,** 4594–4602. ISSN: 0021-8979, 1089-7550. `http://aip.scitation.org/doi/10.1063/1.343813` (2019) (Nov. 1989).

104. Nieminen, T. A., Asavei, T., Loke, V. L., Heckenberg, N. R. & Rubinsztein-Dunlop, H. Symmetry and the generation and measurement of optical torque. *Journal of Quantitative Spectroscopy and Radiative Transfer* **110,** 1472–1482 (2009).

105. Blickle, V. & Bechinger, C. Realization of a Micrometre-Sized Stochastic Heat Engine. en. *Nature Physics* **8,** 143–146. ISSN: 1745-2473, 1745-2481 (Feb. 2012).

106. Dechant, A., Kiesel, N. & Lutz, E. All-Optical Nanomechanical Heat Engine. en. *Physical Review Letters* **114.** ISSN: 0031-9007, 1079-7114 (May 2015).

107. Martınez, I. A., Roldán, É., Dinis, L., Petrov, D., Parrondo, J. M. & Rica, R. A. Brownian carnot engine. *Nature Physics* **12,** 67–70 (2016).

108. Coy, J. J., Townsend, D. P. & Zaretsky, E. V. *Gearing.* tech. rep. (NATIONAL AERONAUTICS and SPACE ADMINISTRATION CLEVELAND OH LEWIS RESEARCH CENTER, 1985).

109. Edmonds, A. R. *Angular momentum in quantum mechanics* (Princeton university press, 1996).

110. Wiscombe, W. J. Improved Mie Scattering Algorithms. en. *Applied Optics* **19,** 1505. ISSN: 0003-6935, 1539-4522. `https://www.osapublishing.org/abstract.cfm?URI=ao-19-9-1505` (2019) (May 1980).

111. Zou, S., Janel, N. & Schatz, G. C. Silver nanoparticle array structures that produce remarkably narrow plasmon lineshapes. *The Journal of Chemical Physics* **120,** 10871–10875 (2004).

112. De Abajo, F. G. Colloquium: Light scattering by particle and hole arrays. *Reviews of Modern Physics* **79,** 1267 (2007).

113. Risken, H. & Vollmer, H. Brownian motion in periodic potentials; nonlinear response to an external force. *Zeitschrift für Physik B Condensed Matter* **33,** 297–305 (1979).

114. Kuznetsov, A. I., Miroshnichenko, A. E., Brongersma, M. L., Kivshar, Y. S. & Luk'yanchuk, B. Optically resonant dielectric nanostructures. *Science* **354** (2016).

115. Nan, F. & Yan, Z. Sorting Metal Nanoparticles with Dynamic and Tunable Optical Driven Forces. *Nano Letters* **18,** 4500–4505 (2018).

116. Dickinson, E., Allison, S. A. & McCammon, J. A. Brownian dynamics with rotation–translation coupling. *Journal of the Chemical Society, Faraday Transactions 2: Molecular and Chemical Physics* **81,** 591–601 (1985).

117. Swan, J. W. & Brady, J. F. Simulation of hydrodynamically interacting particles near a no-slip boundary. *Physics of Fluids* **19,** 113306 (2007).

118. Hall, D. G. Vector-beam solutions of Maxwell's wave equation. *Optics Letters* **21,** 9–11 (1996).

119. Sheikholeslami, S. N., Alaeian, H., Koh, A. L. & Dionne, J. A. A metafluid exhibiting strong optical magnetism. *Nano Letters* **13,** 4137–4141 (2013).

120. Manna, U., Lee, J.-H., Deng, T.-S., Parker, J., Shepherd, N., Weizmann, Y. & Scherer, N. F. Selective induction of optical magnetism. *Nano Letters* **17,** 7196–7206 (2017).

121. Qian, Z., Hastings, S. P., Li, C., Edward, B., McGinn, C. K., Engheta, N., Fakhraai, Z. & Park, S. Raspberry-like metamolecules exhibiting strong magnetic resonances. *ACS Nano* **9,** 1263–1270 (2015).

122. Vallecchi, A., Albani, M. & Capolino, F. *EM characterization of Raspberry-like nanocluster metamaterials* in *Antennas and Propagation Society International Symposium (APSURSI), 2010 IEEE* (2010), 1–4.

123. Veselago, V. G. The electrodynamics of substances with simultaneously negative values of ϵ and μ. *Soviet Physics Uspekhi* **10,** 509 (1968).

124. Smith, D. R., Pendry, J. B. & Wiltshire, M. Metamaterials and negative refractive index. *Science* **305,** 788–792 (2004).

125. Fruhnert, M., Mühlig, S., Lederer, F. & Rockstuhl, C. Towards negative index self-assembled metamaterials. *Physical Review B* **89,** 075408 (2014).

126. Fang, N. & Zhang, X. *Imaging properties of a metamaterial superlens* in *Proceedings of the 2nd IEEE Conference on Nanotechnology* (2002), 225–228.

127. Zharov, A. A., Zharova, N. A., Noskov, R. E., Shadrivov, I. V. & Kivshar, Y. S. Birefringent left-handed metamaterials and perfect lenses for vectorial fields. *New Journal of Physics* **7,** 220 (2005).

128. Cai, W., Chettiar, U. K., Kildishev, A. V. & Shalaev, V. M. Optical cloaking with metamaterials. *Nature Photonics* **1,** 224–227 (2007).

129. Schurig, D., Mock, J. J., Justice, B., Cummer, S. A., Pendry, J. B., Starr, A. F. & Smith, D. R. Metamaterial electromagnetic cloak at microwave frequencies. *Science* **314,** 977–980 (2006).

130. Liu, M., Lee, T.-W., Gray, S. K., Guyot-Sionnest, P., Pelton, M., *et al.* Excitation of dark plasmons in metal nanoparticles by a localized emitter. *Physical Review Letters* **102,** 107401 (2009).

131. Miroshnichenko, A. E., Evlyukhin, A. B., Yu, Y. F., Bakker, R. M., Chipouline, A., Kuznetsov, A. I., Luk'yanchuk, B., Chichkov, B. N. & Kivshar, Y. S. Nonradiating anapole modes in dielectric nanoparticles. *Nature Communications* **6,** 1–8 (2015).

132. Parker, J. A., Sugimoto, H., Coe, B., Eggena, D., Fujii, M., Scherer, N. F., Gray, S. K. & Manna, U. Excitation of nonradiating anapoles in dielectric nanospheres. *Physical Review Letters* **124,** 097402 (2020).

133. Zhan, Q. Cylindrical vector beams: from mathematical concepts to applications. *Advances in Optics and Photonics* **1,** 1–57 (2009).

134. Halas, N. J., Lal, S., Chang, W.-S., Link, S. & Nordlander, P. Plasmons in strongly coupled metallic nanostructures. *Chemical Reviews* **111,** 3913–3961 (2011).

135. Prodan, E., Radloff, C., Halas, N. J. & Nordlander, P. A hybridization model for the plasmon response of complex nanostructures. *Science* **302,** 419–422 (2003).

136. Rengarajan, S. R. & Rahmat-Samii, Y. The field equivalence principle: Illustration of the establishment of the non-intuitive null fields. *IEEE Antennas and Propagation Magazine* **42,** 122–128 (2000).

137. Taflove, A. & Hagness, S. C. Computational electrodynamics: the finite-difference time-domain method. *Norwood, 2nd Edition, MA: Artech House* (1995).

138. Parker, J., Gray, S. & Scherer, N. Multipolar analysis of electric and magnetic modes excited by vector beams in core-satellite nano-structures. *arXiv preprint arXiv:1711.06833* (2017).

139. *MiePy* `https://github.com/johnaparker/miepy`.

140. *StokeD* `https://github.com/johnaparker/stoked`.

141. Xu, Y.-L. Efficient evaluation of vector translation coefficients in multiparticle light-scattering theories. *Journal of Computational Physics* **139,** 137–165 (1998).

142. Hovenier, J. W. Light scattering by non-spherical particles. *J Quant Spectrosc Radiat Transfer* **55.** pg. 269, 535–694 (1996).

143. Auguié, B., Somerville, W. R., Roache, S. & Le Ru, E. C. Numerical investigation of the Rayleigh hypothesis for electromagnetic scattering by a particle. *Journal of Optics* **18,** 075007 (2016).

144. Pulbere, S. & Wriedt, T. Light scattering by cylindrical fibers with high aspect ratio using the null-field method with discrete sources. *Particle & Particle Systems Characterization: Measurement and Description of Particle Properties and Behavior in Powders and Other Disperse Systems* **21,** 213–218 (2004).

145. Egel, A., Kettlitz, S. W. & Lemmer, U. Efficient evaluation of Sommerfeld integrals for the optical simulation of many scattering particles in planarly layered media. *JOSA A* **33,** 698–706 (2016).

146. Egel, A., Eremin, Y., Wriedt, T., Theobald, D., Lemmer, U. & Gomard, G. Extending the applicability of the T-matrix method to light scattering by flat particles on a substrate via truncation of sommerfeld integrals. *Journal of Quantitative Spectroscopy and Radiative Transfer* **202,** 279–285 (2017).

147. Van der Vorst, H. A. Bi-CGSTAB: A fast and smoothly converging variant of Bi-CG for the solution of nonsymmetric linear systems. *SIAM Journal on scientific and Statistical Computing* **13,** 631–644 (1992).

148. Egel, A. & Lemmer, U. Dipole emission in stratified media with multiple spherical scatterers: Enhanced outcoupling from OLEDs. *Journal of Quantitative Spectroscopy and Radiative Transfer* **148,** 165–176 (2014).

149. Egel, A., Theobald, D., Donie, Y., Lemmer, U. & Gomard, G. Light scattering by oblate particles near planar interfaces: on the validity of the T-matrix approach. *Optics Express* **24,** 25154–25168 (2016).

150. Xu, Y.-L. Scattering of electromagnetic waves by periodic particle arrays. *JOSA A* **30,** 1053–1068 (2013).

151. Barton, J., Alexander, D. & Schaub, S. Theoretical determination of net radiation force and torque for a spherical particle illuminated by a focused laser beam. *Journal of Applied Physics* **66,** 4594–4602 (1989).

152. Xu, Y.-l. Electromagnetic scattering by an aggregate of spheres: far field. *Applied Optics* **36,** 9496–9508 (1997).

153. Langevin, P. *On the theory of Brownian motion* (1908).

154. Van Kampen, N. G. *Stochastic processes in physics and chemistry* (Elsevier, 1992).

155. Kuipers, J. B. *Quaternions and rotation sequences: a primer with applications to orbits, aerospace, and virtual reality* (Princeton university press, 1999).

156. Favro, L. D. Theory of the rotational Brownian motion of a free rigid body. *Physical Review* **119,** 53 (1960).

157. Blundell, S. J. & Blundell, K. M. *Concepts in thermal physics* (OUP Oxford, 2009).

158. Iserles, A. Numerical recipes in C—the art of scientific computing, by WH Press, BP Flannery, SA Teukolsky and WT Vetterling. Pp 735.£ 27· 50. 1988. ISBN 0-521-35465-X (Cambridge University Press). *The Mathematical Gazette* **73,** 167–170 (1989).

159. Kim, S. & Karrila, S. J. *Microhydrodynamics: principles and selected applications* (Courier Corporation, 2013).

160. Chang, J. & Cooper, G. A practical difference scheme for Fokker-Planck equations. *Journal of Computational Physics* **6,** 1–16 (1970).

161. Holubec, V., Kroy, K. & Steffenoni, S. Physically consistent numerical solver for time-dependent Fokker-Planck equations. *Physical Review E* **99,** 032117 (2019).

162. Virnau, P. & Müller, M. Calculation of free energy through successive umbrella sampling. *The Journal of chemical physics* **120,** 10925–10930 (2004).

163. Dickinson, E., Allison, S. A. & Mccammon, J. A. Brownian Dynamics with Rotation-Translation Coupling. *J. Chem. SOC. Faraday Trans* **2,** 591–601 (1985).

164. Mazur, P. & van Saarloos, W. Many-sphere hydrodynamic interactions and mobilities in a suspension. *Physica A: Statistical Mechanics and its Applications* **115,** 21–57 (1982).

165. Jeffrey, D. & Onishi, Y. Calculation of the resistance and mobility functions for two unequal rigid spheres in low-Reynolds-number flow. *Journal of Fluid Mechanics* **139,** 261–290 (1984).

166. Butt, H.-J., Graf, K. & Kappl, M. *Physics and chemistry of interfaces* (John Wiley & Sons, 2013).

167. Pöschel, T. & Schwager, T. *Computational granular dynamics: models and algorithms* (Springer Science & Business Media, 2005).

168. Barber, P. & Yeh, C. Scattering of electromagnetic waves by arbitrarily shaped dielectric bodies. *Applied Optics* **14,** 2864–2872 (1975).

169. Mishchenko, M. I., Travis, L. D. & Mackowski, D. W. T-matrix computations of light scattering by nonspherical particles: a review. *Journal of Quantitative Spectroscopy and Radiative Transfer* **55,** 535–575 (1996).

170. Doicu, A., Wriedt, T. & Eremin, Y. A. *Light scattering by systems of particles: null-field method with discrete sources: theory and programs* (Springer, 2006).

171. Coursault, D., Sule, N., Parker, J., Bao, Y. & Scherer, N. F. Dynamics of the optically directed assembly and disassembly of gold nanoplatelet arrays. *Nano Letters* **18,** 3391–3399 (2018).

172. Simpson, S. H. & Hanna, S. Optical trapping of spheroidal particles in Gaussian beams. *JOSA A* **24,** 430–443 (2007).

173. Li, M., Yan, S., Yao, B., Liang, Y., Han, G. & Zhang, P. Optical trapping force and torque on spheroidal Rayleigh particles with arbitrary spatial orientations. *JOSA A* **33,** 1341–1347 (2016).

174. Doicu, A. & Wriedt, T. Calculation of the T matrix in the null-field method with discrete sources. *JOSA A* **16,** 2539–2544 (1999).

175. Gittes, F. & Schmidt, C. F. Interference model for back-focal-plane displacement detection in optical tweezers. *Optics Letters* **23,** 7–9 (1998).

176. Pralle, A., Prummer, M., Florin, E.-L., Stelzer, E. & Hörber, J. Three-dimensional high-resolution particle tracking for optical tweezers by forward scattered light. *Microscopy Research and Technique* **44,** 378–386 (1999).

177. Berg-Sørensen, K. & Flyvbjerg, H. Power spectrum analysis for optical tweezers. *Review of Scientific Instruments* **75,** 594–612 (2004).

178. Zhao, R., Tassin, P., Koschny, T. & Soukoulis, C. M. Optical forces in nanowire pairs and metamaterials. *Optics Express* **18,** 25665–25676 (2010).

179. Ekeroth, R. M. A. Optical interaction between small plasmonic nanowires: a perspective from induced forces and torques. *Journal of Optics* **18,** 085003 (2016).

180. Liu, W. & Kivshar, Y. S. Multipolar interference effects in nanophotonics. *Philosophical Transactions of the Royal Society A: Mathematical, Physical and Engineering Sciences* **375,** 20160317 (2017).

181. Richards, B. & Wolf, E. Electromagnetic diffraction in optical systems, II. Structure of the image field in an aplanatic system. *Proceedings of the Royal Society of London. Series A. Mathematical and Physical Sciences* **253,** 358–379 (1959).

182. Wolf, E. Electromagnetic diffraction in optical systems-I. An integral representation of the image field. *Proceedings of the Royal Society of London. Series A. Mathematical and Physical Sciences* **253,** 349–357 (1959).

183. Nieminen, T. A., Rubinsztein-Dunlop, H. & Heckenberg, N. R. Multipole expansion of strongly focussed laser beams. *Journal of Quantitative Spectroscopy and Radiative Transfer* **79,** 1005–1017 (2003).